IDAHO TRANSPORTATION DEPARTMENT

RESEARCH REPORT

Experimental Validation of Repair Methods for Earthquake-Damaged Bridges Incorporating ITD’s Precast Pier System

RP 302

By

Kathryn Hogarth, Manish Acharya, Arya Ebrahimpour, Mustafa Mashal

Idaho State University

Prepared for

Idaho Transportation Department

ITD Research Program, Planning Services

Highways Development

October 2023

YOUR Safety ••• ▶ YOUR Mobility ••• ▶ YOUR Economic Opportunity

Disclaimer

Technical Report Documentation Page

1. Report No.
FHWA-ID-302

2. Government Accession No.

3. Recipient's Catalog No.

4. Title and Subtitle
Experimental Validation of Repair Methods for Earthquake-Damaged Bridges Incorporating ITD's Precast Pier System

5. Report Date
October 2023

6. Performing Organization Code

7. Author(s)
Kathryn E. Hogarth, Manish Acharya, Arya Ebrahimpour,
Mustafa Mashal, https://orcid.org/0000-0003-4654-0531

8. Performing Organization Report No.
[Billing code]

9. Performing Organization Name and Address
Idaho State University
Department of Civil and Environmental Engineering
921 S. 8th Ave., Mail Stop 8060
Pocatello, ID 83209-8060

10. Work Unit No. (TRAIS)

11. Contract or Grant No.

12. Sponsoring Agency Name and Address
Idaho Transportation Department (SPR)
Highways Construction and Operations, Contracting Services, Research Program
PO Box 7129
Boise, ID 83707-7129

13. Type of Report and Period Covered
Final Report
09/01/2022 – 10/31/2023

14. Sponsoring Agency Code
RP-302

15. Supplementary Notes
Project performed in cooperation with the Idaho Transportation Department and Federal Highway Administration.

16. Abstract

The use of Ultra-High-Performance Concrete (UHPC) is gaining popularity for bridge applications in North America. UHPC has been used both in the construction of new and retrofitting of existing bridges. In this research, a novel use of UHPC as a concrete jacket for retrofitting of plastic hinge zones in cast-in-place and precast piers is proposed. Four large-scale cantilever pier specimens, two cast-in-place and two precast, are tested under cyclic quasi-static loading to drift ratios beyond Maximum Considered Earthquake (MCE). The piers are then retrofitted with UHPC jackets in their plastic hinge zones. The design philosophy for retrofitting is to shift the plastic hinge above the damaged region of a pier, thus re-instating capacity, stiffness, and ductility to the piers. Experimental results from testing of the piers along with guidelines on retrofitting and construction techniques are presented. It is shown that UHPC is indeed a competitive solution for retrofitting of concrete piers subjected to severe earthquake damage. All retrofitted piers achieved a similar level of base shear capacity as the original ones.

17. Key Words
Concrete Jacketing, Seismic Retrofit, Pipe Connection, Large-scale Testing, Ultra-High-Performance Concrete

18. Distribution Statement
Copies available from the [ITD Research Program](#)

19. Security Classification (of this report)
Unclassified

20. Security Classification (of this page)
Unclassified

21. No. of Pages
[Add the total # of pages]

22. Price
None

Acknowledgments

The authors are thankful of assistance from Matt Farrar, P.E. (Project Sponsor), Michael Johnson, P.E. (Project Manager), Dan Gorley, P.E. and Ned Parrish (Members of Technical Advisory Committee) from the Idaho Transportation Department, Ed Miltner, P.E. from the Federal Highway Administration (Idaho Advisor); and Bijan Khaleghi, Ph.D., P.E. (Research Associate Professor) from the Florida International University for peer-reviewing this report. The large-scale experimental testing would not have been possible without the great support from Jared Cantrell, Laboratory Manager and Research Engineer, and many other civil engineering students from the Department of Civil and Environmental Engineering at Idaho State University.

Technical Advisory Committee

Each research project is overseen by a Technical Advisory Committee (TAC), which is led by an ITD project sponsor and project manager. The TAC is responsible for monitoring project progress, reviewing deliverables, ensuring that study objectives are met, and facilitating implementation of research recommendations, as appropriate. ITD's Research Program Manager appreciates the work of the following TAC members in guiding this research study.

- Project Sponsor: Matt Farrar, P.E.
- Project Manager: Michael Johnson, P.E.
- TAC Members: Dan Gorley, P.E., Michael Johnson, P.E., Matt Farrar, P.E., Ned Parrish
- FHWA-Idaho Advisor: Ed Miltner, P.E.

Table of Contents

List of Tables

List of Figures

List of Abbreviations and Acronyms

AASHTO	The American Association of State Highway and Transportation Officials
ABC	Accelerated Bridge Construction
ACI	American Concrete Institute
ADAS	Added Damping, Added Stiffness
ASTM	American Society for Testing and Materials
BFRP	Basalt Fiber-Reinforced Polymer
BRBs	Buckling Restrained Braces
BRD	Buckling-Restrained Dry Damper
BRF	Buckling-Restrained Fused Type Damper
CFSTs	Concrete Filled Steel Tubes
CFRP	Carbon Fiber-Reinforced Polymer
CIP	Cast-in-Place
CTE	Coefficient of Thermal Expansion
DAQ	Data Acquisition System
DDTT	Double-Delayed Thermal Treatment
DTT	Direct Tension Test
DTT	Delayed Thermal Treatment
FEM	Finite Element Method
FHWA	Federal Highway Administration
FIU	Florida International University, Miami, Florida
FRC	Fiber-Reinforced Concrete
FRP	Fiber-Reinforced Polymer
GFRP	Glass Fiber-Reinforced Polymer
HES	High Early Strength
HFRP	Hybrid Fiber-Reinforced Polymer
HF2V	High Force to Volume Damper

HPFRCC	High-Performance Fiber-Reinforced Cement-Based Composites
HSS	Hollow Structural Section
LED	Lead Extrusive Device
LEL	Lillibridge Engineering Building at Idaho State University
ISU	Idaho State University
ITD	Idaho Transportation Department
NSC	Normal Strength Concrete
NTS	Not to Scale
PBES	Prefabricated Bridge Elements and Systems
PET	Polyethylene Terephthalate Fiber-Reinforced Polymer
PFRP	Polyester Fiber-Reinforced Polymer
PVC	Polyvinyl Chloride
RDM	Relative Dynamic Modulus
SC-BRB	Self-Centering Buckling-Restrained Brace
SLAB	Structural Laboratory
SMA	Shaper Memory Alloy
SIBC	Slide-in Bridge Construction
TAC	Technical Advisory Committee
TT	Thermal Treated
UHPC	Ultra-High-Performance Concrete
UHPFRC	Ultra-High-Performance Fiber Reinforced Concrete
UFPs	U-Shaped Flexural Plates
WSDOT	Washington State Department of Transportation
WSU	Washington State University

Executive Summary

Summary

In this project, a novel retrofitting method as part of the post-earthquake repairs are proposed and tested for a precast pier system that incorporates Concrete-Filled Steel Tubes (CFSTs) in the plastic hinges. The seismic performance of the precast pier system was investigated in ITD Report 281 (2021). A similar retrofit method is also incorporated and validated for cast-in-place (CIP) pier connections. The retrofit method offers simplicity in calculation, tolerance in construction, and excellent rehabilitation for concrete piers that have undergone significant seismic damage. The retrofit method utilizes ultra-high-performance concrete (UHPC) jacketing in the plastic hinge zones. In this method, UHPC is shown to provide substantial flexural and shear resistance, rehabilitating the column's original plastic hinge and shifting the plastic hinge to another desired location in the column. Results and observations from large-scale testing illustrate that the proposed retrofit method is successful at reinstating the lateral capacity of the piers. All retrofitted piers achieved a similar level of base shear capacity as the original ones.

Project Objective

The objective of this project is to investigate seismic performance of the proposed UHPC jacket retrofit in comparison with the original design of the columns, for the purpose of proving the retrofit's capabilities, experimentally.

Project Tasks

Task 1. Literature Review

This task includes a review of the technologies available/implemented for retrofit of concrete piers in the context of Accelerated Bridge Construction (ABC) and CIP pier connections. This task includes the following sub-tasks:

- Literature review of existing repair methods for Concrete-Filled Steel Tubes (CFSTs) and other relevant precast connections.
- Advantages and disadvantages for repair methods.
- Practicality and effectiveness of repair methods for concrete bridge piers.
- Literature review of UHPC, in general, as well as UHPC used in retrofit methods.
- Available technologies for seismic retrofit of concrete piers.

- Comparison of past studied retrofit methods from the perspective of seismic performance, constructability, etc.
- Experimental testing techniques for retrofitted columns.
- Review of retrofit methods that have been deployed in actual concrete pier systems.

A significant amount of research has been conducted on retrofit methods. The methods discussed include the use of seismic dissipaters, steel jacket, concrete jacketing, fiber-reinforced polymers (FRP), shape memory alloy (SMA) wire jacketing, and hybrid jacketing. Research for retrofit methods for concrete piers continues to be performed to improve and/or simplify rehabilitation of bridges. The research presented in the report aims to present a new retrofit method for the ITD Precast Pier connection and offer an alternative retrofit method for CIP piers.

Task 2. Experimental Investigation

This task is the main focus of the project and includes large-scale testing of precast and CIP piers with the proposed retrofit method (two precast piers and two CIP piers) under quasi-static cyclic loading. The retrofitted columns are octagonal sections, retrofitted with circular UHPC jackets. This task includes the following sub-tasks:

- Preliminary small-scale testing to quantify characteristics of UHPC to normal structural concrete (NSC) bond.
- Construction of small-scale specimens.
- Design of test set-up for small-scale specimens.
- Design of retrofit methods for specimens for experimental testing.
- Design of test set-up for large-scale testing.
- Construction of large-scale specimens.
- Materials characterization.
- Instrumentation and data acquisition system set-up for experimental testing.
- Experimental testing of the specimens up to failure point.
- Processing of the testing results.

Task 3. Evaluation and Results

This task covers the results from testing and gives in depth results of each test's findings. This task includes:

- Quantifying the effectiveness of the retrofit methods implemented.
- Comparison of the results from testing to the original design and experimental results of the specimens tested in Phase 1 of the project.
- Discussion on design and detailing of repair methods.

The original column designs are used as benchmarks to compare the performance of the retrofit method. The like piers are compared to one another (i.e. precast vs precast, and CIP vs CIP).

Task 4. Design Considerations and Recommendations

This task includes the following subtasks:

- Recommendations for design of piers with the proposed retrofit method.
- Recommendations for construction of the retrofit method.
- Discussion on advantages and disadvantages of the proposed repair method.
- Limitations of the retrofit method.
- Inspection recommendations for the retrofit method.

Task 5. Final Report

This task includes the following sub-tasks:

- Final presentation to ITD.
- Documentation of experimental process and results.
- Peer-review of the final report.
- Final report submission to ITD.

1. Introduction

In the first phase of this project, ITD Report 281 (2021), two half-scale bridge bents were designed and experimentally tested in the Idaho State University (ISU) Structural Lab (SLAB) under earthquake style loading. One of the bents modeled a typical cast-in-place (CIP) bridge connection, meanwhile the other bent modeled a pier connection developed by ISU and Idaho Transportation Department (ITD). The design of the new bridge connection will be discussed later in more detail. Both bridge bents were tested to failure and the results were processed and compared to one another. After testing the bent specimens, ISU and ITD have come back to work together on Phase II of the project, which is to retrofit the half-scale bridge piers and experimentally test and quantify design.

Background

As mentioned, Phase I introduced the telescoping pipe connection that was designed by ISU and ITD. The pipe connection was used in a half-scale bridge bent and tested in comparison with a half-scale CIP bent. Figure 1.1 and Figure 1.2 show diagrams of the telescoping pipe connection. Note that Figure 1.1 and Figure 1.2 are Not to Scale (NTS). The connection incorporates hollow structural sections (HSS) made from steel located within the plastic hinge of the column. HSS is installed at the end of the precast column. Half of the HSS extrudes from both ends of the precast column, and has centering fins welded to the outside edge of the pipe. The reinforcement for the column terminates at the top and bottom of the column with head terminators to improve rebar development length. The rebar is not to extrude from the ends of the column, for the purpose of preventing construction issues with alignment of grouted ducts or couplers. The column connects to the footing and cap by “feeding” the smaller pipe (of the column) into the larger pipe (of the footing/cap). The column pipe will be equipped with centering fins that have been welded at the precast plant, that have been sized to provide a secure fit into the footing/cap pipes, which eliminated the need for cap alignment and additional bracing for either column or cap after erection. The centering fins are not necessary structurally, but rather are only for inserting the column into the footing or cap beam.

Once the precast bent has been dry assembled, High-Early Strength (HES) grout is pumped into the gap between the two pipes to secure the connection after the column is erected. The next step in construction is to fill the hollow cap with HES concrete, which completes the cap installation. The Phase I connection suggests using expansion joint filler or an elastomeric ring placed around the column’s pipe to isolate the cap and column concrete around its perimeter and to allow for some level of deformations without crushing the concrete.

The advantage of the proposed connection is its simplicity, ample installation tolerance, ease of erection, use of hollow/partially hollow/solid pier caps (depending on project specifications), fast construction, use of non-proprietary components/materials, improved site safety, fully segmental construction, allowance of deformation during small movements, and outperformed seismic behavior of CIP bent.

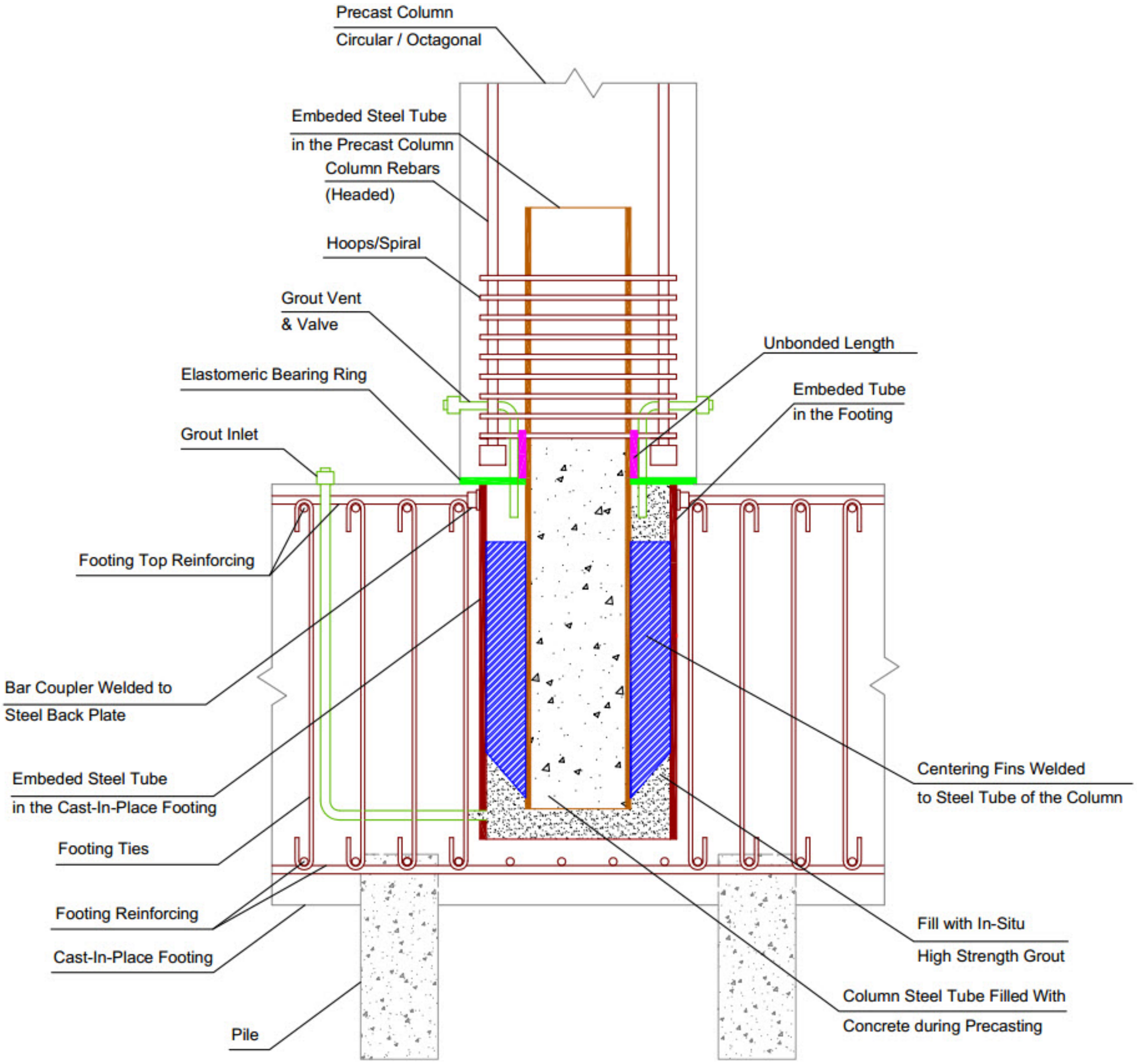

Figure 1.1 Column-to-Footing Connection (NTS)

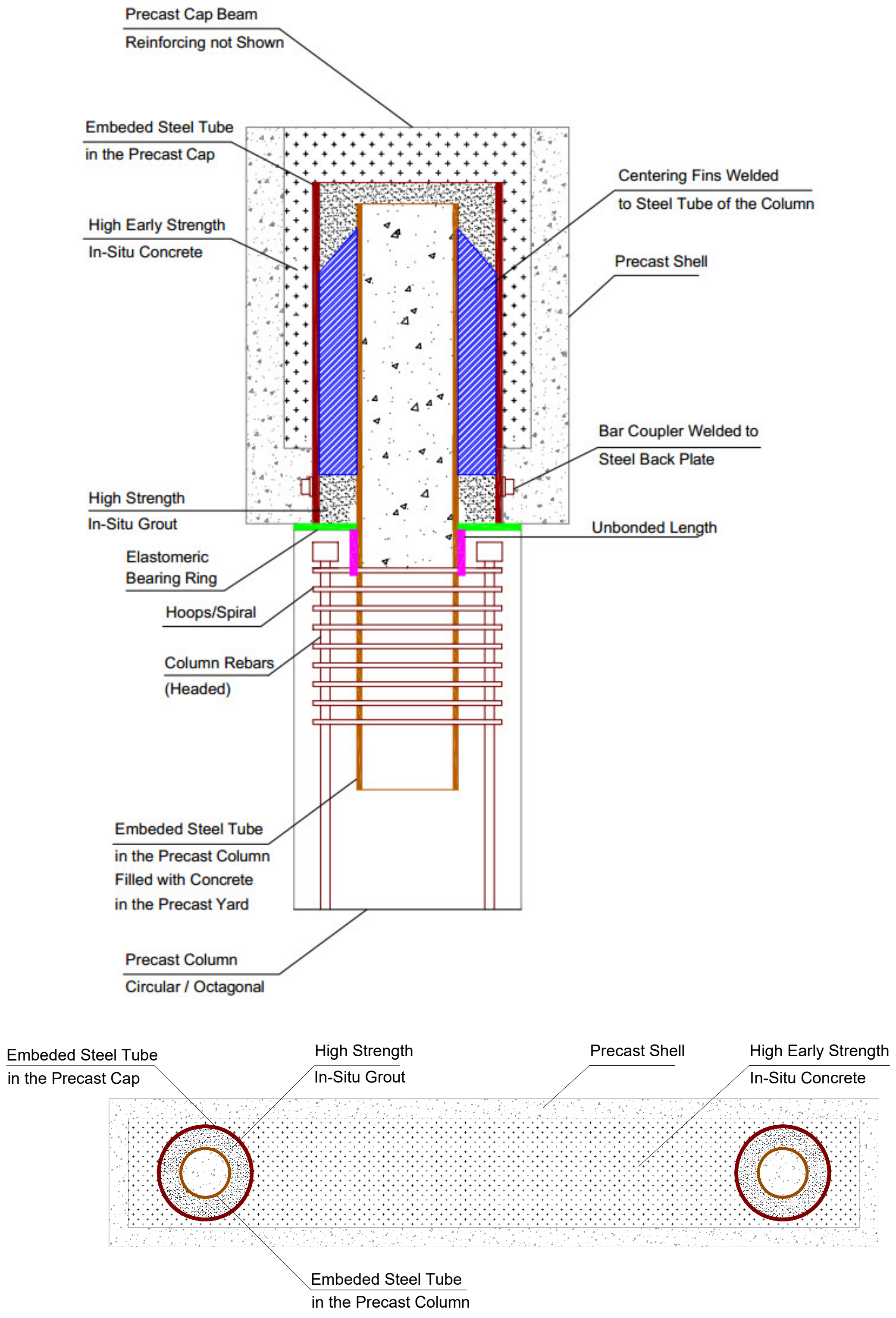

PLAN VIEW

Figure 1.2 Column-to-Cap Beam Connection and Cap Details (NTS)

In Phase I, both the CIP and Precast bents were designed identically in dimensions and performance capacities. Both bents were tested under quasi-static loading in the ISU SLAB using the same loading protocol. The two systems performed similarly during testing. Figure 1.3 gives the hysteresis from testing of the Precast and CIP bents. The Precast bent showed less overall damage than the CIP bent. The Precast bent also achieved a higher moment capacity, 498 kip-ft compared to the moment capacity of 468 kip-ft for the CIP bent. The Precast bent withstood 24 complete loading cycles, with an ultimate drift ratio of 9.15%. The CIP bent only withstood 15 loading cycles, resulting in an ultimate drift ratio of 4.94%. The Precast bent achieved maximum force 71.4 kip at 2.69% drift, while the CIP bent achieved maximum force 66 kip at 2.46% drift. Overall the Precast bent was able to dissipate more energy than the CIP bent. The Precast bent dissipated 2,125 kJ (1,567,320 ft-lb.), while the CIP bent dissipated 342 kJ (252,246 ft-lb.). Table 1.1 gives a summary of the comparison of the CIP bent with the Precast Bent.

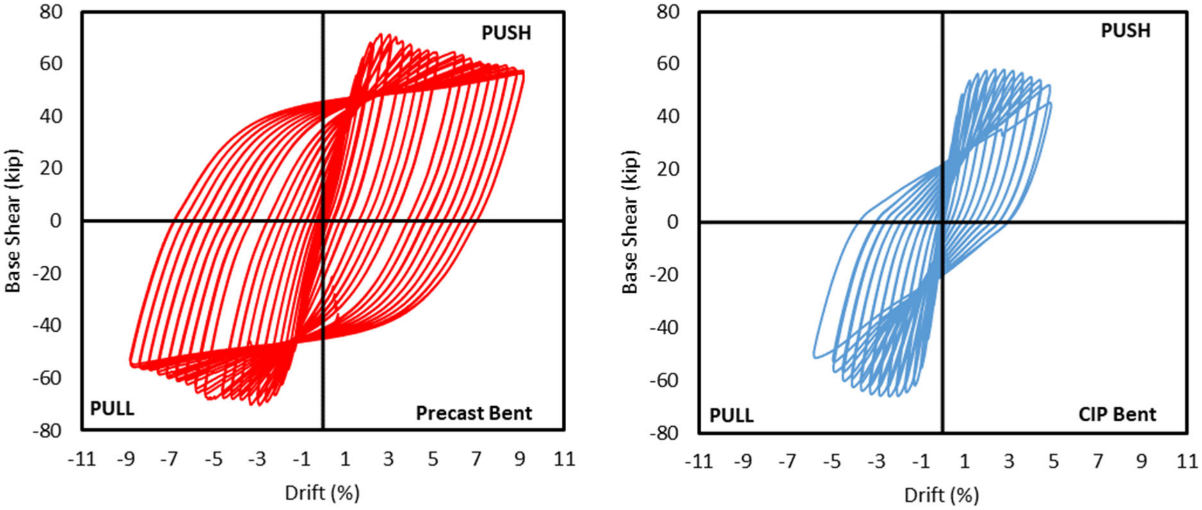

(a) **(b)**

Figure 1.3 Bent Hysteresis: (a) Precast, (b) Cast-in-Place

Table 1.1 Summarized Comparison of CIP and Precast Bents

Performance Factors	**CIP**	**Precast**	**Precast (% Based)**
Maximum Force	66 kip	71.4 kip	108%
Maximum Displacement	4.14 in. (4.94%)	7.66 in. (9.15%)	185%
Moment Capacity	460 kip-ft.	498 kip-ft.	108%
Initial Stiffness	56.7 kip/in.	38.7 kip/in.	68%
Initial Yield	0.5% (0.42 in.)	1.13% (0.95 in.)	226%
Global Yield (Bilinear Approximation)	0.7% (0.596 in.)	1.49% (1.246 in.)	209%
Correlating Moment Capacity at Global Yield	392 kip-ft.	433 kip-ft.	110%
Energy Dissipation	342 kJ (252,246 ft-lb.)	2,125 kJ (1,567,320 ft-lb.) *[466 kJ (343,704 ft-lb.)]	621% *[136%]
Overstrength Factor	1.76	2.18	124%
Displacement Ductility (Ultimate Base Shear)	3.69	2.03	55%
Displacement Ductility (Failure Point)	7.48	6.02	80%

Note: *Precast Cumulative Dissipated Energy at Failure of CIP Bent

The following conclusions were drawn from Phase I of the research:

- Compared to an equivalent CIP pier, the Precast Pier with the proposed pipe connection achieved higher strength and ductility.

- The Precast bent withstood small displacement without suffering hairline cracking due to the presence of the elastomeric bearing pad.
- The Precast bent displayed better confinement through reduced cracking observed throughout the experimental program.
- The Precast bent displayed far more resilience during loading, as it withstood an additional 9 loading cycles than that of the CIP bent.
- The resilience of the Precast bent is demonstrated by the cumulative energy dissipation levels it was capable of achieving during testing.
- Buckling and tearing of the HSS pipe is observed during large drift ratios to be the failure mechanism of the proposed precast connection.
- The Precast pier demonstrates a reduced stiffness as it approached ultimate capacity than that of the CIP bent.
- The Precast bent also exhibited a higher yield displacement of 1.13% drift ratio compared to the 0.5% drift exhibited by the CIP bent.
- The precast bent displayed more energy dissipation than the CIP bent. The Precast bent displayed far less degradation than the CIP bent. The Precast bent was able to withstand additional cycles, compared to the CIP bent.
- The Precast bent with the proposed Precast connection proved capable of successfully emulating the CIP bent under similar quasi-static loading.

Experimental Validation of Repair Methods for Earthquake-Damaged Bridges Incorporating ITD’s Precast Pier System

Now that the bents have been tested and the results have been processed, ITD and ISU have teamed up again for Phase II of the project entitled “Experimental Validation of Repair Methods for Earthquake-Damaged Bridges Incorporating ITD’s Precast Pier System” which covers the retrofit options for the Precast connection, as well as the CIP connection.

After testing of the bents was completed, the structures were dismembered and the piers were stored at ISU. Several pier retrofit options were discussed by ISU and ITD. These options will be discussed further in Chapter 2, Literature Review. From the extensive literature review of repair options for the piers, ISU and ITD decided to use concrete jacketing, specifically ultra-high-performance concrete (UHPC) jacketing, as the retrofit method.

Concept for Retrofit of Concrete Piers in Seismic Regions

After the extensive literature review, and discussion with ITD, the basis of retrofitting the Precast connection is to utilize UHPC jacketing in the plastic hinge zone of the pier. A diagram of the concept can be seen in Figure 1.4. The concept is to "push" the new plastic hinge up to a location right above the jacket.

Investigation is to be completed in this report on UHPC and normal strength concrete (NSC) bond strength to verify if the dowels are necessary for the jacket. This will be conducted through preliminary testing of smaller specimens to quantify bond strength. After the Precast connections are retrofitted and tested, the CIP specimens will also be retrofitted and tested to quantify retrofit methods for CIP piers.

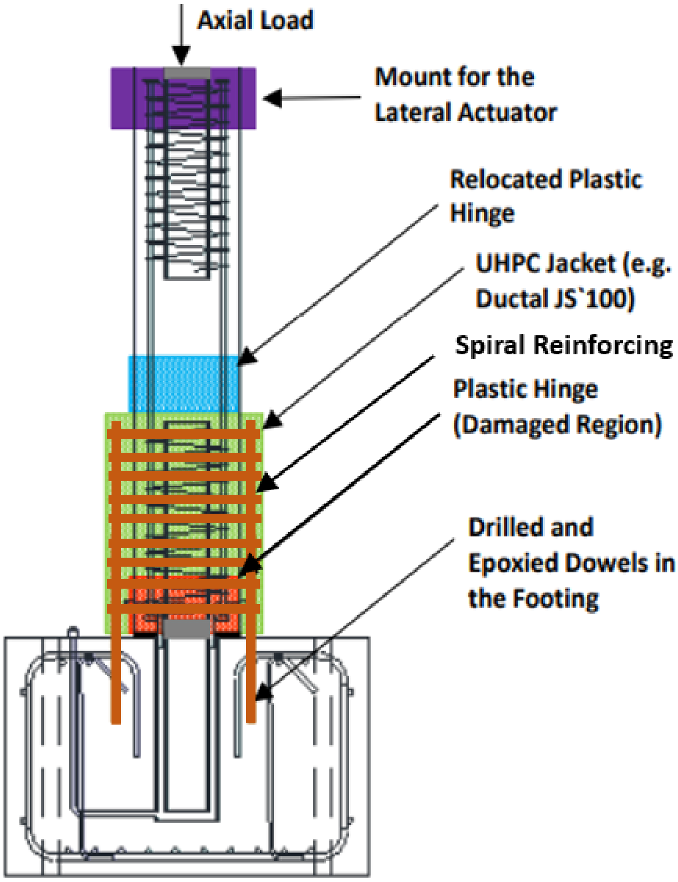

Figure 1.4 Retrofit Concept for Precast Concrete Pier

2. Literature Review

Introduction

Numerous research projects have been dedicated to the development and optimization of retrofitting techniques, considering factors like structural condition, loading requirements, and environmental exposure. This ongoing research has resulted in notable progress in retrofitting methodologies, including advancements in energy efficiency, structural performance, monitoring tools, and life cycle assessments. Institutions such as Idaho State University, University of California Berkeley, Stanford University, University of California San Diego, and the University of Illinois at Urbana-Champaign have made significant contributions to retrofitting research in seismic regions. This chapter provides a brief overview of various literature topics related to bridge construction in seismic zones. It covers an introduction to the subject, the emergence of the Accelerated Bridge Construction (ABC) concept, different types of cast-in-place connections (both emulative and non-emulative), and various retrofitting methodologies ranging from traditional jacketing to advanced Ultra High-Performance Concrete (UHPC). Each retrofitting technique has its own advantages and disadvantages, making it challenging to identify a single method that suits all projects and seismic conditions. However, by considering the extensive research of several researchers presented in this chapter, it is possible to gain a general understanding of the optimal retrofitting technique for specific conditions.

Bridge Construction in Seismic Zones

Bridge structures consist of two main components: the substructure and the superstructure. The superstructure encompasses elements such as the deck, girders, and various structural and non-structural elements. On the other hand, the substructure serves to support the weight of the superstructure and is made up of foundations, piers, abutments, and a cap beam. Its role is to withstand the gravitational and service loads transmitted from the superstructure, as well as to provide a seismic force resistance system for the entire bridge (Mashal 2015).

The majority of bridges worldwide have traditionally been built using the cast-in-place method, which involves constructing monolithic systems. While this approach is suitable and cost-effective for standard column shapes, it lacks flexibility when it comes to modifying the column geometry. Due to this limitation, there has been a transition towards the precast method, which utilizes advanced technology and materials and provides benefits such as faster construction and extended service life for the bridge system. Embracing advanced technology and high-performance materials in bridge construction entails an initial increase in costs. However, Billington et al. (2001) highlights in their research that the economic evaluation of a design should not solely focus on the initial monetary expenditure. It should also consider indirect costs and public benefits resulting from reduced construction time and minimal site impact. The researchers propose the implementation of standardized substructure systems to make precast substructures economically competitive with cast-in-place substructure systems.

A novel concept called Accelerated Bridge Construction (ABC) has emerged, which relies on precast structures as a means of constructing bridges. ABC serves as a viable alternative to monolithic construction methods, enabling faster on-site construction of new bridges. It presents numerous benefits, such as minimizing traffic disruption, expedited project completion, cost savings through reduced formwork requirements, enhanced precision in bridge elements thanks to prefabrication, improved material quality control, decreased machinery and equipment expenses, heightened durability, lighter bridge structures, elevated safety standards, and reduced environmental impact (Mashal 2015). Figure 2.1 illustrates an example of an ABC pier.

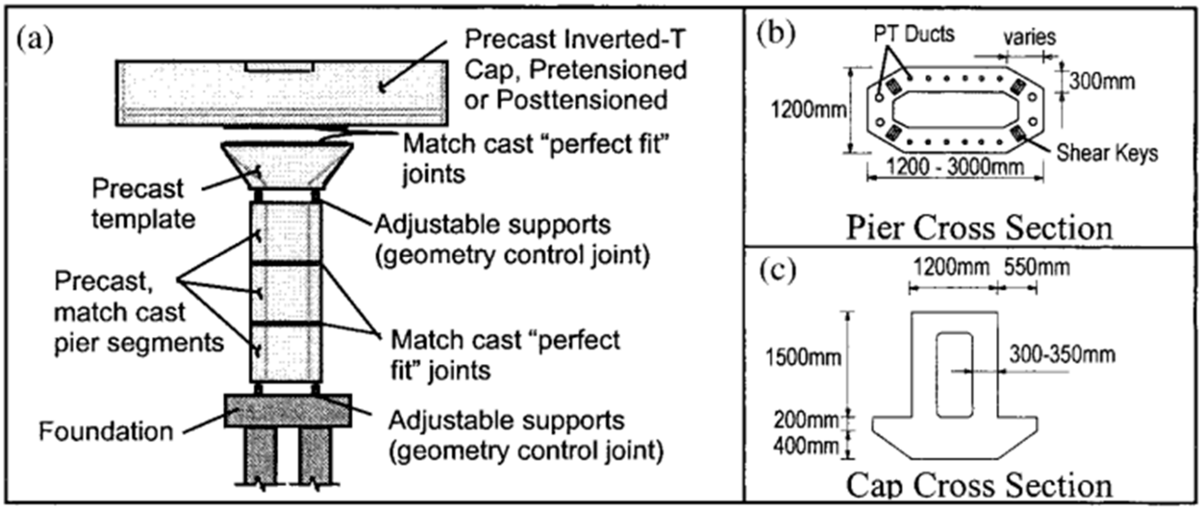

Figure 2.1 Components of Precast Segmental Pier (Billington et al. 2001, p. 91); (1 mm = 0.039 in.)

Strong and resilient connections between precast elements play a critical role in ensuring the required ductility of bridges in seismic regions. In such areas, there are primarily two types of connections used in Accelerated Bridge Construction (ABC): Emulative Cast-In-Place (CIP) or ABC High Damage connections, and Non-Emulative Cast-In-Place or ABC Low Damage connections. ABC High Damage connections are designed to replicate the seismic performance observed in monolithic construction, including the formation of plastic hinges. These connections exhibit similar behavior and performance under seismic forces. On the other hand, ABC Low Damage connections aim to localize and minimize damage within the bridge during a significant earthquake. These connections are designed to limit the extent of damage and reduce the overall impact on the bridge structure. Both connection types serve different purposes in seismic regions, with ABC High Damage connections providing more ductility, as compared to monolithic construction, while ABC Low Damage connections focus on minimizing damage and ensuring the bridge's resilience during seismic events.

Regardless of the type of connections used, the implementation of Accelerated Bridge Construction (ABC) in seismic zones requires careful consideration and additional measures to ensure the integrity and resilience of bridges. In ABC projects in seismic zones, particular attention is given to the connections between precast elements. These connections must be carefully designed to withstand seismic forces and possess the necessary ductility to effectively dissipate energy during an earthquake. Similarly, retrofitting bridges in seismic zones follows similar principles, where the connections between bridge elements are assessed and reinforced to enhance their seismic performance. Retrofitting efforts often involve the integration of specialized devices, such as energy-dissipating systems or base isolators, to enhance the bridge's capacity to withstand ground motions and minimize the transfer of seismic forces to the superstructure.

Retrofitting

The structural integrity and load-carrying capacity of infrastructures such as bridges are significantly reduced because of the harsh environment, loss of reinforcement, and lack of confinement (Farzad et al. 2019). Such undesired phenomena are common in bridges constructed in a seismically active zone. Depending upon the scale of the damage to such infrastructures, a decision must be made whether to replace or rehabilitate the structure. If the seismic assessment of the damaged bridge suggests rehabilitation of the structure, various retrofitting methods can be applied to extend the service life of the bridge and ensure its continued functionality and reliability.

According to Brühwiler and Denarié (2008), considering the socio-economic aspect, the cost of rehabilitating deteriorated concrete infrastructure, such as bridges, can be comparable to the cost of completely replacing them. Therefore, the future of sustainable concrete infrastructure lies in the development of optimal rehabilitation techniques that prioritize preventive maintenance, aiming for minimal intervention and limited-service disruptions. This approach would ensure the longevity and sustainability of concrete infrastructures while minimizing the associated costs.

Retrofitting bridges refers to the process of making structural improvements or modifications to an existing bridge in order to enhance its performance, safety, or capacity. It involves updating or reinforcing various components of the bridge to meet current design standards, address deterioration issues, accommodate increased loads, or incorporate new technologies. Retrofitting measures may include strengthening the bridge's foundations, replacing, or adding structural elements, improving corrosion protection, upgrading the bridge deck, or implementing advanced monitoring and control systems.

Several retrofitting methods and materials are available for strengthening the concrete infrastructures. Researchers have been constantly developing and evaluating techniques, ranging from steel jacketing and concrete encasing to hybrid jacketing, which involve the use of multiple retrofitting methods and materials. The aim is to minimize changes to the structural geometry while maximizing the enhancement of structural capacity (Raza et al. 2019). The next section focuses on typical retrofitting methods.

Steel Jacketing

Steel jacketing is a method where the reinforced concrete (RC) section is expanded by connecting it to a steel section through welding or bolting and the space between the concrete and steel is filled with grout to ensure a solid bond (Raza et al. 2019). Steel jacketing is a realistic, swift, and cost-effective option (Islam and Hoque 2017).

Plating columns through steel jacketing has been identified as an effective technique for improving the seismic performance of columns. Y. F. Wu et al. (2003) conducted a study that demonstrated the effectiveness of this method in retrofitting RC columns by increasing their strength and ductility, particularly in preventing potential plastic hinge failure modes. Despite its advantages, including the utilization of readily available materials and the enhancement of both strength and ductility in concrete structures, this method does have a few drawbacks:

- Rusting and corrosion
- Expensive and labor intensive
- Increase in cross-sectional size leading to change in stiffness and seismic demands.
- Heavy weight

Research on steel jacketing is discussed further.

Strengthening of Reinforced Concrete Columns by Steel Jacketing: A State of Review (Islam and Hoque 2017)

This paper explores the strengthening of RC columns using steel jacketing, RC jacketing, and composite jacketing methods. The research provides a comparative analysis between experimental findings and analytical equations proposed by different researchers. Figure 2.2 and Figure 2.3 show the process of steel jacketing.

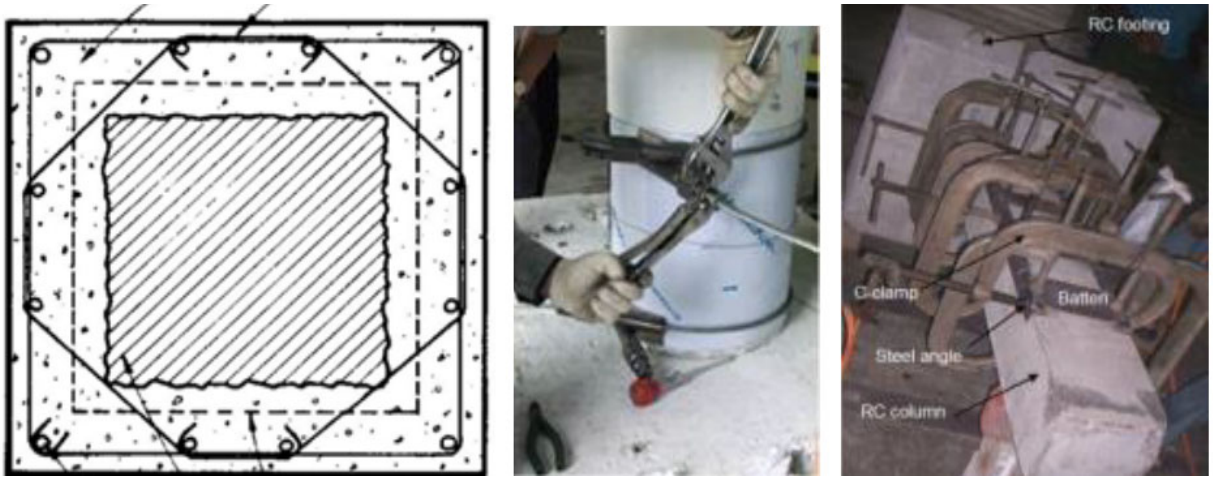

Figure 2.2 Cross-Section of Reinforced Concrete Jacket; Steel Wrapping; Installation of Steel Cage. (Islam & Hoque 2017, p. 6)

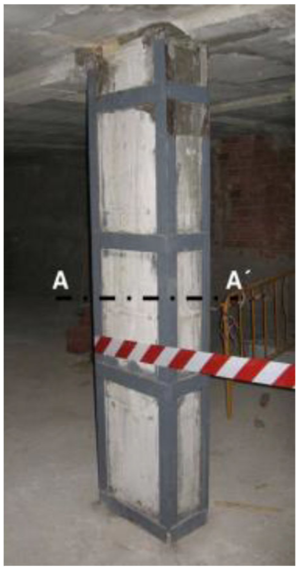

Figure 2.3 Completed Steel Jacketing (Islam & Hoque 2017, p. 7)

Results: The results demonstrate a significant enhancement in axial strength of the steel jacketed column ranging from 18.65% to 109%, as well as an improvement in lateral strength ranging from 63% to 68%, based on the research papers compiled. Additionally, a design example is presented, illustrating the application of these findings to a column with dimensions of 300x300 mm (11.8x11.8 in.) and a height of 3000 mm (118.11 in.).

Strengthening and Repair of Reinforced Concrete Columns by Jacketing: State-of-the-Art Review (Raza et al. 2019)

The purpose of this research is to provide a comprehensive review of different strengthening and repair methods for RC columns proposed by various researchers over the past two decades. The scope of this review paper is limited to jacketing techniques for strengthening and/or repairing both normal- and high-strength RC columns. In addition to reviewing existing methods, the paper aims to identify research gaps and provide insights into the future direction of research in the field of RC column strengthening and repair.

The Concept: In the research, the strengthening and repair techniques for RC columns are classified into six categories: RC/mortar jacketing, steel jacketing, externally bonded fiber-reinforced polymer (FRP) jacketing, near-surface mounted FRP jacketing, shape memory alloy (SMA) jacketing, and hybrid jacketing. A comprehensive review of the literature was conducted, encompassing studies conducted over the past two decades that focused on strengthening RC columns.

Results: By comparing these six methods for jacketing on criteria such as effect on strength; effect on ductility; effective on stiffness; cost of strengthening; aesthetics; and impact to occupants, following findings were made in the paper:

- Steel jacketing, near-surface mounted FRP/steel reinforcement and hybrid jacketing methods resulted in the largest strength increase.
- Externally bonded FRP and hybrid jacketing were typically more effective and resulted in higher levels of ductility.
- Stiffness generally remains unchanged, except for the RC and steel jacketing, where stiffness increased, whereas for SMA wire jacketing, stiffness decreases.
- RC jacketing and steel jacketing generally have lower cost construction materials.

Figure 2.4 and Figure 2.5 summarize the findings from the review conducted. The tables highlight the benefits and drawbacks of each retrofit method.

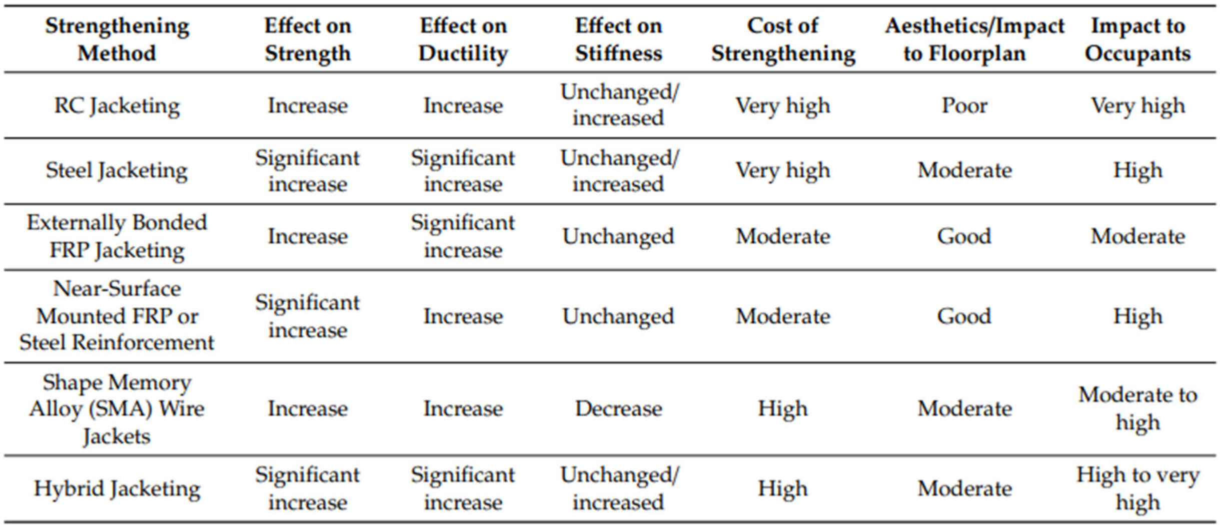

Strengthening Method	Effect on Strength	Effect on Ductility	Effect on Stiffness	Cost of Strengthening	Aesthetics/Impact to Floorplan	Impact to Occupants
RC Jacketing	Increase	Increase	Unchanged/ increased	Very high	Poor	Very high
Steel Jacketing	Significant increase	Significant increase	Unchanged/ increased	Very high	Moderate	High
Externally Bonded FRP Jacketing	Increase	Significant increase	Unchanged	Moderate	Good	Moderate
Near-Surface Mounted FRP or Steel Reinforcement	Significant increase	Increase	Unchanged	Moderate	Good	High
Shape Memory Alloy (SMA) Wire Jackets	Increase	Increase	Decrease	High	Moderate	Moderate to high
Hybrid Jacketing	Significant increase	Significant increase	Unchanged/ increased	High	Moderate	High to very high

Figure 2.4 Comparison of Different Strategies to Strengthen and Repair RC Columns (Raza et al. 2019).

Strengthening Method	Benefits	Drawbacks
RC/Mortar Jacketing	• Commonly used/available material • Familiarity of practicing engineers with the material • Ability of RC to take any shape • Increases both strength and ductility	• Expensive, labor intensive and time consuming due to formwork installation • Change in cross-sectional size leading to change in stiffness and seismic demands • Increase in ductility is small due to brittle nature of concrete • Disruption of occupancy
Steel Jacketing	• Ductile and commonly used/available material • Excellent confinement leading to considerable increase in both strength and ductility	• Expensive and labor intensive. • Rusting and corrosion • Change in cross-sectional size leading to change in stiffness and seismic demands • Heavy weight
Externally Bonded FRP Jacketing	• Ease and speed of installation • Corrosion resistance • Minimum modification to geometry and aesthetics of structure • Minimum disruption of occupancy • High durability, high strength-to-weight ratio • Better work safety and minimum risk hazard • Enhancement in both strength/ductility	• Costly material (but overall cost is low due to small cost of transportation and installation) • Low efficiency (30–35%) due to debonding • Poor properties on exposure to high temperature and wet environment • Increase in strength is relatively small
Near-Surface Mounted FRP or Steel Reinforcement	• Less prone to debonding • Minimum modification to geometry and aesthetics of structure • Less prone to mechanical impact and accidental damage due to protection by concrete cover • Aesthetics of the structure remain unchanged • Enhances strength considerably	• Costly material (but overall cost is low due to small cost of transportation and installation) • Comparatively more labor intensive in comparison to externally bonded FRP, but lesser than RC or steel jacketing • Not much increase in ductility
Shape Memory Alloy (SMA) Wire Jacketing	• Fast installation • No need for adhesive • No danger of peel off • Super elastic and durable • Increases both the strength and ductility	• Costly material • Ineffective composite action with concrete • Enhancement in strength is relatively small
Hybrid Jacketing	• Fast installation • Minimum modification to geometry and aesthetics of structure • High durability • Significant enhancement in both strength and ductility	• Costly material • Comparatively labor intensive as it combines two different retrofitting techniques

Figure 2.5 Overview of Advantages and Disadvantages of Various Repair and Strengthening Methods (Raza et al. 2019).

Concrete Jacketing

RC jacketing adds a thin layer of RC around the existing column, but its effectiveness is limited for rectangular or square cross sections due to section enlargement and the need for dowelling reinforcing bars to the footing (Islam and Hoque 2017). Seismic retrofitting techniques are widely used, with RC Jacketing being the most common for elements with low strength. This technique enhances structural capacities like axial load capacity, shear strength, flexural strength, deformation capacity, and ductility, but poses challenges for small columns requiring jacket thicknesses exceeding 70-100 mm (2.76-3.94 in.) (FIB Bulletin 2003; Koo and Hong 2016). This leads to increased mass, stiffness, and section size.

Traditional RC jacketing involves enlarging the column's section by adding a new RC or mortar section over a portion or the entire length of the column. This new section is securely bonded to the original section using anchor rebar or high-strength bolts. Despite the positive effects of this technique on the column's seismic performance, it is a costly and time-consuming process due to the requirement of formwork installation. Additionally, the enhancement in ductility is limited because the jacketing material, concrete, is inherently brittle (Raza et al. 2019).

The limitations of concrete jacketing can be minimized to a certain extent with the use of high-performance RC materials. Vandoros and Dritsos (2008) conducted tests that showed significant increases in strength and stiffness when applying concrete jackets around columns. Similarly, the use of carbon fiber reinforced polymers (CFRP) significantly enhanced ductility.

Fiber-Reinforced Polymer (FRP)

Composite jacketing utilizes FRP with organic or epoxy resin, but it has drawbacks such as susceptibility to fire and linearly elastic behavior, as well as higher costs. Composite jacketing is more suitable for circular or elliptical column shapes (Islam and Hoque 2017). FRP techniques have gained popularity due to less thickness, low weight, and better constructability but may not effectively increase column strength significantly. Also, ductility matters like fire and corrosion resistance come into consideration when applying these methods.

Several kinds of FRP composites are available and are discussed further.

Carbon Fiber-Reinforced Polymer (CFRP)

CFRP is the most widely used FRP for strengthening and repairing damaged RC columns. The experimental study conducted by Beydokhty and Shariatmadar (2016) reached the conclusion that externally bonded retrofitting using CFRP is a suitable method for enhancing the seismic capacity of joints. This retrofitting technique demonstrated improvements in energy dissipation, structural performance, and resulted in a more favorable damage pattern compared to the initial loading phase of the structure.

In a comparative study conducted by Kalyoncuoğlu et al. (2012) on the performance of mortar-based and CFRP-based rehabilitation for corrosion-damaged columns, it was found that mortar-based repair led to a significant increase in the strength of the damaged columns. However, the improvement in ductility was only marginal. On the other hand, rehabilitation and retrofitting using CFRP sheets exhibited substantial enhancements in both strength and ductility for corrosion-damaged columns. Another comparative study conducted by Galal et al. (2005) investigated the effectiveness of CFRP and GFRP for strengthening short RC columns. The study revealed that employing anchored carbon fiber sheets instead of anchored glass fiber sheets led to an increase in both the shear force and the energy dissipating capacity. Additionally, it resulted in reduced strains in the steel ties and the FRP along the height of the column.

Similarly, a study conducted by Tasdemir et al. (2018) demonstrated that the repair of columns with a single fractured bar can be effectively achieved through the utilization of CFRP sheets and anchors.

Glass Fiber-Reinforced Polymer (GFRP)

GFRP is composed of glass fibers embedded in a polymer matrix, creating a lightweight and high-strength material. It has excellent corrosion resistance, high strength-to-weight ratio, and long service life. Furthermore, it is easy to install and can be tailored to fit different geometries, allowing for flexibility in retrofitting application.

Basalt Fiber-Reinforced Polymer (BFRP)

Recently, basalt fiber-reinforced polymer (BFRP) has gained attention for strengthening applications due to its affordability compared to CFRP and its notable properties such as fire resistance and resistance to chemical corrosion (Raza et al. 2019).

Polyester Fiber-Reinforced Polymer (PFRP)

Polyester fiber-reinforced polymer (PFRP) is recognized for its toughness, flexibility, heat resistance, and durability, making it a suitable choice for strengthening purposes (Raza et al. 2019).

Polyethylene Terephthalate (PET) Fiber-Reinforced Polymer

PET fiber-reinforced polymer is manufactured from recyclable materials and offers advantages such as higher deformability, greater tensile capacity, and lower cost compared to CFRP (Raza et al. 2019).

Hybrid Fiber-Reinforced Polymer (HFRP)

HFRP refers to a composite material that combines two or more types of reinforcing fibers within a polymer matrix. In retrofitting, HFRP is utilized to enhance the performance and durability of existing elements. By combining different types of reinforcing fibers, such as carbon fibers, glass fibers, or aramid fibers, within a polymer matrix, HFRP offers improved strength, stiffness, ductility, and resistance to various structural demands. The use of HFRP in retrofitting provides a versatile solution that can be tailored to specific structural requirements and offers advantages over single-fiber systems in terms of performance and cost-effectiveness.

Research covering implementation of FRP is discussed further in the following section.

Structural Performance of Reinforced Concrete (RC) Moment Frame Connections Strengthened Using FRP Composite Jackets (Maras and Kantarcı 2021)

The objective of this research is to evaluate the effectiveness of different types of FRP (CFRP, AFRP, and GFRP) with various cross-sectional configurations (cross, diagonal, and parallel) in strengthening the connections of a RC moment frame with strong beam/weak column joints. The study compares FRP-wrapped specimens (SBWC2-SBWC7) to a control specimen (SBWC1), considering parameters such as load capacity, ductility index, failure modes, and crack patterns. Additionally, the research utilizes CFRP composites with a thickness of 0.7 mm (0.027 in.) and width of 500 mm (19.7 in.), AFRP composites with a thickness of 0.4 mm (0.016 in.), and GFRP composites with a thickness of 1.2 mm (0.047 in.). The goal is to assess the contribution of these FRP strengthening methods in enhancing the performance and behavior of the moment frame connections within the RC beam-column joint. Figure 2.6 gives examples of the various FRP materials.

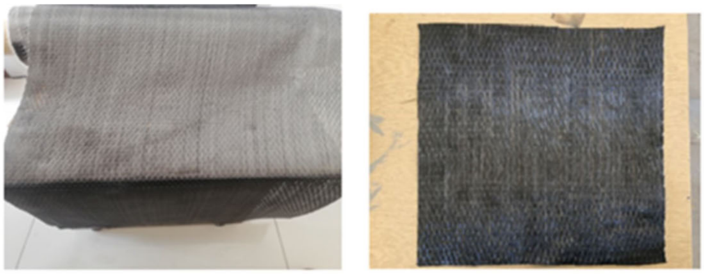

(a) Carbon fabric

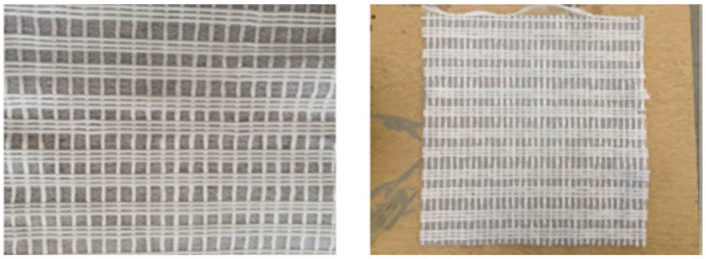

(b) Glass fabric

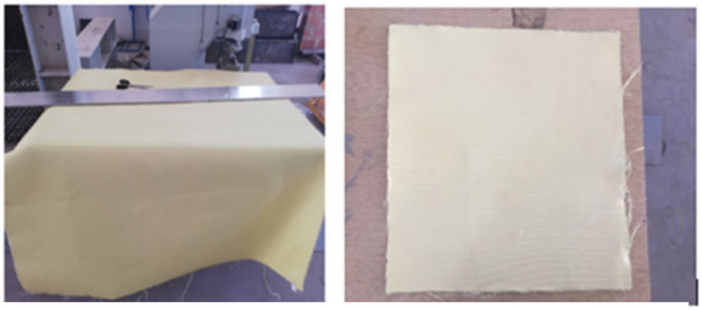

(c) Aramid fabric

Figure 2.6 Various Fibers Fabric: (a) CFRP; (b) GFRP; (c) Aramid (Maras & Kantarcı 2021)

Results: Seven half-scale specimens were tested, with two serving as control specimens. The retrofitted beam column joints using FRP strips were compared to both un-strengthened and strengthened RC beam-column joints. The results showed that the FRP retrofits significantly increased the load capacity and displacements compared to the control specimens. Using CFRP wraps, load values and displacements were over 12.5% and 10.4% higher, respectively, than the control. AFRP wraps exhibited load values and energy dissipation capacities 1.86 and 1.65 times greater than the control, respectively. GFRP wraps showed an ultimate load of 103.2 kN (23.2 kip) and a 10.8% higher load capacity than the control. Additionally, the use of CFRP wraps reduced visible-width shear cracks compared to the control samples.

Behavior of Damaged Exterior RC Beam-Column Joints Strengthened by CFRP Composites (Beydokhty and Shariatmadar 2016)

This research investigates the effectiveness of CFRP sheets in enhancing the seismic capacity and stiffness of 8 external beam-column joints without transverse reinforcement or special stirrups. The joints are designed for gravity loads, and their beam and column dimensions adhere to CSA A23.3-04 (2004).

The testing conducted in this study comprises two phases. In the first phase, different levels of damage are induced in the beam-column joints. The NS5 specimen serves as the reference, representing joints with non-seismic details. Loading is gradually increased until the appearance of the first crack near the column. The load is then increased at various drift levels (0.5%, 1%, 1.5%, 2%, 2.5%, 3%, 4%, and 5%). At 5% drift, the load recorded is 86 kN (19.3 kip) with a 6 mm (0.24 in.) bending crack width. Diagonal cracks predominantly develop in the joint, concentrating in the beam's critical zone. In this phase, NS1 is damaged up to 1% storey drift, NS2 up to 1.5% storey drift, and NS3 up to 3% drift, with NS5 serving as the reference. In Phase 2, the damaged specimens are retrofitted with one ply of FRP sheet below and above the beam, as well as around the joint area.

Results: The retrofitted specimens demonstrated increased load carrying capacity and reduced plastic rotations compared to the reference specimen at each story drift. Moreover, the capacity of the joints is enhanced through the strengthening process.

Rapid Seismic Repair of Reinforced Concrete Bridge Columns (Wu and Pantelides 2017)

The purpose of this study is to investigate and present experimental results on the seismic repair of RC bridge columns using a carbon fiber-reinforced polymer (CFRP) shell and epoxy-anchored headed steel bars. The study aims to assess the effectiveness of this repair technique in relocating the column plastic hinge and restoring the strength and displacement capacity of the damaged columns. The experimental setup includes two columns designed according to current standards, subjected to cyclic forces to induce damage. The damage includes longitudinal bar fracture, buckling across multiple spiral hoops, and concrete damage in the plastic hinge region. Finite element analysis is employed to design the CFRP shell, while the headed bars are designed to accommodate the increased flexural demand on the repaired section.

The Concept: Conventional repairs typically involve time-consuming processes such as core concrete removal and replacement of buckled and fractured reinforcement, which can be challenging to execute on-site for bridge structures. To address this issue, a repair method is proposed that involves minimal intervention and utilizes a CFRP cylindrical shell and epoxy-anchored headed steel bars to relocate the column plastic hinge. The CFRP shell encompasses the headed steel bars and is filled with non-shrink concrete, forming a CFRP "donut." Apart from providing confinement, the shell also acts as a stay-in-place form. The proposed method incorporates fibers in both the hoop and vertical directions of the CFRP shell and is applied to two severely damaged specimens: one with a cap beam-to-column connection and another with a footing-to-column connection. Figure 2.7 illustrates the design for the retrofit.

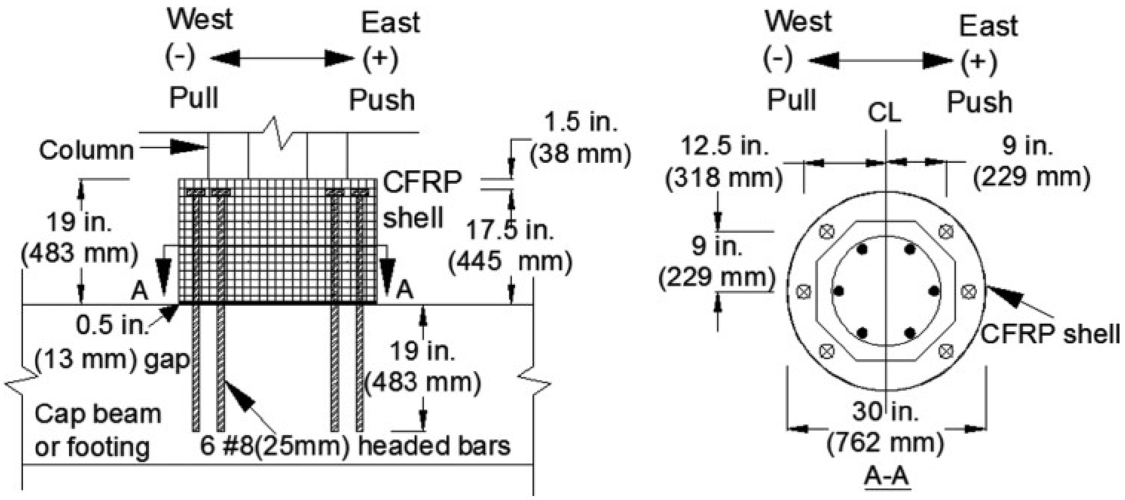

Figure 2.7 Design Details for Repair of Reinforced Concrete Bridge Columns (Wu & Pantelides 2017, p. 1343)

Results:

- The repaired samples achieved a displacement ductility that either met or exceeded the ductility demand of 5.0 for single-column bridge bents, as well as the displacement ductility demand of 6.0 for multi-column bridge bents, as recommended by the AASHTO Guide Specifications.
- The bending moment capacity of the repaired specimens is larger than the moment capacity of the original specimens.
- The measured strains provide confirmation that the post-installed headed steel bars effectively transmit tensile and compressive forces between the column and the cap beam/footing through the CFRP donut.

The experimental results demonstrated that the proposed repair method effectively restored the lateral force and displacement capacity of severely damaged RC columns. Even in cases where the columns had crushed concrete in the core and buckled and fractured steel bars, the repair technique was successful in achieving the desired outcomes. The intervention required for the repair was minimal, and the entire process for each column was completed in less than 3 days. By implementing the installation of headed bars, CFRP shell, and non-shrink grout simultaneously across multiple columns, the repair process could be efficiently carried out within a relatively short timeframe.

Seismic Performance of High-Performance Fiber-Reinforced Cement-Based Composite Structural Members: A Review (Shao et al. 2022)

This research provides a comprehensive review of the knowledge and research advancements in the field of High-performance fiber-reinforced cement-based composites (HPFRCC) for seismic-resistant structures and aims to identify future research needs in this area.

The Concept: HPFRCC materials differ from conventional fiber-reinforced concrete (FRC) due to their improved tensile behavior. In contrast to concrete or FRC, which experience a complete or gradual loss of tensile strength after cracking, HPFRCC materials maintain a higher tensile strength even after cracking until the fiber-bridging mechanism fails. This unique characteristic is commonly referred to as pseudo-strain hardening. It also exhibits high damage tolerance, high bond strength, high cracking resistance, and high corrosion protection for steel bars, thus making it suitable for earthquake engineering.

Results:

The paper summarizes the experimental findings proposed by different researchers on four core areas:

a. Seismic performance of HPFRCC materials
    - Fiber-bridging degradation under cyclic loading is dependent on the fiber type (material, aspect ratio, and geometry), fiber-matrix bond performance, and loading history.
    - Under cyclic loading, the envelope of HPFRCC cyclic compression response follows the monotonic compression response.
    - The enhanced tensile behavior of HPFRCC improves the bond performance by restraining splitting cracks through fiber-bridging.

b. Seismic performance of reinforce HPFRCC flexure-dominant members.
    - Under both monotonic and cyclic loading, R/HPFRCC shows different failure paths than RC.
    - R/HPFRCC shows two unique failure paths: failure after crack localization or failure after gradual strain hardening.
    - Gradual strain hardening of reinforcement is achievable in R/HPFRCC due to its high crushing resistance.

c. Seismic performance of reinforced HPFRCC shear-dominant members.

- For diagonally reinforced HPFRCC coupling beams, HPFRCC and transverse reinforcements resist the shear load whereas only diagonal reinforcement resists shear load in diagonally RC coupling beams.
- While the HPFRCC matrix and transverse reinforcement contribute to resisting a portion of the shear demand, the presence of diagonal bars remains a crucial shear-resistant mechanism. The absence of diagonal bars can result in a reduced drift capacity.
- When comparing squat walls made of R/HPFRCC to RC, R/HPFRCC leads to narrower and more evenly distributed shear cracks in the web of the walls, enhancing the damage tolerance of the walls.

d. Seismic performance of HPFRCC beam-columns

- HPFRCC exterior joints fail by joint shear failure with a shear strength between 0.52 (fc') 0.5 and 0.80 (fc') 0.5.
- Minimum joint depth limit to prevent bond failure can be relaxed while using R/HPFRCC due to its high bond performance. Interior joints can adopt a joint depth i.e., 10 % to 30 % smaller than the recommended depth.

R/HPFRCC structural members exhibit superior seismic performance than RC due to its enhanced tension and compression performance. Fiber-bridging plays a vital role in R/HPFRCC performance so, a systematic study in this area is essential to widen the scope of R/HPFRCC in earthquake engineering.

Seismic Repair of Severely Damaged Precast Reinforced Concrete Bridge Columns Connected with Grouted Splice Sleeves (Parks et al. 2016)

The authors explore the effectiveness and feasibility of a repair technique that uses a carbon fiber-reinforced polymer (CFRP) shell and epoxy-anchored headed bars in restoring the structural integrity and seismic resilience of severely damaged precast RC bridge columns connected with grouted splice sleeves (GSS).

The Concept: Capacity-based bridge design aims to direct damage to bridge columns to protect the pier caps and footings. Various techniques have been employed for repairing damaged bridge columns, including the use of externally bonded carbon fiber-reinforced polymer (CFRP) jackets, steel jackets, and concrete jackets. With the advent of Accelerated bridge construction (ABC), GSS has emerged as a potential precast concrete connection method for ABC in seismic regions. As the use of GSS connections in moderate to high seismic regions is imminent, it becomes crucial to develop practical post-earthquake repair strategies that align with this new technology. Recent findings from ABC research indicate that columns connected using GSS connectors concentrate damage within the column and reduce the effective length of the plastic hinge compared to traditional monolithic construction, particularly when GSS connectors are incorporated at the ends of the columns. These damage characteristics offer advantages for repair methods using CFRP shell and epoxy- anchored headed bars.

Research: Four precast RC specimens, designed according to current seismic bridge standards, were constructed to represent half-scale bridge elements. These specimens featured octagonal cross sections, measuring 21 inches wide, and stood at a height of 8.5 feet. The longitudinal reinforcement consisted of six No. 8 Grade 60 bars arranged in a circular pattern. The experimentation involved the utilization of two distinct GSS (grouted splice sleeve) systems. Specifically, NM-O1 and LE-O1 employed GSS connectors in the footing and pier cap, respectively, while NM-O2 and LE-O2 featured GSS connectors in the columns. The geometry and dimensions of the specimens is shown in Figure 2.8. To simulate real-world conditions, a lateral load was applied at a specific location representing the inflection point of a bridge column. This loading regime consisted of a constant axial load equal to 6% of the column's axial load capacity, in addition to displacement-controlled, cyclic, quasi-static lateral loads.

The aim of the repair was to enhance the strength of the original plastic hinge area and shift the plastic hinge to an adjacent column section. This objective was achieved by enlarging the octagonal cross section from 21 inches to a reinforced circular cross section with a diameter of 30 inches (Figure 2.8). The repair process involved the installation of epoxy-anchored headed bars to facilitate additional transfer of tensile forces. Subsequently, a carbon fiber-reinforced polymer (CFRP) shell was filled with non-shrink or expansive concrete to complete the repair.

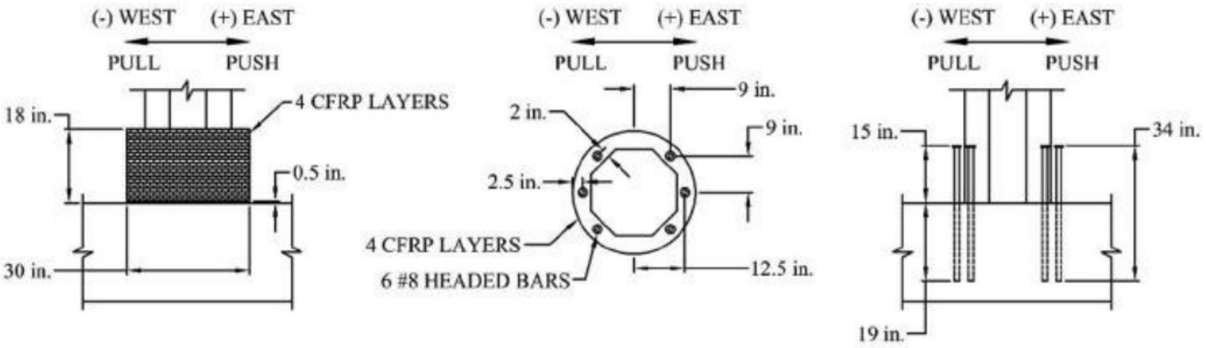

Figure 2.8 Repair design of column (Parks et al. 2016, p. 618)

Results:

- The application of a CFRP shell effectively provided confinement, shear strength, and peripheral tension to the repair, with particular emphasis on the top region of the CFRP shell.
- The installation of post-installed headed bars proved successful in enhancing the flexural capacity of the repaired section, allowing for the relocation of the plastic hinge.

- The headed bars served to transfer the tension that was lost due to the fracture of the original longitudinal bars connecting the columns to the footing or pier caps.

Considering the overall results obtained from the half-scale experiments, it can be concluded that this repair technique is a feasible option for addressing damaged columns in regions with moderate to high seismic activity. The repair technique showcased rapidity, meeting the requirements of accelerated bridge construction. This indicates that it is a time-efficient solution for repairing damaged columns.

Shape Memory Alloy (SMA) Wire Jacketing

SMAs are known for their remarkable super elasticity, durability, and shape memory effect and unlike FRP, do not require adhesives for installation, making the process easier and eliminating the risk of peel-off issues (Raza et al. 2019). When SMA wires are used for jacketing bridge columns, they can enhance the column's strength, ductility, and energy dissipation capacity. During an earthquake or other dynamic loading events, the SMA wires help to confine the concrete, preventing premature failure and reducing the risk of column collapse. The retrofitting process involves wrapping SMA wires around the bridge columns and applying a pre-stress to achieve the desired level of confinement. The activation of the SMA wires can be controlled by external heating or cooling methods, enabling them to exert pressure on the column and enhance its performance.

Hybrid Jacketing

Hybrid jacketing is a technique that combines multiple strengthening methods/materials to improve the seismic performance of a column. By integrating two or more different approaches, hybrid jacketing leverages the respective advantages of each method, resulting in enhanced overall performance (Raza et al. 2019). This approach allows for a customized and efficient retrofit solution that addresses the specific needs and challenges of the structure being upgraded.

Dampers

Dampers are commonly used as retrofit solutions in bridges to improve their seismic performance. Dampers are devices designed to absorb or dissipate energy, reducing the response of the bridge to seismic forces. They are typically installed at strategic locations within the bridge structure to mitigate the effects of earthquakes. Dampers can be installed in various locations, such as between bridge piers and beams, at the expansion joints, or within the superstructure. The specific retrofitting approach depends on the bridge's design and the desired level of seismic performance improvement. By integrating dampers into bridge structures, the retrofitting process aims to enhance the bridge's ability to absorb and dissipate seismic energy, reducing the potential for damage and improving the overall structural integrity during earthquakes.

Many types of dampers are available, some of these in the context of bridges are described below.

Metallic Dampers

Metallic dampers, also referred to as metallic energy dissipation devices, are commonly utilized as retrofit solutions in bridges to enhance their seismic performance. These dampers function by utilizing the yielding and inelastic deformation properties of metals. The energy dissipation mechanism in metallic dampers is based on controlled plastic deformation of high-strength steel elements, such as plates or rods that are strategically placed within the bridge structure. This deformation absorbs and dissipates energy, thereby mitigating the forces transmitted to the bridge components during seismic events (Mashal 2015). The yielding mechanism in metallic dampers can involve flexural, shear, or axial deformation, depending on the specific design and application. The following are different types of metallic dampers.

Lead Extrusion Device (LED): LED offers several advantages, including stable hysteretic behavior over numerous cycles, no low-cycle fatigue failure due to lead re-crystallization at room temperature, minimal impact of environmental factors on LED behavior, independence from strain rate on the hysteretic response, and negligible aging effects. These characteristics make LED reliable and durable dampers, ensuring their consistent performance. However, low application of this type of damper is due to high cost as it would require high precision for the machining of parts.

Buckling-Restrained Braces (BRBs): BRBs are the most common type of metallic dampers. BRBs consist of a steel core surrounded by a casing or jacket that prevents buckling under compressive forces. The steel core undergoes yielding and plastic deformation during seismic events, absorbing and dissipating energy. BRBs offer several advantages, including improved seismic performance, reliable hysteretic behavior, ease of installation, and the ability to be designed for specific performance objectives. Examples of BRBs are shown in Figure 2.9.

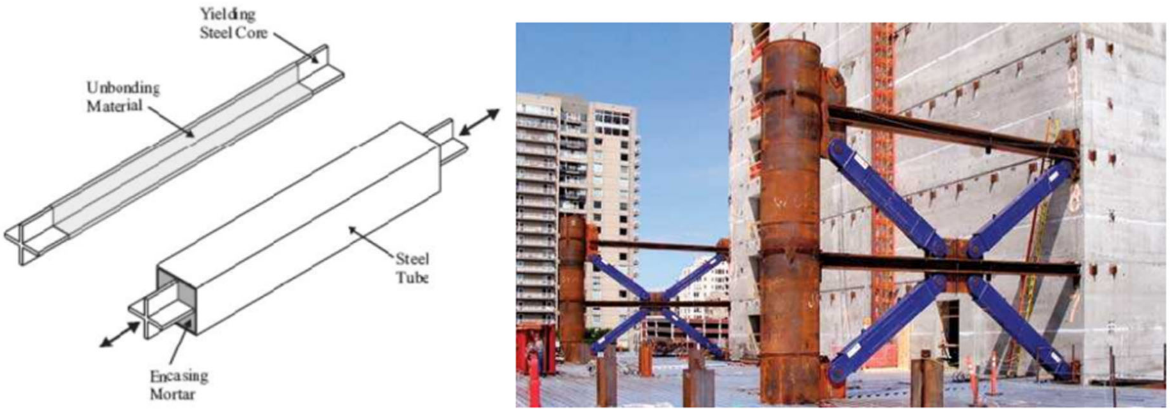

(a) Components of a BRB **(b) BRBs in a building (courtesy of Structure Archives)**

Figure 2.9 Buckling Restrained Braces (Christopoulos and Filiatrault 2006)

Bazaez and Dusicka (2018) experimentally investigated the lateral performance of seismically deficient reinforced concrete bridge bents retrofitted with BRBs (Figure 2.10). Results from the research showed the BRBs were effective in achieving both life-safety and operational performance levels for the retrofitted bent.

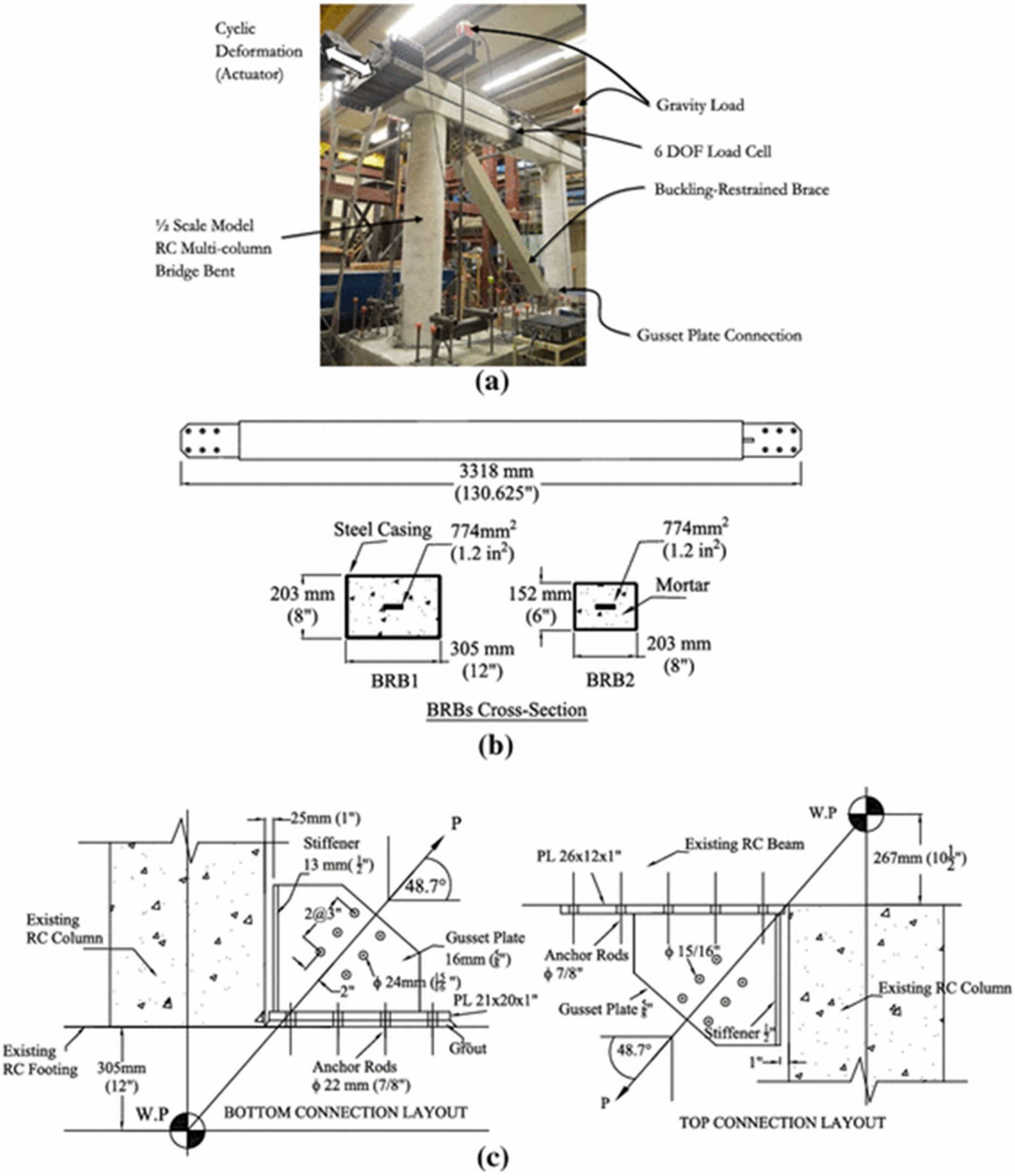

Figure 2.10 Bridge Retrofitting using BRBs (Bazaez and Dusicka 2018)

Torsional Beam Damper: In this type of damper, energy dissipation is achieved through torsional yielding of a steel bar loaded by a central transverse plate (arm), while the bar remains fixed at both ends (Figure 2.11). When torsional vibrations occur, the damper absorbs and dissipates the energy, effectively reducing the magnitude and duration of the vibrations. Torsional beam dampers offer several benefits, including improved structural stability, enhanced fatigue life, and reduced damage to structural components. However, to enable broader application in buildings or columns with solid sections, further development is needed to make the damper more compact (Mashal 2015).

One great example of a bridge in a seismic zone that uses torsional beam dampers is the South Rangitikei Viaduct in New Zealand (Figure 2.12). These dampers are vital in limiting the impact of vibrations and potential structural damage during seismic events by absorbing and dispersing energy.

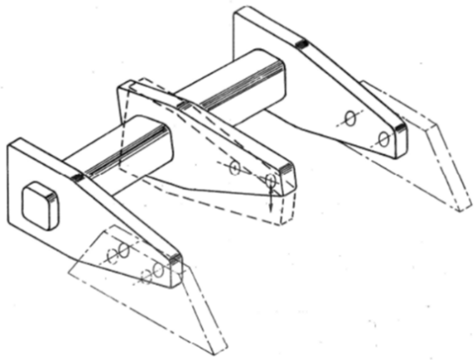

Figure 2.11 Working Mechanism of Torsional Beam Damper (Kelly et al. 1972)

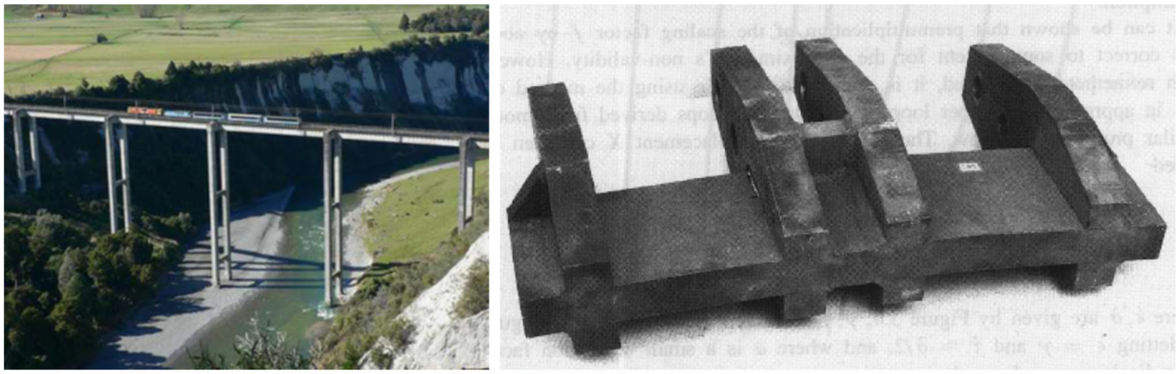

(a) South Rangitikei Viaduct **(b) Torsional damper with transverse loading arms**

Figure 2.12 Application of Torsional Beam Damper (Beck and Skinner 1974)

U-Shaped Flexural Plates (UFPs): UFPs are a type of energy dissipation device that utilizes the flexural yielding of U-shaped steel plates to dissipate energy in structures subjected to seismic forces. When seismic vibrations occur, the UFPs undergo flexural deformation, absorbing and dissipating energy, thereby reducing the amplitude and duration of the vibrations. UFPs are typically constructed using readily available mild steel plates. UFPs offers several advantages, including lower fabrication costs, stable hysteretic behavior, minimal low-cycle fatigue, and limited strength degradation during cyclic loading. UFPs can accommodate large displacements and possess higher load-carrying capacity. Figure 2.13 presents a schematic for the working mechanism of UFPs from Iqbal et. al. (2010). Mashal (2015) extended the use of UFPs in dissipative controlled rocking connections for bridges (Figure 2.14).

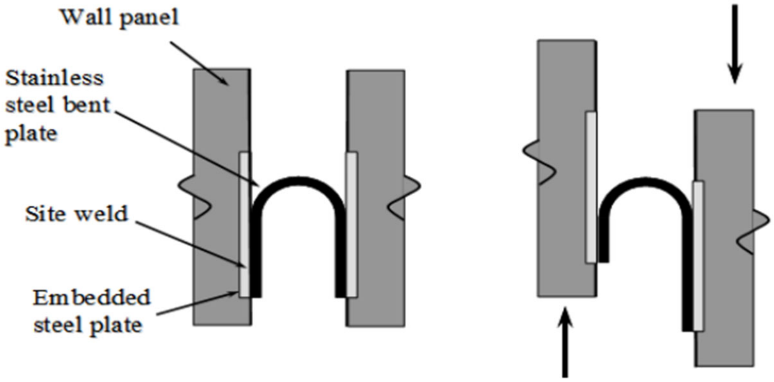

Figure 2.13 Installation and Working Mechanism of U-Shaped Flexural Plates (Iqbal et. al. 2010)

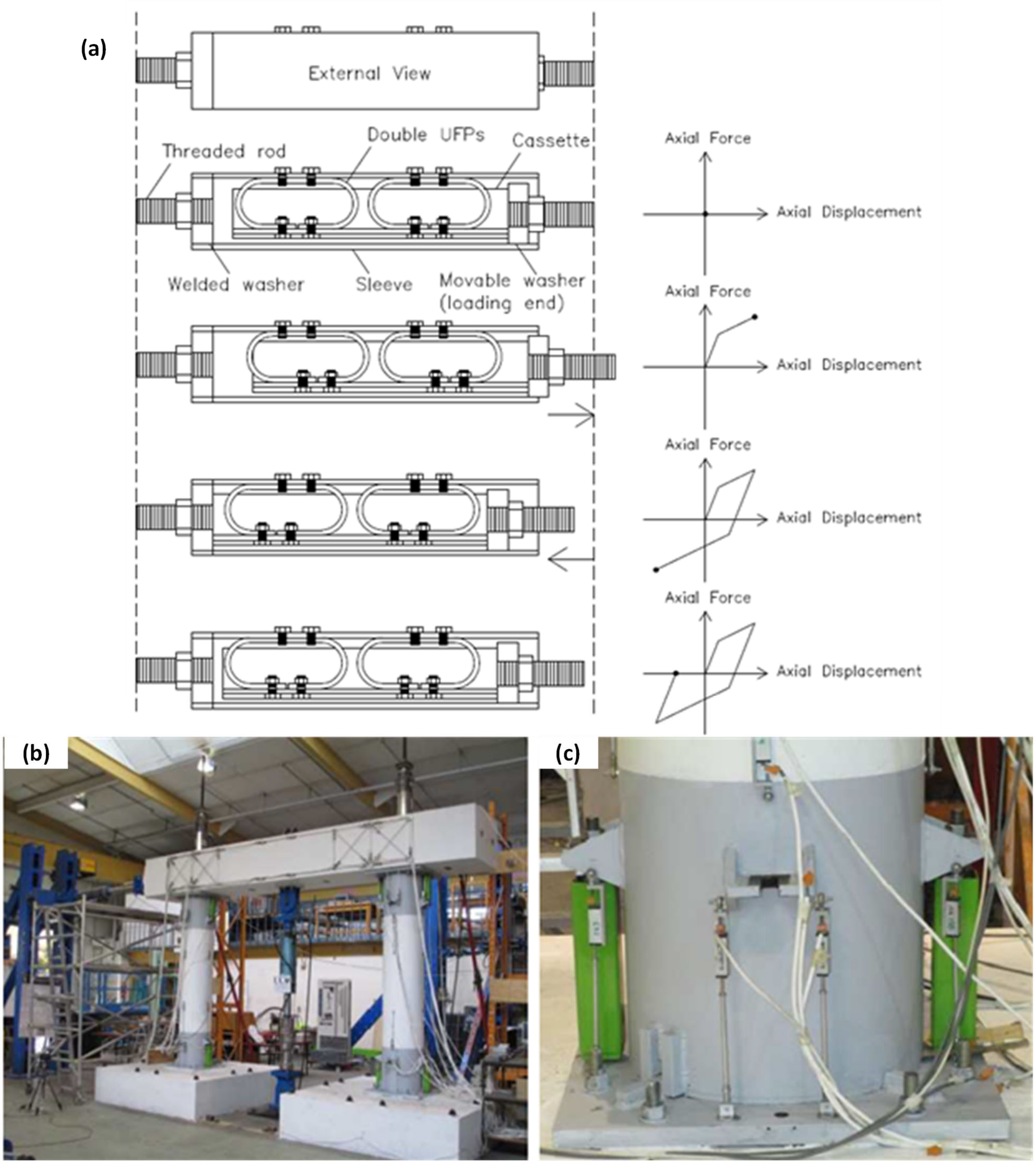

Figure 2.14 (a) Mini UFP Dissipaters (Keats, Palermo, and Mashal 2015), (b) Dissipative Controlled Rocking (DCR) Bent (Mashal 2015), (c) Typical DCR Connection with UFP Dissipaters (Mashal 2015)

Buckling-Restrained Fused Type (BRF): The BRF damper combines the advantages of buckling-restrained braces and fused type dampers to provide effective energy dissipation and improve the overall ductility of the structure. The BRF damper consists of a core element, typically a steel fuse, surrounded by a buckling-restraining casing. The core element is designed to yield and dissipate energy during seismic events, while the casing provides stability and prevents buckling of the core. This combination allows the BRF damper to absorb and dissipate significant amounts of energy, reducing the forces transmitted to the structure and enhancing its seismic resilience.

One of the key advantages of BRF dampers is their ability to provide stable and reliable performance over multiple cycles. The fused type design ensures that the damper retains its strength and functionality even after multiple seismic events. Additionally, BRF dampers offer a high level of ductility, enabling them to withstand large displacements and deformations during earthquakes.

Buckling-Restrained Dry (BRD) Dampers: These dampers combine the advantages of buckling-restrained braces with a dry friction mechanism to effectively dissipate energy during seismic events. The BRD dampers consist of a core element, typically a steel brace, surrounded by a restraining casing. The core element is designed to undergo yielding and plastic deformation, while the restraining casing prevents buckling and provides stability. The dry friction mechanism is employed to introduce additional damping and dissipate energy through the frictional sliding between the components.

One of the key advantages of BRD dampers is their reliable and stable performance over multiple cycles. They exhibit minimal strength degradation and low-cycle fatigue, allowing them to maintain their energy dissipation capacity over time. Furthermore, BRD dampers possess a high capacity for energy dissipation, accommodating significant displacements and deformations during seismic events.

The Wigram-Magdala Link Bridge in Christchurch, New Zealand, is one significant example of how BRD technology has been used. This bridge has BRD dampers built into its controlled rocking joints, which improves its seismic performance in an area prone to earthquakes. Furthermore, White and Palermo (2016) have highlighted the potential of BRP dampers in conjunction with FRP wraps for retrofitting plastic hinges within the existing structures.

Several variations of BRD are Split Tube Type Dissipater, Deformed Tube Type Dissipater, Supported Bar Type Dissipater, and Grooved Bar Dissipater. The grooved bar dissipater is shown in Figure 2.15 for reference.

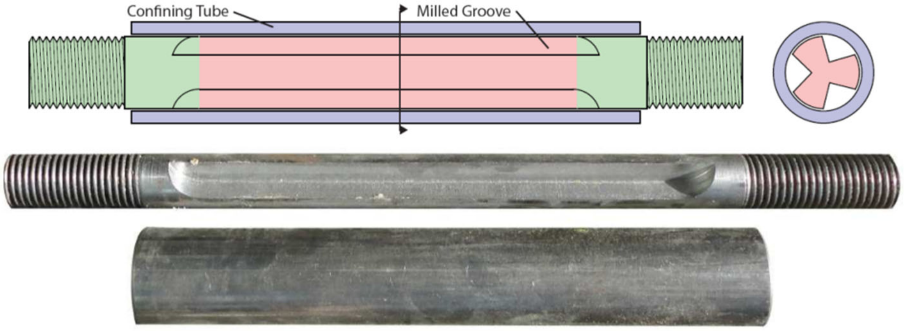

(a)

(b)

Figure 2.15 (a) Grooved Bar Dissipater (White 2014), (b) Wigram-Magdala Link Bridge in Christchurch, New Zealand (Courtesy of Jeremy Kelleher)

Viscous Dampers

Viscous dampers are predominantly velocity-dependent systems that efficiently dissipate energy through the mechanism of viscous friction. These dampers find extensive application in areas characterized by high levels of wind and seismic activity. Due to their inherent velocity dependency, viscous dampers exhibit exceptional performance, especially in the context of near-fault earthquakes, where the ground motions typically exhibit high velocity content. The following are different types of viscous dampers.

Fluid Viscous Dampers: Fluid viscous dampers are a prevalent type of viscous damper used for structural applications. They typically comprise a stainless-steel piston with a bronze orifice head housed inside a cylinder. The damper is filled with silicone oil. When subjected to loads, the orifices in the piston head alter the flow characteristics of the fluid in response to its relative velocity. The force exerted by the damper is generated by the pressure difference across the piston head (Mashal 2015). It has advantages like high energy dissipation without strength degradation, however, fabrication and the life-cycle maintenance costs are potential issues with these types of dampers. They perform well in near-fault ground motions. So, they have been used in a number of bridges including Seo-Hae Grand, Ok- Yeo, Chun-Su, E-Po, Kang-Dong, Dong-Yun bridges (INFANTI et al. 2004). A detail of a fluid viscous damper is given in Figure 2.16.

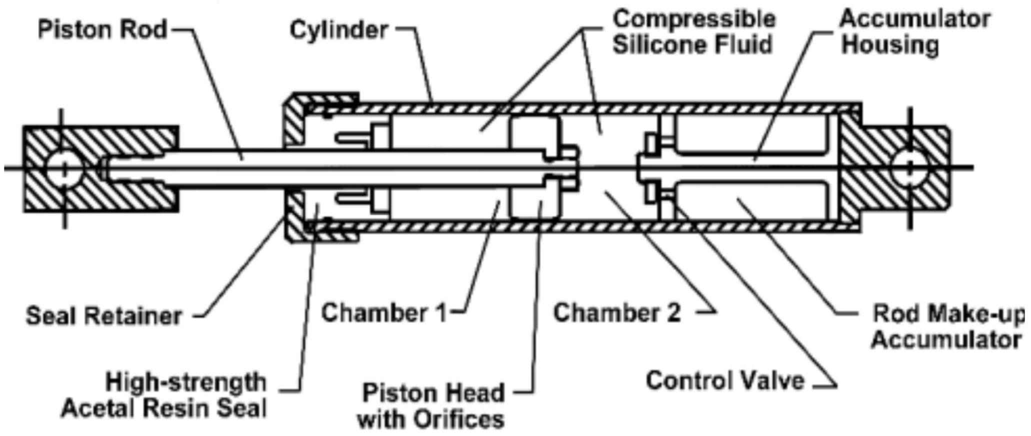

Figure 2.16 Schematic of a fluid viscous damper (Lee 2001)

Ultra-High-Performance Concrete (UHPC)

The outstanding qualities of UHPC, a cutting-edge cementitious material, include high strength, stiffness, extraordinary durability, and steel fiber reinforcing. It is highly sought after in bridge applications due to its self-consolidating capabilities and outstanding mechanical characteristics. UHPC demonstrates better freeze/thaw resistance, fast chloride permeability resistance, and prolonged tensile capacity. Although UHPC may be more expensive in terms of volume, it is advised to use it optimally and to take life-cycle costs into account. It is used in many different types of construction, including pre-stressed girders, precast deck panels, field-cast joint fill, columns, and decorative features. It has a creep coefficient of 0.3 to 0.8, a compressive strength of 18 to 35 ksi, and an elastic modulus of 6,200 to 8,000 ksi. A typical composition of UHPC includes 28.5% Portland cement, 9.3% silica fume, 8.5% ground quartz, 41.0% fine sand, 6.3% steel fibers, 1.2% superplasticizer, and 5.2% water by weight (Graybeal 2020), whereas a typical concrete consists of cement, sand, aggregate and water.

Figure 2.17 Composition of UHPC

According to U.S. Department of Transportation (2021), there were 341 in-service bridges in US that use UHPC as of 2021, and this number is increasing every year. The challenge of connecting prefabricated components has led to the implementation of field-cast UHPC connections between modular precast concrete elements. The UHPC Joint Testing project was conducted over a period of 12 months to thoroughly assess the viability of UHPC connections. The results of the testing demonstrated that UHPC connections offer a practical and effective solution. As a result, numerous bridges have been constructed utilizing UHPC joints and connections. The use of UHPC not only eliminates the need for post-tensioning but also ensures long-term joint performance, providing a sustainable and durable solution for bridge construction (Graybeal 2020).

Research conducted by Shafieifar and Azizinamini (2018) compared the performance UHPC to Normal Strength Concrete (NSC) and highlighted that the compressive and tensile strength, ductility, and modulus of elasticity of UHPC were notably higher than normal strength concrete. These exceptional mechanical and durability properties of UHPC make it suitable for ABC and retrofitting works in seismically active regions. Some specific applications of UHPC include:

- Jointless Connections: UHPC can be used to create jointless connections between precast bridge elements, such as beams and deck panels. These connections offer high load transfer capacity, excellent durability, and reduced maintenance needs. UHPC joints eliminate the need for traditional cast-in-place joints, which require longer curing times.

- Precast Bridge Elements: UHPC is commonly used in the fabrication of precast bridge components, such as beams, columns, and deck panels. Its high strength and stiffness allow for the design of slender and lightweight elements, which are easier to transport, handle, and install. Precast elements made with UHPC can be rapidly assembled on-site, accelerating the overall construction process.

- Full-Depth Prefabricated Bridge Deck Panels: UHPC can be utilized in the production of full-depth precast bridge deck panels. These panels can be manufactured off-site and transported to the construction site, allowing for fast installation. The use of UHPC in deck panels enhances their resistance to corrosion, freeze-thaw cycles, and abrasion, resulting in longer service life.

- Connection Reinforcement: UHPC can be employed to reinforce the connections between precast elements, improving their load-carrying capacity and robustness. By using UHPC for connection reinforcement, bridge construction time can be significantly reduced compared to traditional construction methods.

- Field-Cast UHPC Joints: UHPC can also be used for field-cast joints in ABC. These joints provide high-performance connections between precast elements and can be quickly fabricated and installed. Field-cast UHPC joints offer superior durability and can reduce maintenance needs compared to conventional joint types.

The next section presents the research conducted on UHPC.

Retrofitting of Bridge Columns Using UHPC (Farzad et al. 2019)

The research completed by Farzad et. al. focuses on the repair of bridge piers using UHPC. The research investigated the thickness of UHPC jacketing required, lapping of UHPC with NSC, and surface preparation when installing the UHPC. The repaired columns are tested under cyclic loading and compared to each other, as well as a benchmark specimen.

The Concept: A set of 11 RC columns were manufactured and deliberately subjected to damage. Out of these 11 columns, seven were repaired utilizing UHPC, one with normal strength concrete (NSC), while one column was left unrepaired to serve as a baseline reference. Additionally, two intact columns were fabricated as reference specimens. The dimensions of the 11 specimens are provided in Figure 2.18. The scaling of the specimens followed a 1:4 ratio of a typical bridge column, maintaining a height-to-diameter ratio of 5. Furthermore, two cantilever columns, equipped with separate loading caps, were embedded into a RC footing, and subjected to independent testing procedures.

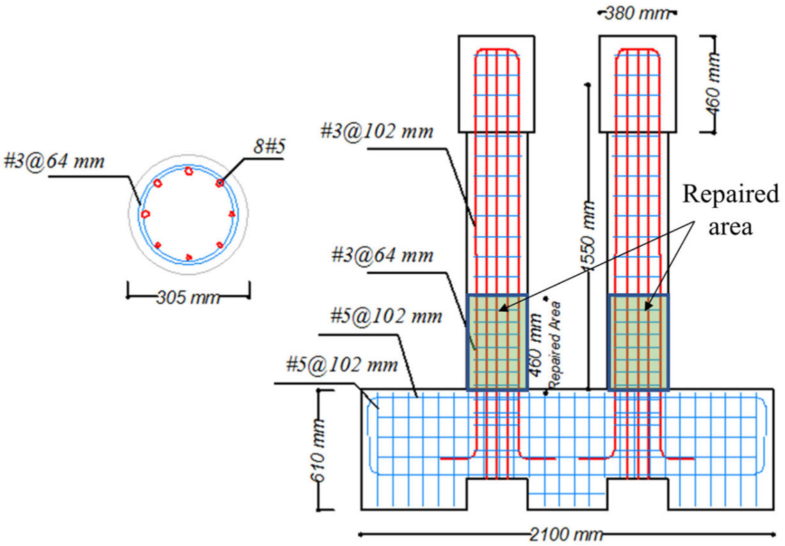

(a)

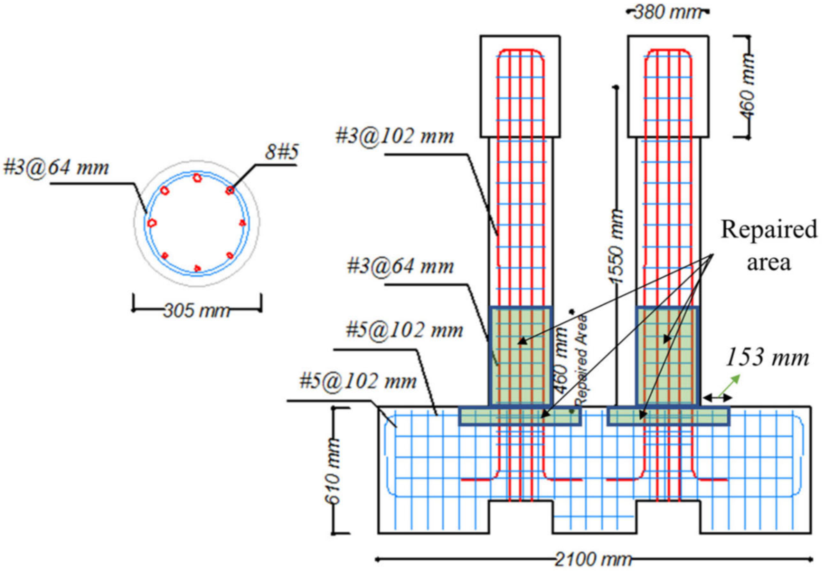

(b)

Figure 2.18 Dimensions of Test Specimen: (a) Footing not Repaired, (b) With Footing Repair (Farzad et al. 2019)

Results: The experimental findings demonstrate that the use of UHPC shell enhances the strength of damaged elements without increasing their size. The UHPC repair scheme proves effective in terms of lateral strength, deformation, energy dissipation, and stiffness degradation. Proper surface preparation ensures no delamination, while the steel fibers in UHPC limit crack development, improving material integrity. The test results also reveal that a short lap splice length in the UHPC repair area is sufficient, and different fiber contents exhibit similar strength behavior. It is important to consider changes in UHPC shell thickness as it can impact the failure location above or below the repaired section in design considerations.

Simplified Method to Estimate the Moment Capacity of Circular Columns Repaired with UHPC (Farzad et al. 2019)

This research addresses the findings of the earlier study completed by Farzad et. al. The previous research illustrated the need of incorporating UHPC shell thickness as a factor in the repair design consideration to minimize the potential issue of the critical section being relocated to undesired locations due to over-strengthening of the repaired section. This research proposes a new simplified analytical approach, relying on hand calculations and fundamental material characteristics, like compressive and tensile strengths, to calculate the bending moment capacity of the repaired section. The research also uses a well-established numerical sectional analysis to validate the results of this simplified approach.

The Concept: In the UHPC method for repairing RC elements, the damaged surface concrete is replaced with a UHPC shell. The retrofitted columns with UHPC are efficient regarding lateral strength, deformation, energy dissipation capacity, and stiffness degradation. Furthermore, UHPC has higher strength compared to substrate material that consequently makes repaired section stronger than the original designed section. However, repairing columns with UHPC method leads to significant change in the behavior of the structure. This change in the sectional properties of the repaired section of the column may cause the critical section (or plastic hinge) to relocate to adjacent unrepaired sections or footing/cap-beam, which put them at risk.

Thus, the need to investigate the sectional changes due to use of UHPC while retrofitting columns is evident. Most of the analytical solutions available to calculate the sectional properties i.e., moment capacity of beam sections after repair are limited to the rectangular cross-section, however typical RC bridge columns have a circular cross-section. Furthermore, use of design software for such calculation inherently depends upon the availability of the stress-strain curves for the substrate and repair materials.

This paper aims to address these concerns by offering streamlined and simplified analytical solutions to assist professional engineers in evaluating the sectional properties of circular RC columns following UHPC repair.

The following assumptions are considered during calculation and modeling:

- Repair material (UHPC) and substrate concrete (Normal Strength Concrete) have perfect bond and act composite in section.
- Reinforcing steel has a rigid–ideally plastic material behavior.
- Flexural strength of NSC is simplified using a rectangular stress block.

- UHPC has linear stress distribution.
- The tensile strength of NSC is small and thus ignored.
- Tensile strength of UHPC is considered and has constant distribution.

Results: The first step involves the determination of the location of neutral axis (NA) using force-equilibrium in the section (Figure 2.19). The forces involved are tensile and compressive strength in NSC, tensile and compressive strength in UHPC, tensile and compressive strength in reinforcing steel, and external axial load. The calculations for these forces are shown in Figure 2.20. From equilibrium of forces the following equation is found:

$$N_{cNSC} - N_{tNSC} + N_{cUHPC} - N_{tUHPC} + N'_s - N_s = P$$

Where:

N_{cNSC} = Compressive force in NSC, in kips per square inch
N_{tNSC} = Tensile force in NSC, in kips per square inch
N_{cUHPC} = Compressive force in UHPC, in kips per square inch
N_{tUHPC} = Tensile force in UHPC, in kips per square inch
N'_s = Compressive force in steel reinforcement, in kips per square inch
N_s = Tensile force in steel reinforcement, in kips per square inch
P = External axial load, in kips per square inch

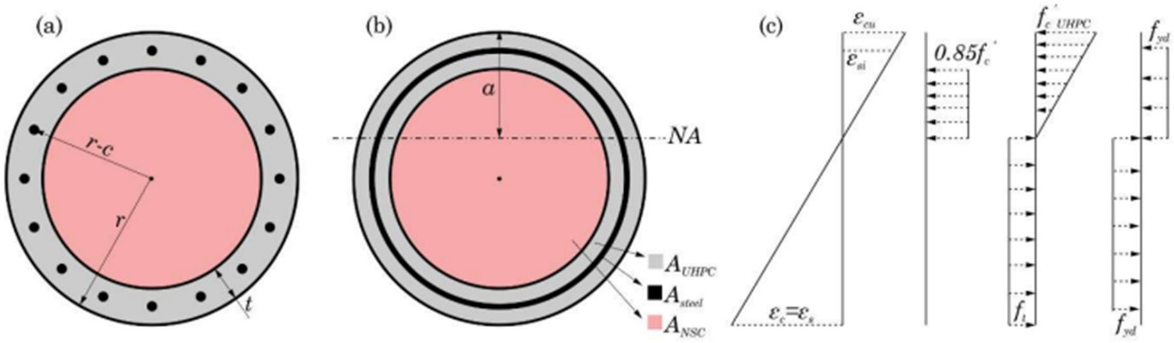

Figure 2.19 (a) Repaired Section Schematic, (b) Simplified Section Schematic, (c) Strain and Stress Diagram for the Cross-Section (Farzad et. al. 2019)

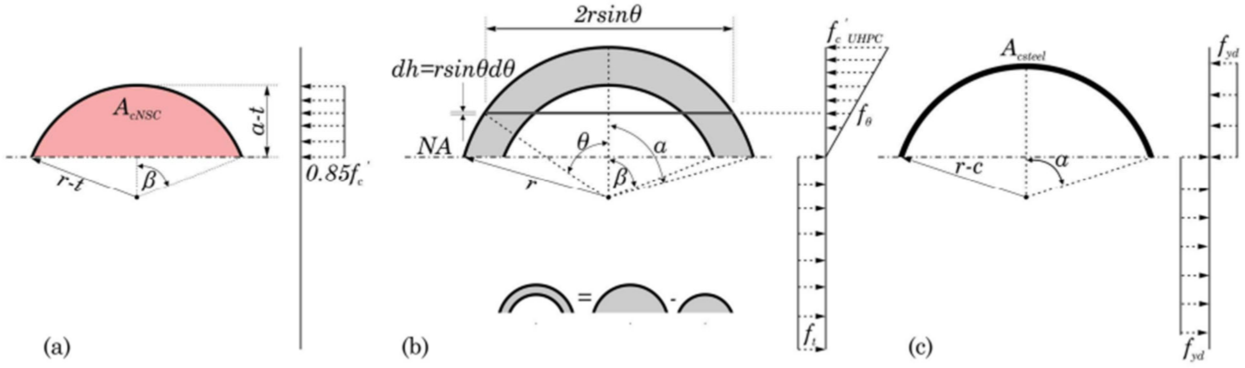

Figure 2.20 Diagram for Calculation of Forces in: (a) Substrate Concrete, (b) UHPC Shell, and (c) Steel Reinforcement (Farzad et. al. 2019)

Using the calculated forces from Figure 2.20 and the previous equation, the following equation is produced through substitution:

$$\left(\frac{2r^2 f'_{cUHPC}}{1-cos\alpha}\right)\left(\frac{1}{3}sin^3 \propto -\frac{\alpha}{2}cos\alpha+\frac{1}{4}cos\alpha sin2\alpha\right)-\left(\frac{\pi-\alpha}{\pi}\right)A_{UHPC}f'_{tUHPC}+\left(\frac{2\alpha -}{\pi}\right)A_s f_{yd}=P$$

Where:

r = Radius of the entire cross-section, in inches

f'_{cUHPC} = Nominal 28-day compressive strength of UHPC, in kips per square inch

α = One half of the angle subtended at the center of the cross-section by the UHPC compression sector

A_{UHPC} = Gross area of UHPC, in square inches

f'_{tUHPC} = Nominal 28-day tensile strength of UHPC, in kips per square inch

A_s = Area of steel reinforcement of steel ring, in square inches

f_{yd} = Design value of steel yield strength, in kips per square inch

The second step computes the moment capacity of the section (M_{Rd}) by summing the moments of each force about the NA.

$$M_{Rd} = M_{cNSC} + M_{cUHPC} + M_{tUHPC} + M_{csteel} + M_{tSteel}$$

Where:

M_{cNSC} = Moment contributed by NSC compressive force, in kip-inches

M_{cUHPC} = Moment contributed by UHPC compressive force, in kip-inches

M_{tUHPC} = Moment contributed by UHPC tensile force, in kip-inches

M_{csteel} = Moment contributed by steel reinforcement compressive force, in kip-inches

M_{tsteel} = Moment contributed by steel reinforcement tensile force, in kip-inches

and,

$$M_{cUHPC} = \left(\frac{2f'_{CUHPC} r^3}{1 - \cos \propto}\right)\left(\frac{\propto}{8} - \frac{1}{3}\cos \propto \sin^3 \propto - \frac{1}{32}\sin 4 \propto\right)$$

$$M_{cNSC} = \frac{2}{3}(r - t)^3 \sin^3 \beta f_{cd}$$

$$M_{steel} = 2(r - c)\left(\frac{\sin\alpha}{\pi}\right) A_s f_{yd}$$

$$M_{tUHPC} = \frac{2}{3} f_t \sin^3 \propto (r^3 - (r - t)^3)$$

Where:

t = UHPC repair thickness, in inches

β = One half of the angle subtended at the center of the cross-section by the NSC compression sector

f_{cd} = Design value of the NSC compressive strength ($0.85f'_c$), in kips per square inch

c = Structural cover concrete, in inches

f_t = Tension strength contributed by UHPC, in kips per square inch

Finally, the proposed approach is evaluated in comparison with the widely recognized moment-curvature method. To conduct this evaluation, three sets of numerical experiments are devised using prototype columns of three common sizes (ranging from 686 to 1067 mm in diameter) (27 to 42 inches). Each set involves the repair of the columns using three different thicknesses of UHPC shells (with ratios of t/r equal to 0.1, 0.2, and 0.5) and subjecting them to three distinct axial loads (P = 0%, 10%, 20%). The moment capacity of each repaired configuration is determined using the proposed simplified method and then compared with the moment-curvature data. Both methods employ the following material characteristics: substrate concrete, UHPC, and steel are defined by f_{0c} = 41 MPa (6 ksi), f_{0c}UHPC = 165 MPa (24 ksi), and f_y = 450 MPa (6.5 ksi), respectively. The results can be seen in Figure 2.21.

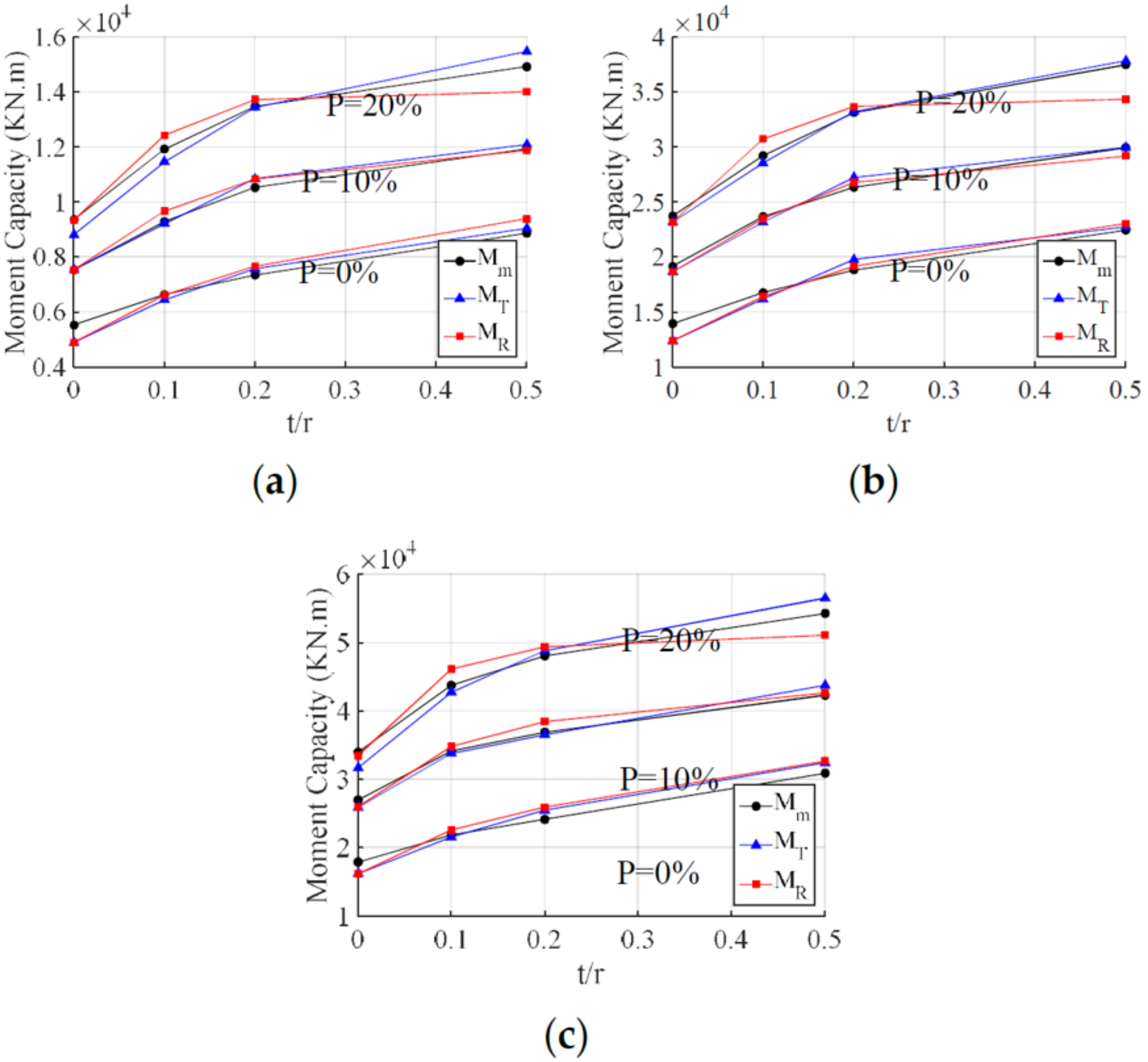

Figure 2.21 Comparison of Moment capacity for: (a) Set 1, r = 686 mm (27 in.), (b) Set 2, r = 914 mm (36 in.), (c) Set 3, r = 1067 mm (42 in.), (1 kN-m = 8.85 kip-in) (Farzad et. al. 2019)

The comparison shows that the average ratio between design load carrying capacity of eccentrically compressed RC members of circular cross-section determined by the proposed method with triangular stress distribution of UHPC in compression (M_T), and the moment-curvature ones (M_M) is 0.98 with a maximum value of M_M / M_T as 1.05. These values for the rectangular stress distribution of UHPC in compression (M_M / M_R) are 0.99 and 1.07 for the average and maximum values, respectively. These results indicate that the proposed method is highly suitable for thinner UHPC thicknesses and an axial load level of 10%, which is a commonly encountered condition.

The level of precision provided by the proposed analytical approach in calculating the moment capacity of the circular columns repaired with the UHPC method is confirmed with the results obtained from a wide range of design cases and resemblance to the output from moment-curvature analysis. Thus, this method can be used by professionals to quantify the strengthening of circular columns when repaired with a UHPC layer.

Strengthening RC columns with Ultra High-Performance Concrete (Koo and Hong 2016)

This research involved four column specimens measuring 300x300x1260 mm (11.8x11.8x49.6 in.) with a span-to-depth ratio of 4.15. The specimens were reinforced with eight 22 mm (0.86 in.) diameter longitudinal bars and transverse reinforcement in the form of 10 mm (0.39 in.) diameter stirrups spaced at 150 mm (5.9 in.) intervals. One specimen served as the control, while specimen 3 was retrofitted with a ultra-high-performance-fiber-reinforced-concrete (UHPFRC) Jacket, varying in thickness and stirrup configuration. The objective of the experiment was to enhance the shear capacity of the RC column using the UHPFRC Jacket. The test was conducted using a double curvature cyclic load test setup. Table 2.1 shows the different levels of reinforcement for each specimen.

Table 2.1 Details of Specimens

	R0	**R3**	**R5**	**R5S**
Retrofit method	Un-strengthened	30mm (1.18 in.) jacket (10% thickness of column)	50mm (1.96 in.) jacket (16.7% thickness of column)	50mm (1.96 in.) jacket + stirrups (D10@150) (D0.39@5.9)
Section	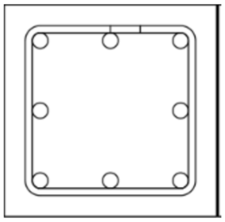	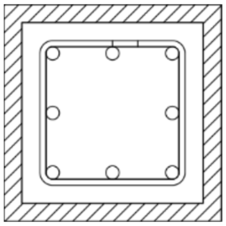	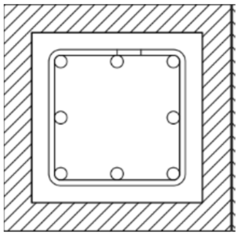	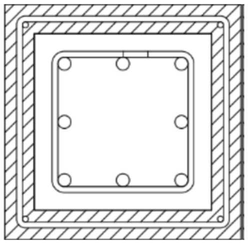

Results: In specimen R0, flexural cracks initially appeared at both ends, followed by flexural shear cracks. At a drift ratio of 1.16%, vertical splitting cracks occurred, resulting in sudden strength degradation due to bond splitting failure. In R3, large diagonal tension cracks emerged at a drift ratio of 1.16%, leading to shear failure. R5 exhibited similar behavior to R3 but with longitudinal reinforcement yielding before crack occurrence. R5S showed unique behavior with initial cracks not extending to diagonal tension cracks due to transverse reinforcements, resulting in flexural yielding. The additional transverse reinforcements in R5 and R5S influenced stiffness and flexural strength to a lesser extent but prevented large diagonal tension cracks, enhancing shear strength and ductility.

A 10% thickness jacket resulted in a 70% increase in shear strength, while a 16.7% thickness led to a 125% strength increase. Although retrofitted specimens (R3, R5) exhibited brittle shear failure in the experiment, the jacket can potentially change the failure mode to flexural shear failure, improving column ductility.

Rehabilitation of concrete structures using Ultra-High-Performance Fiber Reinforced Concrete (Brühwiler and Denarié 2008)

The Concept: This research proposes using UHPFRC to strengthen areas of structures exposed to severe environmental and mechanical loads, while using conventional structural concrete for parts with moderate exposure. This combination effectively enhances protection, resistance, durability, and life-cycle costs of the rehabilitated structure. The concept is suitable for bridges and can be applied to buildings, galleries, tunnels, and retaining walls. Validation through four applications will be discussed further.

Rehabilitation and widening of Road Bridge:

A heavily trafficked road bridge was rehabilitated and widened using Ultra-High-Performance Fiber-Reinforced Concrete (UHPFRC) (Figure 2.22). The 10-meter (32.8 ft) deck surface was rehabilitated in three steps, including the installation of a new downstream UHPFRC curb, replacement of chloride-contaminated concrete with 3 cm (1.18 in.) of UHPFRC, and replacement of the upstream curb with 3 cm (1.18 in.) of UHPFRC.

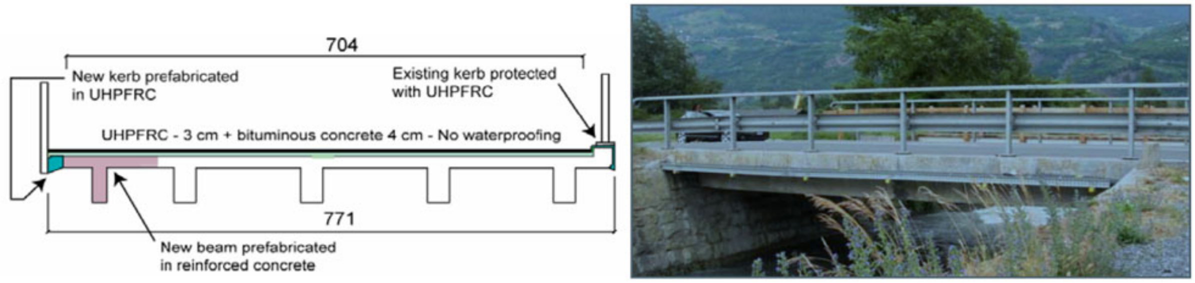

Figure 2.22 Left: Bridge Cross Section After Rehabilitation (Dimensions in cm) and Right: Photo Taken in 2006 (Brühwiler & Denarié 2008)

Result: Air permeability tests using the Torrent method confirmed the UHPFRC layer's significantly low permeability, approximately 30 times lower than conventional concretes. On 28 days, the UHPFRC exhibited an average compressive strength of 182 MPa (2.6 ksi) and modulus of elasticity of 47 GPa (145 ksi). Uniaxial tensile tests on specimens showed remarkable properties with a tensile strength of 14 MPa (2 ksi) and an average maximum tensile deformation in the strain-hardening domain of 1.5 %. Although UHPFRC rehabilitation was 10% costlier than the conventional approach using waterproofing membrane and repair mortar, it offered superior durability and reduced construction time, thereby minimizing traffic disruptions and associated user costs. With wider adoption, UHPFRC is expected to become a more cost-effective option for bridge rehabilitation.

UHPFRC Protection Layer on a Crash Barrier Wall:

A UHPFRC layer was applied to the crash barrier walls of a highway bridge in September 2006 to ensure their long-term durability. Future rehabilitation interventions would disrupt traffic flow due to high volume, hence the need for durability. The UHPFRC layer had to be free of transverse macro-cracks and exhibit extremely low permeability to water and chloride ions. The UHPFRC mixture included 1100 kg/m³ (68.6 lb/ft^3) cement, 26% silica fume, quartz-sand, 6% steel fibers, superplasticizer, and a water-to-cement ratio of 0.17.

Result: Fresh self-compacting UHPFRC was produced at a concrete plant, transported to the site, and applied to create a successful UHPFRC coating in a thin slot. In-situ and laboratory tests confirmed the desired mechanical properties and protective function. The surface appeared smooth and aesthetically appealing with few voids, and after four months, no cracks were observed, aligning with predicted numerical simulations.

Rehabilitation of a Bridge Pier using Prefabricated UHPFRC Shell Elements:

A 4 cm (1.57 in.) thick UHPFRC shell element was fabricated as an outer protective shield for a 40-year-old RC bridge pier. In 2007, the UHPFRC elements were produced, transported, and installed on-site. Epoxy resin bonded the joints, and a self-compacting mortar filled the remaining space. The UHPFRC mixture comprised 1300 kg/m^3 (81.2 lb/ft^3) cement, a water-to-cement ratio of 0.155, and additives like silica fume, quartz sand, steel fibers, and superplasticizer. An image of the project is shown in Figure 2.23.

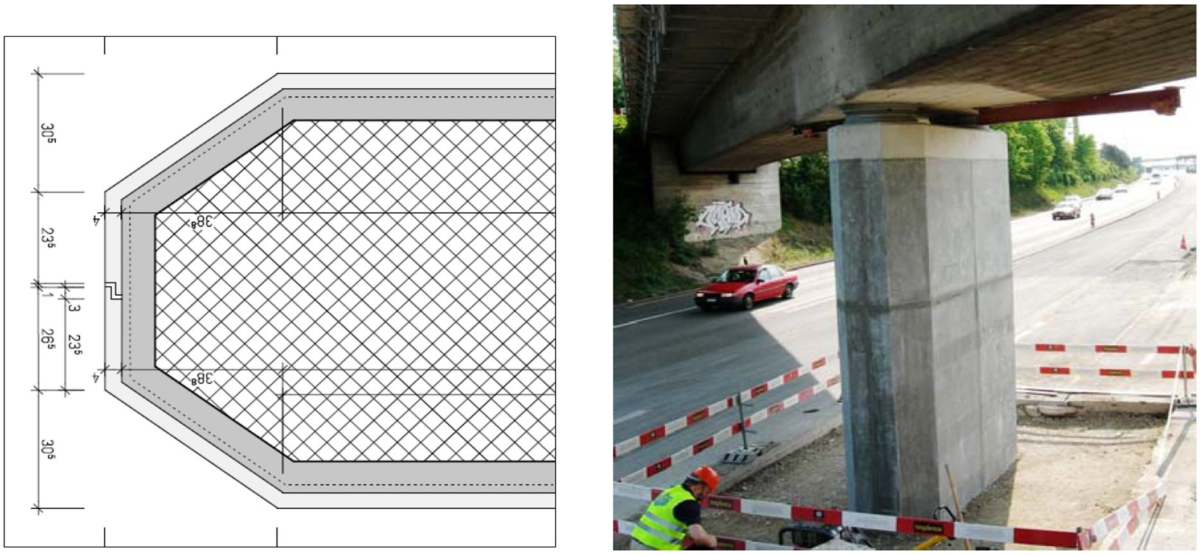

Figure 2.23 Rehabilitated Bridge Pier: Cross Section and General View (Brühwiler & Denarié 2008)

Result: Quality testing confirmed the absence of transverse cracks in the UHPFRC shield, ensuring its expected long-term durability.

Strengthening of an Industrial Floor:

The load carrying capacity of a 50-year-old RC floor in a fire brigade building needed to be enhanced. A 4 cm (1.57 in.) thick UHPFRC layer was proposed to be poured on top of the existing slab, covering an area of 720 m^2 (7750 ft^2). This process aimed to increase the floor's structural strength and performance.

Result: UHPFRC was fabricated in a manufacturing plant and transported to the construction site via trucks. The decision to utilize UHPFRC proved to be highly cost-effective in comparison to the alternative of demolishing and reconstructing the slab, resulting in significant cost savings.

Dowels effectiveness investigation between ultra-high-performance fiber reinforced concrete and reinforced concrete (Paschalis and Lampropoulos 2022)

The study aimed to investigate the effectiveness of using UHPFRC as a strengthening material with dowels at the interface between RC members and the UHPFRC layer. Six beams were tested: two control beams without any layer, two beams with UHPFRC layers added on the tensile side, and two beams with UHPFRC and dowels added at the interface. Figure 2.24 illustrates the reinforcement and dimensions of the beam without any dowels, while Figure 2.25 shows the dimensions of the layers and the position of the dowels. The UHPFRC mix included 3% steel fibers, fine sand, GGBS, silica fume, superplasticizer, and high-strength cement. The dowels were placed using a drill.

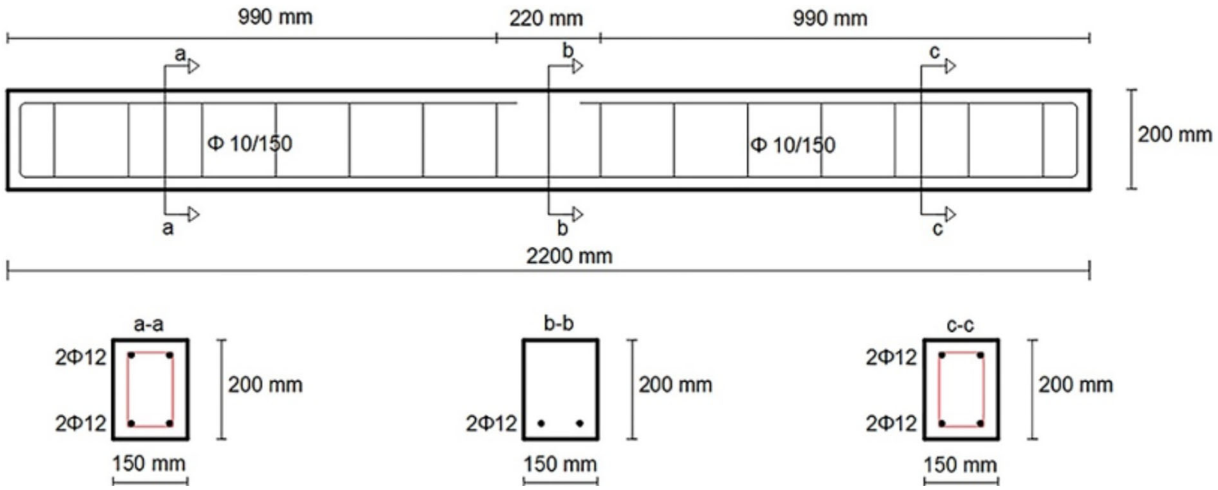

Figure 2.24 Control Beam (Paschalis and Lampropoulos 2022); (1 mm = 0.039 in.)

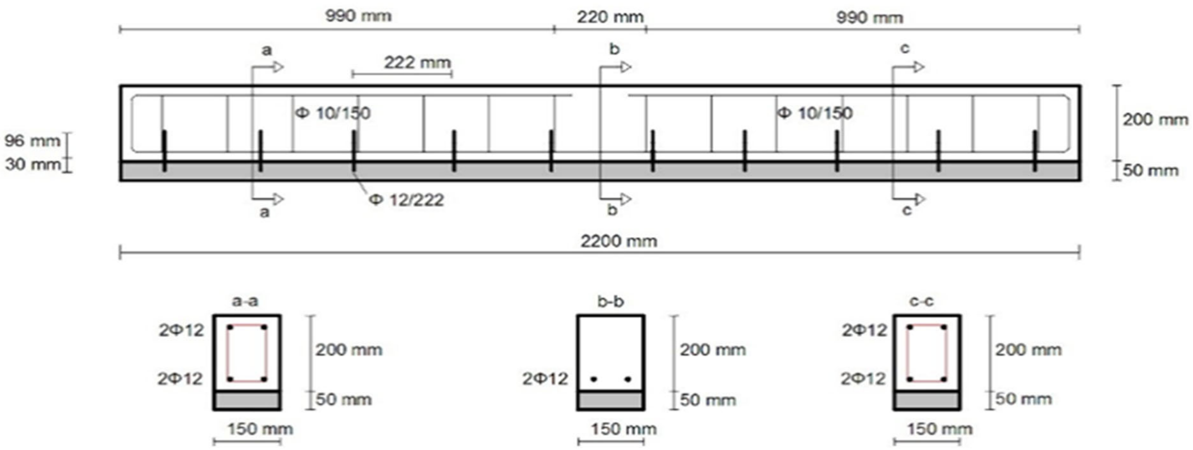

Figure 2.25 Strengthened Beam Using Dowels (Paschalis and Lampropoulos 2022); (1 mm = 0.039 in.)

Result: The study confirmed the effectiveness of dowels. The combination of UHPFRC layers and dowels significantly increased the load carrying capacity by 22.5%, while using layers alone resulted in a 1.5% increase. Control beams experienced major cracks, while beams with UHPFRC layers exhibited crack propagation. Debonding at the interface was observed in beams with both layers and dowels, but the presence of dowels delayed crack formation. Control beams cracked at 5 kN (1.12 kip), strengthened beams with layers at 15 kN (3.37 kip), and beams with layers and dowels at 24 kN (5.4 kip). Notably, beams with dowels demonstrated lower slip values compared to those without dowels. Figure 2.26 illustrates the failure modes of the beams.

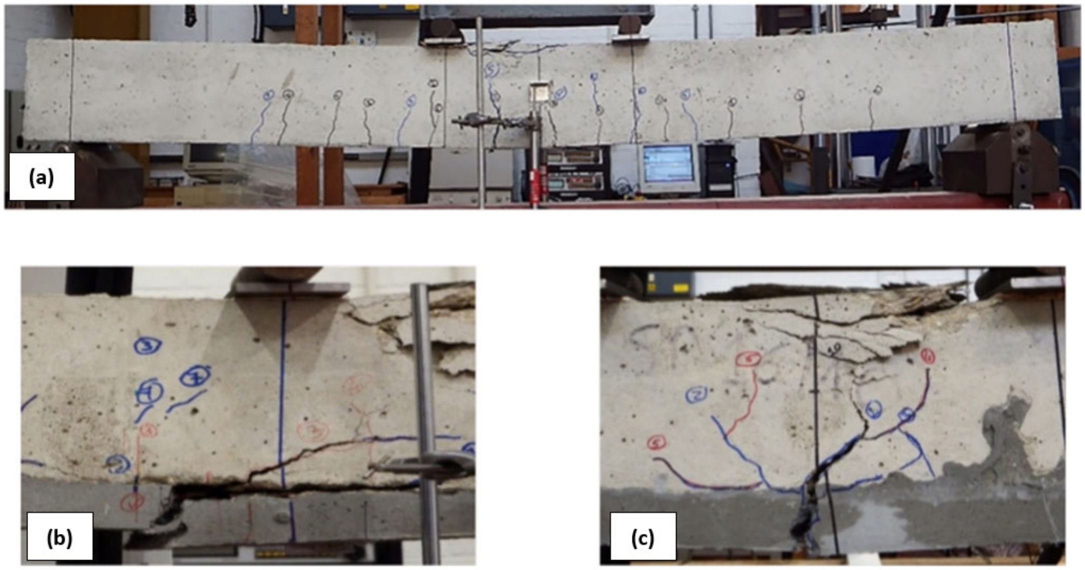

Figure 2.26 Mode of Failure: (a) Control Beam, (b) Beam Strengthened With UHPFRC Layer, (c) Beam Strengthened With UHPFRC Layer and Dowels (Paschalis and Lampropoulos 2022)

Seismic Behavior and Shear Bearing Capacity of Ultra-High-Performance Fiber-Reinforced Concrete (UHPFRC) Beam-Column Joints (Wang et al. 2018)

The primary aim of this research paper is to investigate the seismic behavior and shear bearing capacity of UHPFRC beam-column joints. The study examines nine beam-column joints, comprising five exterior and four interior reinforced UHPFRC joints. The dimensions of the beams and columns were 150x250 mm (5.9x9.8 in.) and 200x200 mm (7.8x7.8 in.), respectively. The experimental investigation considered several variables, such as joint type, nominal yielding strength of longitudinal bars, axial compression load ratio of the column, and stirrup volume ratio in the joint area. These factors were carefully analyzed to determine their influence on the research outcomes. Quasi-static testing was conducted to gather data for analysis and evaluation.

Result: All nine specimens exhibited a consistent failure pattern, with the sequence of events as follows: initiation of a flexural crack in the beam adjacent to the joint region, subsequent development of diagonal cracks in the joint core, and ultimately, shear failure in the joint core.

Comparatively, reinforced UHPFRC beam-column joints demonstrated higher initial cracking strength and shear carrying capacity than non-composite (NC) joints. The shear strengths of exterior joints were approximately 80-90% of those observed in interior joints. Furthermore, incorporating HRB600 grade high-strength steel bars with higher yield strain and lower elastic modulus can enhance the ductility and strength degradation characteristics of UHPFRC joints.

Ultra-high-performance fiber-reinforced concrete jacket for the repair and the seismic retrofitting of Italian and Chinese RC bridges (Lavorato et al. 2017)

The study focuses on a Chinese RC Bridge, which has experienced damage at the base of cantilever RC piers due to cyclic loading. To address the need for rapid repair and seismic upgrade, innovative interventions are required. The central pier, measuring 7 meters (22.9 ft) in length, undergoes the highest stress during seismic events. To investigate the behavior of a 7-meter (22.9 ft) pier, scaled pier specimens at a ratio of 1:6 was constructed and subjected to axial load. Two repair strategies, PR1 and PR2, are employed. PR1 involves using self-compacting concrete and CFRP wrapping, while PR2 utilizes UHPFRC with 2% steel fiber. Both strategies employ rebar parts to replace damaged longitudinal rebar, allowing for seismic energy dissipation through steel plastic deformations, while also offering time and cost savings.

Specimens P16-1 and P16-2 were initially damaged by applying the same vertical load and displacement history as seen by the bridge. Subsequently, both specimens underwent retrofitting and repair using two different procedures. The repaired specimens were subjected to the same load and displacements as before. At the end of the tests, no connection ruptures were observed in either specimen. While both retrofit techniques proved effective, the use of UHPFRC for retrofitting demonstrated superior performance compared to CFRP wrapping and stirrups. The UHPFRC retrofitting approach saved time and costs as it eliminated the need for additional reinforcements, making it the preferred method for enhancing the structural integrity of the specimens.

Column and Joint Retrofitting with High Performance Fiber Reinforced Concrete Jacketing (Beschi et al. 2011)

In this research, the application of the HPFRC technique on a school building in Rome is presented. For the column and joints, a 40 mm (1.57 in.) thick jacket made of HPFRC was used, while 40 mm 1.57 in.) FRP sheets were used for the beams. Two full-scale tests with cyclic loads were conducted to assess the effectiveness of the retrofitting. In the column test, a specimen was subjected to an axial load of 170 kN (38.2 kip) to simulate the conditions during the application of the jacket.

The test conducted on the strengthened column involved applying constant axial force along with maximum design bending moment and shear force in both directions. No cracks were observed on the strengthening jacket at this point. To assess its effectiveness, horizontal load with cyclic loading was then applied, gradually increasing in amplitude until failure. The test was stopped during the third cycle at a drift level of 6%. Although the first visible crack in the jacket appeared at 1% drift, the behavior remained stable until failure with only limited damage. Local damage was observed at the jacket-foundation interface, and the main crack extended to the base of the column near the foundation. The test also demonstrated the stable dissipation of energy during the cyclic loading.

In the beam-column joint test, the column surface was prepared by applying a 40 mm (1.57 in.) thick jacket of FRC. The upper faces of the beams were also covered with FRP sheets that were bent at a 90° angle, glued to the column, and enclosed within an HPFRC jacket. After the column was prepared, it was subjected to axial load.

To simulate critical design load combinations, an axial load of 140 kN (31.5 kip) was applied to the top of the column using two hydraulic jacks. Subsequently, a horizontal cyclic load was applied at the top of the column. Initially, multiple forces were applied to represent the service loads acting on the joint. The horizontal load was then increased in amplitude in cycles until failure occurred. Specifically, three cycles were carried out for drift levels of 0.5%, 1%, 1.5%, 2%, and 2.5%, and additional cycles were performed with a 0.5% increment in drift until failure was reached.

Results: The joint exhibited stable behavior up to a drift level of 0.95%, which is higher than the design force at the ultimate limit state. At a drift level of 0.5%, a single hairline crack was observed at the top of the column base within the jacket. However, at a drift level of 4%, the top of the column failed due to concrete crushing at the joint's top and detachment of the HPFRC layer encasing the FRP sheet. Although no visible damage was observed on the joint surface, removing the HPFRC revealed severe damage to the internal part of the joint.

The application of the jacket in both the column and beam-column joint specimens resulted in an increase in their bearing capacity. Additionally, the ductility of the specimens was also enhanced. This retrofit technique is particularly suitable for structures with low concrete strength and low reinforcement ratio. Moreover, the use of a thin jacket addresses the drawback of traditional retrofit methods by not significantly altering the stiffness of the structure.

Cost and Ecological Feasibility of using UHPC in Bridge Piers (Joe and Moustafa 2016)

This study aims to redesign a specific substructure component of a three-span highway bridge using UHPC. The bridge prototype is a typical RC box-girder bridge from the Caltrans Department of Transportation. The focus is on the bridge pier (bent) consisting of two columns and an integral bent cap beam. The objective is to explore different UHPC mixes and optimize the design for cost-effectiveness and environmental friendliness. Three mix designs with varying characteristics were analyzed, and their mechanical properties are summarized in Table 2.2 and Table 2.3.

Table 2.2 Mix Design Summary of UHPC lb/yd^3 (kg/m^3), (Joe and Moustafa 2016)

	Mix #1	Mix #2	Mix #3
Cement	1,200 (712)	1,180 (700)	1,402 (832)
Fine Sand	1,720 (1020)	1,778 (1055)	-
Microsand	-	369 (219)	-
Ground Quartz	355 (211)	295 (175)	349 (207)
Quartz Sand	-	-	1,643 (975)
Silica Fume	390 (231)	74 (44)	228 (135)
High Range Water Reducer	51.8 (31)	77.4 (46)	50 (30)
Accelerator	50.5 (30)	-	-
Steel Fibers	263 (156)	82 (49)	324 (192)
Water	184 (109)	341 (202)	280 (166)
W/C	0.15	0.29	0.20
Source	Graybeal (2006)	Yu et al. (2014)	Ritter & Curbach (2015)

Table 2.3 Mechanical Properties of UHPC, (Joe and Moustafa, 2016)

	Mix #1	Mix #2	Mix #3
Compressive Strength (f'c), psi (MPa)	17,200 (119)	21,611 (149)	25,240 (174)
Modulus of Elasticity (E), psi (MPa)	6.07E+6 (41851)	6.79E+6 (46815)	7.33E+06 (50,539)
Source	Graybeal (2006)	Yu et al. (2014)	Ritter & Curbach (2015)

Result: The use of UHPC in column design yields increased shear capacities and reduced axial load. The results indicate significant changes in design parameters and costs compared to the original design, as shown in Table 2.4. The cross-sectional area decreases between 33.3% and 50%, total reinforcing steel decreases between 52.9% and 72.7%, and cement content decreases by 3.5-36.6%, leading to a reduction in CO_2 emissions. However, the cost of UHPC is considerably higher, with up to a 790% increase in cost per column. Mix #1 achieves break-even in terms of cement and CO_2 content, while Mix #3 demonstrates the best properties. Despite high concrete costs, the reduction in the required volume and potential cost benefits are worth considering, particularly if UHPC becomes more affordable. Additional cost benefits may arise from time savings during construction and extended service life.

Table 2.4 Percentage of Change in UHPC Design Parameter and Costs with respect to the original conventional concrete design

Design Per Column	Mix #1	Mix #2	Mix #3
Column Diameter	33.3%	41.7%	50%
Longitudinal Reinforcement	52.2%	60.9%	72.6%
Transverse Reinforcement	87.3%	92.3%	93.5%
Volume of Concrete	55.5%	65.9%	75%
Weight of Cement Consumed	3.5%	27.4%	36.6%
Weight of Steel Consumed	52.9%	61.8%	72.7%
Total Cost of Concrete	-790%*	-578%*	-400%*
Total Cost of Steel	52.9%	61.8%	72.7%
CO2 Produced	3.5%	27.4%	36.6%

*minus sign indicates an increase not a reduction, i.e. unfavorable change with respect to original design

UHPC pier repair/retrofit examples of completed projects in North America (Doiron 2016)

This study's major goal is to demonstrate the effectiveness of UHPC in solving complex repair and retrofit problems, which will increase infrastructure longevity and lower maintenance needs. In particular, the Ductal® brand was used in four different North American projects that used customized UHPC technologies. These projects were selected because they each had a special application for UHPC, such as improving durability in a pier jacketing project, implementing seismic retrofitting on an existing bridge pier, creating effective connections between a new precast pier cap and existing columns, and providing encasement for the lower levels of corroded steel structures. Each project is presented and discussed in this section.

CN Rail Bridge Pier Jacketing, Montreal, Quebec, Canada

Challenge: Finding a novel, long-lasting repair for a rail bridge pier in Montreal with constrained space, a thin repair cover, and a parallelogram cross-section was a challenge. The repair was intended to last beyond a typical concrete retrofit by protecting against chloride and freeze/thaw degradation. One lane of traffic and continuous train traffic on the bridge were required during construction.

Solution: The solution involves repairing the damage with fluid, self-leveling UHPC. A galvanized rebar cage was erected, the degraded layer was taken off, and forms for 100 mm (3.93 in.) thick new concrete were laid up. Design engineers created watertight forms that could endure hydrostatic pressure. Around

11 m^3 (388.4 ft^3) of UHPC were utilized in the project, which was successfully finished in October 2013. Phases of construction can be seen in Figure 2.27 to Figure 2.29.

Figure 2.27 Surface of CN Rail Bridge Before Repair (Doiron 2016)

Figure 2.28 Setting-up the Formwork for Casting (Doiron 2016)

Figure 2.29 Finished Surface (Doiron 2016)

Mission Bridge Seismic Retrofit, Abbotsford, British Columbia, Canada

Challenge: V-Shaped concrete pier (Pier S4) of the Mission Bridge, a vital link in a seismically active area, needed to be retrofitted to maintain its integrity. The area's soil had liquefiable sand, and Pier S4's light-reinforced rectangular concrete columns were susceptible to collapse and excessive displacement from earthquake stress.

Solution: Associated Engineering recommended using UHPC jackets for retrofit after weighing the pros and cons of other choices. By adopting thin jackets, this method offered cost benefits, aesthetic appeal, and a high seismic deformation capacity. New 225 mm (8.86 in.) thick UHPC jackets were applied after the original columns were cleaned, dowels, and a rebar cage were added. An image showing before and after the construction project is shown in Figure 2.30. After being successfully finished, the retrofit was given the "ACI Excellence in Concrete Award."

(a) (b)

Figure 2.30 (a) Surface of Mission Bridge Pier Before Retrofit (b) Surface of Bridge Pier After Retrofit (Doiron 2016)

Hooper Road, Town of Union, New York

Challenge: The challenging task was replacing the superstructure of the bridge while attaching new precast piers to existing columns. It appeared impossible to determine where the rebar were in the columns, prevent conflicts while drilling new holes, and match the locations with ducts formed in the new piers. A solution that might shorten the connecting process's duration was needed due to the complexity of the situation and the rigorous construction timetable.

Solution: The project relied on UHPC to join the fresh precast piers to the old columns. It was possible to maintain continuity with new dowels extending from the underside of the new piers by exposing and cutting the existing rebar. UHPC made it possible to create structures quickly because the smaller diameter dowels didn't require individual duct grouting. The use of UHPC connectors allowed for simple changes, reduced the need for two extra days, and removed uncertainty about misalignment. The project was completed within 21 days. Figure 2.31 shows the pier retrofit process.

(a) (b)

Figure 2.31 (a) Condition of Existing Rebars and New Dowels, (b) Completed Retrofit (Doiron 2016)

Hagwilget Bridge, New Hazelton, British Columbia, Canada

Challenge: Strengthening the suspension bridge's bent steel legs, which had acquired localized corrosion at their base, was a difficulty. In a confined and crowded space, the solution had to address the weak spots, offer corrosion protection, and guarantee load transfer. High strength, great flow ability, little shrinkage, low permeability, and strong tensile capacity were required. The renovation had to be done while the bridge was still open to traffic, which made the job more challenging.

Solution: UHPC was used to encase the bent steel legs as a fix. To distribute the vertical load to the top of the UHPC encasement and facilitate load transfer, steel plates were fastened on either side of the flanges. 32 bent leg bases were repaired, offering good corrosion protection and durable weight transfer capacities.

Conclusion

The examples show that based on project needs, UHPC is selected for pier/column repair and retrofit. Its selection is influenced by elements including resistance to chloride and freeze-thaw, ductility, aesthetics, cost savings, speed of execution, uncomplicated details, confinement, and high compressive strength. UHPC offers a promising approach for reducing continuing maintenance costs and assuring permanent repairs for the remaining life of structures, but its implementation requires collaboration and adjustments.

Characterization of Strength and Durability of Ultra-High-Performance Concrete Under Variable Curing Conditions (Ahlborn et al. 2011)

The study primarily focuses on investigating the effects of curing regimes and specimen age on the strength and durability of fiber reinforced UHPC. In addition, UHPC using two curing regimes is compared to determine resistance to rapid chloride penetration and freeze-thaw and coefficient of thermal expansion (CTE) testing. Secondarily, this paper endeavors to aid in development of draft standards for testing some UHPC material properties in the USA by employing modified versions of ASTM and AASHTO standard testing methods.

The Concept: The mechanical properties of UHPC structures such as compressive strength, modulus of elasticity, Poisson's ratio, and flexural strength at first crack at ages up to 28 days varies under variable curing regimes, thermal treatments, and specimen age. Validation of UHPC research test findings conducted overseas is necessary in the United States. This validation is sought by American engineers and designers who value adherence to ASTM and AASHTO testing standards.

Experiments and Results: In this research, various mechanical and durability characteristics of UHPC are studied under four different curing regimes:

- Ambient air curing
- TT (48-h thermal steam treatment),
- DTT (delayed thermal steam treatment: 10-day delay before curing is applied)
- DDTT (double-delayed thermal steam treatment: 24-day delay before curing is applied).

Results:

- Compressive Strength:

  Despite the air-cured specimens exhibiting an increase in strength over the course of 28 days, the analysis revealed no variation in compressive stress following the application of thermal treatment. The average compressive stress for all cylinders subjected to thermal treatment (TT), double thermal treatment (DTT), and double delayed thermal treatment (DDTT) was determined to be 30.1 ksi. The compressive stress remained consistent regardless of the age at which thermal treatment was administered or the age at which the specimens were tested after thermal treatment.

- Modulus of Elasticity and Poisson's Ratio:

  The modulus of elasticity exhibited an increase over time for the air-cured specimens during the early stages. Similarly, the three curing regimes (TT, DTT, and DDTT) showed no significant difference in their population mean, with a combined modulus of elasticity of 8,150 ksi. A less prominent trend observed in the data was a decrease in the modulus of elasticity when the fibers were excluded from the mixture.

Interestingly, the four curing regimes had no influence on Poisson's ratio, as all specimens, regardless of their age or curing method, demonstrated the same population mean. The mean value for all samples was 0.21, which aligns with the recommendations of the Association Française de Génie Civil (AFGC) and slightly exceeds the commonly accepted value of 0.20 for normal-strength concrete (NSC) in the United States.

- Flexural Strength at First Crack:

  The results of the flexural testing indicated that the mechanical properties tested in this research exhibited the highest coefficient of variation (COV). However, the COV reported was only slightly higher than the one-sigma limit of 7% required in ASTM C1018 for the first-crack flexural stress.

- Rapid Chloride Penetration:

  All specimens demonstrated minimal chloride ion penetration, falling within the negligible range of less than 100°C passed. The total charge passing through the thermally treated (TT) specimens was found to be lower compared to the air-cured specimens. A t-test statistical analysis further confirmed that the amount of charge passed in the thermally treated specimens was significantly lower than in the air-cured specimens. Another statistical analysis conducted on the thermally treated specimens indicated that ionic movement was not influenced by the duration of treatment, whether the specimen was tested at 7 or 28 days, within a 95% confidence interval.

- Freeze-Thaw Cyclic Testing**:**

  The wet-dry air-cured specimens’ Relative Dynamic Modulus (RDM) increased with a similar trend to that of the air-cured freeze-thaw specimens. However, the increase of the TT specimens was small in comparison to that of the air-cured specimens. This difference can be primarily attributed to the greater amounts of un-hydrated cement particles in the air-cured specimens that can become hydrated in the presence of water.

- CTE Testing**:**

  The results revealed that the age of the specimen at the time of testing had an impact on the CTE for air-cured UHPC specimens but not for TT-cured specimens. Furthermore, a statistical t-test confirmed that regardless of the specimen age, TT-cured UHPC specimens exhibited a significantly higher CTE value compared to the air-cured specimens.

Numerical Investigation on Plastic Hinge Length of Ultra-High-Performance Concrete Column under Cyclic Load (Ren et al. 2022)

The purpose of this paper is to investigate the plastic hinge lengths of UHPC columns under cyclic load through numerical analysis. Due to the high cost of experimental testing, the study focuses on using the finite element method (FEM) with the software OpenSees for analysis. The study aims to determine the effect of various parameters such as horizontal loading angle, axial force ratio, reinforcement diameter, yield strength of reinforcement, and column length on the plastic hinge length of UHPC columns.

The Concept: The plastic hinge length refers to the portion of a column that experiences continuous plastic deformation and significant damage at the base or both ends during extreme events like earthquakes. Accurately determining the appropriate plastic hinge length is crucial for seismic retrofitting of existing structures and seismic design in new projects. However, there is a lack of sufficient research on the plastic hinge length of UHPC members, highlighting the need for further investigation to fill this knowledge gap. Given the high cost associated with testing, conducting numerical analysis to study the seismic behavior of structures presents a viable alternative.

The analysis was conducted using the finite element method (FEM) and the OpenSees software, which was calibrated using test results. A parametric analysis was performed to evaluate the influence of key parameters on the length of the plastic zone. The simulated results were then compared with existing empirical models for RC columns to assess their applicability to UHPC columns. Additionally, a multivariate regression analysis was carried out to develop an expression that could estimate the equivalent plastic hinge lengths of UHPC columns.

Results:

- By disregarding the damage resulting from cyclic loading and the inherent inaccuracies of constitutive models, it is possible to reasonably predict the seismic behavior of UHPC columns. This can be achieved by employing suitable materials and elements from the OpenSees platform, combined with an integrated UHPC model.
- The plastic zone length of UHPC columns demonstrated a decrease as the axial load ratio increased, while it exhibited a continuous increase with the length of the column. Additionally, an initial increase followed by a decrease in the plastic zone length was observed as the horizontal loading angle, reinforcement diameter, and yield strength of reinforcement increased.
- The utilization of empirical models developed for RC columns to estimate the equivalent plastic hinge lengths of UHPC columns resulted in significant errors, generally underestimating the plastic deformation of UHPC columns. In contrast, the proposed expression for the equivalent plastic hinge length of UHPC columns showed reasonable agreement with the results obtained from FEM.

Rapid Repair of Reinforced Concrete Bridge Columns Via Plastic Hinge Relocation Utilizing Conventional Materials (Krish et al. 2018)

The scope of this research is to investigate the effectiveness of conventional materials in plastic hinge relocation while repairing extensively damaged RC bridge columns. The study involves repair and retesting of six large-scale cantilever bridge columns that have been subjected to varying levels of damage.

The Concept: Capacity design principles in modern design methods tackle the shortcomings of older structures by focusing on localizing damage to specific regions known as plastic hinges, while safeguarding other areas against potential damage. For small earthquakes, the damage can result in loss of cover and moderate yielding of longitudinal bars whereas for large earthquake, the damage can range from buckling to the fracture of longitudinal steel. These damages are previously considered beyond the scope of repair, however, repair of the structures designed to modern standards, especially with fractured reinforcement, can be feasible with plastic hinge relocation technique that aims to repair and strengthen original hinge location and force a new plastic hinge to form in previously undamaged location in the column.

Six columns each 108 inches tall from the top of footing to the center of loading with an outer diameter of 24 inches (L/D = 4.56) and axial load of 191 kips ($P / f'_c A_g = 6.0$ to 7.5%) and with varying degree of damage were repaired and tested. Figure 2.32 shows the damage to each column and the repair method for each.

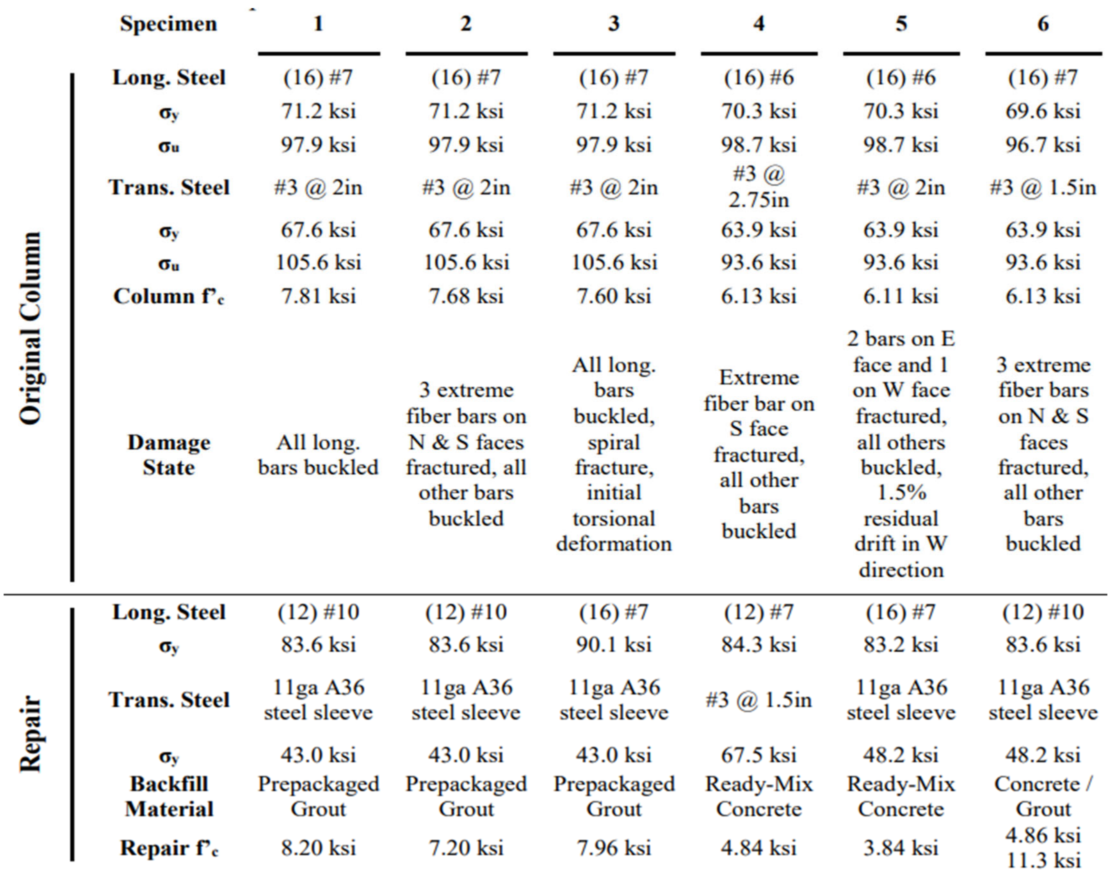

	Specimen	1	2	3	4	5	6
Original Column	Long. Steel	(16) #7	(16) #7	(16) #7	(16) #6	(16) #6	(16) #7
	σ_y	71.2 ksi	71.2 ksi	71.2 ksi	70.3 ksi	70.3 ksi	69.6 ksi
	σ_u	97.9 ksi	97.9 ksi	97.9 ksi	98.7 ksi	98.7 ksi	96.7 ksi
	Trans. Steel	#3 @ 2in	#3 @ 2in	#3 @ 2in	#3 @ 2.75in	#3 @ 2in	#3 @ 1.5in
	σ_y	67.6 ksi	67.6 ksi	67.6 ksi	63.9 ksi	63.9 ksi	63.9 ksi
	σ_u	105.6 ksi	105.6 ksi	105.6 ksi	93.6 ksi	93.6 ksi	93.6 ksi
	Column f'_c	7.81 ksi	7.68 ksi	7.60 ksi	6.13 ksi	6.11 ksi	6.13 ksi
	Damage State	All long. bars buckled	3 extreme fiber bars on N & S faces fractured, all other bars buckled	All long. bars buckled, spiral fracture, initial torsional deformation	Extreme fiber bar on S face fractured, all other bars buckled	2 bars on E face and 1 on W face fractured, all others buckled, 1.5% residual drift in W direction	3 extreme fiber bars on N & S faces fractured, all other bars buckled
Repair	Long. Steel	(12) #10	(12) #10	(16) #7	(12) #7	(16) #7	(12) #10
	σ_y	83.6 ksi	83.6 ksi	90.1 ksi	84.3 ksi	83.2 ksi	83.6 ksi
	Trans. Steel	11ga A36 steel sleeve	11ga A36 steel sleeve	11ga A36 steel sleeve	#3 @ 1.5in	11ga A36 steel sleeve	11ga A36 steel sleeve
	σ_y	43.0 ksi	43.0 ksi	43.0 ksi	67.5 ksi	48.2 ksi	48.2 ksi
	Backfill Material	Prepackaged Grout	Prepackaged Grout	Prepackaged Grout	Ready-Mix Concrete	Ready-Mix Concrete	Concrete / Grout
	Repair f'_c	8.20 ksi	7.20 ksi	7.96 ksi	4.84 ksi	3.84 ksi	4.86 ksi 11.3 ksi

Figure 2.32 Test Matrix for Column Repair (Krish et al. 2018)

Results: The main objective of each test was to utilize the plastic hinge relocation method to restore the original strength and displacement capacity of the columns. In terms of this overarching objective, each repair performed effectively and successfully achieved at least one of these goals, with most repairs accomplishing both simultaneously. The repair technique demonstrated its ability to consistently restore the strength and displacement capacity of severely damaged columns.

Repair of Concrete Filled Steel Tubes (CFSTs)

Repair Strategies for Earthquake-Damaged CFST Bridge Columns (Bumstead et al. 2019)

The earthquake-damaged CFST connections repair methods following seismic occurrences are the main topic of this research. The stiffness and strength of the column are restored using several techniques including: enclosing the damaged CFST zone in a concrete pedestal and transferring stresses using shear studs, steel rings, or weld beads.

The Concept: The study focuses on plastic hinge relocation repair techniques for RC columns. This entails limiting the damaged area of a CFST with a steel tube and surrounding it with a RC pedestal. The pedestal is fastened to the cap beam or foundation to resist the plastic moment strength of the CFST. For adequate moment strength in the RC section, the pedestal's diameter is 1.5 times that of the steel tube. For efficient force transfer, the pedestal's height is the same as the diameter of the steel tube. In the study, three force transmission techniques—a welded embedded ring, shear studs, and straightforward weld beads—were assessed.

The ABAQUS, an finite element analysis software, model geometry incorporates various components such as steel tubes, annular rings, concrete cores, RC foundations, grout, and repair pedestals. Different element types and mesh densities were employed to account for anticipated inelastic deformation in different geometries. Surface-surface interactions were established for steel-concrete contacts. The earthquake damage was simulated by removing the steel tube and introducing a pre-crack in the concrete fill. Fixed base and symmetry conditions were implemented for efficient computation. The loading technique involved an initial axial load followed by monotonic displacement. A summary of the model is shown in Figure 2.33.

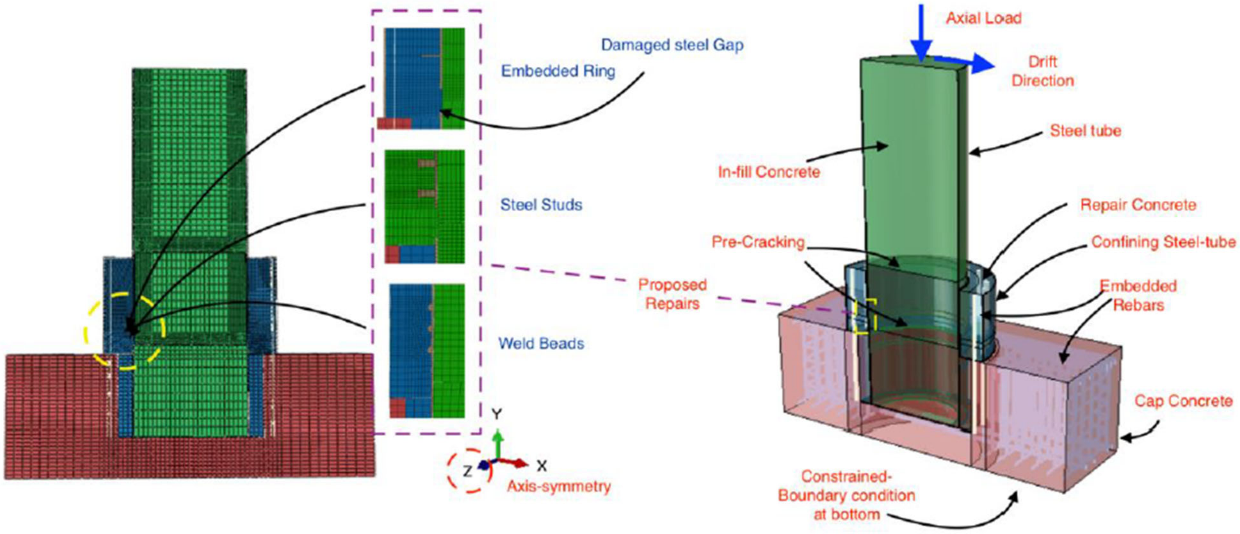

Figure 2.33 ABAQUS Numerical Model (Bumstead et al. 2019)

Result: The performance of three repair techniques for moment-drift and pedestal rotation is compared in Figure 2.34. For the comparison, the configurations ER-2x4t (embedded ring), SS-x4 (shear studs), WB-x3 (weld beads), and WB-x3-1 (weld beads) were chosen, with WB-x3 and WB-x3-1 displaying the maximum stiffness and strength and the lowest pedestal rotations. The weld bead designs outperformed the embedded ring and shear stud arrangements in terms of stiffness and strength. This shows that the efficiency of the repair method depends critically on the transfer mechanism's rigidity.

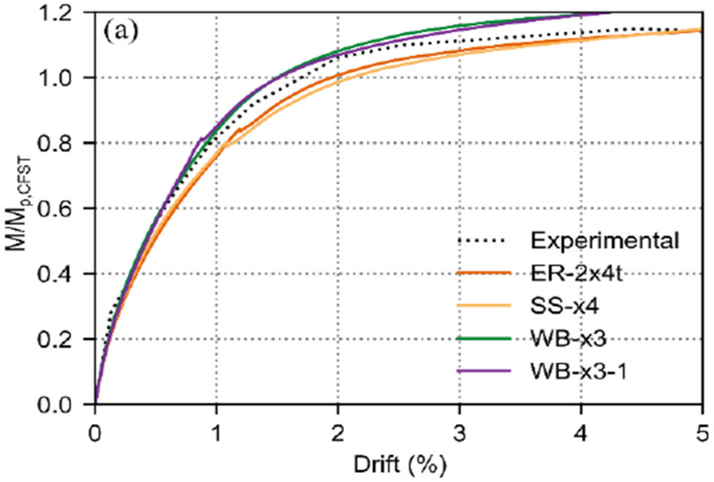

Figure 2.34 Comparison of Moment-Drift Behavior in Different Repair Strategy (Bumstead et al. 2019)

3. Experimental Investigation

This chapter follows the experimental investigation of the project. The flow chart in Figure 3.1 gives the layout for the chapter. The retrofitting methods start with the precast columns, with the CIP columns following. The retrofit methods are referred to as: Precast 1, Precast 2, CIP 1, and CIP 2, and will be presented in this order. The experimental investigation begins with preliminary testing of small-scale specimens. Success is defined in each retrofit as the ability to relocate the plastic hinge above the jacket.

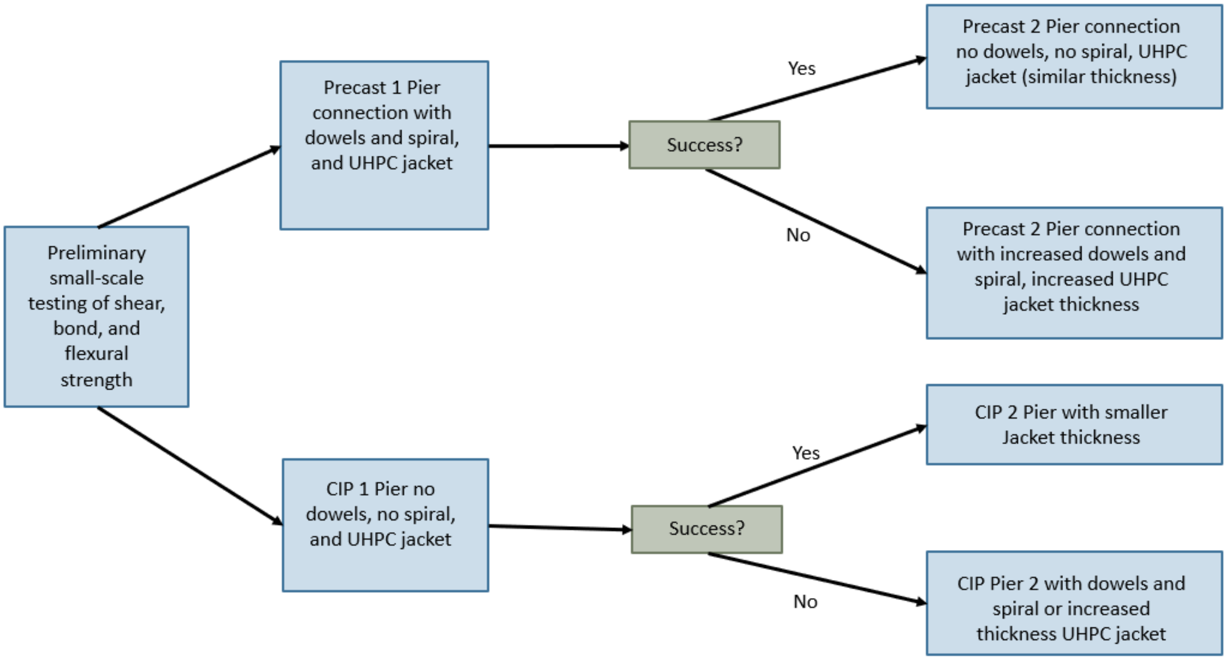

Figure 3.1 Flow Chart for Experimental Investigation

Preliminary Testing

Introduction

This section covers the construction, testing, and results from materials to be used in the experimental program. In this section, the compressive strength of NSC and UHPC are quantified, along with tension strength of NSC and UHPC, and lastly the bond strength between NSC and UHPC. The preliminary testing is necessary to make sure the correct values of concrete strength are used to design the retrofit method. Table 3.1 illustrates the preliminary testing to be completed for the project.

Table 3.1 Preliminary Testing

Test	**Size**	**Number of Specimens**	**Test Set-up**
Four-Point Bend Test	6 in. x 6 in. x 21 in.	6	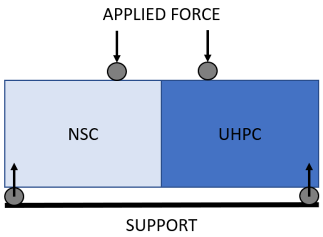
Direct Shear Test, Single Interface	6 in. x 6 in. x 6 in.	6	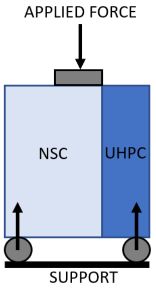
Direct Shear Test, Double Interface	6 in. x 6 in. x 8 in.	6	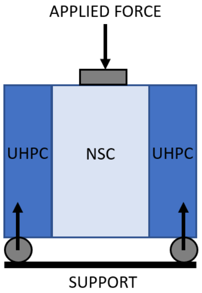
Compression	4 in. x 8 in. (NSC) 3 in. x 6 in. (UHPC) 2 in. x 2 in. x 2 in. (UHPC)	12 each	

Test	Size	Number of Specimens	Test Set-up
Tension	6 in. x 12 in. (NSC) Dog-bone Test (UHPC)	12 each	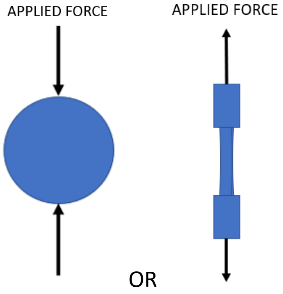

Four-Point Bend Test

The first small-scale test is the four-point bend test, which follows ASTM C293/C293M – 10. This test quantifies the flexural strength of the specimen at the NSC/UHPC interface. Figure 3.2 shows the pouring of the specimens; they are 6 in. x 6 in. x 21 in. Six specimens are prepared for testing. The NSC is poured first with a mix design of 4 ksi concrete (to match the strength of the pier specimens). After the NSC is poured and cured for 28 days, the surface of the NSC is roughened with a chisel and hammer (approximately ¼ in. deep). After the NSC surface is roughened, the specimens are placed back in their forms, the interface is wetted and the UHPC is poured according to the JS 1000 Ductal® instructions. The specimens are then cured for another 28 days before testing.

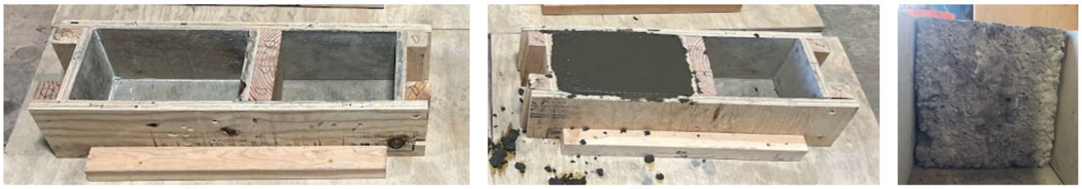

(a) Empty Form (b) NSC Poured (c) Roughened Surface

(d) NSC Ready For UHPC (e) UHPC Poured (f) Specimen Deformed

Figure 3.2 Four-Point Bend Specimen Construction

Testing is completed in the materials Lab at Lillibridge Engineering Building (LEL) at ISU. Testing involves a data acquisition system (DAQ) that is connected to a Tinus Olsen machine, the test set-up is shown in Figure 3.3. The specimen is loaded at 150 psi/min, as recommended by the ASTM. All six specimens are tested and then measurements are taken and results are processed.

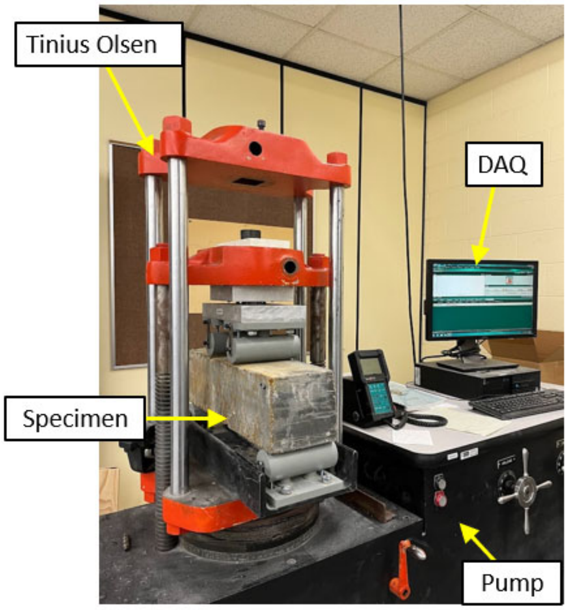

Figure 3.3 Four-Point Bend Test Set-Up

Results

Figure 3.4 shows the failure plane of each specimen (A to F). The red line signifies the line of fracture. The NSC is on the left and the UHPC is on the right in each photo. The surfaces of the failure planes are shown also in Figure 3.4. The black line on the specimens signifies the interface between NSC and UHPC. Figure 3.4 shows that most specimens fractured close to the NSC/UHPC interface. Table 3.2 gives the approximate location of fracture for each specimen. Included with the table is Figure 3.5 for reference of fracture location.

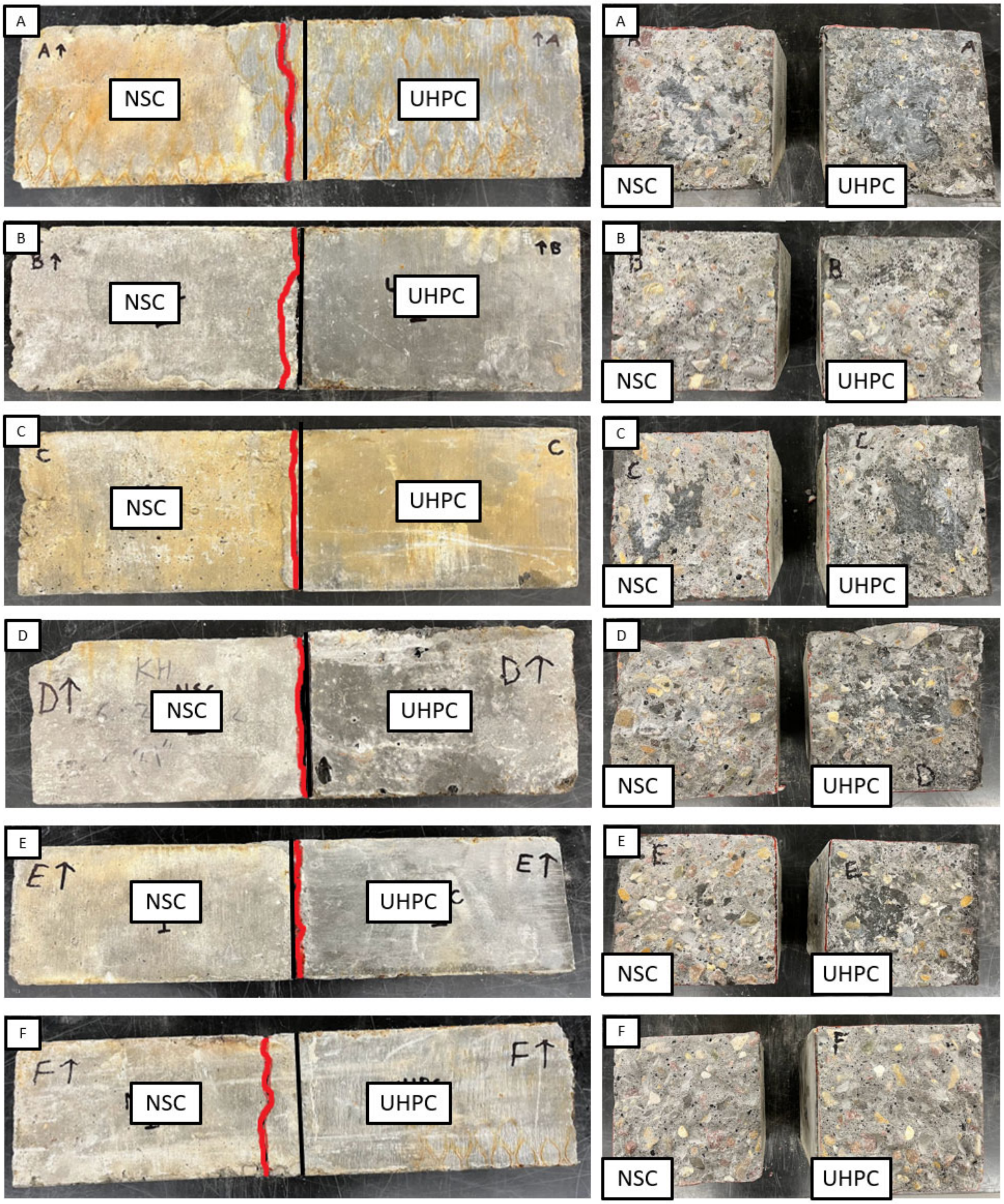

Figure 3.4 Four-Point Bend Fracture Planes

Table 3.2 Four-Point Bend Test Average Fracture Plane

Specimen	**Location of the Fracture Plane from the Interface (in.)**
A	-0.447
B	-0.256
C	-0.230
D	-0.221
E	+0.274
F	-0.937
Average	-0.229

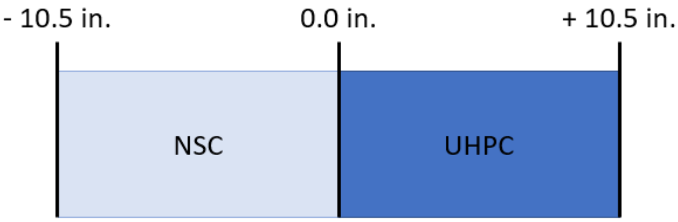

Figure 3.5 Four-Point Bend Test Fracture Plane Scale (in.)

The modulus of rupture is calculated using the formula from ASTM C293/C293M – 10:

$$R = \frac{3PL}{2bd^2}$$

Where:

R = modulus of rupture, in pounds per square inch
P = maximum applied load indicated by the testing machine, in pounds
L = span length, in inches
b = average width of the specimen at the fracture, in inches
d = average depth of the specimen at the fracture, in inches

The results for modulus of rupture for each specimen are given in Table 3.3. Furthermore, Figure 3.6 gives the load versus deflection plots for each specimen. Notice that Specimen A was the first tested and is taken as a “dummy test” to ensure the test set-up and the loading rate correct; therefore, data from Specimen A is not included in the average calculation for modulus of rupture.

Table 3.3 Four-Point Bend Test Results

Specimen	Maximum Load (lb.)	Span (in.)	Width (in.)	Depth (in.)	Modulus of Rupture (psi)
A*	1,510	21.07	6.17	6.12	---
B	8,810	20.90	6.19	6.10	1,199
C	6,740	21.08	6.12	6.09	939
D	7,020	20.94	6.22	6.16	935
E	6,910	20.85	6.10	6.20	922
F	8,060	20.93	6.15	6.16	1,087
Average	---	---	---	---	1,016.40

* Specimen not included in average calculation

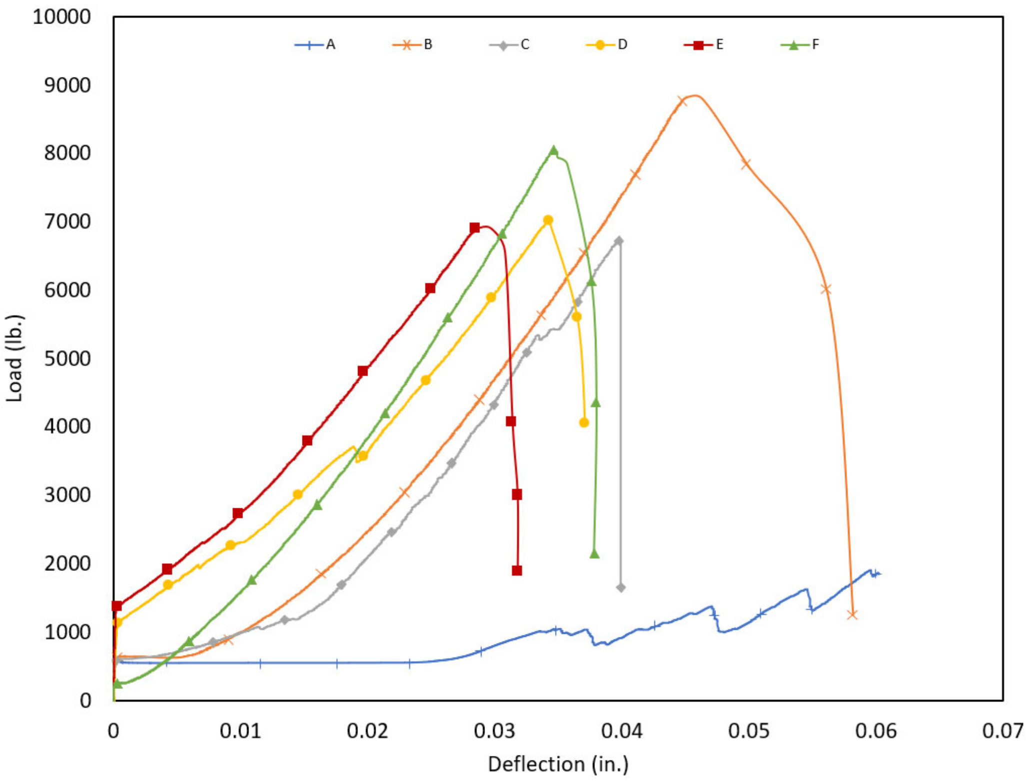

Figure 3.6 Load vs Deflection Four-Point Bend Test

Direct Shear Test, Single Interface

The second preliminary test is the direct shear test with a single interface. This style of direct shear testing is taken from research completed by the Florida International University (FIU) in Miami, Florida. The test set-up mimicked the study by Valikhani et al. (2020). The testing is done to quantify the shear strength between NSC and the UHPC. The specimens are 6 in. x 6 in. x 6 in. Six specimens are casted for testing. The NSC is casted first and cured for 28 days, the NSC portion is 6 in. x 6 in. x 4 in. After the NSC is cured the surface roughened with a chisel, approximately ¼” deep. After the NSC is prepared, the specimen is placed back in the form, the NSC surface is wetted and the UHPC is poured according to the JS1000 Ductal® instructions. The UHPC portion is 6 in. x 6 in. x 2 in. The construction process can be seen in Figure 3.7. After the specimens are poured, they are cured for 28 days and then tested in the LEL Materials Lab at ISU.

(a) NSC Poured (b) NSC Cured and Roughened

(c) UHPC Poured (d) Specimen Deformed

Figure 3.7 Direct Shear, Single Interface Specimen Construction

The test set-up for the direct shear, single interface test is shown in Figure 3.8. The specimen is centered under the Tinius Olsen, with 2 in. on the left support, 2 in. unsupported in the middle, and 2 in. on the right support. The unsupported 2 in. length in the middle is loaded with a metal block. The NSC is on the left and the UHPC is on the right in the figure. The interface is denoted by the black line. The loading rate of the specimen is 175.2 psi/min, as recommended by the FIU study. The Tinius Olsen is hooked up to the DAQ to monitor loading rate, maximum load, and deflection. All six specimens are tested and then measurements are taken and results are processed.

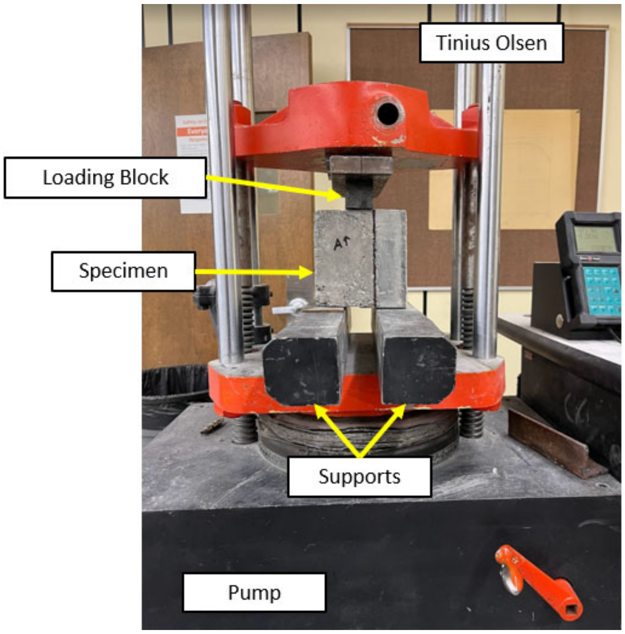

Figure 3.8 Direct Shear, Single Interface Test Set-Up

Results

Using the research completed at FIU as a guideline, three modes of failure are defined as follows:

1. Cohesive Failure – occurs due to NSC concrete crushing and no UHPC exposure
2. Adhesive Failure – occurs due to debonding at the interface, significant UHPC exposure
3. Mixed Failure – occurs when failure is occurs in both the bond interface and NSC, little UHPC exposure

Figure 3.9 shows the failure plane of each specimen (A to F). The red line signifies the line of fracture. The black line on the specimens signifies the interface between NSC and UHPC. The NSC is on the left and the UHPC is on the right in each photo. The surfaces of the failure planes are shown also in Figure 3.9, with the NSC surface on the left and the UHPC surface on the right. Figure 3.9 shows that most specimens fractured close to the NSC/UHPC interface. Table 3.4 gives the approximate location of fracture for each specimen, as well as the mode of failure that occurred in each specimen. Included with the table is Figure 3.10 for reference of fracture location.

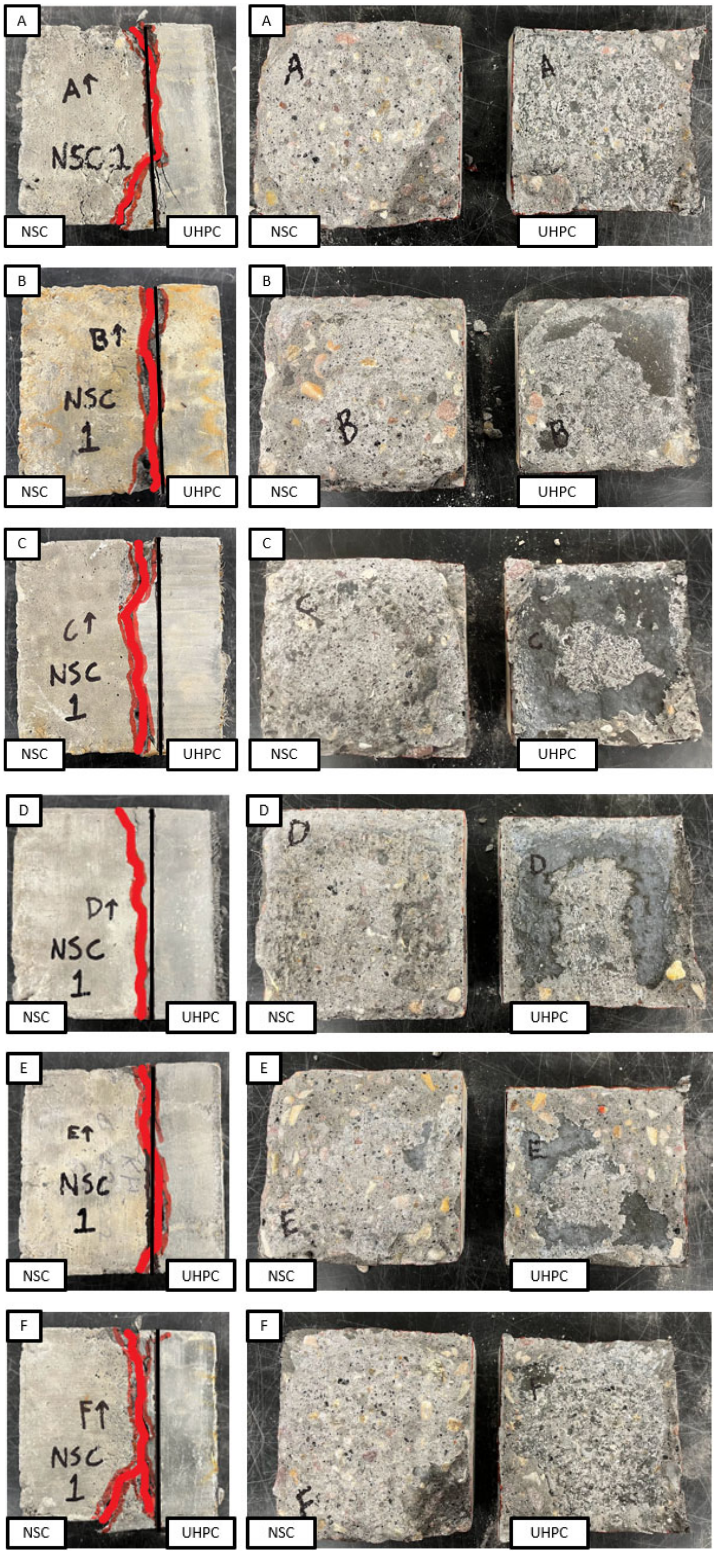

Figure 3.9 Direct Shear, Single Interface Fracture Planes

Table 3.4 Direct Shear, Single Interface Average Fracture Plane and Failure Mode

Specimen	Location of Fracture Plane (in.)	Failure Mode
A	-0.008	Cohesive Failure
B	+0.143	Mixed Failure
C	+0.045	Adhesive Failure
D	+0.055	Adhesive Failure
E	-0.018	Mixed Failure
F	-0.030	Cohesive Failure
Average	+0.031	---

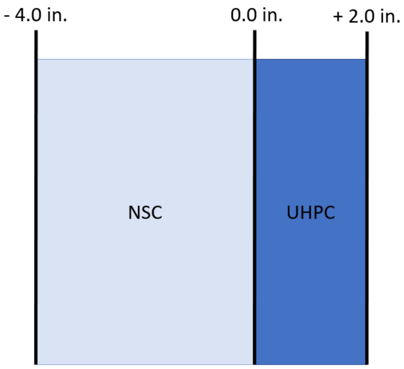

Figure 3.10 Direct Shear, Single Interface Fracture Plane Scale (in.)

The bond strength at the interface is calculated using the equation from the FIU research:

$$\tau = \frac{P}{2bd}$$

Where:

τ = bond strength, in pounds per square inch
P = maximum applied load indicated by the testing machine, in pounds
b = average width of the specimen at the fracture, in inches
d = average depth of the specimen at the fracture, in inches

The results for bond strength for each specimen are given in Table 3.5. Furthermore, Figure 3.11 gives the load versus deflection plots for each specimen. Note that Specimen A was the first tested and is taken as a "dummy test" to ensure the test set-up and the loading rate correct; therefore, data from Specimen A is not included in the average calculation for bond strength, as it is an outlier.

Table 3.5 Direct Shear Test, Single Interface Results

Specimen	**Maximum Load (lb.)**	**Width (in.)**	**Depth (in.)**	**Bond Strength (psi)**
A*	34,300	6.12	6.12	457
B	22,400	6.07	6.14	301
C	14,000	6.14	6.12	186
D	17,500	6.10	6.02	239
E	25,600	6.12	6.12	342
F	20,200	6.10	6.12	271
Average	---	---	---	267.80

* Specimen not included in average calculation

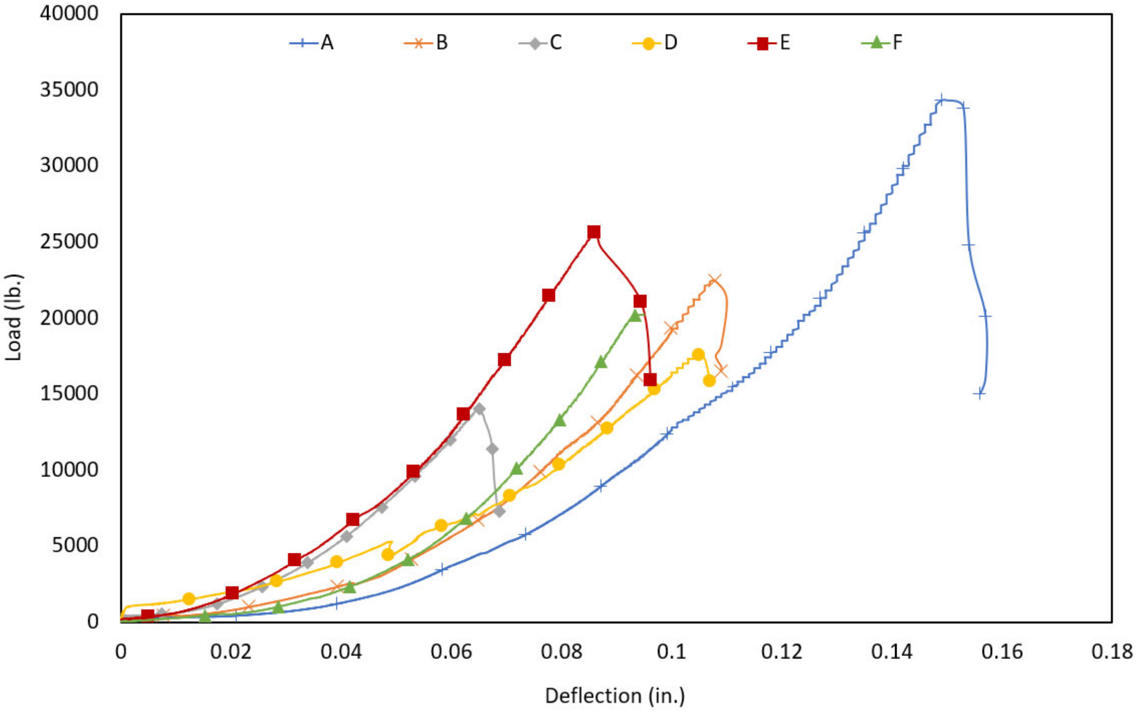

Figure 3.11 Load vs. Deflection - Direct Shear, Single Interface

Direct Shear, Double Interface

The third preliminary test is the direct shear test with a double interface. This test has not been completed before, and has no specification to follow (from previous research). The concept of the test came from ISU's Dr. Mustafa Mashal, for the purpose of quantifying bond strength of NSC with UHPC. Due to the lack of specification, the FIU study is used as a guideline for the test.

The direct shear, double interface specimens are 8 in. x 6 in. x 6 in. Like the other specimens, the NSC is poured first with the dimensions of 4 in. x 6 in. x 6 in. The NSC is allowed to cure, and is then roughened with a chisel at approximately ¼" depth on both sides of the 4 in. length. The specimen is then placed back in the form, the roughened surface of the NSC is wetted, and the UHPC is poured according to the JS1000, Ductal® instructions on both sides of the NSC block. This creates two UHPC sections, one at each end of the block, which are 2 in. x 6 in. x 6 in. The specimens are then deformed and allowed to cure for 28 days prior to testing. Figure 3.12 illustrates the construction method.

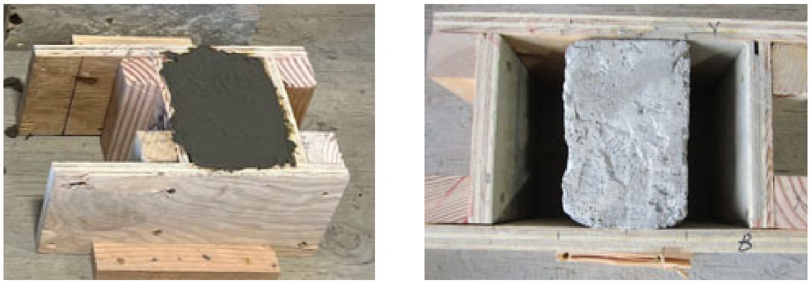
(a) NSC Poured (b) NSC Cured and Roughened


(c) UHPC Poured (d) Specimen Deformed

Figure 3.12 Construction of Direct Shear, Double Interface Specimens

The specimens are tested at ISU in LEL Materials Lab using the Tinius Olsen. The test set-up is shown in Figure 3.13. Each specimen is centered in the Tinius Olsen with the 2 in. UHPC sections on individual supports, and the 4 in. NSC section unsupported. The load is applied across the 4 in. NSC section using a steel plate and a steel loading block. The loading rate used is 175.2 psi/min. The Tinius Olsen is hooked up to the DAQ to monitor loading rate, maximum load, and deflection. All six specimens are tested and then measurements are taken and results are processed.

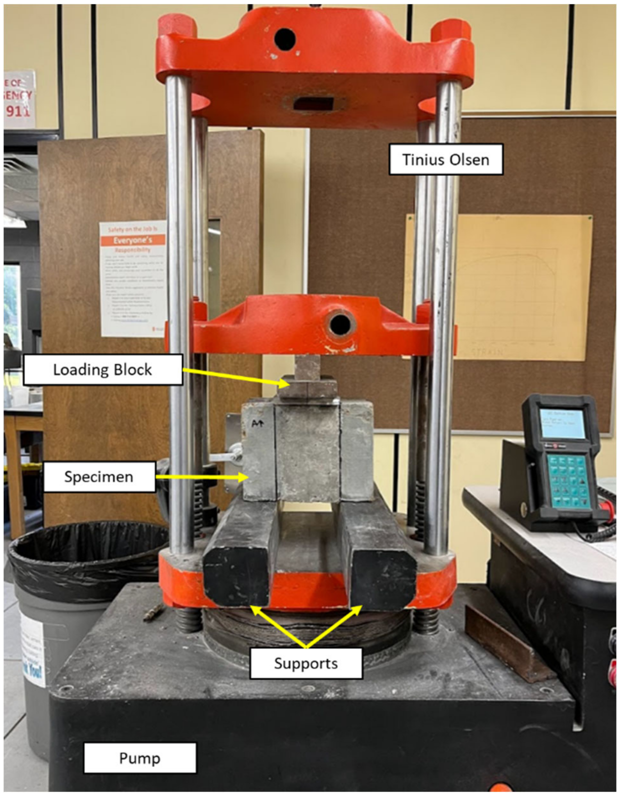

Figure 3.13 Direct Shear, Double Interface Test Set-Up

Results

The modes of failure for the double interface test are the same as the modes of failure from the single interface test: (1) cohesive failure, (2) adhesive failure, and (3) mixed failure. The fracture planes from the direct shear, double interface test can be seen in Figure 3.14, along with the fracture surfaces. The redline denotes the fracture plane, while the black line denotes the NSC/UHPC interface. Specimen A is the only specimen that fractured on both interfaces. The figure follows the build of the specimen for the fracture surfaces: UHPC on the left, NSC in the middle, and UHPC on the right. UHPC-L and UHPC-R are used to help the reader denote which side of the specimen fractured. Similarly, NSC-L and NSC-R are used to help the reader denote which side of the specimen fractured. Right and left are determined according to the test set-up in Figure 3.13. Furthermore, Table 3.6 gives the approximate location of the fracture on the specimen, while Figure 3.15 gives the scale for the location of fracture. Table 3.6 also gives the failure mode of each specimen.

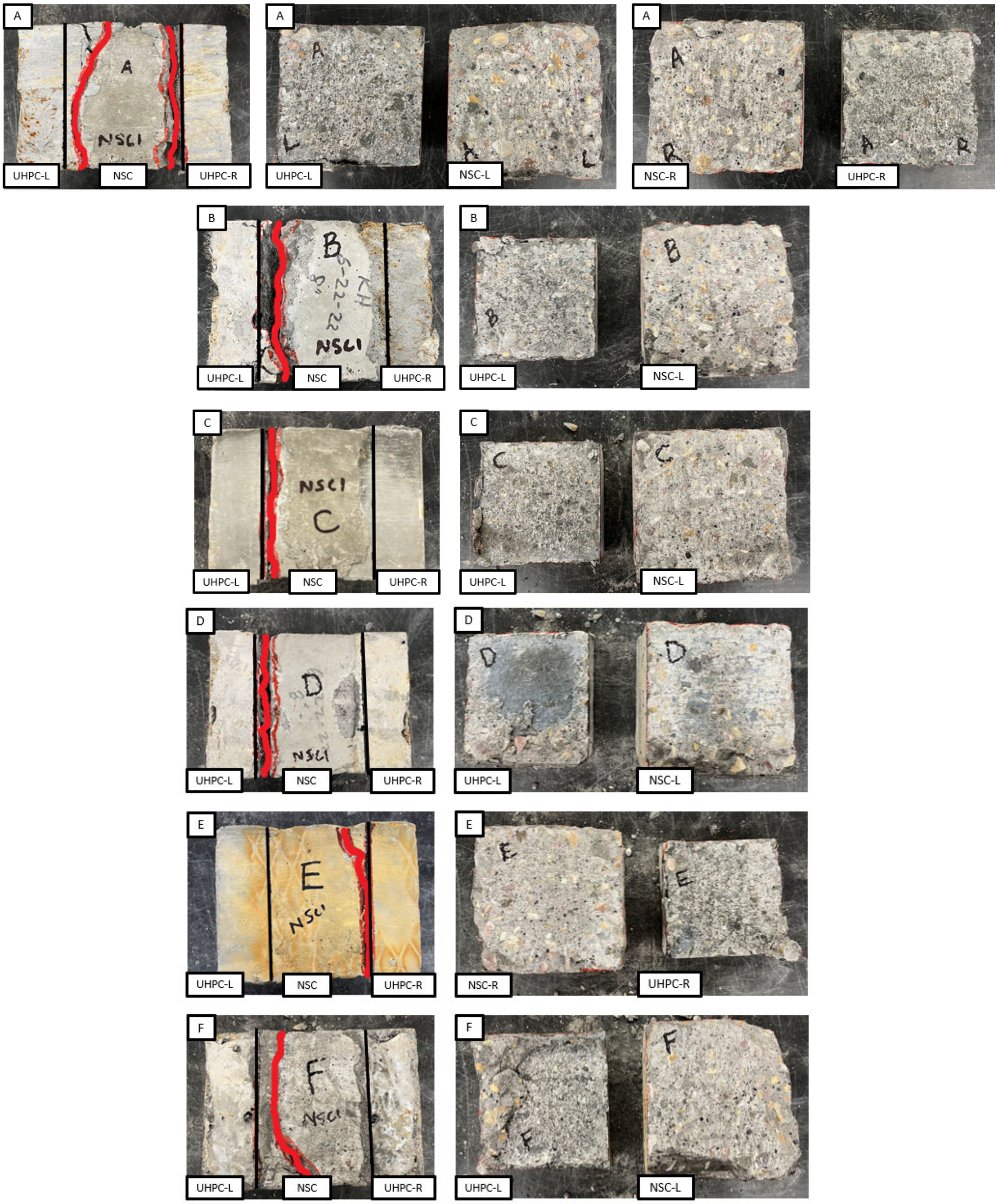

Figure 3.14 Direct Shear, Double Interface Fracture Planes

Table 3.6 Direct Shear, Double Interface Average Fracture Plane and Failure Mode

Specimen	Fracture Plane(s) (in.)		Failure Mode
A	Left	-1.649	Mixed Failure
	Right	+1.929	
B	Left	-1.911	Cohesive Failure
	Right	N/A	
C	Left	-1.769	Cohesive Failure
	Right	N/A	
D	Left	-1.859	Adhesive Failure
	Right	N/A	
E	Left	N/A	Mixed Failure
	Right	+1.964	
F	Left	-1.593	Cohesive Failure
	Right	N/A	
Average	Left	-1.756	---
	Right	+1.947	

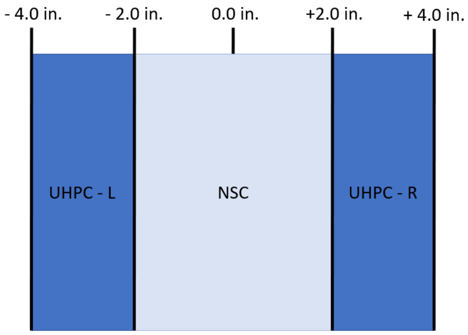

Figure 3.15 Direct Shear, Double Interface Fracture Plane Scale (in.)

The bond strength at the interface is calculated using the same equation for the direct shear, single interface test. The results for bond strength for each specimen are given in Table 3.7. Furthermore, Figure 3.16 gives the load versus deflection plots for each specimen.

Table 3.7 Direct Shear Test, Double Interface Results

Specimen	Maximum Load (lb.)	Width (in.)	Depth (in.)	Bond Strength (psi)
A	21,500	6.14	6.15	285
B	23,200	6.12	6.19	306
C	27,700	6.11	6.12	370
D	18,800	6.22	6.28	241
E	21,900	6.25	6.16	284
F	30,100	6.12	6.27	392
Average	---	---	---	313.10

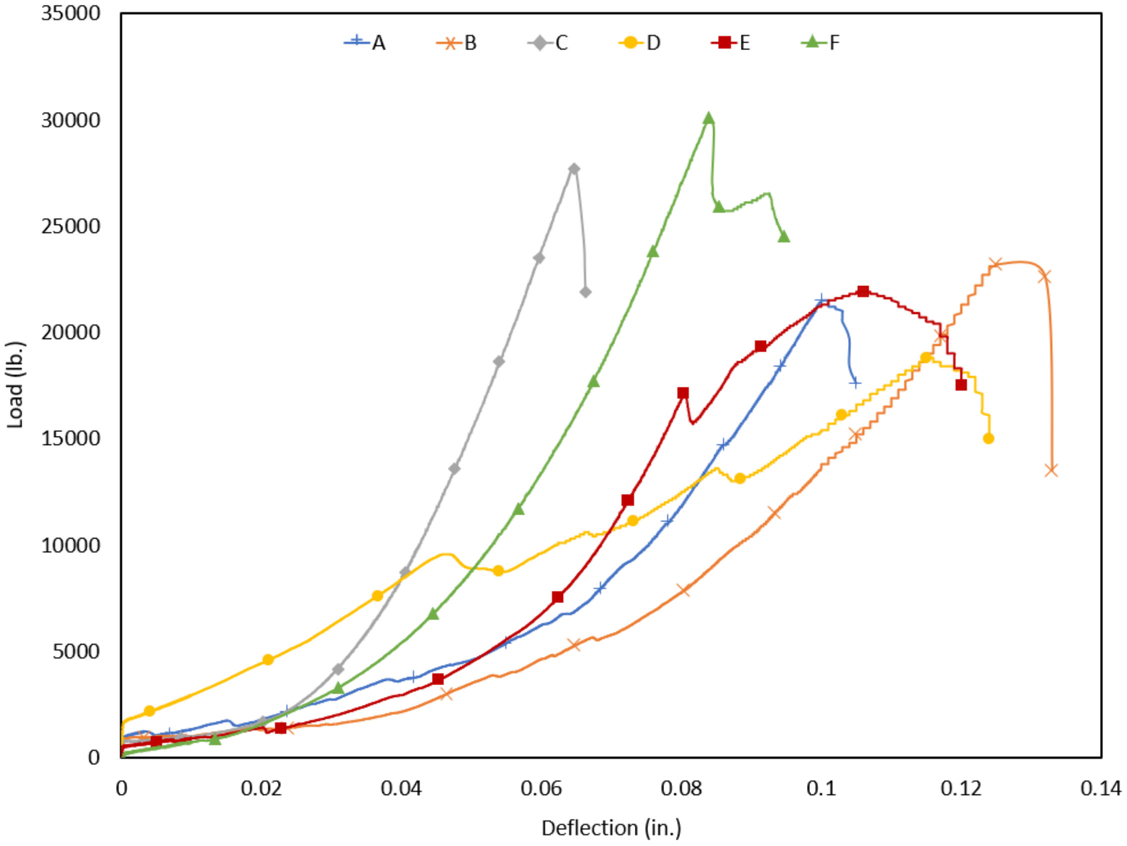

Figure 3.16 Load vs. Deflection - Direct Shear, Double Interface

Compression

Compression testing follows ASTM C39/C39M-21, for NSC specimens, ASTM C1856/C1856M-17, for UHPC cylinder specimens, and ASTM C109/C109M-20 for UHPC cube specimens. Compression testing is completed on six specimens of each type to get an accurate average.

NSC Compression Cylinders

The NSC specimens are prepared according to the ASTM. They are 8 in. x 4 in, length and diameter respectively. After pouring, the specimens are cured in the curing tank for twenty-eight days, and then brought to the materials lab in LEL for testing. Prior to testing measurements are taken of each cylinder to find the average diameter. The specimens are tested in the Gilson Testing Machine. For testing the specimens are capped and loaded at a rate of 20-50 psi/sec. The test set-up is shown in Figure 3.17. The failure of the specimens is shown in Figure 3.18. The ASTM specifies six different modes of failure, they are depicted in Figure 3.19. Table 3.8 gives the results from the NSC testing.

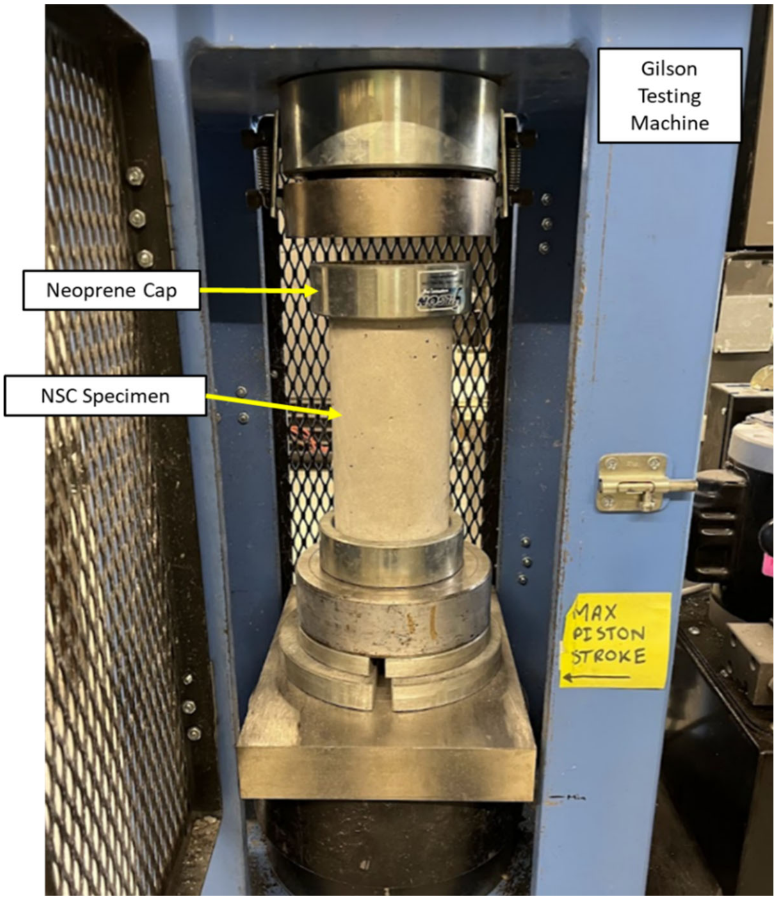

Figure 3.17 NSC Compression Test Set-Up

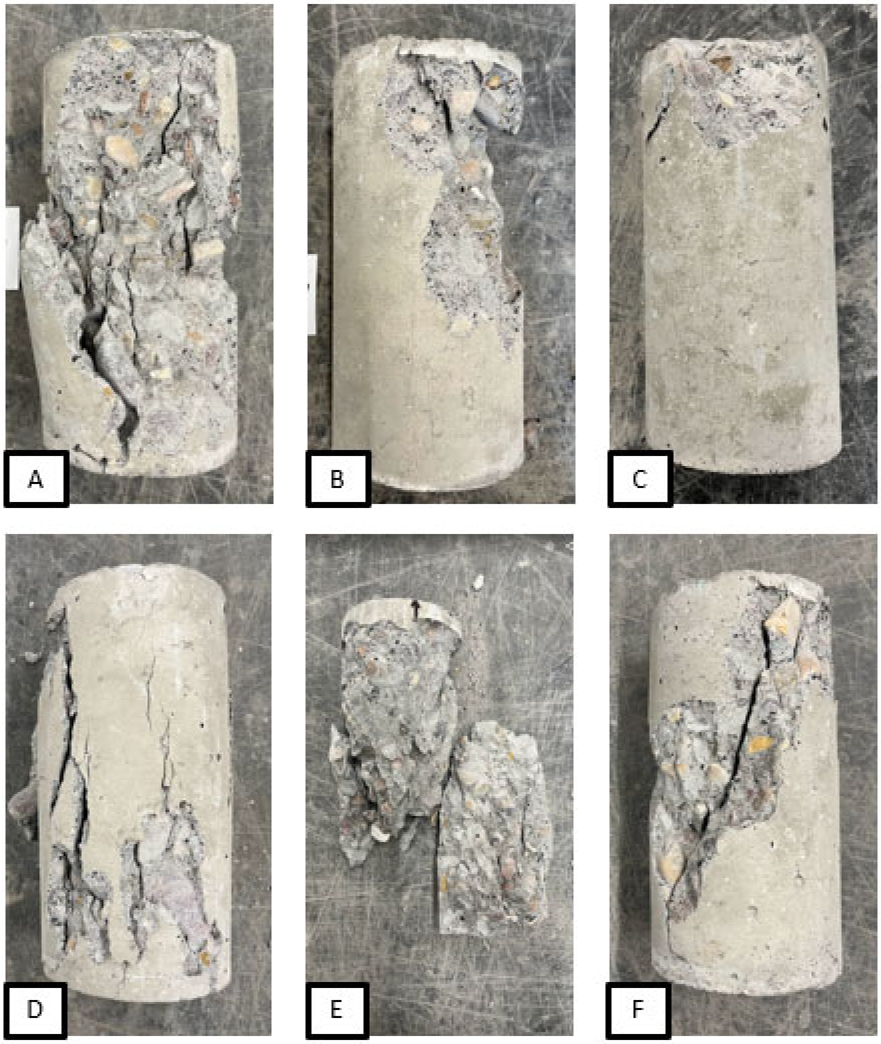

Figure 3.18 Failure of NSC Compression Specimens

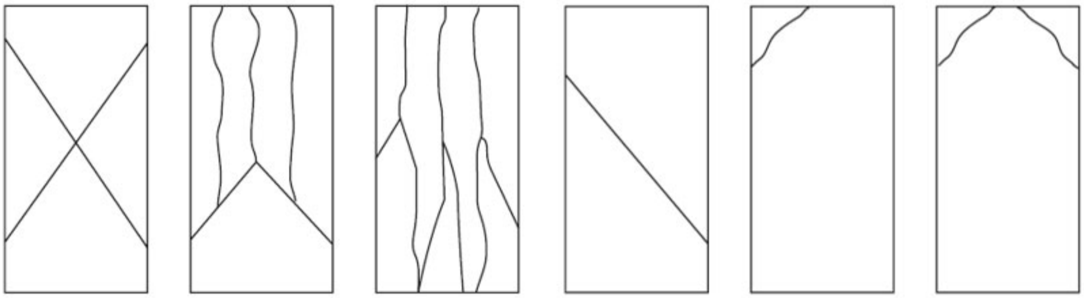

Type 1: Cones on both ends

Type 2: Cone on one end and vertical cracks

Type 3: Vertical cracks

Type 4: Diagonal Fracture

Type 5: Side Fracture

Type 6: Side fractures with pointed ends

Figure 3.19 Concrete Cylinder Failure Modes (Manlouk & Zaniewski, 2011)

Table 3.8 NSC Compression Test Results

Specimen	**Average Diameter (in.)**	**Area (in.^{2})**	**Maximum Load (lb.)**	**Compressive Strength, f'c (psi)**	**Mode of Failure**
A	3.997	12.55	80,530	6,419	Type 3
B	3.975	12.41	86,900	7,003	Type 5
C	3.998	12.56	86,210	6,866	Type 5
D	3.995	12.54	75,840	6,050	Type 2
E	3.996	12.54	82,070	6,544	Type 1
F	4.004	12.59	91,320	7,254	Type 4
Average	---	---	---	6,682	---

UHPC Compression Test

Two methods of compression testing are used for UHPC: 3 in. x 6 in. cylinders and 2 in. x 2 in. x 2 in. cubes. The methods follow their respective ASTMs. After pouring, the specimens are cured in the curing tank for twenty-eight days, and then brought to the materials lab in LEL for testing. Prior to testing measurements are taken of each cylinder and cube to find the average cross section area. The specimens are tested in the Gilson Testing Machine. For testing the specimens are loaded at a rate of 145 psi/sec. The test set-up is shown in Figure 3.20.

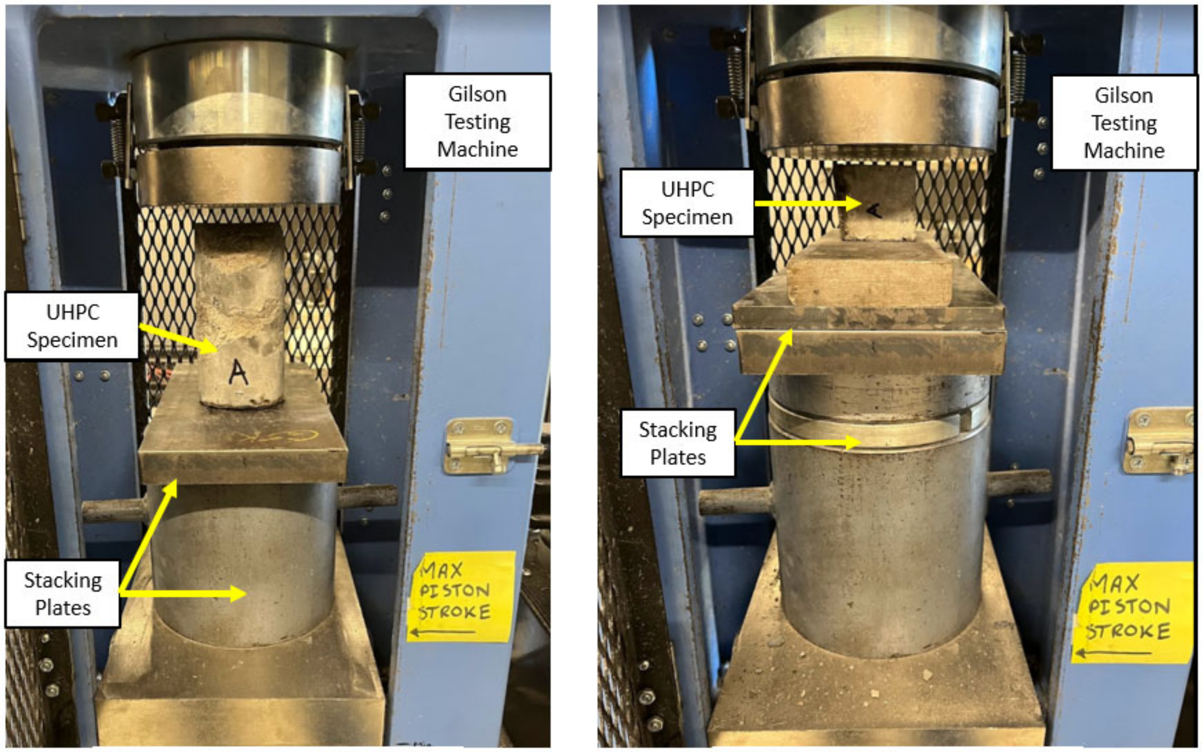

(a) Cylinder Compression Test (b) Cube Compression Test

Figure 3.20 UHPC Compression Test Set-Up

The failure of the specimens is shown in Figure 3.21 and Figure 3.22. Furthermore, Table 3.9 and Table 3.10 give the results of the compression tests. The UHPC cylinder yielded a much lower result than the cubes, likely due to human error in pouring or grinding of the specimens. The JS1000 specifies a value of greater than 21 ksi for the compressive strength of the concrete.

Table 3.9 UHPC Cylinder Compression Test Results

Specimen	Average Diameter (in.)	Area (in.^{2})	Maximum Load (lb.)	Compressive Strength, f'c (psi)
A	3.073	7.418	88,130	11,880
B	3.004	7.087	119,650	16,882
C	3.046	7.285	119,700	16,430
D	3.031	7.214	105,640	14,644
E	3.006	7.188	102,420	14,248
F	3.023	7.179	102,700	14,306
Average	---	---	---	14,732

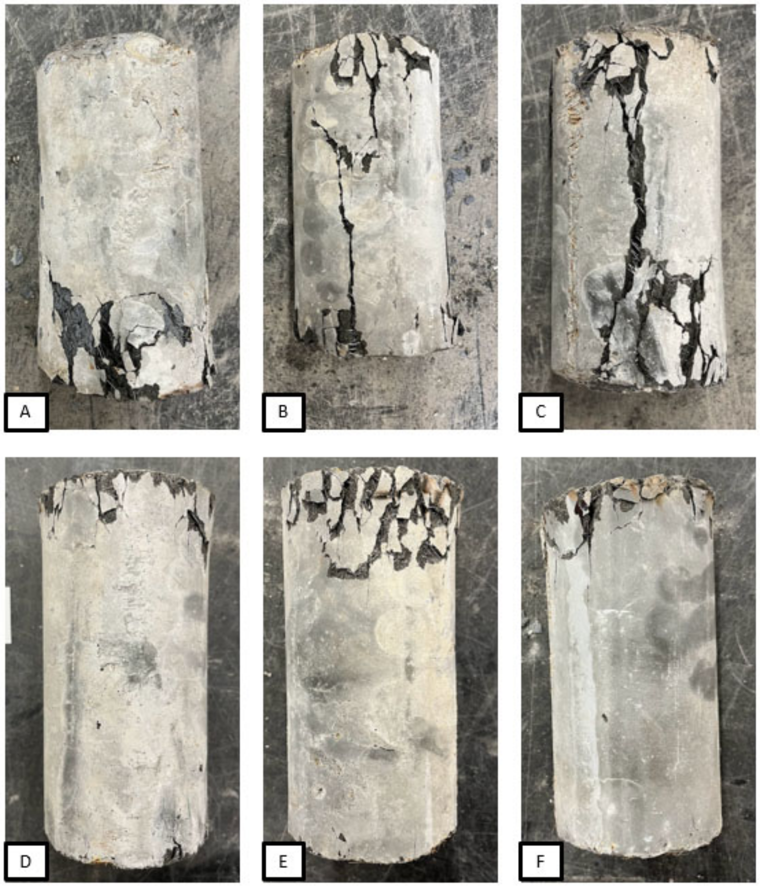

Figure 3.21 Failure of UHPC Cylinder Compression Specimens

Table 3.10 UHPC Cube Compression Test Results

Specimen	Average Width (in.)	Average Length (in.)	Area (in.^{2})	Maximum Load (lb.)	Compressive Strength, f'c (psi)
A	2.103	2.030	4.270	77,820	18,223
B	2.135	2.048	4.362	86,200	19,762
C	2.186	2.040	4.454	81,030	18,191
D	2.036	2.050	4.174	73,830	17,686
E	2.038	2.037	4.151	74,000	17,825
F	2.058	2.066	4.233	76,940	18,175
Average	---	---	---	---	18,310

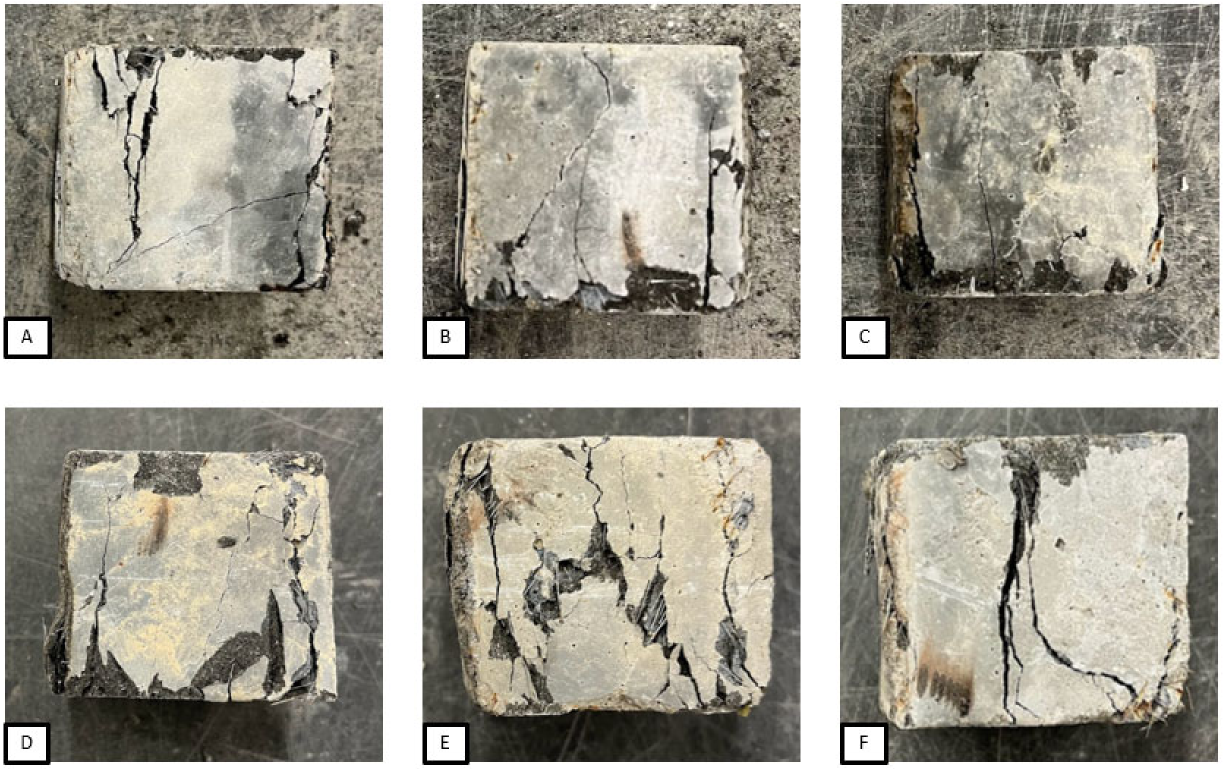

Figure 3.22 Failure of UHPC Cube Compression Specimens

Tension

Tension testing of concrete follows ASTM C496-96, for indirect tension testing of concrete cylinders. Four specimens each are tested for the tensile strength for NSC and UHPC. Another test is also used for the tensile strength of UHPC, which follows the study completed at Washington State University (WSU). It is a form of direct tension testing (DTT). This test incorporates dog-bone-style tensile testing for UHPC and will be discussed further in this section. Six specimens are poured and tested using WSU's methods.

NSC Split Cylinder

The NSC specimens are poured according to the corresponding ASTM. The NSC specimens are 6 in. x 12 in., diameter and length. The specimens are cured for 28 days prior to testing. Measurements are taken to find the average dimensions of the specimens. The specimens are then loaded in the Gilson Testing Machine at a loading rate of 3.0 psi/sec. Figure 3.23 gives the test set-up for the tension testing. Furthermore, Figure 3.24 shows the failure of each specimen, and Table 3.11 gives the results from testing.

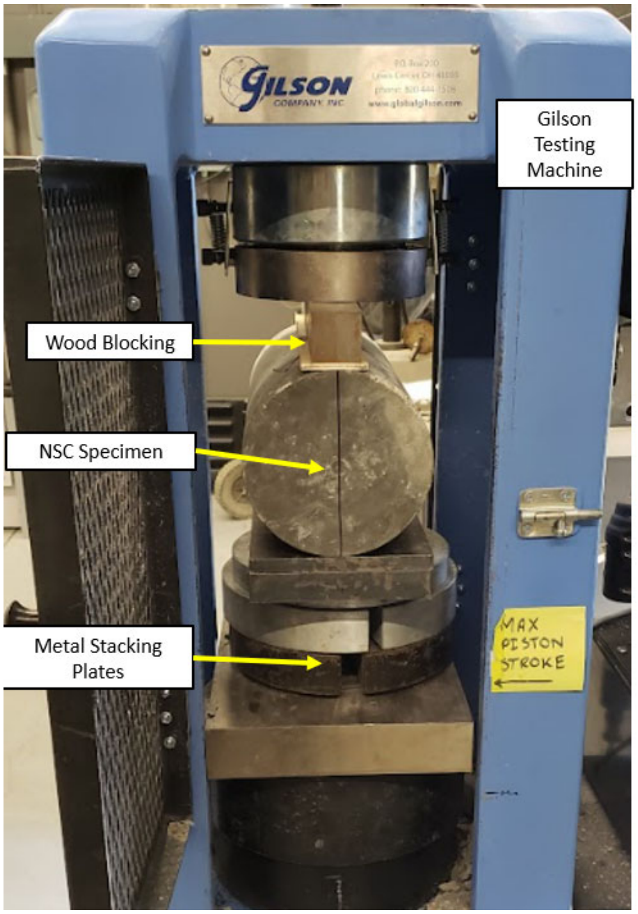

Figure 3.23 NSC Tension Test Set-Up

Table 3.11 NSC Tension Test Results

Specimen	Average Diameter (in.)	Average Length (in.)	Area (in.^{2})	Maximum Load (lb.)	Tensile Strength, f’ct (psi)
A	6.040	12.112	73.152	53,460	465
B	6.058	12.104	73.322	45,520	395
C	6.102	12.069	73.641	52,850	457
D	6.065	12.149	73.688	46,040	398
Average	---	---	---	---	430

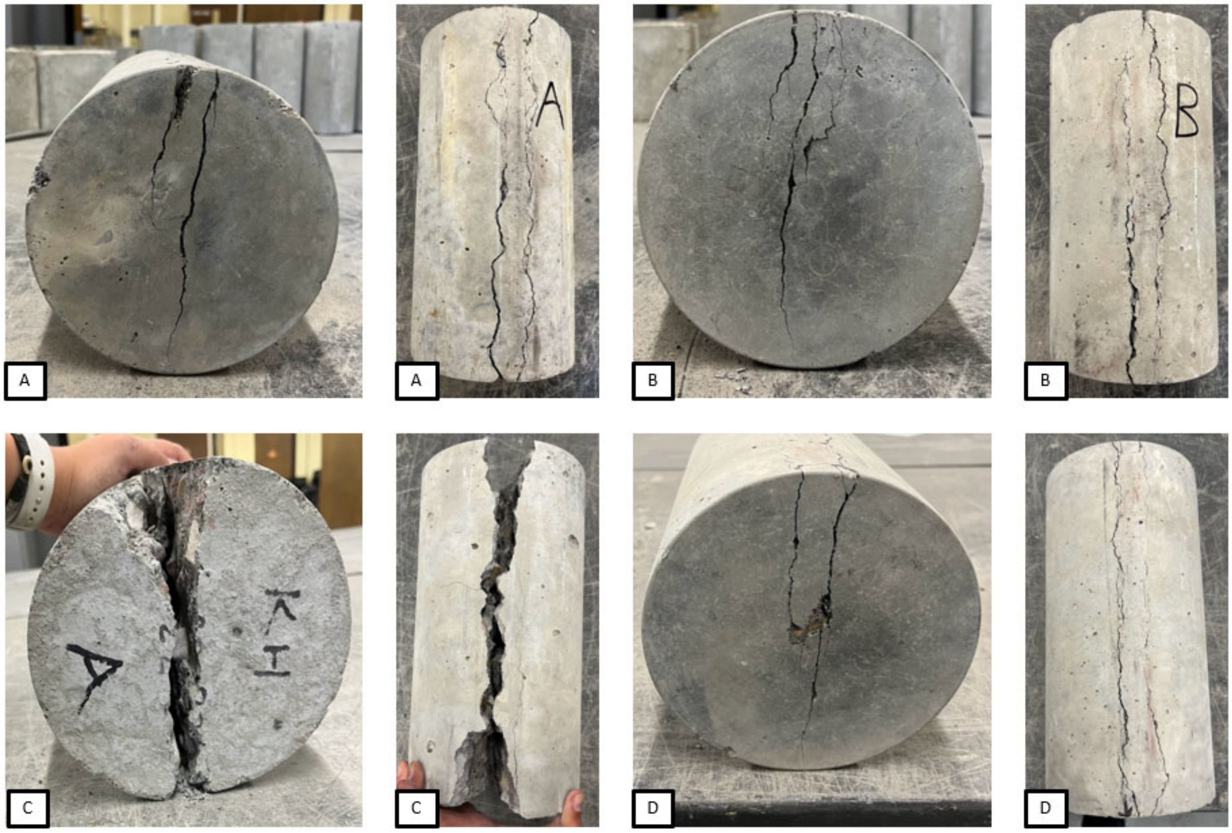

Figure 3.24 Failure of NSC Split-Cylinder Test

UHPC Split Cylinder

The UHPC specimens are poured according to the ASTM, they are 4 in. x 8 in., diameter and length, respectively. The specimens are cured for 28 days after pouring and then tested in the Gilson Testing

Machine in LEL. Measurements are taken prior to testing to find the average dimensions of each specimen. Figure 3.25 gives the test set-up for the UHPC cylinders. Figure 3.26 shows the failure of each specimen, and Table 3.12 gives the results of testing.

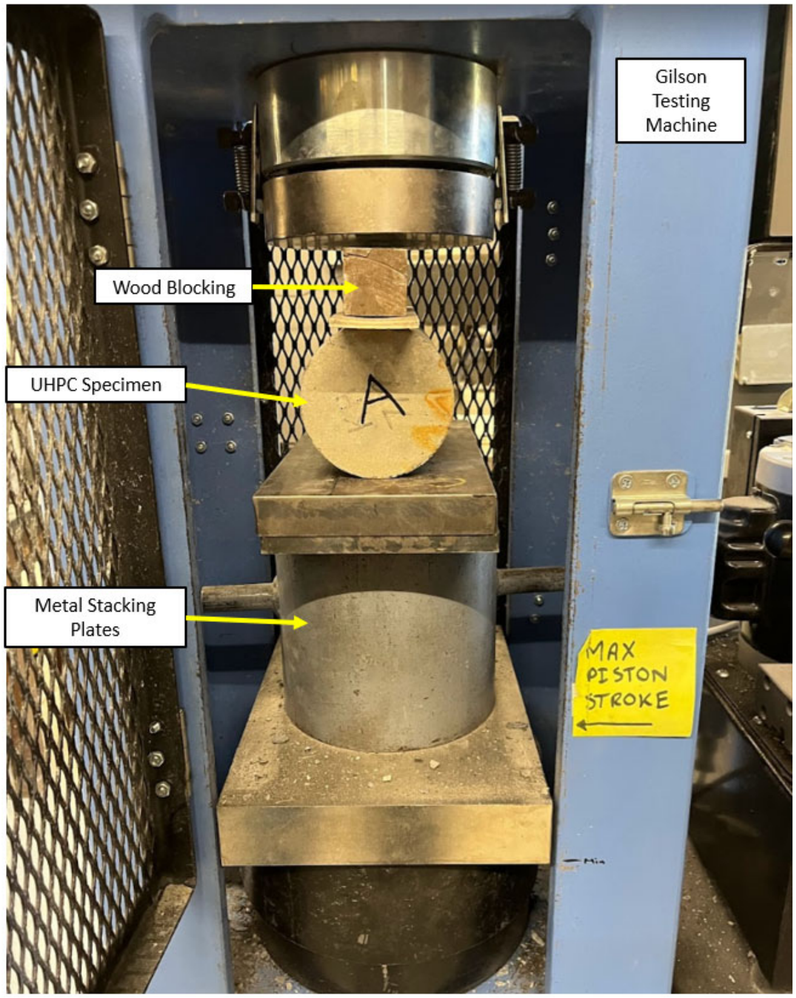

Figure 3.25 UHPC Cylinder Tension Test Set-Up

Table 3.12 UHPC Tension Cylinder Test Results

Specimen	Average Diameter (in.)	Average Length (in.)	Area (in.^{2})	Maximum Load (lb.)	Tensile Strength, f'ct (psi)
A	4.044	8.184	32.771	86,030	1,671
B	3.984	8.271	32.954	133,770	2,584
C	3.990	8.107	32.344	124,870	2,458
D	3.984	8.222	32.756	81,440	1,583
Average	---	---	---	---	2,074

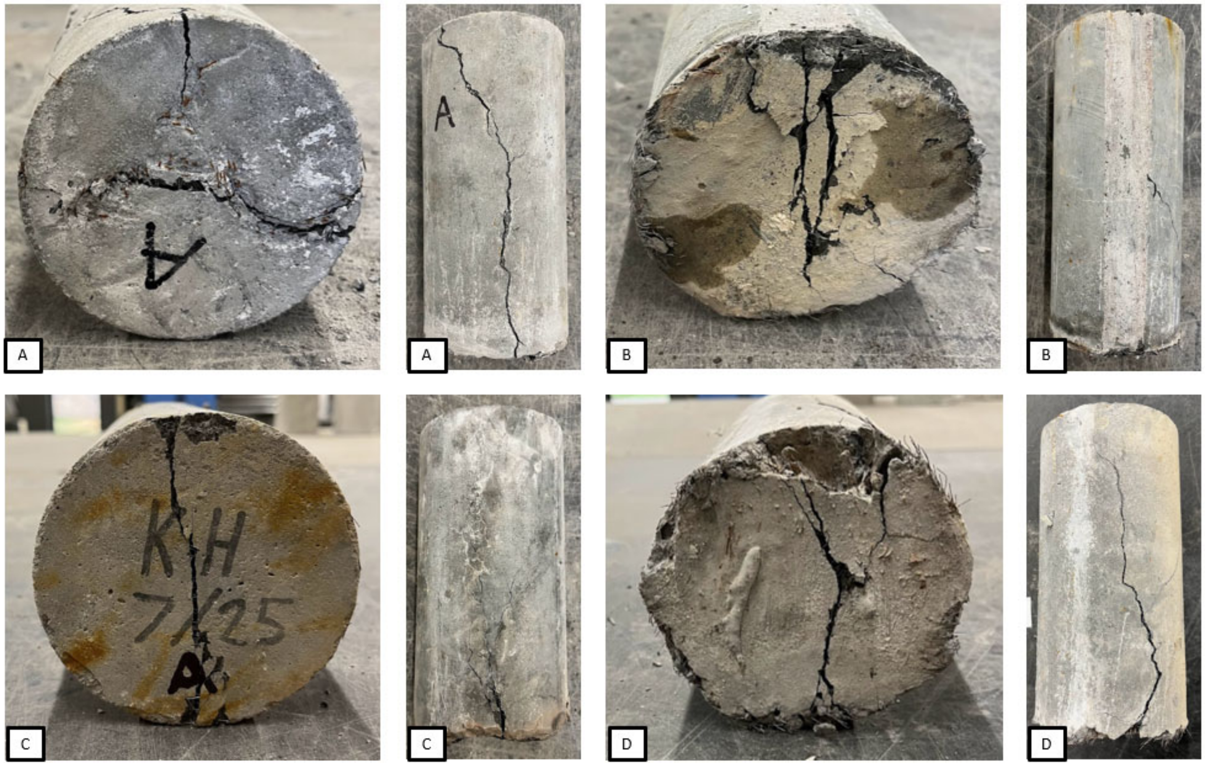

Figure 3.26 Failure of UHPC Tension Cylinders

UHPC Direct Tension Test (DTT)

This test follows research completed by WSU on UHPC Direct Tension testing (Zhou and Qiao 2020, 2730-2749). The design of the specimen can be seen in Figure 3.27. Threaded rods of 5/8 in. diameter are imbedded into the specimen to attach to the United Testing Machine (UTM). The specimens are poured in wooden forms and are cured for 28 days using burlap and plastic wrapping. The threaded rod is taped prior to curing to not damage and rust the connection point.

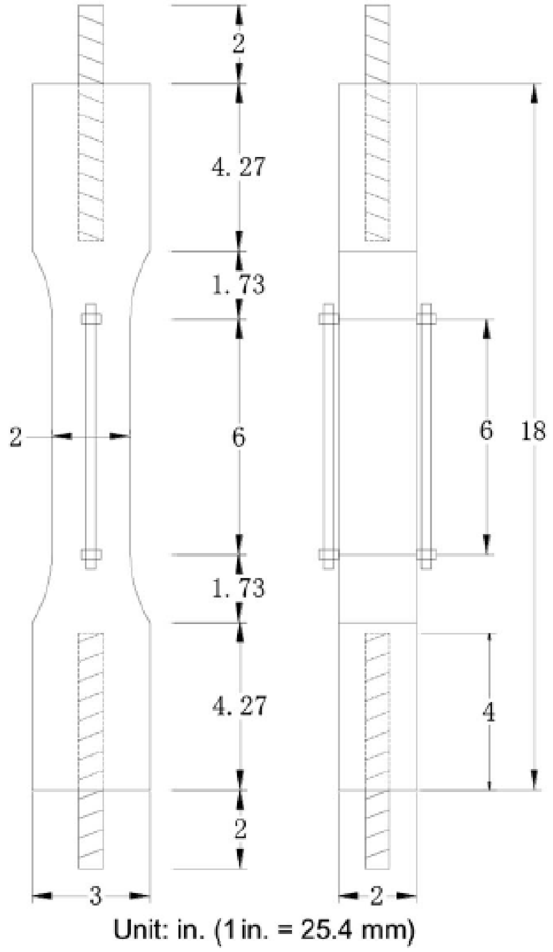

Figure 3.27 UHPC DTT Specimen Design (Zhou and Qiao, 2020)

After curing the specimens are brought to LEL and measured to find the average dimensions. Each specimen is then placed in the UTM and tested. The specimens are tested at a loading rate of 1 in./min. The test set-up can be seen in Figure 3.28. The failure of each specimen can be seen in Figure 3.29, the black lines mark the gauge length beginning and end, the red line denotes the fracture. The results from the DTT for the UHPC specimens can be seen in Table 3.13. Note that specimen A did not record data, therefore it is not included in the data set.

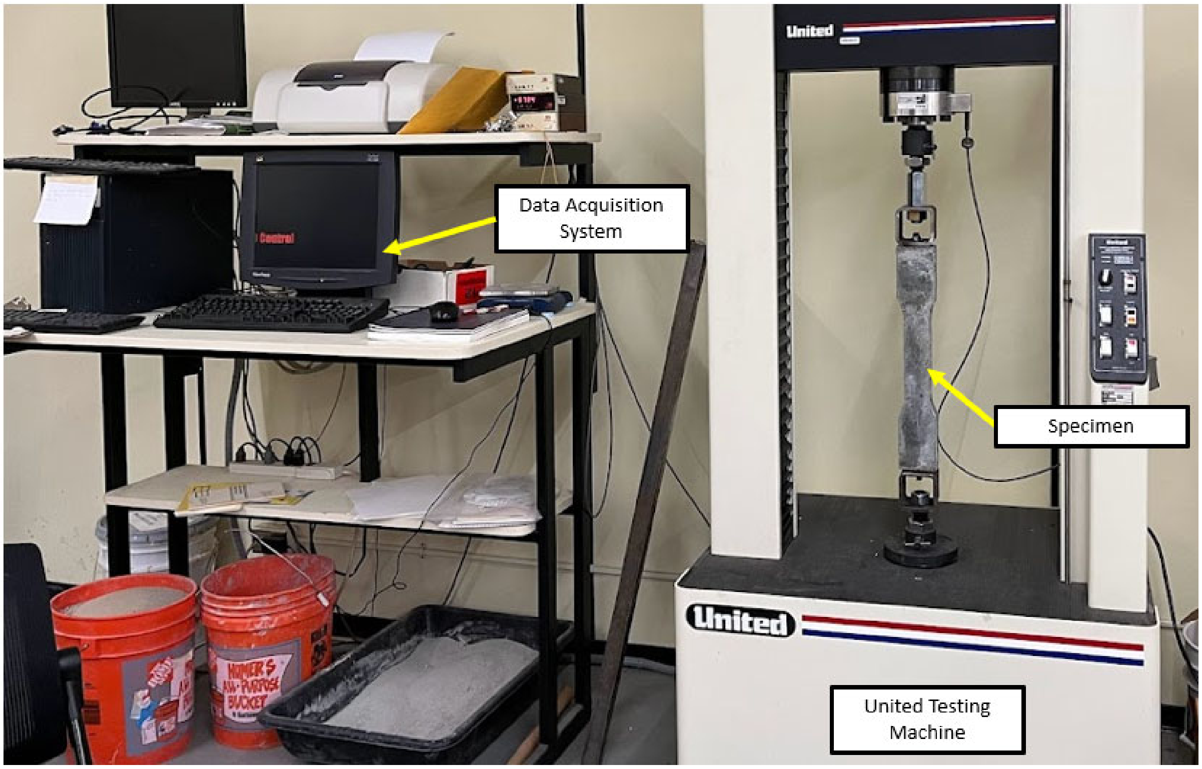

Figure 3.28 UHPC DTT Test Set-Up

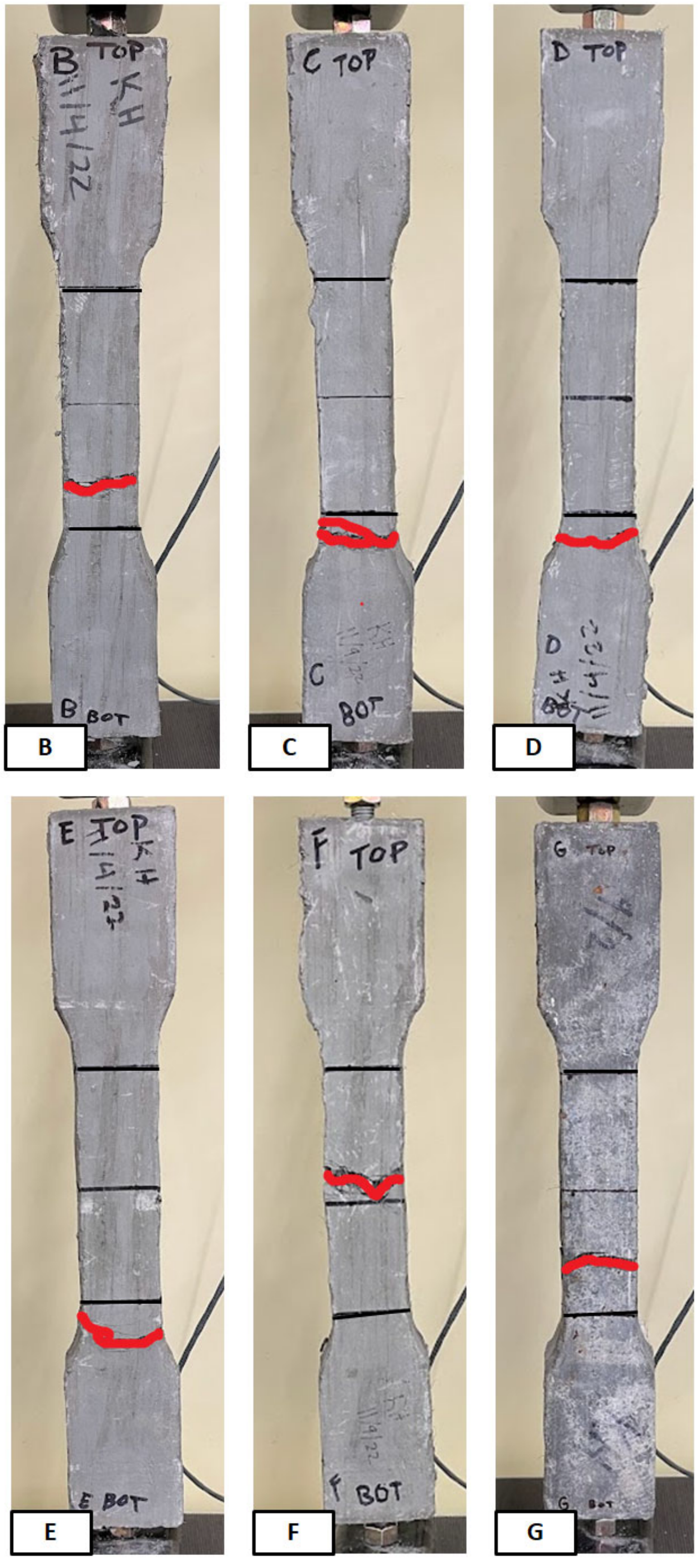

Figure 3.29 Failure of UHPC DTT Specimens

Table 3.13 UHPC DTT Results

Specimen	Average Width (in.)	Average Depth (in.)	Average Cross-sectional Area (in.^{2})	Peak Load (kip)	Tensile Strength (ksi)
B	2.105	1.948	4.101	3.702	0.903
C	2.085	2.023	4.217	3.175	0.753
D	2.043	2.030	4.146	2.657	0.641
E	2.134	2.034	4.340	2.102	0.485
F	2.078	2.093	4.349	3.048	0.701
G	2.029	2.046	4.152	3.058	0.737
Average	---	---	---	---	0.703

Precast 1 Retrofit

Introduction

This section presents the design, construction, and testing of a precast column retrofit with UHPC with the intention of establishing a performance level in which to compare to the other retrofit methods. A review of the construction process is presented, discussing the challenges faced during the construction of Precast 1. The full testing arrangement used for the experimental work is presented and discussed, followed by the experimental testing carried out and its resulting performance.

This chapter also shows the process for design of a precast column for a theoretical benchmark specimen to compare to Precast 1. Precast 1 is compared to the Precast Bent columns from Phase I of the ITD report, however certain limitations exist for a complete analysis and comparison to the bent columns, therefore the theoretical column is also used as a benchmark.

Theoretical Benchmark Specimen

The cross section of the precast bent is shown for reference in Figure 3.30. This benchmark is designed based on the original Precast Bent. The benchmark is a single column that has the same cross-sectional dimensions as the precast bent columns, but differs in height. The purpose of the benchmark is to show the design process for the telescoping pipe connection and show the design moment of the theoretical pier to be later compared with the retrofit for the precast specimens.

The design of the pier follows Washington State Department of Transportation (WSDOT) Bridge Design Manual. The first step in design is to size the HSS member (pipe) in the column. The following equation is used for member sizing to ensure ductile behavior and buckling criteria (WSDOT 2019):

$$\frac{D}{t} \leq 0.15\frac{E}{F_y}$$

Where:

D = Outside diameter of the HSS member, in inches
t = Wall thickness of the HSS member, in inches
E = Modulus of Elasticity of the member, in kips per square inch
F_y = Yield strength of the member, in kips per square inch

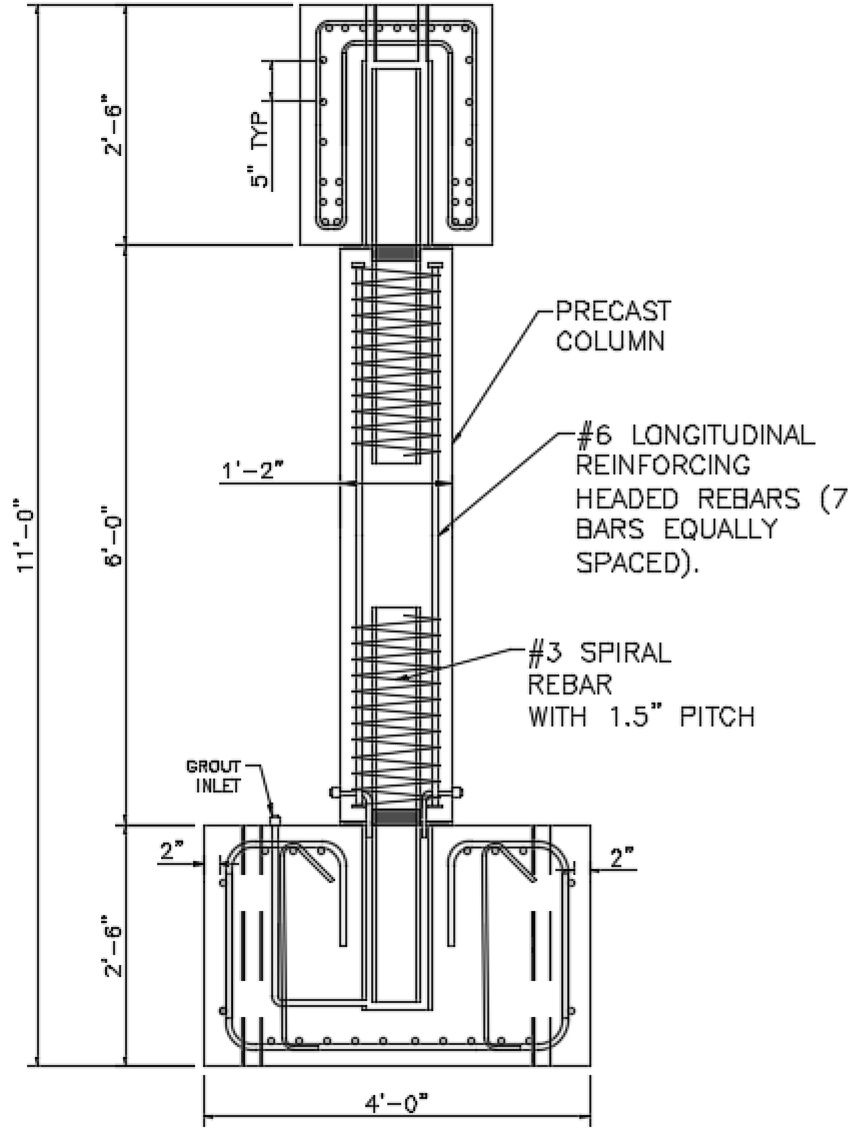

Figure 3.30 Original Precast Bent Pier Details (Side View)

Using the equation, an HSS section is selected of HSS6x0.500, with the following properties: 6 in. diameter, 0.465 in. wall thickness, 29,000 ksi modulus of elasticity, 42 ksi yield strength, and 58 ksi ultimate strength (F_u). Using the equation, D/t yields a value of 12.9 and $0.15E/F_y$ yields a value of 103.6, both values are dimensionless. Since 12.9 is less than 103.6, the equation checks out and it is fine to continue with the HSS6x0.500 member.

After checking ductile behavior/buckling criteria, the moment capacity of the connection is determined. The following equation is used to determine moment capacity ($M_n(y)$), (WSDOT 2019):

$$M_n(y) = \left(c\left(r_i^2 - y^2\right) - \frac{c^3}{3}\right) * 0.95f_c' + 4ct\frac{r_m^2}{r_i}F_y$$

Where:

c = One half cord length of the compressive block, in inches
r_i = Mean radius of internal reinforcement, in inches
r_m = Mean radius of HSS member, in inches
y = Vertical distance of neutral axis from center of HSS in plastic stress distribution method, in inches
f'_c = Compressive strength of the concrete, in kips per square inch
t = Thickness of the HSS member, in inches

The first step to use the moment capacity equation is to find the value of c. To do this, the following equation is used:

$$c = r_i \cos\theta$$

Where:

r_i = Mean radius to the inside of the steel tube, in inches

and θ is calculated using:

$$\theta = \sin^{-1}\left(\frac{y}{r_m}\right)$$

Where:

y = Distance from the centroid of the specimen to the neutral axis during a seismic event, in inches
r_m = Radius to the center of the steel tube, in inches

The neutral axis is assumed to be at the centroid for calculation; therefore, y is taken as 0. After y is determined, θ is calculated to be 0. To calculate c, r_i is measured to be 2.54 in.; plugging in 0 for θ, c is calculated to be 2.54 in. The last step is to determine the moment capacity of the connection using the main equation. For the moment capacity equation, the following values are used: c = 2.54 in., r_i = 2.54 in., r_m = 2.86 in., y = 0 in., f'_c = 4 ksi, and t = 0.465 in. Using the values of the variables given, the moment capacity of the connection is calculated to be 56.7 kip-ft, which is the same as the original bent pier. The difference is that the loading height of the column. The bent pier was loaded at 83.75 in., while the retrofit will be loaded at 66 in. The base shear of one connection for the bent was 8.1 kip, while the base shear for the retrofit is calculated to be 10.3 kip. Furthermore, the results of the precast bent testing showed that each connection was able to with stand 124.5 kip-ft with a base shear force of 17.9 kip at each connection. A summary of the precast bent values from design and experimental testing can be seen in Table 3.14, along with the values for the design of the theoretical column.

Table 3.14 Summary of Moment Capacity, Base Shear, and Loading Height for Precast Bent Pier vs. Theoretical Column

Specimen	**Connection Moment Capacity, $M_n(y)$ (kip-ft)**	**Connection Base Shear, V_b (kip)**	**Loading Height* (ft.)**
Theoretical Column Design	56.7	10.3	5.5
Precast Bent Pier Design	56.7	8.1	6.98
Precast Bent Pier Experimental	124.5	17.8	6.98

*Loading height is taken from the top of the footing to the center of the actuator

Design

Precast 1 is designed using a computer modeling program, SAP2000, to determine the expected yield moment of the retrofit. The goal is to bring the original column from the precast bent back to its original moment capacity and push the plastic hinge up the face of the column, above the jacket. The yield moment (M_y) of the original column is 117.89 kip-ft, the plastic moment (M_p) of the original column is 168.3 kip-ft. During testing of the precast bent, the pipe connecting the column to the footing fractured. Therefore, in the design process, the moment capacity contribution from the pipe is negligible, to be conservative. Furthermore, Figure 3.31 shows that the cover concrete around the base of the pipe spalled, therefore the entire section, excluding the pipe, is taken to be UHPC for the retrofit.

Figure 3.31 Original Precast Bent Pier with Concrete Spalled

The retrofit is designed using moment-curvature analysis of the cross section. The moment-curvature analysis is performed in SAP2000, an axial load is placed on the column of 30 kip, to correspond to the 5% gravity load of the bent specimen during testing. Using SAP2000, the dowels are selected to be number 6 grade 60 rebar, and the circular ties are chosen as number 3 grade 60 rebar. The dowels are to be epoxied into the footing using HILTI HT-HY 100 anchoring epoxy. The specifications detail a design strength of 23,885 lb. in tension (ϕN_n) and 51,448 lb. in shear (ϕV_n) (HIT-HY 100 Technical Supplement 2018, 5). The dowels extend 12.5 in. from the top of the footing into the jacket, allowing for 1.5 in. cover at the top of the jacket. The dimensions of the ties are designed according to ACI 318-19 25.7.2 (ACI 318-19 2019, p. 501-502). The cover for the circular ties is 1-3/4 in. The model placed into SAP2000 of the original precast pier cross section and Precast 1 retrofit are shown in Figure 3.32. The model is run with varying thicknesses to determine the ideal jacket thickness.

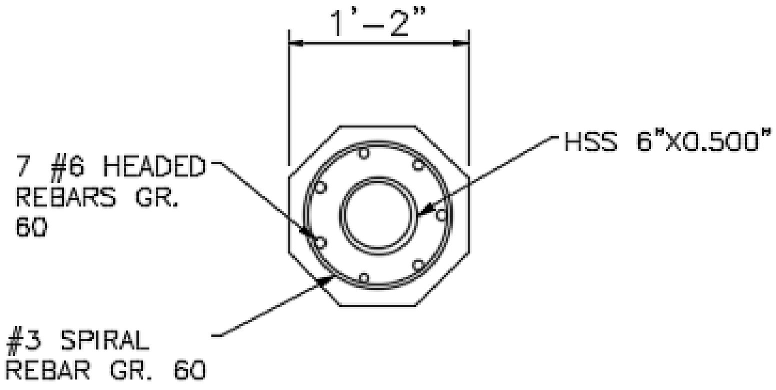

ORIGINAL COLUMN DETAIL

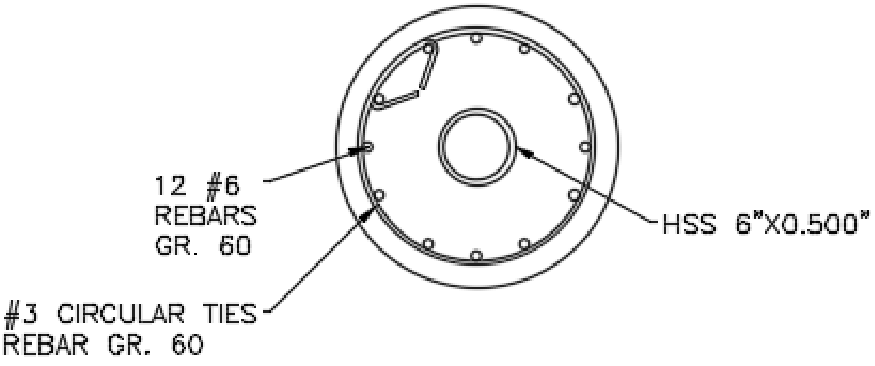

PRECAST 1 RETROFIT SAP2000 MODEL

Figure 3.32 Precast 1 Column Cross-Section

The results from the SAP2000 model are shown in Figure 3.33 and Table 3.15. The results show that a jacket of 3.0 in. thickness would be sufficient, however for construction convenience, the thickness of 4.0 in. is selected to provide sufficient room for the dowels to be anchored into place. Figure 3.34 explains the necessity of the 4 in. thick jacket; the necessity comes from construction tolerance. If the 3 in. thickness was to be used, the holes for the dowels could not be drilled.

Table 3.15 Moment-Curvature Analysis of Precast 1 Retrofit

Jacket Thickness (in.)	Moment Yield Capacity, M_y (kip-ft)	Plastic Moment, M_p (kip-ft)
3.0	162.23	255.21
3.5	173.87	275.77
4.0	185.16	300.34
Original Precast Pier	114.37	166.12

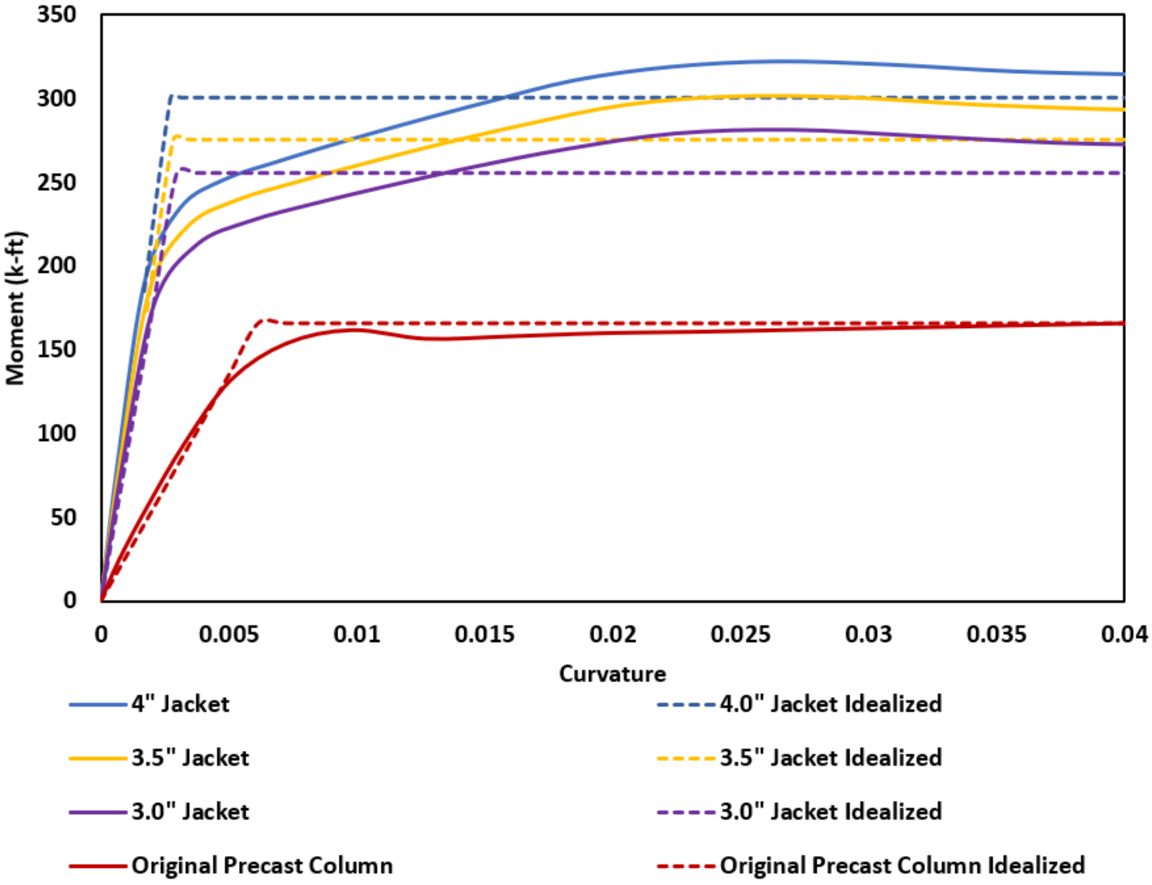

Figure 3.33 Moment-Curvature Analysis of Precast 1 Retrofit

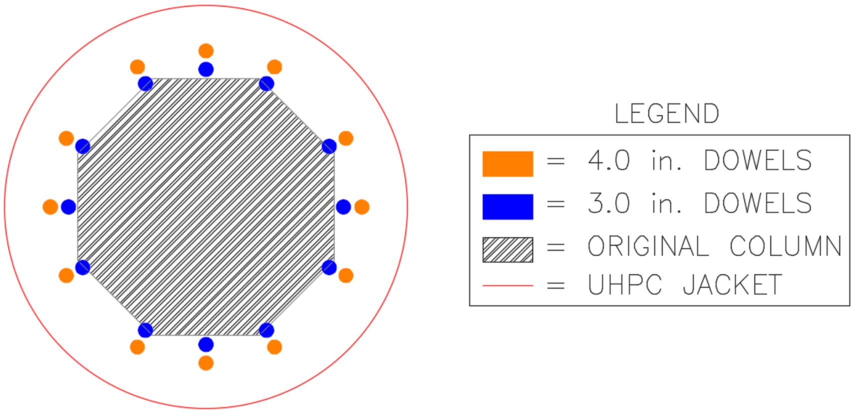

Figure 3.34 Diagram of Possible Rebar Dowels

The height of the jacket is determined to be equivalent to the thickness of the original column width (14 in.). The overall design for Precast 1's retrofit is shown in Figure 3.35.

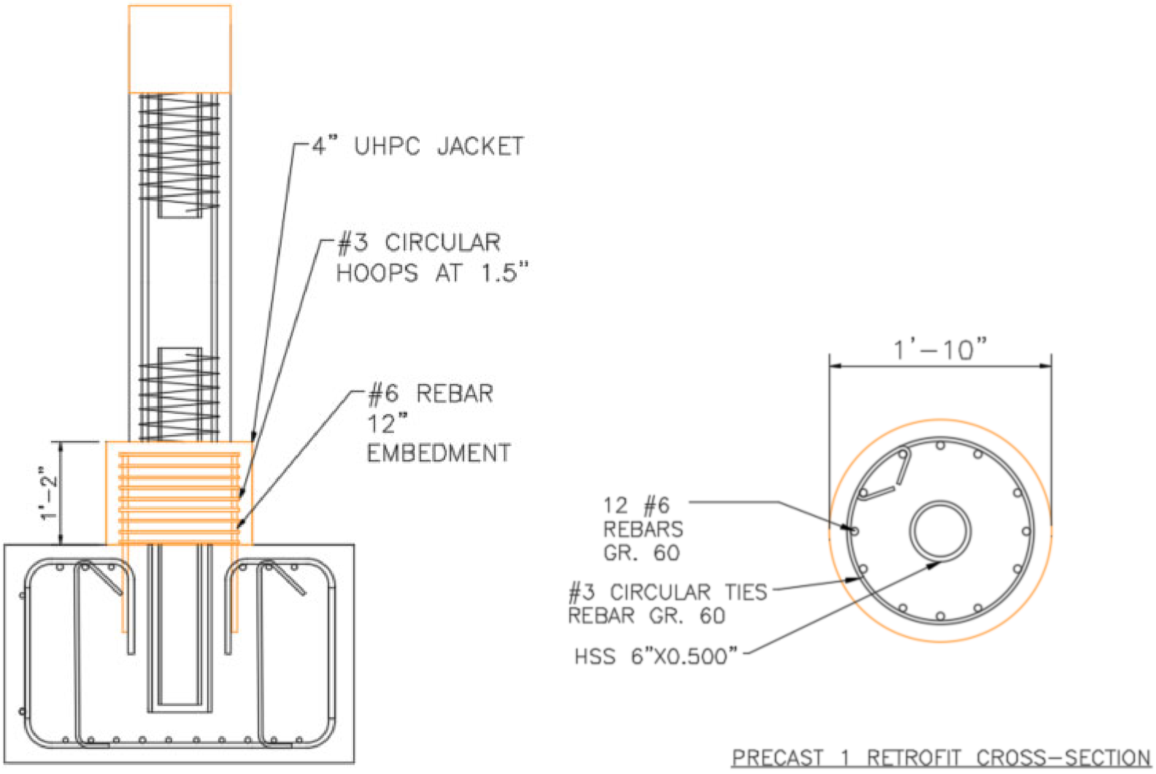

Figure 3.35 Precast 1 Retrofit Detail

Construction

The first step in the construction process is to repair the top of the column so that it can accept the gravity and lateral loads during testing. The top of the column is cleaned off and then formed with the original formwork from Phase I of the project, with the same dimensions. The form is caulked and then a new UHPC cap is poured for the top of the column. The cap of the column adds no structural benefit to the retrofit, it is merely for testing purposes.

Construction of Precast 1 Retrofit starts with preparing the surface of the concrete for UHPC. This is done using a chisel and hammer. The 22 in. diameter base around the column is chipped to a ¼ in. depth to allow for a good bonding surface. After the foundation surface is chipped, the column is chipped down to the spiral ties for the height of the jacket (14 in.). The column is chipped to get rid of the cover concrete that has already been damaged and ensure good contact between the UHPC and the column.

After the surface has been prepared, twelve, 7/8 in. holes are drilled to allow the dowels to be epoxied into place. The holes are drilled to a depth of 12 in., to allow for sufficient embedment. Figure 3.36a shows the prepared column after surface preparation and drilling. After the holes are drilled, the rebar is cut and epoxied into place using HILTI HIT-HY Adhesive Anchor. The next step of construction is to tie the transverse reinforcing. The circular ties are purchased with a lap splice; the hook to grip the dowels is bent in the lab. After the ties are completed, they are slipped over the column and down around the dowels. The ties are then secured into place. The completed cage is shown in Figure 3.36b. The next step is to prepare the form for the jacket. A 24 in. diameter Sonotube is cut to a 22 in. diameter and lapped to make the circular form. Due to the lap in the Sonotube, additional form work is added to support the circular form. After the support form is constructed, the Sonotube is slipped over the column and into the support form. The Sonotube is sealed on the bottom using caulk. The support form is then strapped down to the footing to prevent movement during pouring. The final form work can be seen in Figure 3.36c.

Before the jacket can be poured the column must be placed under gravity load (30 kip) to simulate the superstructure of the bridge during a retrofit. Precast 1 is moved into the SLAB and anchored to the strong floor. The gravity load is then added through a pump, hollow-core hydraulic jack, and loadcell. The set-up for pouring is shown in Figure 3.37.

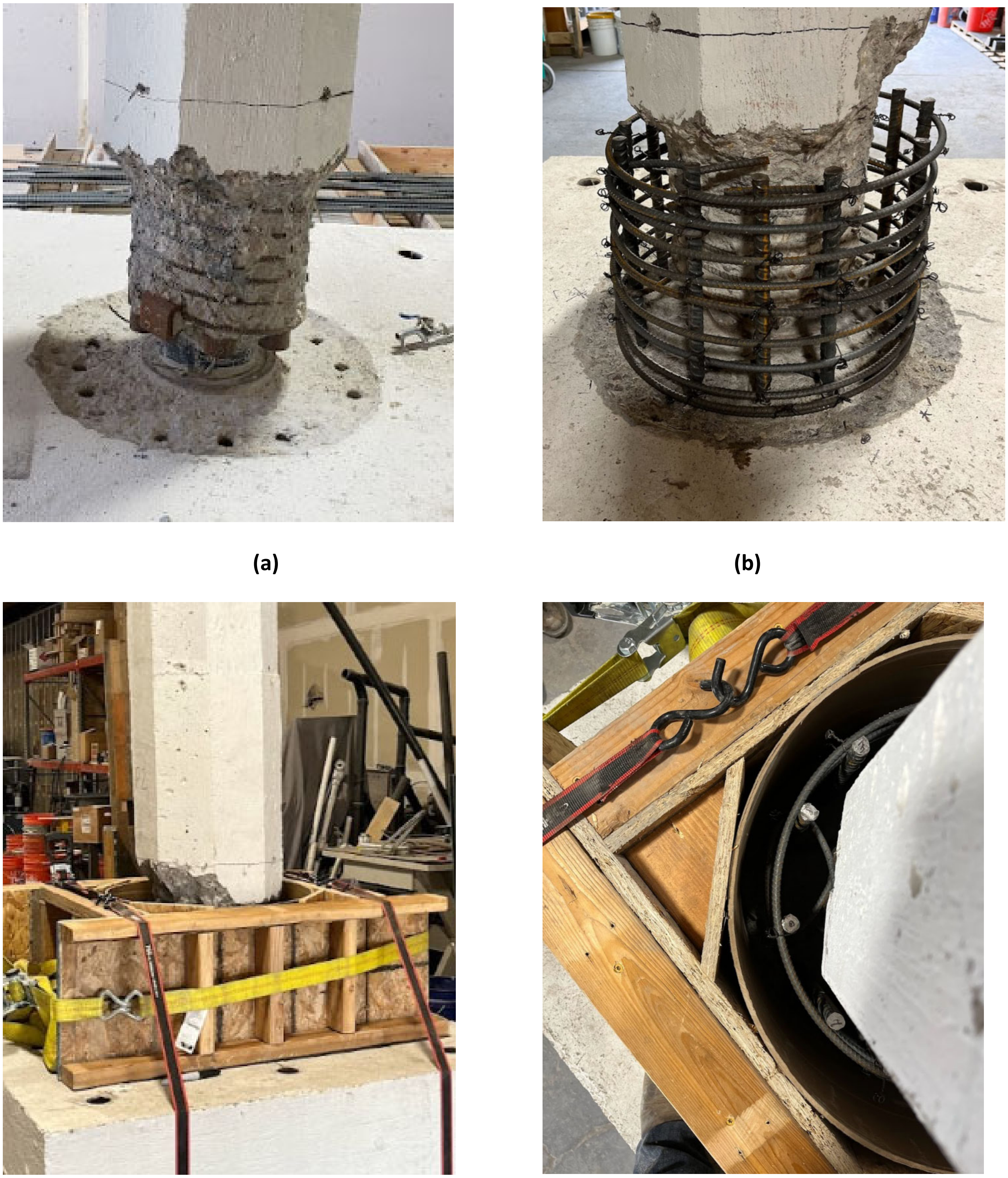

(a)

(b)

(c)

Figure 3.36 Construction of Precast 1 Retrofit: (a) Prepared Specimen, (b) Completed Cage, (c) Precast 1 Form work

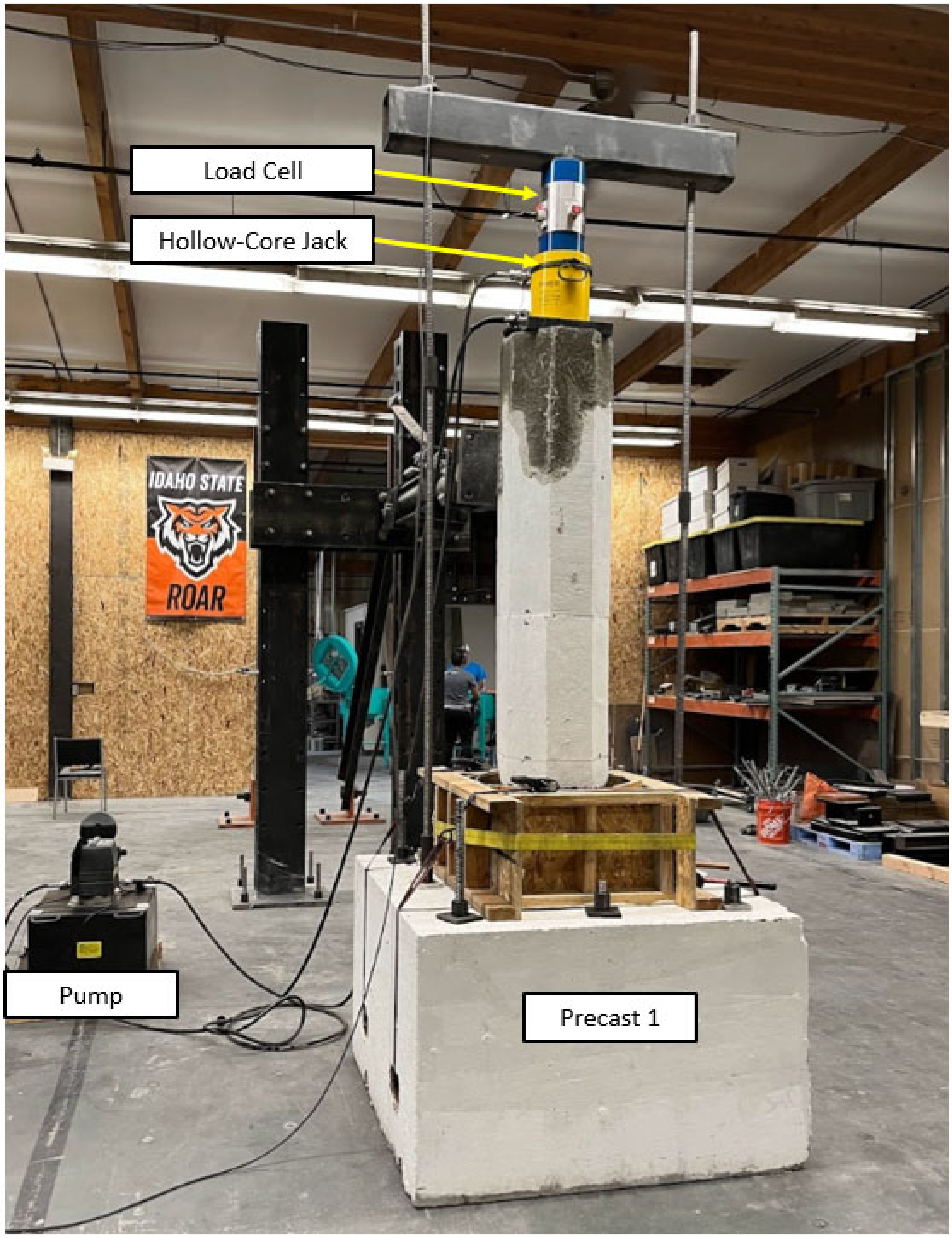

Figure 3.37 Gravity Load Assembled for Precast 1 Pour

Now that the cage, form, and gravity load have been assembled, the UHPC can be poured. JS1000 UHPC from Ductal® is used for the jacket. The UHPC is poured according to the instructions given by Ductal®. The UHPC consists of high range water reducer, steel fibers, water, and Ductal® Premix (pre-blended cement, sand, ground quartz, silica fume). The Ductal® Premix is added to the mixer first followed by the water and admixture, and finally the steel fibers. Once the UHPC is done mixing and ready to pour, it is removed from the mixer in buckets and poured into the form. Note that due to the capacity of the mixers in the lab, the jacket must be poured in two lifts. The completed pour is shown in Figure 3.38. After the jacket is poured the column is held under the gravity load for 72 hours until the UHPC has hardened. After 72 hours, the gravity load and form work are removed. The jacket is then covered with burlap and plastic and wetted twice a day for 28 days while it cures.

Figure 3.38 Precast 1 Completed Pour

Some cosmetic patchwork is completed after curing with high-strength grout. The patch is purely for aesthetics and to help monitor cracking in the face of the column during testing. After the jacket has been cured and patched, it is painted and marked for Finite Element Modeling (1 in. grid). The completed retrofit is shown in Figure 3.39, and is now ready for testing.

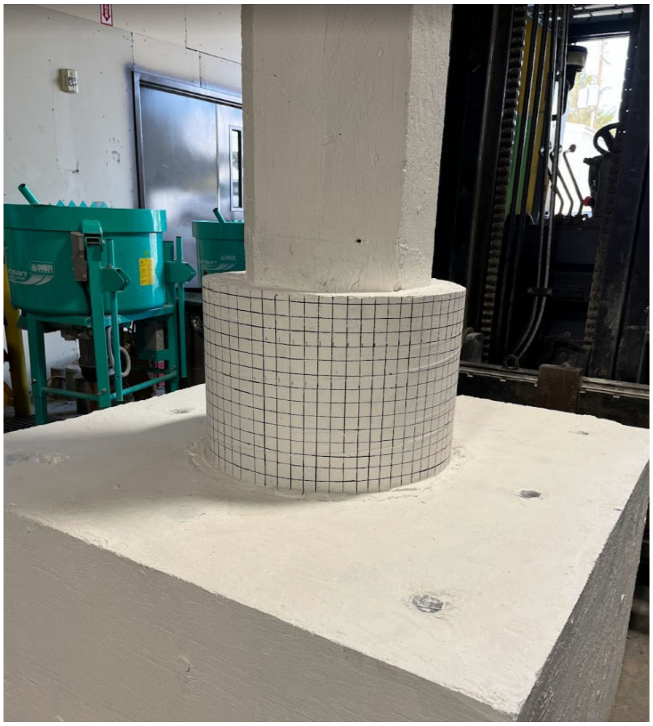

Figure 3.39 Precast 1 Retrofitted Column

Testing Arrangement

After the construction of Precast 1 is complete, the testing arrangement is erected. Testing includes a uniaxial load in the transverse direction and a gravity load to simulate a bridge structure. The lateral load is applied in a cyclic manner in accordance with ACI (ACI Committee 374, 2013) via a hydraulic actuator. The actuator has a total stroke of 24 in. A 225-kip tension/compression load cell is mounted in line with the actuator to monitor the force exerted on the column. The actuator is mounted on the reaction frame, which is then braced with wide flange angle bracing. The reaction frame is anchored to the strong floor in the SLAB. After the actuator is hung, the head is attached to the column using a clamping mechanism designed for testing. The clamp consists of a 1 in. plate recessed with 7/8 in. bolt holes to mount to the actuator with another set of holes on a 19 in. by 11 in. hole pattern and another 1 in. plate to grip the column on the other side. The two plates are connected using 1 in. diameter high-strength threaded rods. The specimen is then secured to the strong floor using eight high-strength threaded rods which have been post-tensioned into the floor to 75-kip per bolt. The specimen is anchored and post-tensioned to eliminate rocking in the footing and ensure a fixed connection at the base.

The final step of the test set-up is to reapply the gravity load as it was before during pouring. The vertical force is applied in the center of the column with a target value of 5% of the axial compressive capacity of the specimen. The following equation is used to determine a gravity load of 30 kips:

$$Gravity\ Force = 0.045(A_g f_c')$$

Where:

A_g = Gross cross-sectional area of the column, in square inches
f'_c = Compressive strength of concrete, in kips per square inch

In the equation, the cross-sectional area of the column is approximately 163 in^2 and the concrete compressive strength is 4 ksi. A reaction beam is placed across the top of the loadcell and two high-strength threaded rods are tied to the strong floor to resist the downward force provided by the gravity load. Figure 3.40 shows the overall test set-up for Precast 1.

Figure 3.40 Overall Test Set-Up

Instrumentation

Throughout testing measurements are taken using a Data Acquisition System (DAQ) and potentiometers (POTs). Three types of POTs are used: string and linear (spring and non-spring). The instruments are programmed using the Campbell Scientific DAQ. The system is programmed for a total of 54 instruments and set to take five readings per second throughout testing. Figure 3.41 and Figure 3.42 give a visual of the instrumentation layout for the north and south face of the column, respectively. Instruments that are not depicted in the figures are F1, F2, R1, R2, and ACT, and are used to monitor footing movement, reaction frame movement and true actuator displacement, respectively.

The CAP-INPLANE instrument is a string POT which measures the actual displacement of the top of the column. The CAP-INPLANE POT is mounted to the instrumentation tower and directly in line with the center of the actuator.

The groups of instruments from A to H are a combination of spring and non-spring, linear POTs. These POTs have various lengths of aluminum extensions to cover the distance required. Groups D, G, H, and I monitor the possible/expected plastic hinge zones in the column. The other groups are used to monitor any curvature experienced by the column which falls outside the plastic hinge zone.

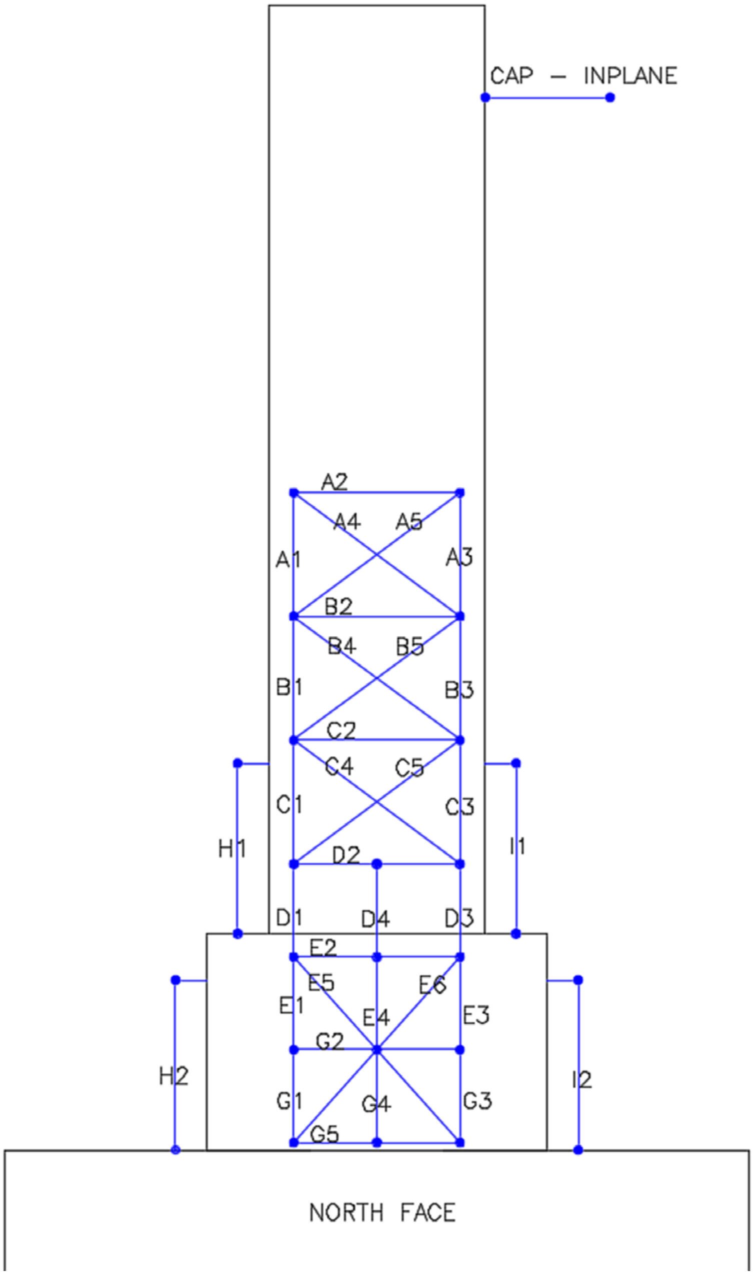

Figure 3.41 Instrumentation Precast 1 - North Face

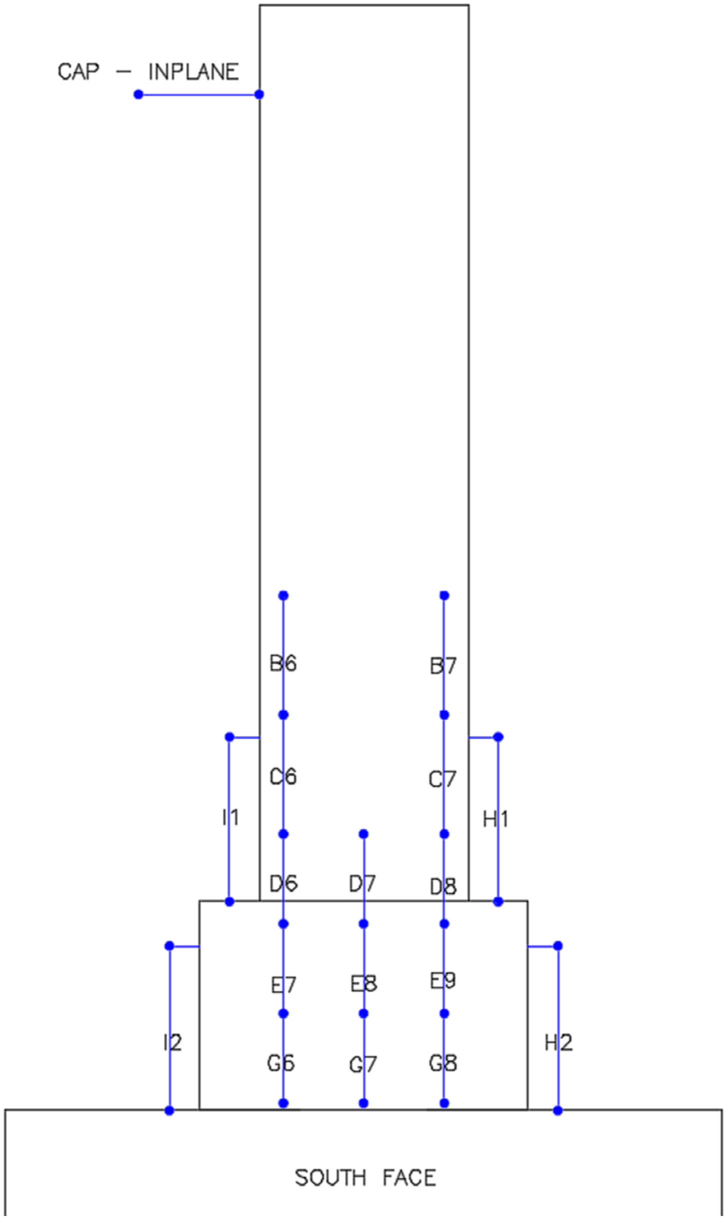

Figure 3.42 Instrumentation Precast 1 - South Face

Amongst the POTs, two 225-kip load cells are used to monitor the load acting on the column. One cell monitors the transverse loading, and the other monitors the gravity load on the column.

Loading Protocol

The loading protocol for the retrofit is determined in accordance with ACI Committee 374 (ACI Committee 374, 2013) and comparison with the benchmark bent specimens. The quasi-static cyclic loading protocol utilizes the yield displacement of the specimen to generate the required displacements for each cycle. The yield displacement is determined using the equations provided by Priestley et. al., 2007:

$$\Delta_y = \Delta_{y1} + \Delta_{y2}$$

$$\Delta_{y1} = \varphi_y \frac{(L_1 + L_{sp})^2}{3}$$

$$\Delta_{y2} = \varphi_y \frac{(L_2 + L_{sp})^2}{3}$$

$$\varphi_y = 2.25 \frac{F_{ye}}{ED}$$

$$L_{sp} = 0.15 F_{ye} d_b$$

Where:

Δ_y = Total yield displacement of the column, in inches
Δ_{y1} and Δ_{y2} = Yield drift for each short column, in inches
φ_y = Curvature in the column corresponding to the first longitudinal bar yield point, in one over inches (in.$^{-1}$)
L_1 and L_2 = Column height, in inches
L_{sp} = Strain penetration length, in inches
F_{ye} = 1.1 times the yield strength of steel, in kips per square inch
E = Modulus of elasticity of steel, in kips per square
D = Diameter of the column, in inches
d_b = Diameter of the reinforcing longitudinal bar, in inches

Figure 3.43 gives a visual of the parameters used in the equations derived by Priestley et. al., 2007. Furthermore, Table 3.16 shows the values of the parameters used to calculate the loading protocol and the yield displacement used. Note that the calculated yield displacement is different from the yield displacement used for programming. Like the bent laboratory model, the smaller value is used to ensure two full cycles of testing for instrumentation/test set-up purposes before yielding the column.

Note, even though the height of the column from the top of the footing to the center of the actuator is 66 in., a height of 52 in. is used because the retrofit is assumed to be fixed to the footing and creates a shorter column height. 52 in. is the distance from the top of the jacket to the center of the actuator. Also note, for calculation purposes L_1 and L_2 are taken to be half the column height, even though this is likely not true during testing.

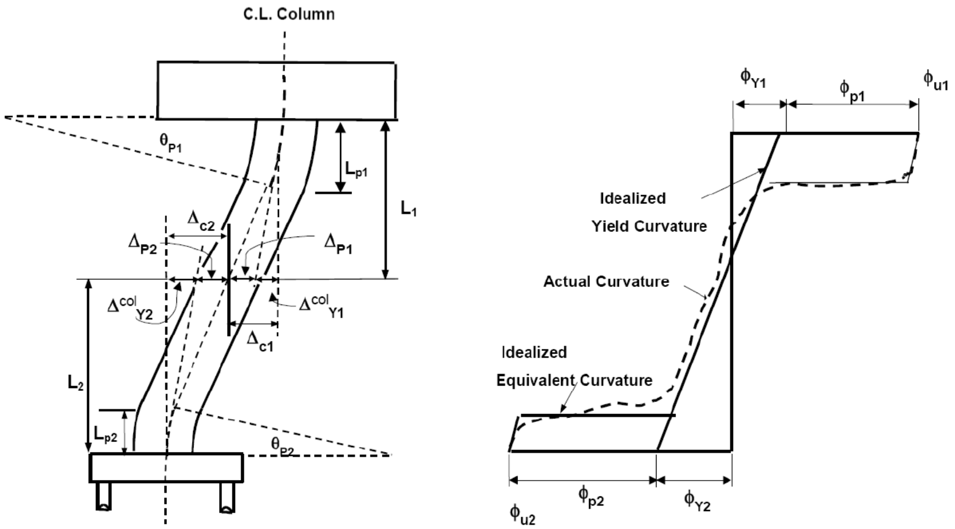

Figure 3.43 Displacement Capacity of a Pier in a Bent with Fixed-Fixed Supports (Caltrans, 2013)

Table 3.16 Loading Protocol Calculation

Loading Protocol Parameter	**Pier Retrofit Value Used/Calculated**	**Original Bent Value Used/Calculated**
L_1 and L_2	25 in.	36 in.
F_{ye}	66 ksi	66 ksi
E	29,000 ksi	29,000 ksi
D	14 in.	14 in.
d_b	0.75 in.	0.75 in.
Δ_{y1} and Δ_{y2} (calculated)	0.128 in.	0.230 in.
Δ_{y1} and Δ_{y2} (used)	0.098 in.	0.176 in.
L_{sp}	7.425 in.	7.425 in.
φ_y	0.000366 in.$^{-1}$	0.000366 in.$^{-1}$
Δ_y (calculated)	0.256 in.	0.460 in.
Δ_y (used)	0.196 in.	0.352 in.

Furthermore, the yield drift is calculated using the equation given by (Priestley et. al., 2007):

$$\theta_{y,short} = \frac{\Delta_{y1,2}}{L_{1,2}} \cdot 100$$

$$\theta_y = \frac{2\Delta_{y1,2}}{L_1 + L_2} \cdot 100$$

Where:

$\theta_{y,\,short}$ = Yield drift of short column, in percent
Δ_{y1} and Δ_{y2} = Yield drift for each short column, in inches
L_1 and L_2 = Column height, in inches
θ_y = Yield drift of entire column, in percent

Using the equations, the short column yield drift and the total column yield drift are determined to be 0.378%. The short column yield drift and the total column yield drift for the original bent specimen are determined to be 0.42%. After the calculations are completed, the following loading protocol is determined (Figure 3.44 and Table 3.17). Note the Δ_y is rounded up from 0.196 in. to 0.20 in.

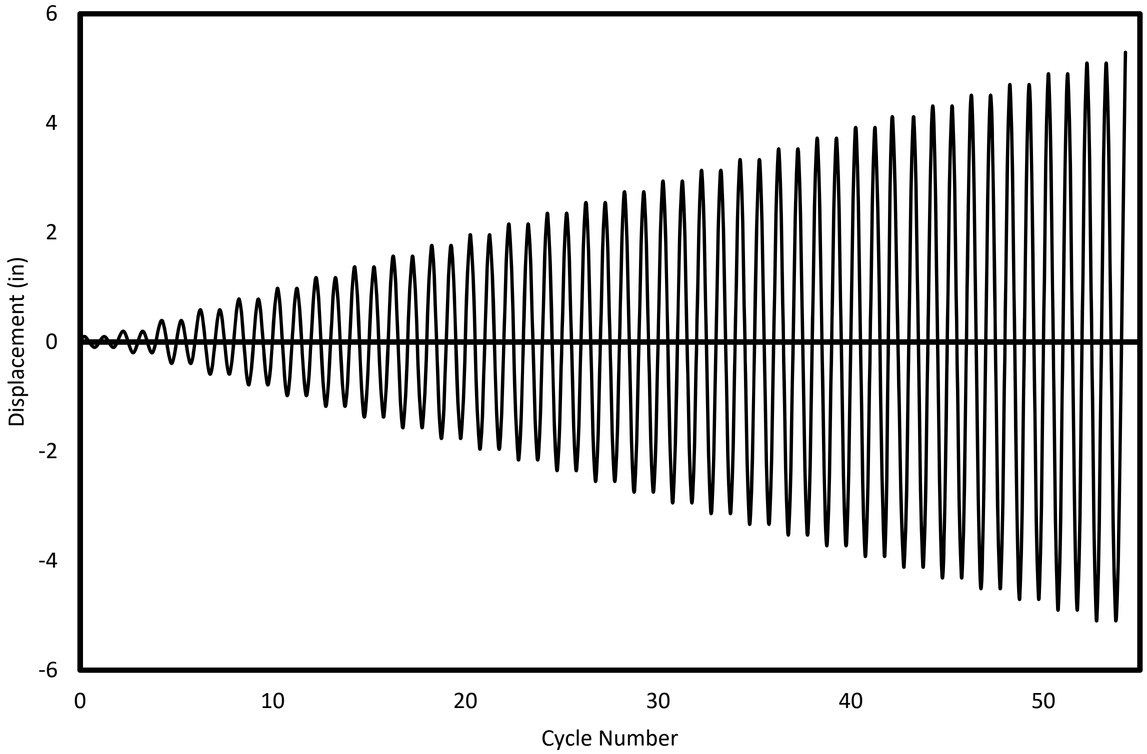

Figure 3.44 Loading Protocol for Retrofitted Pier

Table 3.17 Loading Protocol for Retrofitted Pier

Delta	**Displacement (in.)**	**Drift (%)**
$0.5\Delta_y$	0.10	0.196
Δ_y	0.20	0.392
$2\Delta_y$	0.39	0.784
$3\Delta_y$	0.59	1.177
$4\Delta_y$	0.78	1.569
$5\Delta_y$	0.98	1.961
$6\Delta_y$	1.18	2.353
$7\Delta_y$	1.37	2.746
$8\Delta_y$	1.57	3.138
$9\Delta_y$	1.77	3.530
$10\Delta_y$	1.96	3.922
$11\Delta_y$	2.16	4.315
$12\Delta_y$	2.35	4.707
$13\Delta_y$	2.55	5.099
$14\Delta_y$	2.75	5.491
$15\Delta_y$	2.94	5.883
$16\Delta_y$	3.14	6.276
$17\Delta_y$	3.33	6.668
$18\Delta_y$	3.53	7.060
$19\Delta_y$	3.73	7.452
$20\Delta_y$	3.92	7.845
$21\Delta_y$	4.12	8.237
$22\Delta_y$	4.31	8.629
$23\Delta_y$	4.51	9.021
$24\Delta_y$	4.71	9.414
$25\Delta_y$	4.90	9.806

Delta	**Displacement (in.)**	**Drift (%)**
$26\Delta_y$	5.10	10.198
$27\Delta_y$	5.30	10.590
$28\Delta_y$	5.49	10.983

*Note drift is calculated from the top of the jacket, i.e. Drift (%) = (Displacement/50 in.)*100

Testing Results

Starting the test at $0.5\Delta_y$, no cracks appeared. Old cracks began to surface on the east and west face of the column during the Δ_y cycle. These are noted as “old” cracks as they were caused by initial testing in the bent and simply surfaced through the paint of the specimen. The first hairline cracking due to the retrofit testing occurred at the $4\Delta_y$ cycle. The location of the hairline cracks was at the top of the jacket at the column interface on both the east and west sides of the pier. As the hairline cracks appeared during the $4\Delta_y$ cycle, the old cracks began to spread across the face of the column on both east and west sides. During the $4\Delta_y$ a crack also appeared in the jacket where the joint was created during pouring. The crack on the jacket was minor. Figure 3.45 shows both the east (green cracks) and west (red cracks) sides of the column after the $4\Delta_y$ cycle.

As testing continued, no more cracks appeared on the jacket, however hairline cracks continued to propagate and grow in size. After cycle $7\Delta_y$, the largest crack size was 0.08 in. and 0.06 in. on the east and west sides of the column, respectively (Figure 3.46). The cold joint crack did not expand in this time. As testing continued, spalling began to occur after the $9\Delta_y$ cycle on the west face of the column (Figure 3.47). The spalling was due to the high-strength grout patch detaching from the original concrete of the pier.

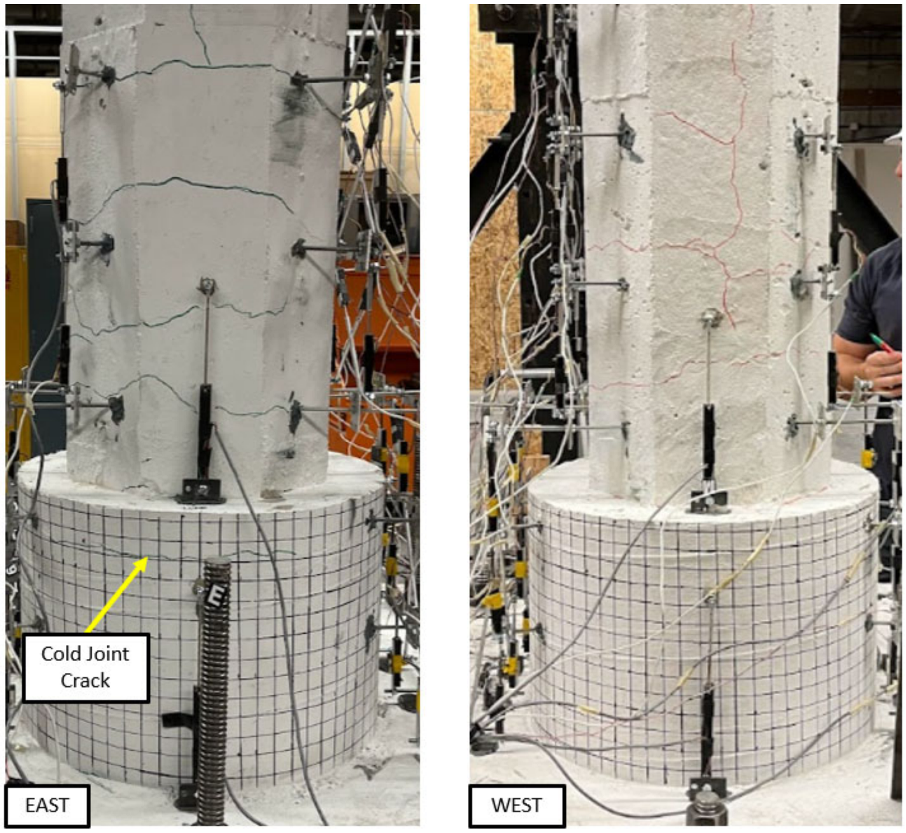

Figure 3.45 Precast 1 after $4\Delta_y$ Cycle

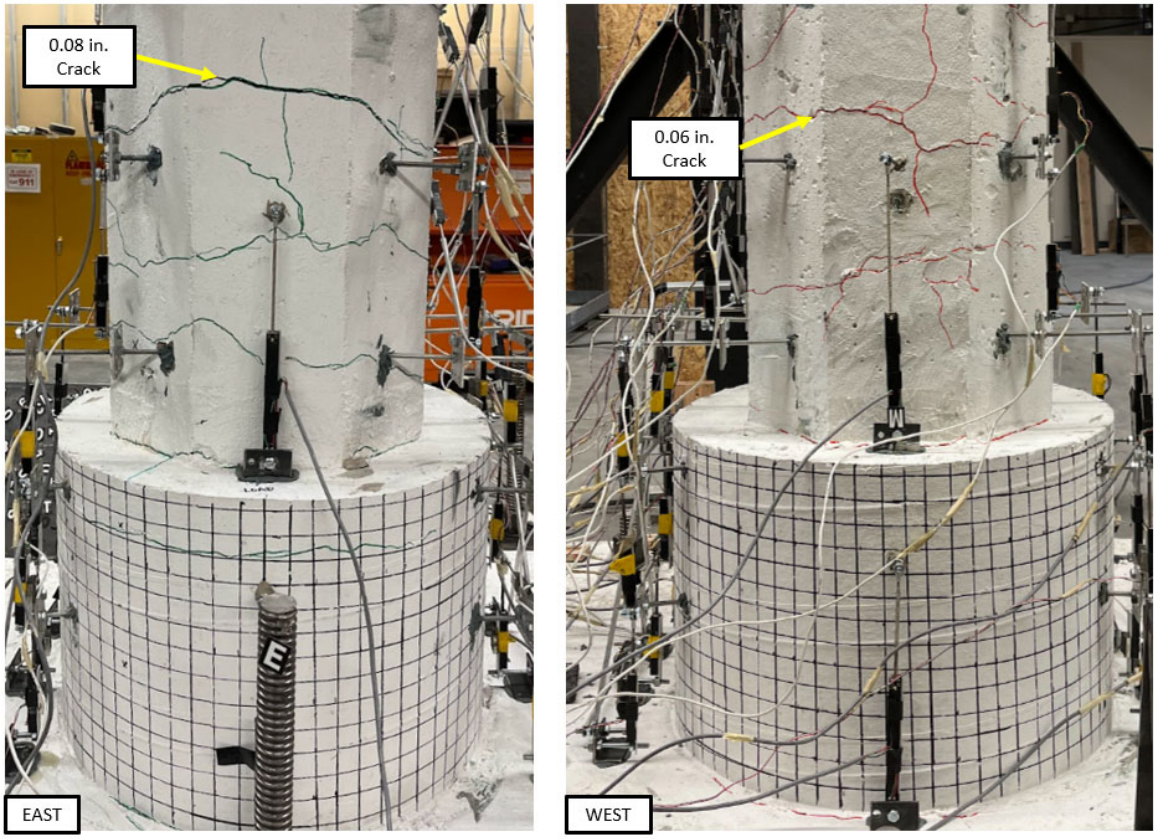

Figure 3.46 Precast 1 after $7\Delta_y$ Cycle

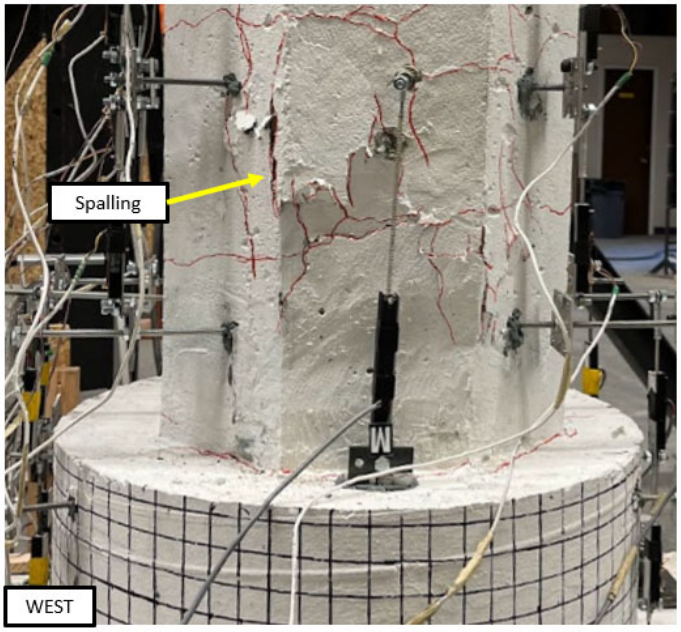

Figure 3.47 Spalling on West Face of Precast 1 after $9\Delta_y$ Cycle

By cycle $12\Delta_y$, spalling had continued on the west face of the column, leading to exposed stirrups. On the other hand, the east face of the column still had not undergone spalling; however, the crack highlighted in Figure 3.48 had expanded to 0.125 in. Spalling began on the east face during cycle $13\Delta_y$, leading to exposed stirrups. After cycle $15\Delta_y$ longitudinal rebar was visible on both the east and west face of the column (Figure 3.49). As testing continued, the core of the column crushed on both faces, eventually leading to a longitudinal bar fracture on the east side of the column during the $21\Delta_y$ cycle, which terminated testing (Figure 3.50).

After the initial cold joint cracking, Precast 1 did not experience any cracks in the jacket. Furthermore, Precast 1 did not experience any uplift from the jacket-to-footing interface. The retrofit was successful in pushing the plastic hinge of the column above the jacket. An overall image of Precast 1 after failure can been seen in Figure 3.51.

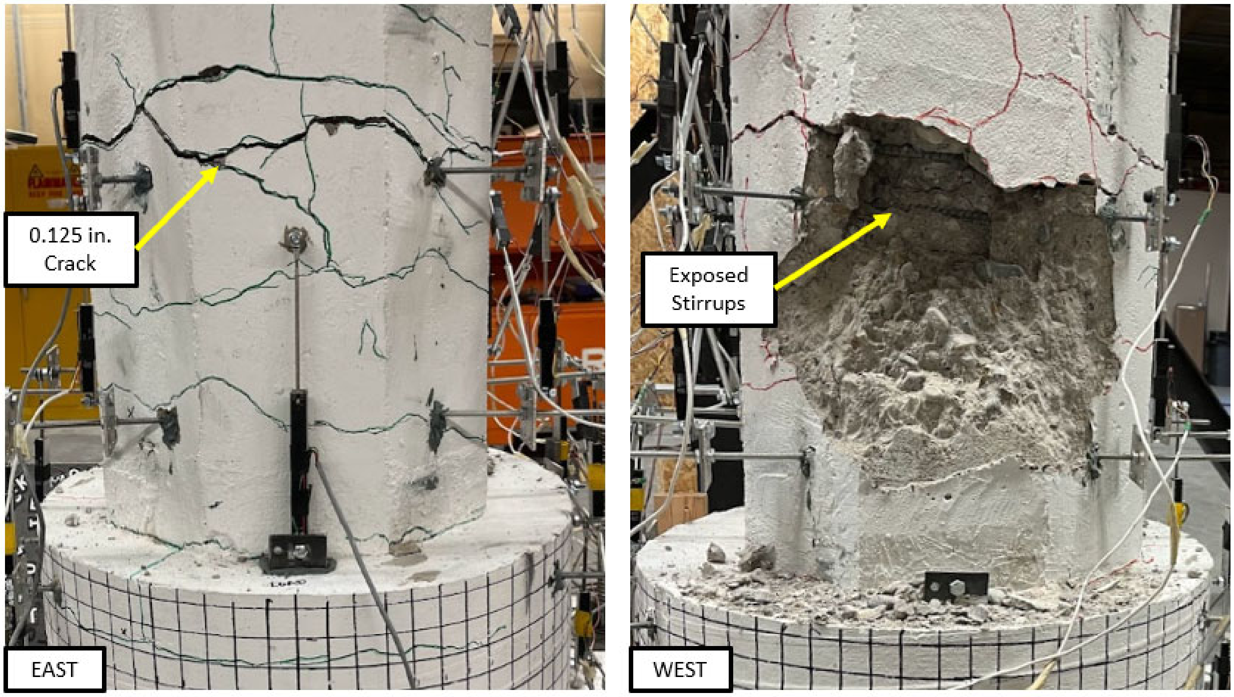

Figure 3.48 Precast 1 after $12\Delta_y$ Cycle

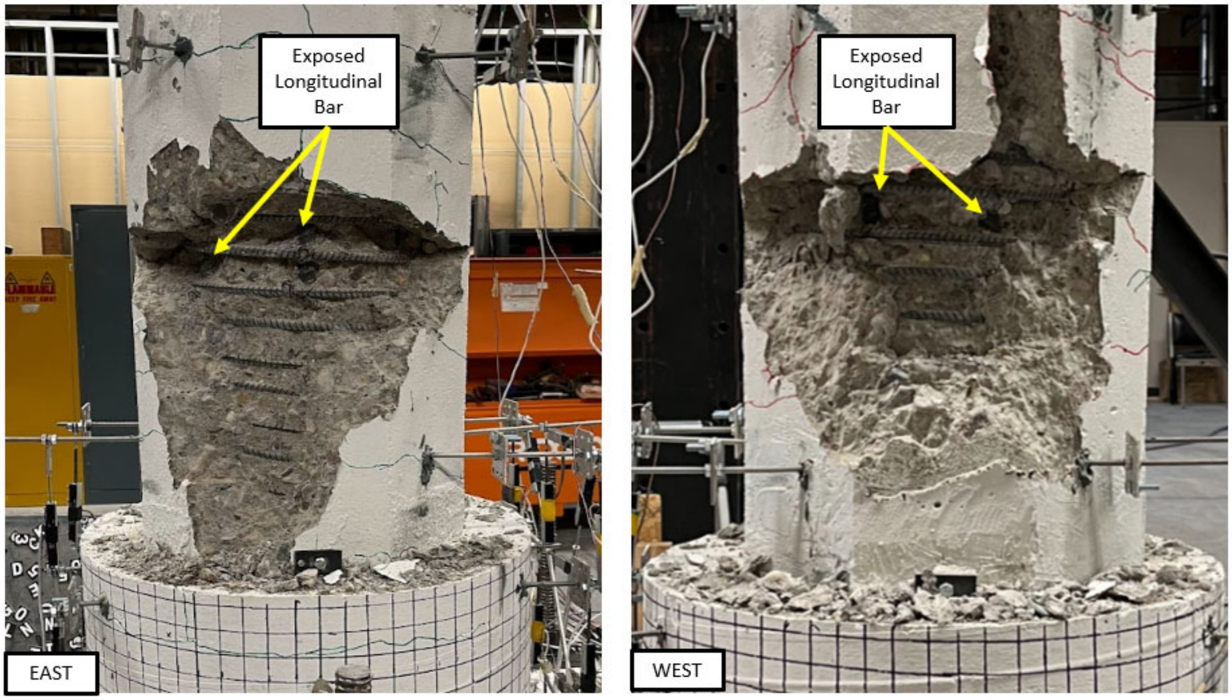

Figure 3.49 Precast 1 after 15Δ_Y Cycle

Figure 3.50 Precast 1 Ruptured Longitudinal Bar, East Face

Figure 3.51 Precast 1 Post-Test

The programmed vs actual achieved displacements and drift are summarized in Table 3.18. From here on, in this section, each cycle will be referred to as its correlating actual drift value.

Table 3.18 Precast 1 Loading Protocol Summary

Cycle	Programmed Displacement (in.)	Programmed Drift (%)	Actual Displacement (in.)	Actual Drift (%)
$0.5\Delta_y$	0.10	0.196	0.07	0.139
Δ_y	0.20	0.392	0.14	0.27
$2\Delta_y$	0.39	0.784	0.30	0.60
$3\Delta_y$	0.59	1.177	0.56	0.92
$4\Delta_y$	0.78	1.569	0.60	1.20
$5\Delta_y$	0.98	1.961	0.78	1.56
$6\Delta_y$	1.18	2.353	0.97	1.94
$7\Delta_y$	1.37	2.746	1.16	2.32
$8\Delta_y$	1.57	3.138	1.37	2.74
$9\Delta_y$	1.77	3.530	1.59	3.17
$10\Delta_y$	1.96	3.922	1.79	3.58
$11\Delta_y$	2.16	4.315	2.00	4.00
$12\Delta_y$	2.35	4.707	2.20	4.40
$13\Delta_y$	2.55	5.099	2.41	4.82
$14\Delta_y$	2.75	5.491	2.62	5.23
$15\Delta_y$	2.94	5.883	2.81	5.62
$16\Delta_y$	3.14	6.276	3.01	6.02
$17\Delta_y$	3.33	6.668	3.23	6.47
$18\Delta_y$	3.53	7.060	3.44	6.87
$19\Delta_y$	3.73	7.452	3.64	7.28
$20\Delta_y$	3.92	7.845	3.83	7.67
$21\Delta_y$	4.12	8.237	4.08	8.16

*Note drift is calculated from the top of the jacket, i.e. Drift (%) = (Displacement/50 in.)*100

The ultimate displacement achieved during testing was 4.08 in. (8.16% drift), while the ultimate force achieved was 30.76 kip. The ultimate lateral load correlates to a total moment capacity of 164.05 kip-ft, which exceeds the theoretical design column moment capacity of 56.7 kip-ft.

Using Bilinear approximation, the yield force (F_y) and yield displacement (δ_y) are determined for Precast 1. The method used mimics that of research completed by (Kaveh & Zakian, 2012) (Figure **3.52**). The goal of this method is to optimize the yield force and yield displacement simultaneously. The following constraints must be present to use this method:

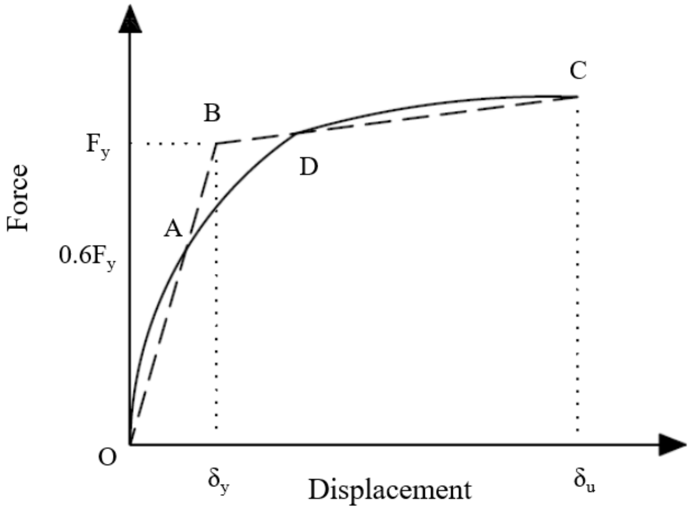

Figure 3.52 Force-Displacement Curve and its Bilinear Approximation; (Kaveh & Zakian 2012, p. 403)

1. Variable Limitations:
    a. $0 < F_y < F_u$
    b. $0 < \delta_y < \delta_u$

   Where:

   F_u = Ultimate Force, in kips
   δ_u = Displacement corresponding to ultimate force, in inches

2. An objective function is created, $H(x) = |S_2 - S_1|$ that is to be minimized as close to zero as possible.

   Where:

   S_2 = Area between the segment OB, segment BC, and the experimental data curve, prior to point D

S_1 = Area between the experimental curve and segment BC, after point D

3. Interpolate a displacement ($\delta_{0.6Fy}$) value corresponding to $0.6F_y$ of the experimental curve. This point is also the initial yield of the structure.
4. Calculate the linear equation of segment OB from the current iteration of optimized variables.
5. Using the equation from segment OB and the optimization variables, calculate an equation for segment BC.
6. Integrate the bilinear curve and experimental curve using the current iteration optimization variables, so that the objective function is approximately equal to zero.

Using this method, the following equations are determined for segment OB and segment BC:

$$\overline{OB}: \; y = 42.681x$$
$$\overline{BC}: \; y = 10.853x + 17.293$$

The experimental data is placed into an EXCEL file and a quadratic regression is used to determine the best suitable equation for the experimental data. The following equation is determined:

$$Experimental: \quad y = -19.1x^2 + 48.268x + 0.2086$$

After the equations are determined the following equation, along with this iteration of optimization variables, are used to equate the two areas, S_1 and S_2:

$$S_1 = \int_{\delta'_y}^{\delta_u} Experimental\,dx - \int_{\delta'_y}^{\delta_u} \overline{BC}\,dx$$

$$S_2 = \int_{\delta_{0.6Fy}}^{\delta_y} \overline{OB}\,dx + \int_{\delta_y}^{\delta'_y} \overline{BC}\,dx - \int_{\delta_{0.6Fy}}^{\delta'_y} Experimental\,dx$$

Where:

δ'_y = Intersection of segment BC and the Experimental Curve, i.e. the displacement value corresponding to point D

Using the above equations, S_1 is calculated to be 0.42026 and S_2 is calculated to be 0.42579. Now, the constraint;

$$|S_2 - S_1| \cong 0$$

is applied. The difference calculated between S_2 and S_1 is 0.00553, which is approximately equivalent to zero. Therefore, the values in Table 3.19 are calculated for the bilinear approximation. Similarly, Figure 3.53 gives the graph for the bilinear approximation.

Table 3.19 Bilinear Approximation Values Calculated for Precast 1

Parameter	Value
$\delta_{0.6Fy}$	0.326
δ_y	0.543
δ'_y	0.725
δ_u	1.239
$0.6F_y$	13.91
F_y	23.19
F'_y	25.20
F_u	30.74

*Where F'_y is the values corresponding to δ'_y

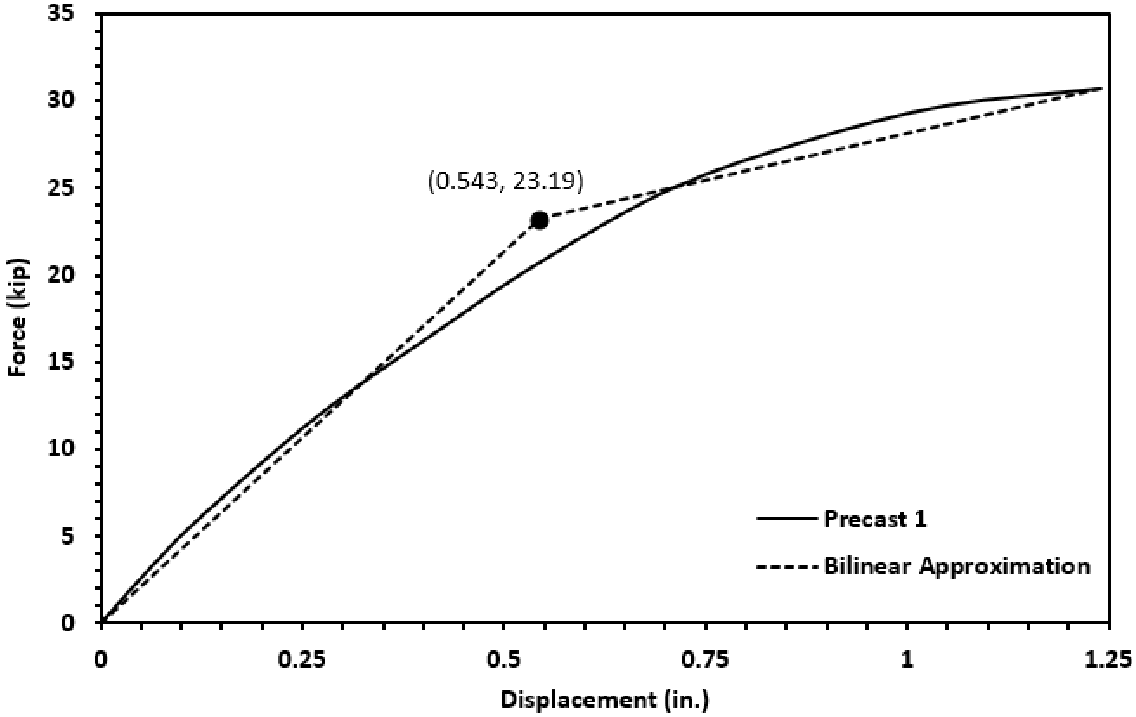

Figure 3.53 Bilinear Approximation of Precast 1

Furthermore, the hysteresis of Precast 1 is mapped in Figure 3.54 (force-displacement) and 3.55 (force-drift). The yield displacement is marked on both graphs. The yield displacement of 0.543 in. correlates to a drift value of 1.09%. It can also be noted that Precast 1 surpassed the theoretical benchmark base shear of 10.3 kip, which is also noted on both graphs. Note, quadrant I for both figures signifies the is column in push, while quadrant III signifies the column is in pull. From observation of Figure 3.54 and Figure 3.55, Precast 1 had similar strength and displacement in both push and pull.

Figure 3.56 provides the force-drift backbone curve for Precast 1. The performance points for Precast 1 are also given in Figure 3.56. The backbone is created using the maximum force, and its corresponding displacement, of each cycle. Note that the maximum force does not always correspond with the maximum displacement; therefore, the maximum drift seen on Figure 3.56 is 7.38%. Using the backbone curve, the initial stiffness of Precast 1 can be calculated from the slope of the curve prior to yield. The initial stiffness of Precast 1 is calculated to be 38.17 kip/in.

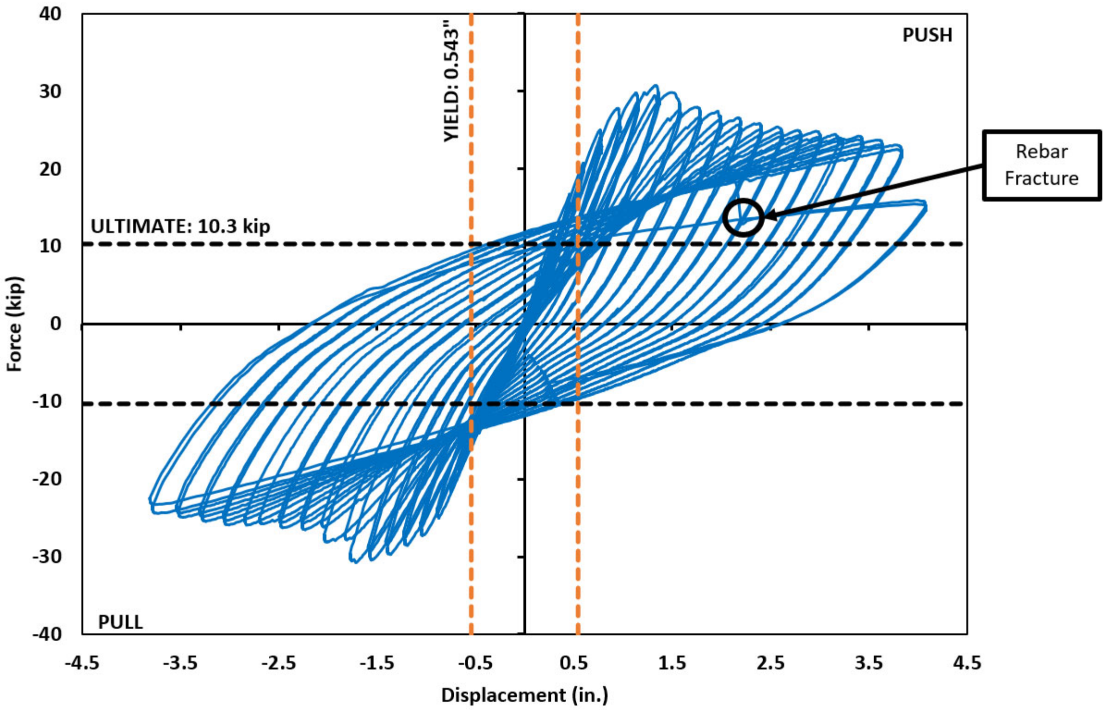

Figure 3.54 Precast 1 Force-Displacement Hysteresis

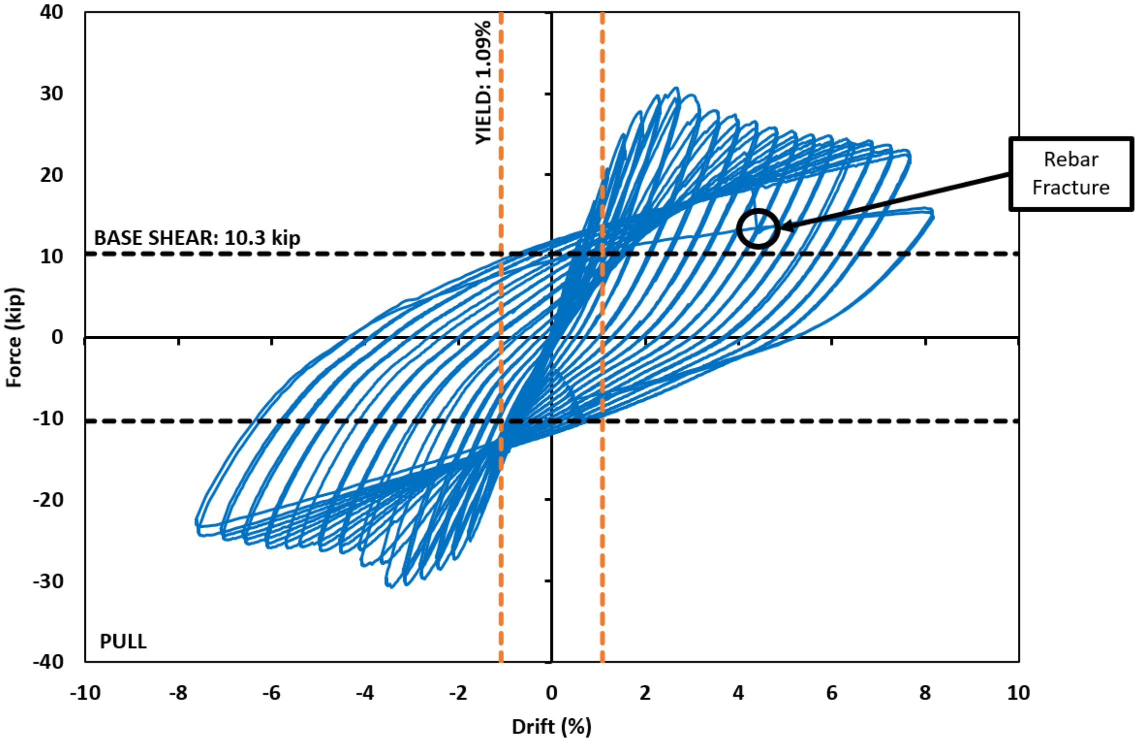

Figure 3.55 Precast 1 Force-Drift Hysteresis

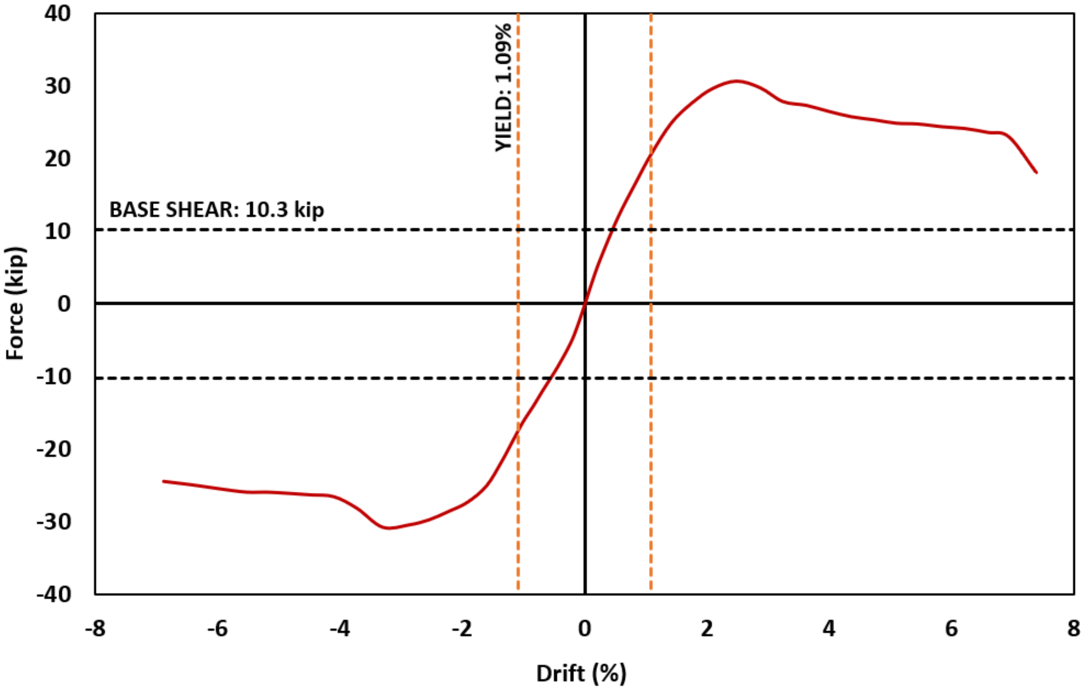

Figure 3.56 Precast 1 Force-Drift Backbone Curve

Instrumentation from testing is used to map the moment-curvature of Precast 1 (Figure 3.57). Similarly, the average gap opening of Precast 1 can also be mapped using the potentiometer data (Figure 3.58). The graph gives the average gap opening, along with the corresponding moment achieved during each cycle of testing. Figure 3.58 highlights the development of the plastic hinge in the column. As testing progresses, gap opening increases until the plastic hinge forms. After the plastic hinge begins to deform the column, the gap opening decreases. The maximum gap opening of Precast 1 was 0.0104 in. at a moment of 152.03 kip-ft.

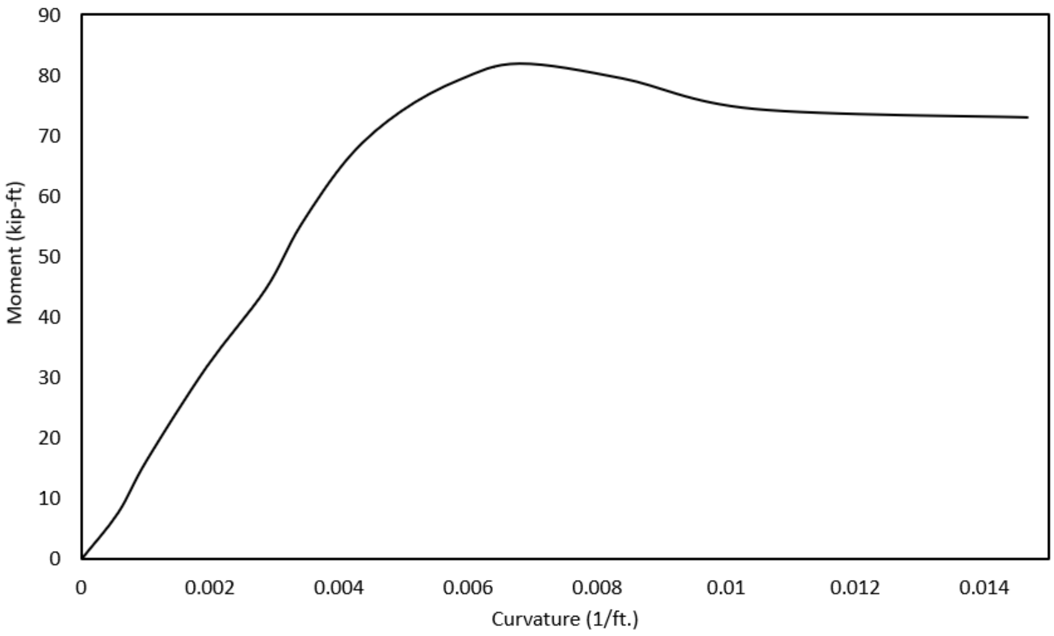

Figure 3.57 Precast 1 Moment-Curvature from the Plastic Hinge Location

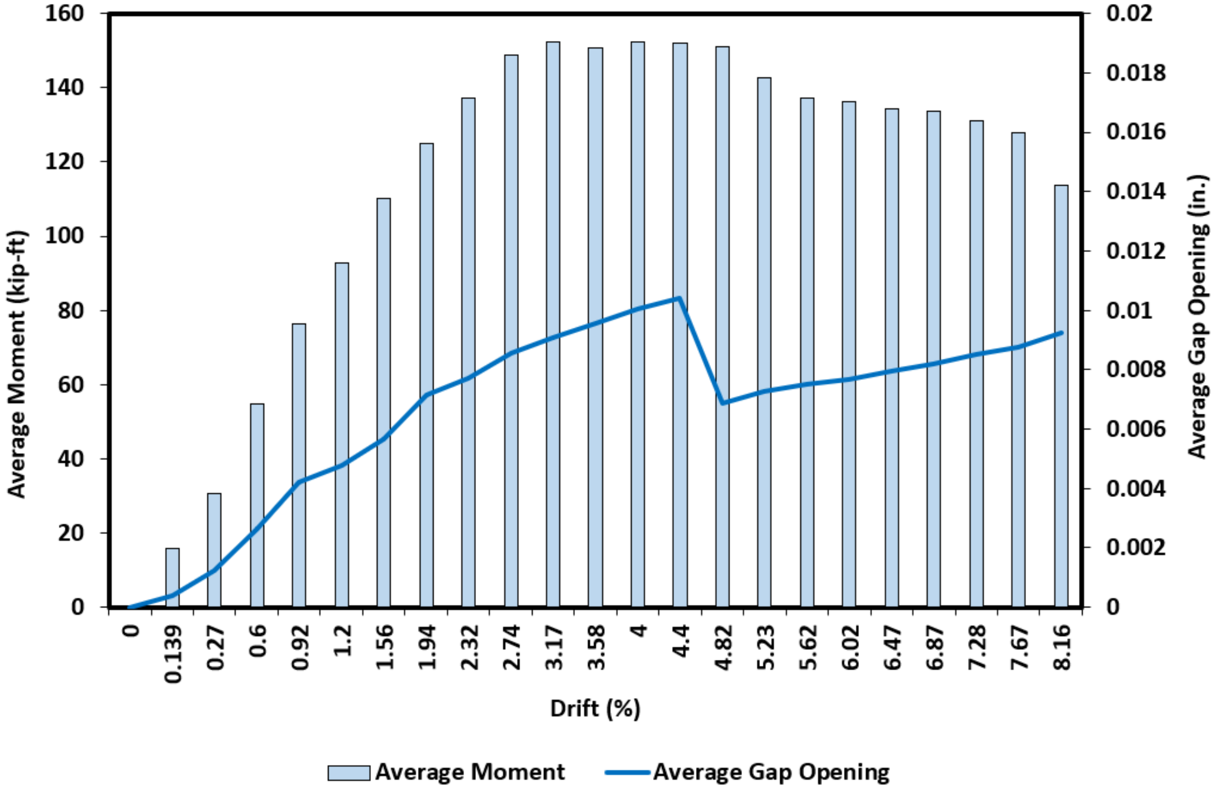

Figure 3.58 Precast 1 Average Moment and Gap Opening vs Column drift

The next step in processing results is to calculate the energy dissipation of Precast 1. The energy dissipation is calculated for each drift by approximating the area inside each hysteresis loop of the force-displacement hysteresis. The area in each loop is calculated using a program built in MATLAB. The results can be seen in Figure 3.59. The graph shows the energy dissipated during the first and second cycle of each drift. Figure 3.59 also shows the cumulative dissipated energy after each drift. Precast 1 was able to dissipate a total of 216.51 kJ.

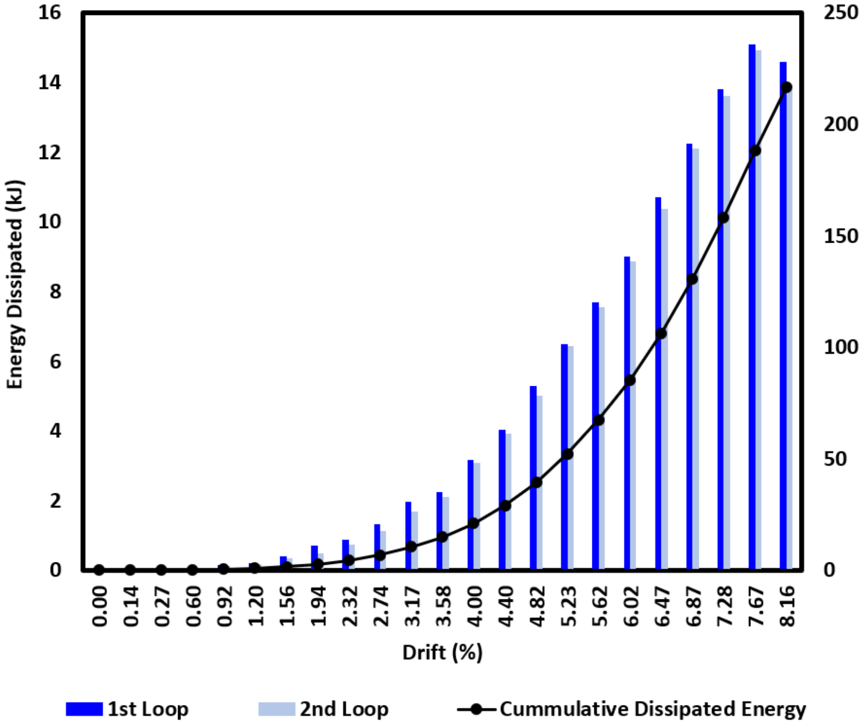

Figure 3.59 Precast 1 Dissipated Energy

Further analysis of the experimental results allows the determination of the overstrength factor (Ω_0). The overstrength factor is calculated using the following equation:

$$\Omega_0 = \frac{V_{ultimate}}{V_{yield}}$$

Where:

$V_{ultimate}$ = Base shear at the ultimate capacity of the column, in kips
V_y = Base shear at the initial yield of the column, in kips

Using the equation, the overstrength factor is calculated to be 2.21. Similarly, the displacement ductility for ultimate (μ_u) and failure (μ_f) can be calculated using the following equations:

$$\mu_u = \frac{\Delta_u}{\Delta_y}$$

$$\mu_f = \frac{\Delta_{0.8V_u}}{\Delta_y}$$

Where:

Δ_u = Displacement at the ultimate base shear of the column, in inches
$\Delta_{0.8Vu}$ = Displacement after 20% degradation of the ultimate base shear (i.e. $0.8V_u$), in inches
Δ_y = Displacement at global yield of the column, in inches

From the equations, the ultimate displacement ductility is calculated to be 2.28, and the failure displacement ductility is calculated to be 5.39.

Summary

Precast 1 is retrofitted to determine the ability of UHPC jacketing as a retrofit method for ABC connections, like the ITD connection. The retrofit is designed using SAP2000 modeling capabilities to design the thickness of the jacket. Precast 1 is rehabilitated in the SLAB, instrumented, and then tested under quasi-static, cycling loading. The loading protocol is based off of the original protocol used during Phase I (ITD Report 281, 2021). Testing results showed that Precast 1 performed excellently. Precast 1 was able to achieve, and go beyond the original experimental moment capacity of the connection (124.5 kip-ft), achieving an overall moment capacity of 164.05 kip-ft. The maximum force experienced by Precast 1 is 30.74 kip. The stiffness calculated from testing is 38.17 kip/in. Precast 1 was able to achieve a 0.543 yield displacement and a 1.239 ultimate displacement. Precast 1 saw no gap opening at the jacket-to-footing interface. On top of this, the UHPC jacket saw negligible damage. The only damage seen on the jacket is the cold joint crack, which did not develop. Precast 1 is able to dissipate 216.51 kJ of energy, while achieving an overstrength factor of 2.21, an ultimate displacement ductility of 2.28, and a failure displacement ductility of 5.39.

Precast 2 Retrofit

Introduction

This section presents the design, construction, and testing of a precast column retrofit with UHPC to compare with the previous retrofitted column (Precast 1). A review of the construction process is presented, for Precast 2. The testing arrangement, instrumentation, and experimental results for Precast 2 are also discussed.

Design

Precast 2 is designed using a computer modeling program, SAP2000, to determine the expected moment capacity of the retrofit. The goal is to bring the original column from the precast bent back to its original moment capacity and push the plastic hinge up the face of the column, above the jacket. The moment yield capacity (M_y) of the original column is 117.89 kip-ft, the plastic moment (M_p) of the original column is 168.3 kip-ft. During testing of the precast bent, the pipe connecting the column to the footing fractured. Therefore, in the design process, the moment capacity contribution from the pipe is negligible, to be conservative. Furthermore, the cover concrete around the base of the pipe spalled, therefore the entire section, excluding the pipe, is taken to be UHPC for the retrofit.

The retrofit is designed using moment-curvature analysis of the cross section. The moment-curvature analysis is performed in SAP2000, an axial load is placed on the column of 30 kip, to correspond to the 5% gravity load of the bent specimen during testing. Precast 2 is designed without dowels. The purpose of not including the dowels is to see if they are necessary in a retrofit design. Since the dowels are the main variable between Precast 1 and Precast 2, the jacket thickness is decided to be kept the same, with a value of 4 in. The model placed into SAP2000 of the original precast pier cross section, the Precast 1 retrofit, and the Precast 2 retrofit are shown in Figure 3.60. The model is checked against the original pier cross-section to ensure that the Precast 2 retrofit has a strong enough moment capacity. The results from the SAP2000 model are shown in Figure 3.61 and Table 3.20. The results show that a jacket of 4.0 in. thickness would be sufficient.

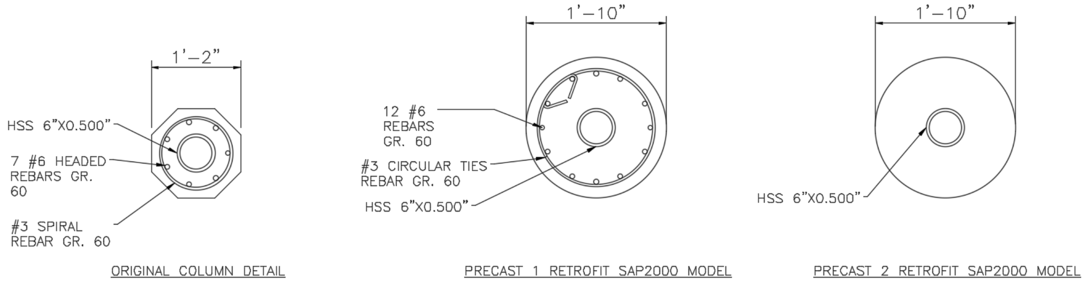

Figure 3.60 Original Pier, Precast 1, and Precast 2 SAP2000 Cross-Sections

Table 3.20 Moment-Curvature Analysis of Precast 1 Retrofit

Jacket Thickness (in.)	Moment Yield Capacity, M_y (kip-ft)	Plastic Moment, M_p (kip-ft)
3.0	258.50	300.88
3.5	282.83	319.95
4.0	307.56	338.94
Original Precast Pier	114.37	166.12
Precast 1	185.16	300.34

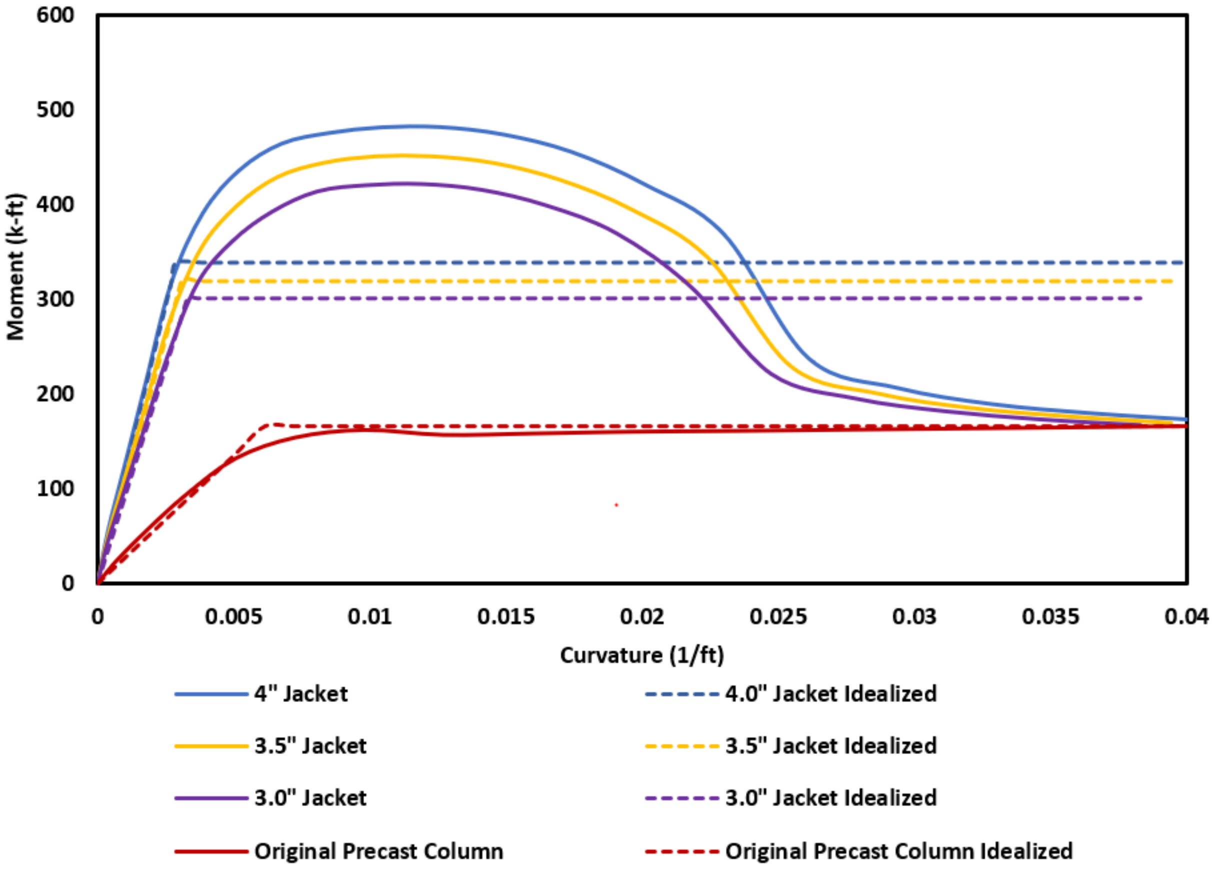

Figure 3.61 Moment-Curvature Analysis of Precast 1 Retrofit

The height of the jacket is to be equivalent to Precast 1 jacket height (14 in.). The overall design for Precast 2 is shown in Figure 3.62.

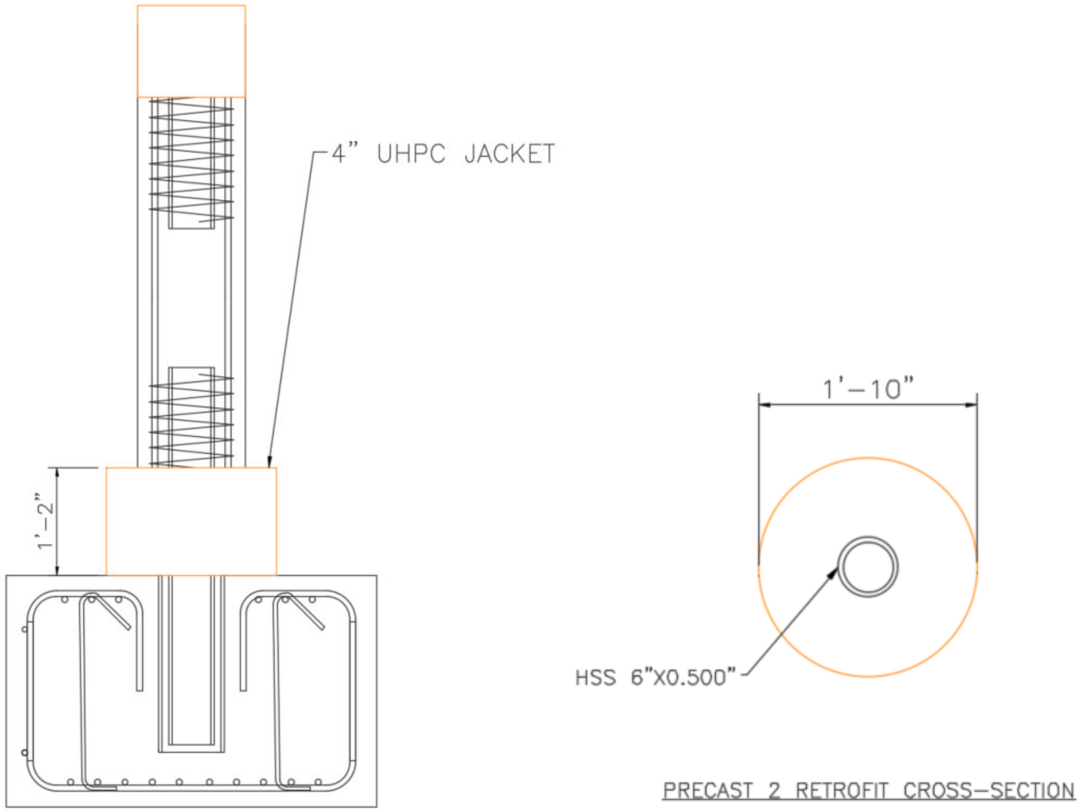

Figure 3.62 Precast 2 Retrofit Detail

Construction

The construction process for Precast 2 follows the same steps as Precast 1, with the exception of the dowels and stirrups. The surface of Precast 2 is roughened and the formwork is mounted for the jacket. The form work is the same formwork used for Precast 1.

Precast 2 is poured under a 30-kip gravity load to simulate the load of the superstructure. Precast 2 is allowed to cure for72 hours under the gravity load. After 72 hours the load is removed and the formwork is removed. High-strength grout is used for cosmetic patching between the column and jacket. The jacket is then cured for 28 days. After the jacket is cured, it is painted and marked with a 1 in. grid for monitoring of cracks.

Testing Arrangement

The testing arrangement of Precast 2 is the exact same as Precast 1. There are no changes made between the two set-ups. Precast 2 is placed under a gravity load of 30 kip, while lateral loading is applied using the hydraulic actuator.

Instrumentation

To make comparisons between data of Precast 1 and Precast 2, the instrumentation set up used for Precast 2 is the exact same as the set up used for Precast 1.

Loading Protocol

Similarly, the loading protocol is kept consistent with Precast 1 through testing of Precast 2.

Testing Results

Starting the test at $0.5\Delta_y$, no cracks appeared. Hairline began to surface on the east and west face of the column during the Δ_y cycle. Hairline cracking continued to spread through the $2\Delta_y$ cycle. During the $2\Delta_y$ cycle, lifting at the base of the jacket was observed, resulting in a hairline crack around the entire base of the jacket. After the $3\Delta_y$ cycle, the crack at the base of the jacket had opened to 0.05 in. (Figure 3.63).

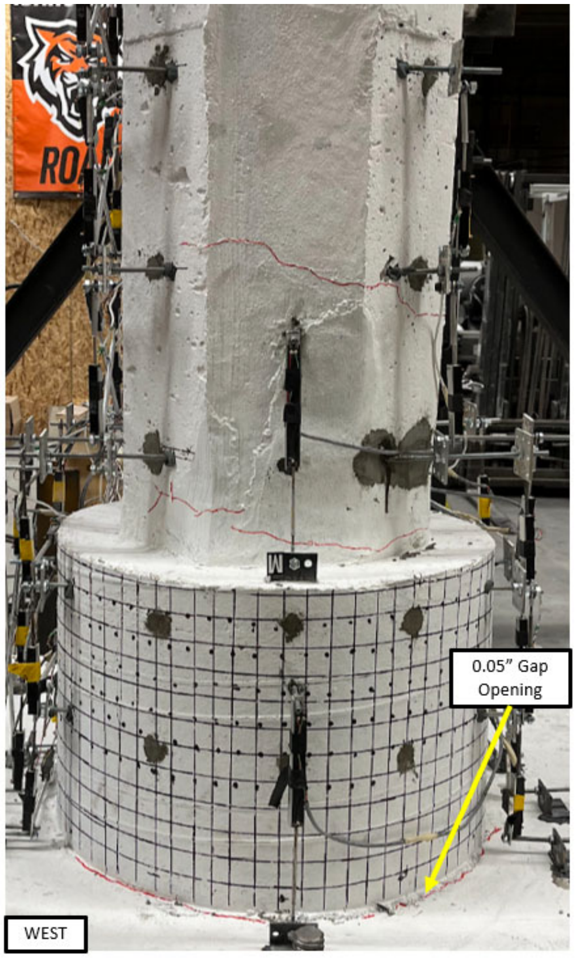

Figure 3.63 Precast 2 after Cycle $3\Delta_y$

As testing continued, no more cracks appeared on the jacket, however the gap opening continued to grow in size. After cycle 5Δ_y, the gap opening was 0.07 in. on the east face, and 0.08 in. on the west face. At this time, the hairline cracks above the jacket continued to propagate and grow in size. By cycle 7Δ_y the largest crack above the jacket was 0.02 in. on both the east and west faces of the column. As testing continued, spalling began to occur after the 14Δ_y cycle on the west face of the column (Figure 3.64). The spalling was due to the high-strength grout patch detaching from the original concrete of the pier. At this time, rebar from the spiral of the column was also exposed on the west face.

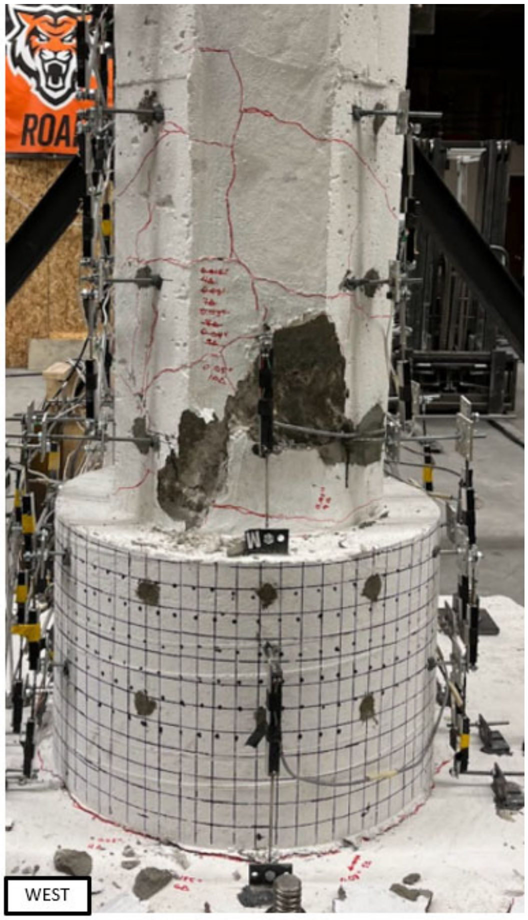

Figure 3.64 Precast 2 after Cycle 14Δ_y

As testing continued, the gap opening at the jacket-to-footing interface continued to grow, as the plastic hinge continued to form above the jacket. By cycle 16Δ_y, spalling had continued on the west face of the column, leading to an exposed longitudinal bar in cycle 19Δ_y. Spalling began on the east face during cycle 19Δ_y, leading to exposed stirrups on the east face. After cycle 20Δ_y longitudinal rebar was visible on both the east and west face of the column (Figure 3.65). The gap opening peaked at a value of 0.596 in. in the 18Δ_y cycle (Figure 3.66). As the plastic hinge continued to deteriorate the gap opening did not increase in size. By 22Δ_y the gap opening extended approximately 6 in. into the column on both faces. The core of the column continued to crush on both faces, eventually leading to longitudinal bars buckling on the east face, which resulted in two longitudinal bars fracturing in cycle 25Δ_y (Figure 3.67).

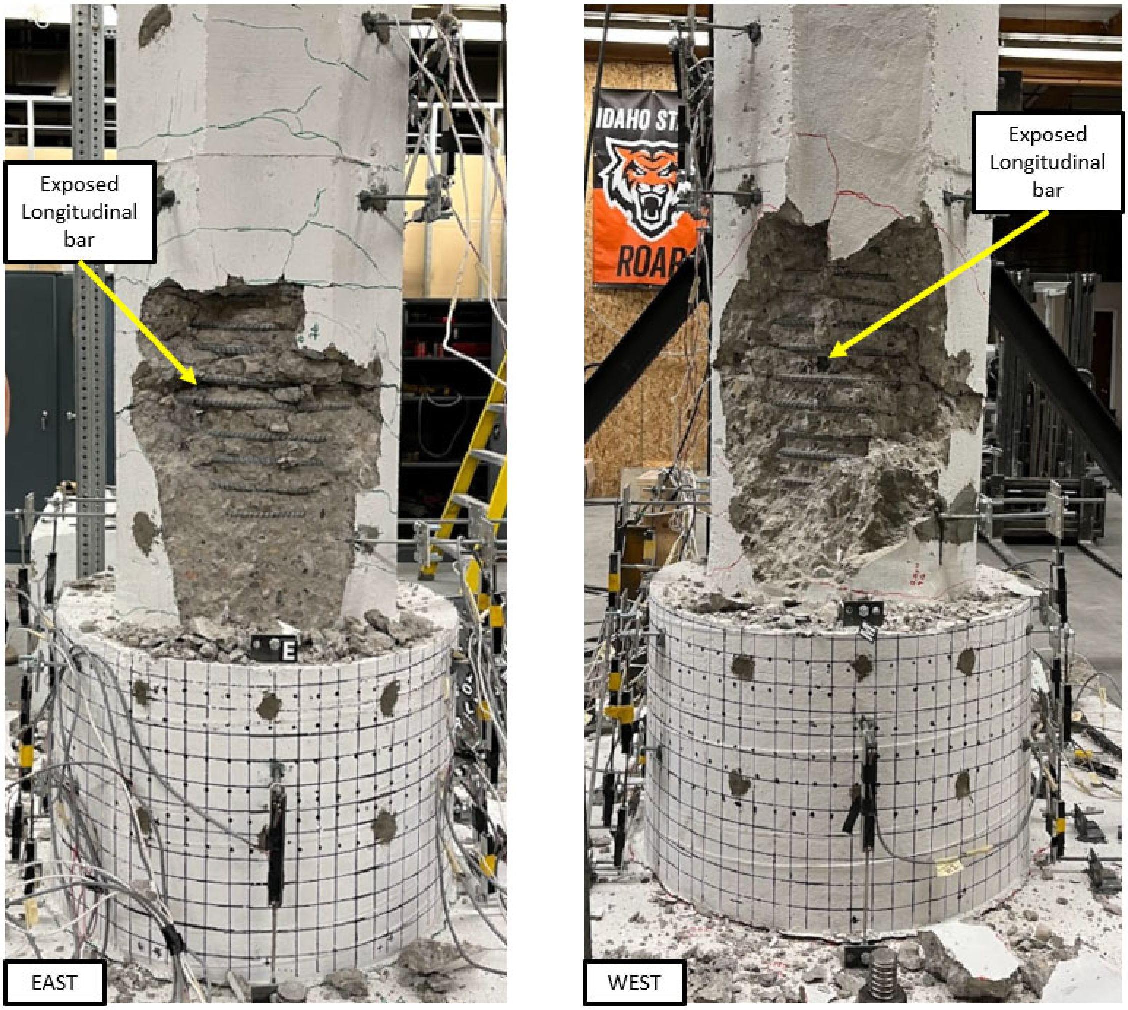

Figure 3.65 Precast 2 after Cycle 20Δ_y

Figure 3.66 Precast 2 Maximum gap Opening at Cycle 18Δ_y

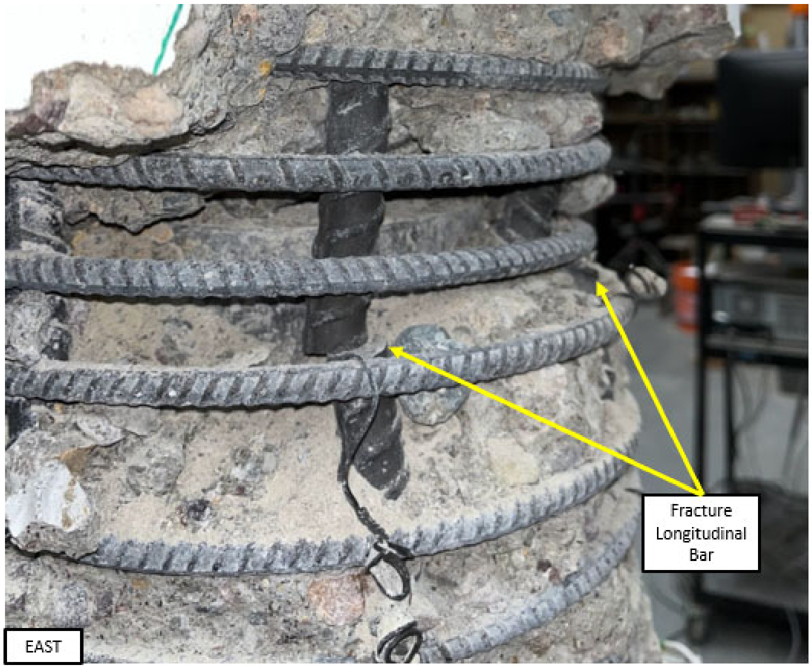

Figure 3.67 Precast 2 Fractured Rebar

Precast 2 experienced significant uplift in the jacket-to-footing interface. However, the Precast 2 retrofit was successful in pushing the plastic hinge of the column above the jacket. An overall image of Precast 2 after failure can been seen in Figure 3.68.

Figure 3.68 Precast 2 Post-Test

The programmed vs actual achieved displacements and drift are summarized in Table 3.21. From here on out, in this section, each cycle will be referred to as its correlating actual drift value.

Table 3.21 Precast 2 Loading Protocol Summary

Cycle	Programmed Displacement (in.)	Programmed Drift (%)	Actual Displacement (in.)	Actual Drift (%)
$0.5\Delta_y$	0.10	0.196	0.10	0.195
Δ_y	0.20	0.392	0.18	0.365
$2\Delta_y$	0.39	0.784	0.32	0.634
$3\Delta_y$	0.59	1.177	0.43	0.859
$4\Delta_y$	0.78	1.569	0.56	1.129
$5\Delta_y$	0.98	1.961	0.71	1.424
$6\Delta_y$	1.18	2.353	0.87	1.730
$7\Delta_y$	1.37	2.746	1.05	2.098
$8\Delta_y$	1.57	3.138	1.22	2.446
$9\Delta_y$	1.77	3.530	1.41	2.810
$10\Delta_y$	1.96	3.922	1.58	3.163
$11\Delta_y$	2.16	4.315	1.77	3.540
$12\Delta_y$	2.35	4.707	1.95	3.892
$13\Delta_y$	2.55	5.099	2.13	4.257
$14\Delta_y$	2.75	5.491	2.32	4.648
$15\Delta_y$	2.94	5.883	2.51	5.019
$16\Delta_y$	3.14	6.276	2.71	5.416
$17\Delta_y$	3.33	6.668	2.89	5.781
$18\Delta_y$	3.53	7.060	3.10	6.205
$19\Delta_y$	3.73	7.452	3.32	6.643
$20\Delta_y$	3.92	7.845	3.55	7.109
$21\Delta_y$	4.12	8.237	3.76	7.523
$22\Delta_y$	4.31	8.629	3.98	7.968
$23\Delta_y$	4.51	9.021	4.19	8.377

Cycle	Programmed Displacement (in.)	Programmed Drift (%)	Actual Displacement (in.)	Actual Drift (%)
$24\Delta_y$	4.71	9.414	4.42	8.843
$25\Delta_y$	4.90	9.806	4.69	9.379

*Note drift is calculated from the top of the jacket, i.e. Drift (%) = (Displacement/50 in.)*100

The ultimate displacement achieved during testing was 4.69 in. (9.38% drift), while the ultimate force achieved was 30.65 kip. The ultimate lateral load correlates to a total moment capacity of 163.47 kip-ft, which exceeds the theoretical design column moment capacity of 56.7 kip-ft.

Using Bilinear approximation, the yield force (F_y) and yield displacement (δ_y) are determined for Precast 2. The method used is the same method used for Precast 1.

Using the method, the following equations are determined for segment OB and segment BC:

$$\overline{OB}:\ y = 26.89x$$
$$\overline{BC}:\ y = 8.280x + 13.586$$

The experimental data is placed into an EXCEL file and a quartic regression is used to determine the best suitable equation for the experimental data. Note that a quartic function fit the data better than a quadratic function for Precast 2. The following equation is determined:

$$Experimental:\quad y = -1.234x^4 + 8.233x^3 - 23.031x^2 + 39.091x - 1.572$$

Using the equations in the previous section, S_1 is calculated to be 0.58449 and S_2 is calculated to be 0.58375. When the constraint is applied, the difference calculated between S_2 and S_1 is 0.00074, which is approximately equivalent to zero. Therefore, the values in

Table 3.22 are calculated for the bilinear approximation. Similarly, Figure 3.69 shows the graph for the bilinear approximation of Precast 2.

Table 3.22 Bilinear Approximation Values Calculated for Precast 2

Parameter	Value
$\delta_{0.6Fy}$	0.438
δ_y	0.730
δ'_y	1.090
δ_u	2.061
$0.6F_y$	11.778
F_y	19.630
F'_y	22.600
F_u	30.645

*Where F'_y is the values corresponding to δ'_y

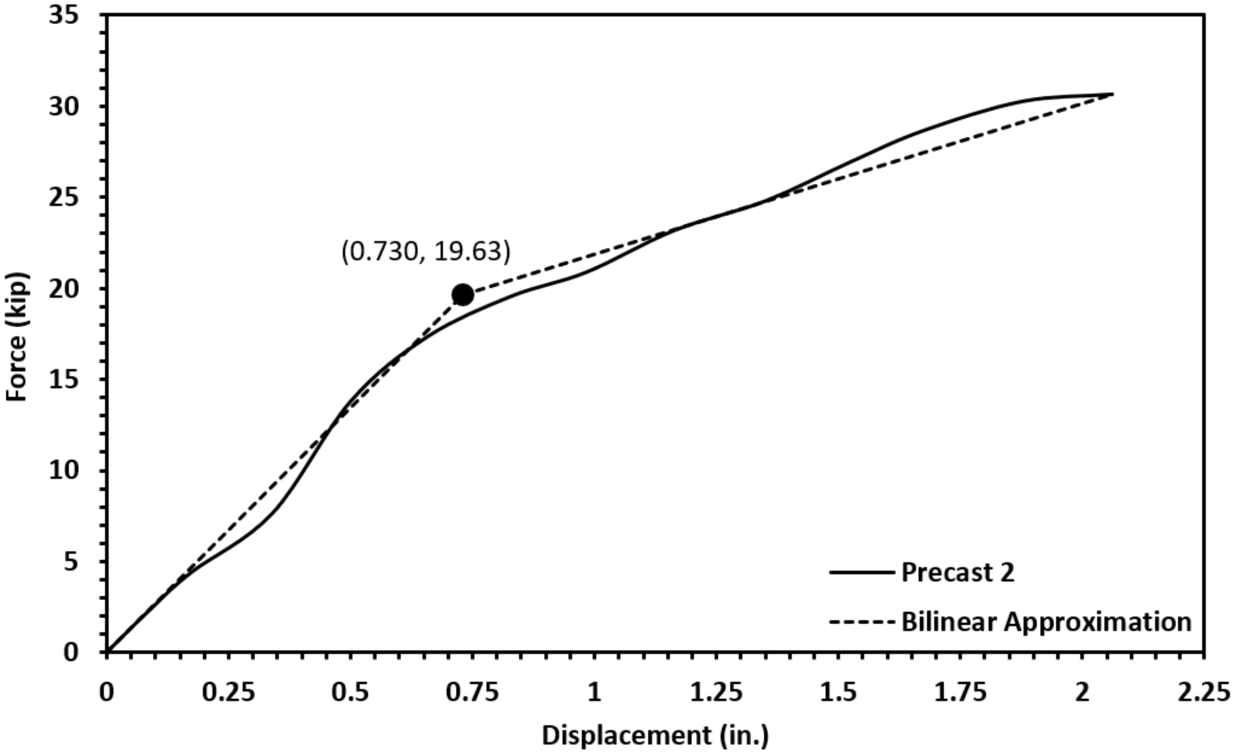

Figure 3.69 Bilinear Approximation of Precast 2

Furthermore, the hysteresis of Precast 2 is mapped in Figure 3.70 (force-displacement) and Figure 3.71 (force-drift). The yield displacement is marked on both graphs. The yield displacement of 0.730 in. correlates to a drift value of 1.46%. It can also be noted that Precast 2 surpassed the theoretical benchmark base shear of 10.3 kip, which is also noted on both graphs. Note, quadrant I for both figures signifies the is column in push, while quadrant III signifies the column is in pull. From observation of Figure 3.70 and Figure 3.71, Precast 2 had similar strength and displacement in both push and pull.

Figure 3.72 provides the force-drift backbone curve for Precast 2. The performance points for Precast 2 are also given in Figure 3.72. The backbone is created using the maximum force, and its corresponding displacement, of each cycle. Note that the maximum force does not always correspond with the maximum displacement; therefore, the maximum drift seen on Figure 3.72 is 8.73%. Using the backbone curve, the initial stiffness of Precast 2 can be calculated from the slope of the curve prior to yield. The initial stiffness of Precast 2 is calculated to be 23.60 kip/in.

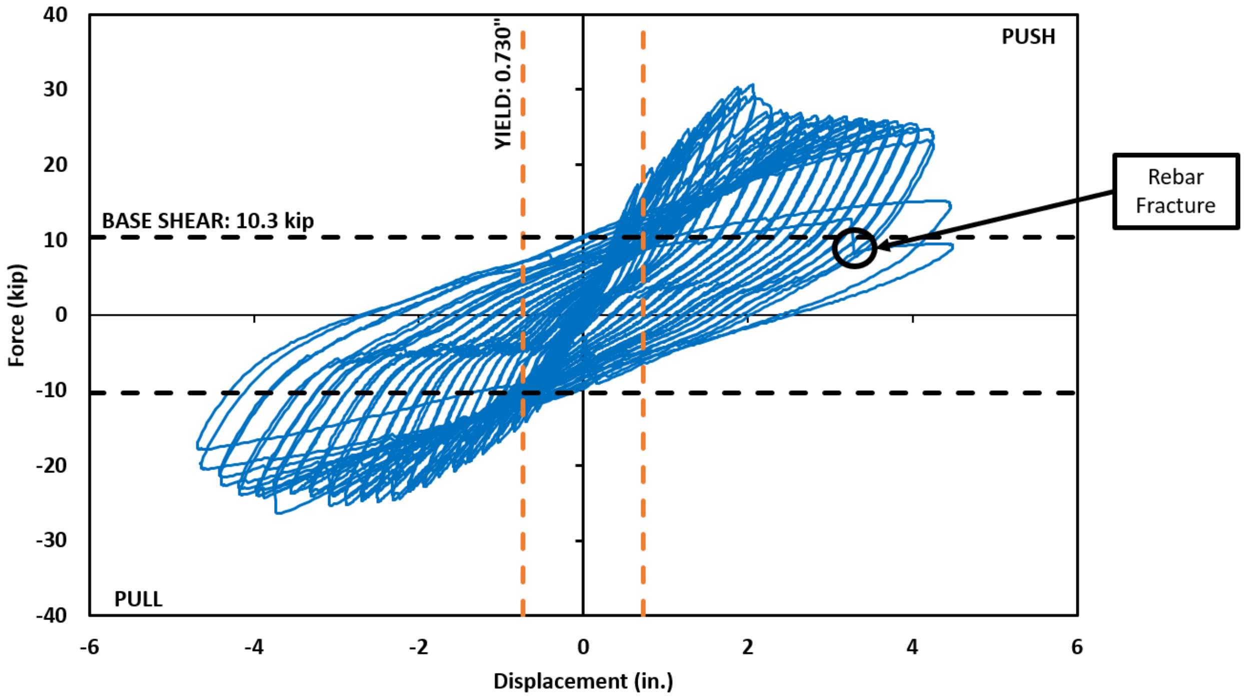

Figure 3.70 Precast 2 Force-Displacement Hysteresis

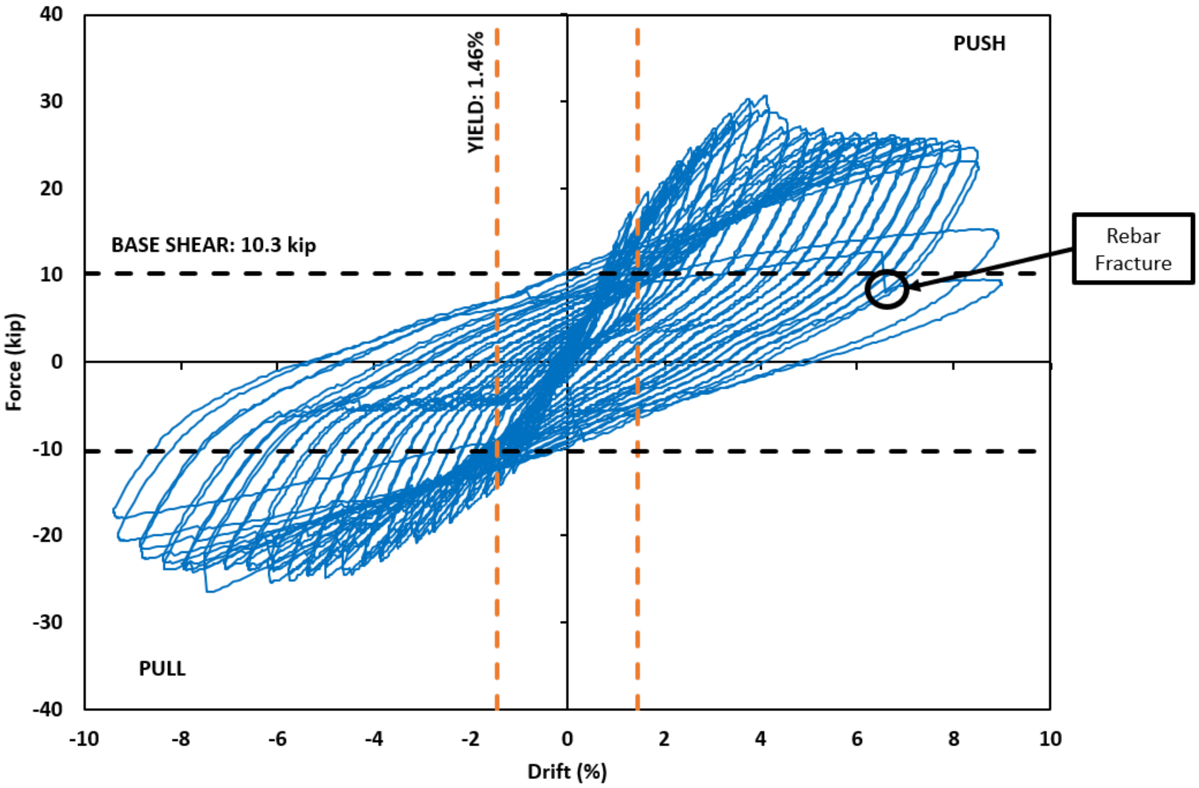

Figure 3.71 Precast 2 Force-Drift Hysteresis

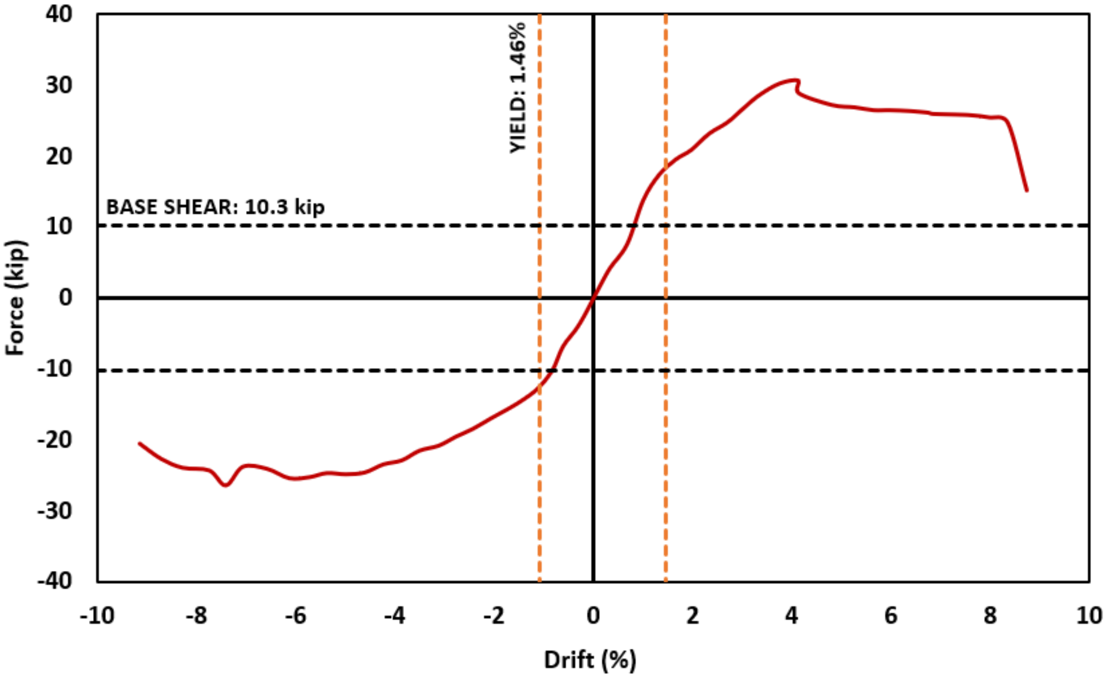

Figure 3.72 Precast 2 Force-Drift Backbone Curve

Instrumentation from testing is used to map the moment-curvature of Precast 2 (Figure 3.73). Note that the linear potentiometers had to be removed during the 12Δ_y cycle; therefore Figure 3.73 is mapped up to the 11Δ_y cycle.

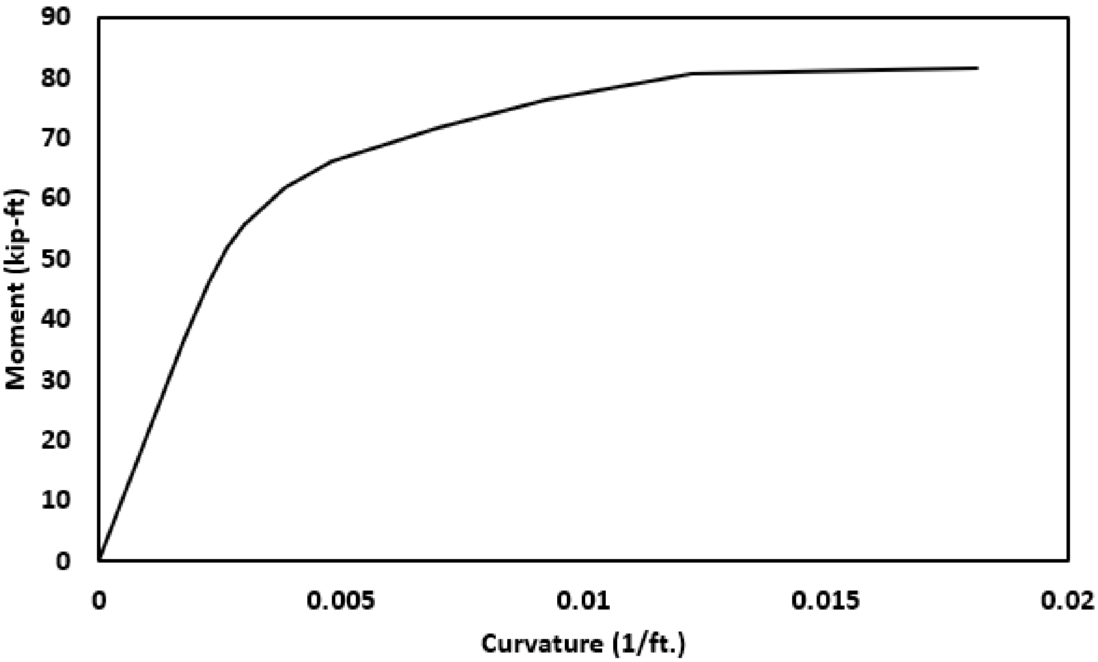

Figure 3.73 Precast 2 Moment-Curvature from the Plastic Hinge

Similarly, the average gap opening of Precast 2 can also be mapped using the potentiometer data (Figure 3.74). The graph gives the average gap opening, along with the corresponding moment achieved during each cycle of testing. Figure 3.74 highlights the development of the plastic hinge in the column. As testing progresses, gap opening increases until the plastic hinge forms. After the plastic hinge begins to deform the column, the gap opening decreases. The maximum gap opening of Precast 2 was 0.492 in. at a moment of 133.83 kip-ft.

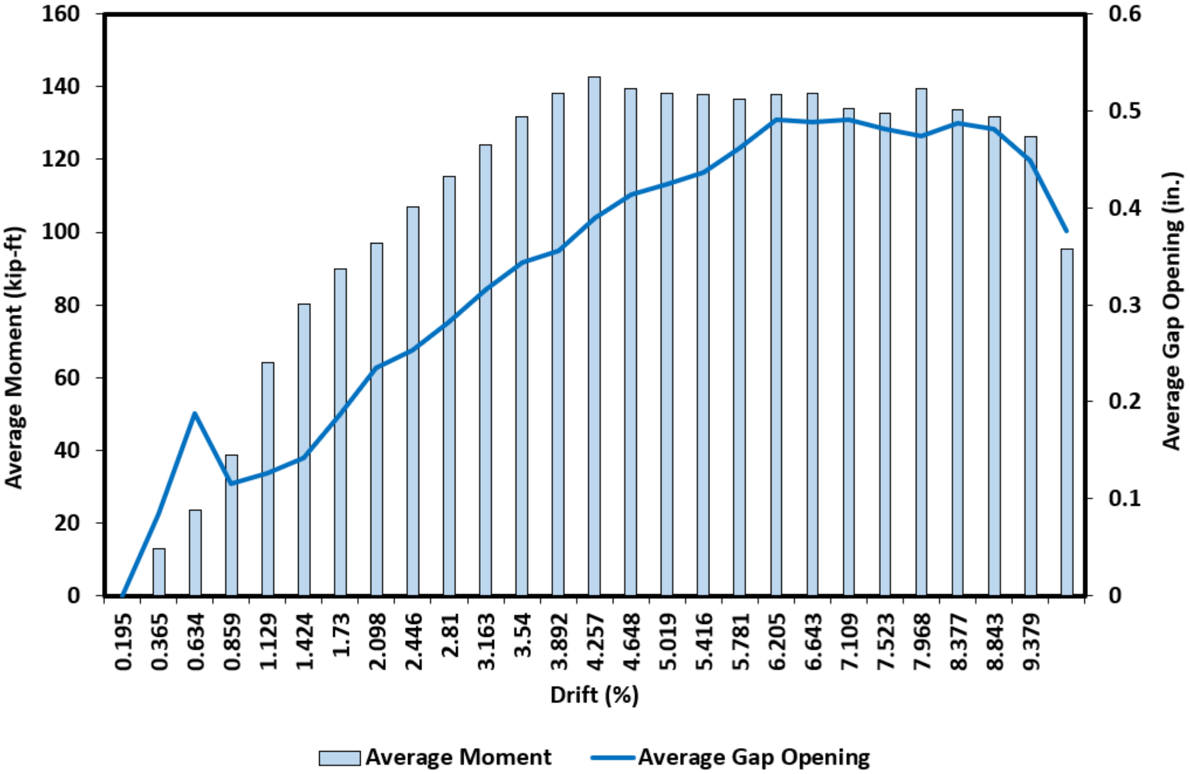

Figure 3.74 Precast 2 Average Moment and Gap Opening vs Drift

The next step in processing results is to calculate the energy dissipation of Precast 2. The energy dissipation is calculated using the same method used for Precast 1. The results can be seen in Figure 3.75. The graph shows the energy dissipated during the first and second cycle of each drift. Figure 3.75 also shows the cumulative dissipated energy after each drift. Precast 2 was able to dissipate a total of 262.70 kJ.

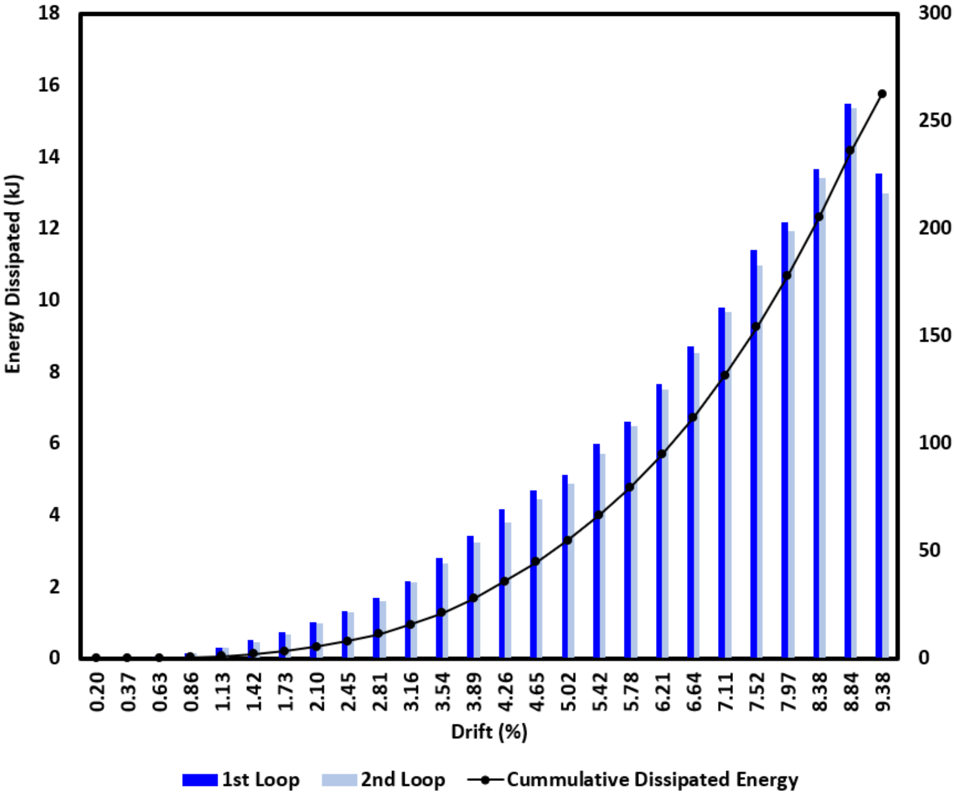

Figure 3.75 Precast 2 Dissipated Energy

Further analysis of the experimental results allows the determination of the overstrength factor (Ω_0), using the equation from the previous section, the overstrength factor is calculated to be 2.60. Similarly, the displacement ductility for ultimate (μ_u) and failure (μ_f) are calculated to be 2.82 and 5.72, respectively.

Summary

Precast 2 is retrofitted to determine the ability of UHPC jacketing as a retrofit method for ABC connections, like the ITD connection. The retrofit is designed using SAP2000 modeling capabilities to design the thickness of the jacket. Precast 2 is rehabilitated in the SLAB, instrumented, and then tested under quasi-static, cycling loading. The loading protocol is based off of the original protocol used during Phase I (ITD Report 281, 2021). Testing results showed that Precast 2 performed well. Precast 2 was able to achieve, and go beyond the original experimental moment capacity of the connection (124.5 kip-ft), achieving an overall moment capacity of 163.47 kip-ft. The maximum force experienced by Precast 2 is 30.65 kip. The stiffness calculated from testing is 23.60 kip/in. Precast 2 was able to achieve a 0.730 in. yield displacement and a 4.69 in. ultimate displacement. Precast 2 saw significant gap opening at the jacket-to-footing interface. Despite this, the UHPC jacket saw negligible damage. Precast 2 is able to dissipate 262.7- kJ of energy, while achieving an overstrength factor of 2.60, an ultimate displacement ductility of 2.82, and a failure displacement ductility of 5.72.

Precast Columns: Precast 1 Retrofit vs. Precast 2 Retrofit

Both precast column retrofits performed as expected and designed. Both retrofits utilized the same geometry and loading protocol. The difference between Precast 1 and Precast was the reinforcement in the jacketed section. Precast 1 had 12 no. 6 longitudinal bars that were anchored into the foundation, along with no. 3 circular hoops. Precast 2 had no reinforcing in the jacketed section. Despite the reinforcement, both retrofits exhibited similar capacity, and were successful at pushing the plastic hinge of the column above the termination of the pipe inside the columns.

Despite the success of both retrofits, Precast 2 debonded from the footing, which caused significant gap opening at the jacket-to-footing interface of Precast 2. To place the gap opening into perspective, Figure 3.76 shows the width of the gap over the span of the test for Precast 1 and Precast 2. As shown in Figure 3.76, Precast 1 (blue) exhibited negligible gap opening, while Precast 2 had a maximum opening of 0.492 in.

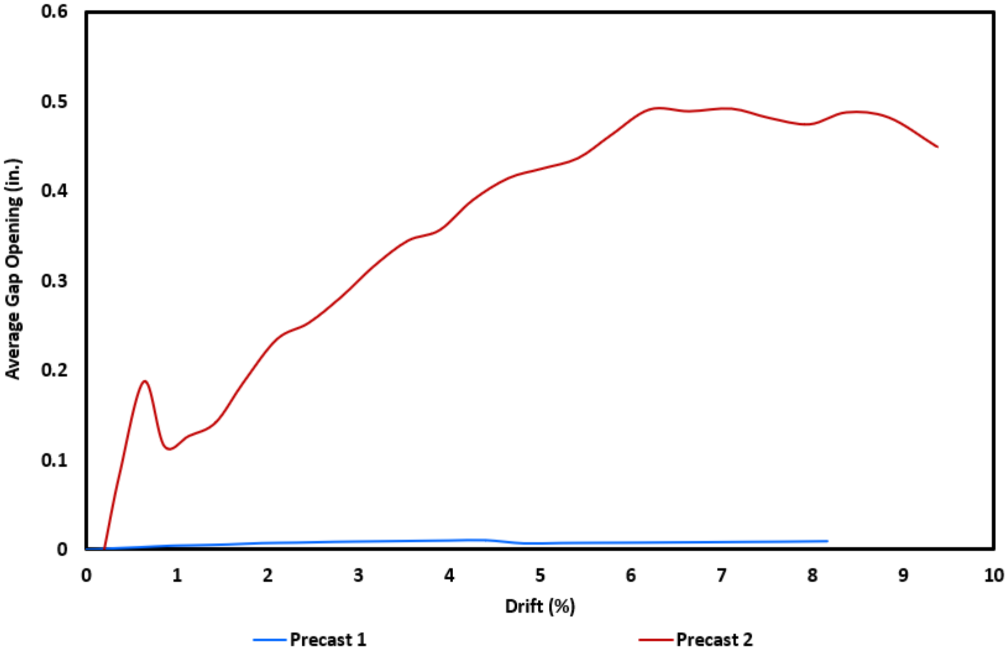

Figure 3.76 Average Gap Opening of Precast Columns

Furthermore, the lack of dowels allowed for Precast 2 to withstand more cycles, and therefore a higher drift value than Precast 1. Precast 2 had a maximum drift of 9.38%, while Precast 1 attained a maximum drift of 8.16%. Precast 2 had an increased drift ratio, but similar capacity to Precast 1, which reinforces the fact that Precast 2 is less stiff than Precast 1. Precast 1 had a stiffness of 38.17 kip/in, while Precast 2 only produced 23.60 kip/in, in stiffness. The difference in stiffness can be seen in the Backbone curves in Figure 3.77. Furthermore, a summary of the results from Precast 1 and Precast 2 can be seen in Table 3.23.

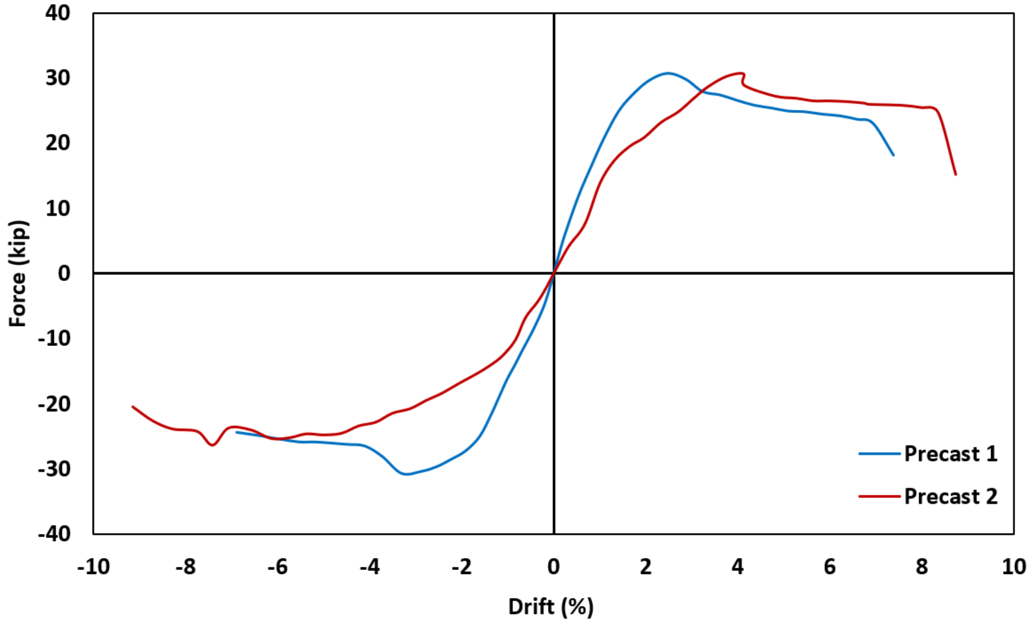

Figure 3.77 Precast Columns Backbone Curves

While both Precast 1 and Precast 2 achieved similar strength, Precast 1 exhibited a higher initial stiffness (40% more than Precast 2). Also, Precast 2 required more displacement to achieve the same strength as Precast 1. The lower stiffness and higher displacement of Precast 2 results in more gap opening at the jacket-to-footing interface. Due to higher displacement values, Precast 2 also experienced more energy dissipation. Despite the higher overall energy dissipation of Precast 2, Table 3.23 illustrates that at the same drift ratio, Precast 1 had higher energy dissipation. This means that Precast 2 was only able to achieve higher energy dissipation due to its larger displacement capacity.

Table 3.23 Precast Columns Results Summary

	Precast 1 (Dowels)	Precast 2 (No Dowels)
Maximum Force	30.76 kip	30.65 kip
Maximum Displacement	4.08 in. (8.16%)	4.69 in. (9.38%)
Moment Capacity	164.05 kip-ft	163.47 kip-ft
Initial Stiffness	38.17 kip/in.	23.60 kip/in.
Initial Yield	0.326 in. (0.65%)	0.438 in. (0.88%)
Global Yield (Bilinear Approximation)	0.543 in. (1.09%)	0.730 in. (1.46%)
Moment at Global Yield	96.63 kip-ft	81.79 kip-ft
Energy Dissipation	216.51 kJ	262.70 kJ (154.1 kJ)*
Overstrength Factor	2.21	2.60
Displacement Ductility (Ultimate Base Shear)	2.28	2.82
Displacement Ductility (Failure Point)	5.39	5.72

*Precast 2 Cumulative Dissipated Energy at Failure of Precast 1

Cast-in-Place 1 Retrofit

Introduction

This section presents the design, construction, and testing of a CIP column retrofit with UHPC with the intention of establishing a performance level in which to compare to the other retrofit method for a CIP column. A review of the construction process is presented. The full testing arrangement used for the experimental work is presented, followed by the experimental testing carried out and its resulting performance.

Design

CIP 1 is designed using SAP2000 to determine the expected moment capacity of the retrofit. The goal is to bring the original column from the CIP bent back to its original moment capacity and push the plastic hinge up the face of the column, above the jacket. The moment yield capacity (M_y) of the original column is 55.79 kip-ft, the plastic moment (M_p) of the original column is 81.84 kip-ft. During testing of the CIP bent, one of the longitudinal bars fractured. Therefore, in the design process, CIP 1 is modeled with 6 longitudinal bars.

The retrofit is designed using moment-curvature analysis of the cross section. The moment-curvature analysis is performed in SAP2000, an axial load is placed on the column of 30 kip, to correspond to the 5% gravity load of the bent specimen during testing. CIP 1 is designed without dowels and caging. The purpose of not including the dowels is to see if they are necessary in a retrofit design for a CIP column. The model placed into SAP2000 of the original CIP pier cross section and the CIP 1 retrofit are shown in Figure 3.78.

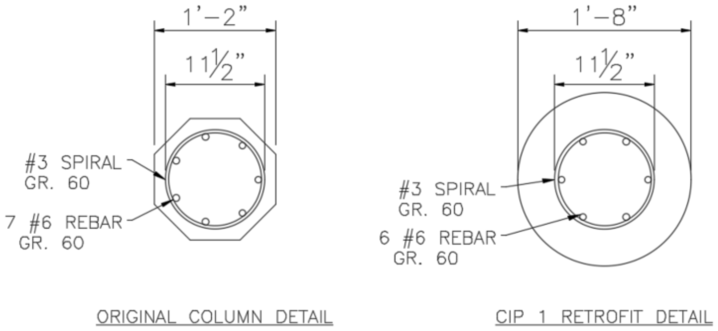

ORIGINAL COLUMN DETAIL

CIP 1 RETROFIT DETAIL

Figure 3.78 Original CIP Pier and CIP 1 Retrofit 2 SAP2000 Cross-Sections

The model is checked against the original pier cross-section to ensure that the CIP 1 retrofit has a strong enough moment capacity. Furthermore, different jacket sizes are analyzed to see with size will work best for CIP 1. The results from the SAP2000 model are shown in Figure 3.79 and Table 3.24. The results show that a jacket of 3.0 in. thickness would be sufficient. The height of the jacket is to be equivalent to Precast 1 jacket height (14 in.). The overall design for CIP 1 is shown in Figure 3.80.

Table 3.24 Moment-Curvature Analysis of CIP 1 Retrofit

Jacket Thickness (in.)	Moment Yield Capacity, M_y (kip-ft)	Plastic Moment, M_p (kip-ft)
3.0	89.83	116.71
3.5	95.03	124.01
4.0	100.44	128.26
Original CIP Pier	55.79	81.84
CIP 1	89.83	116.71

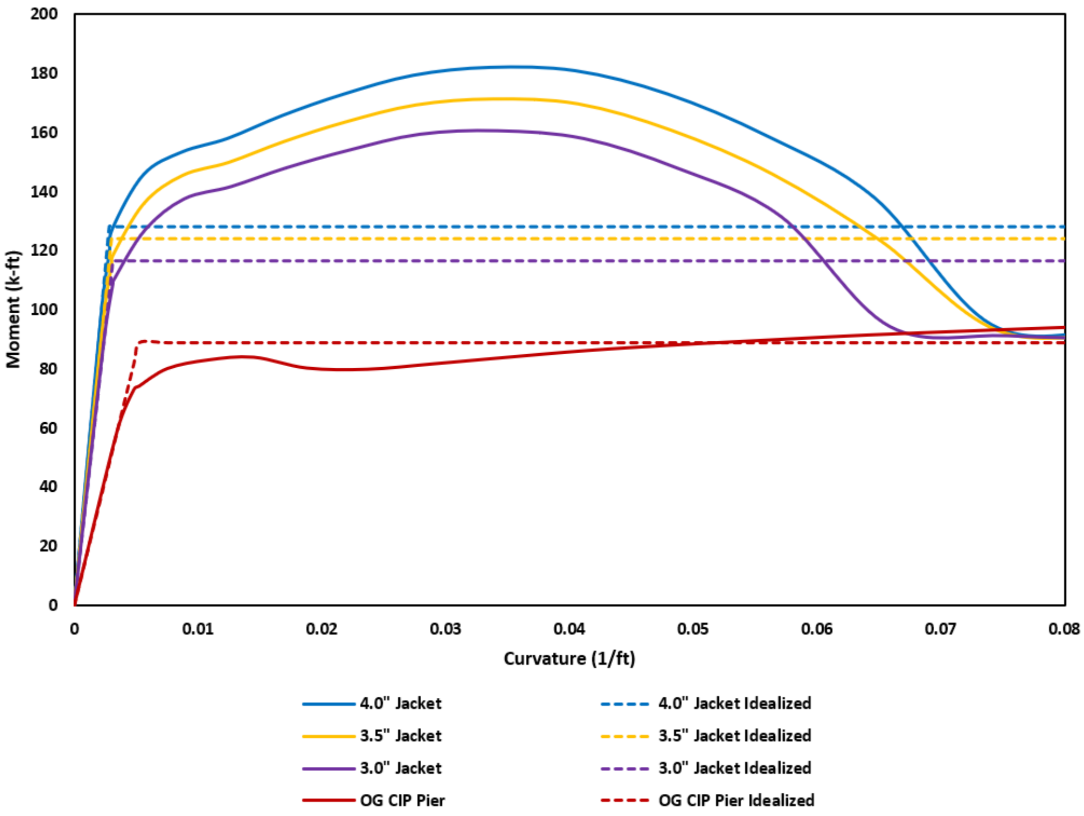

Figure 3.79 Moment-Curvature Analysis of CIP 1 Retrofit

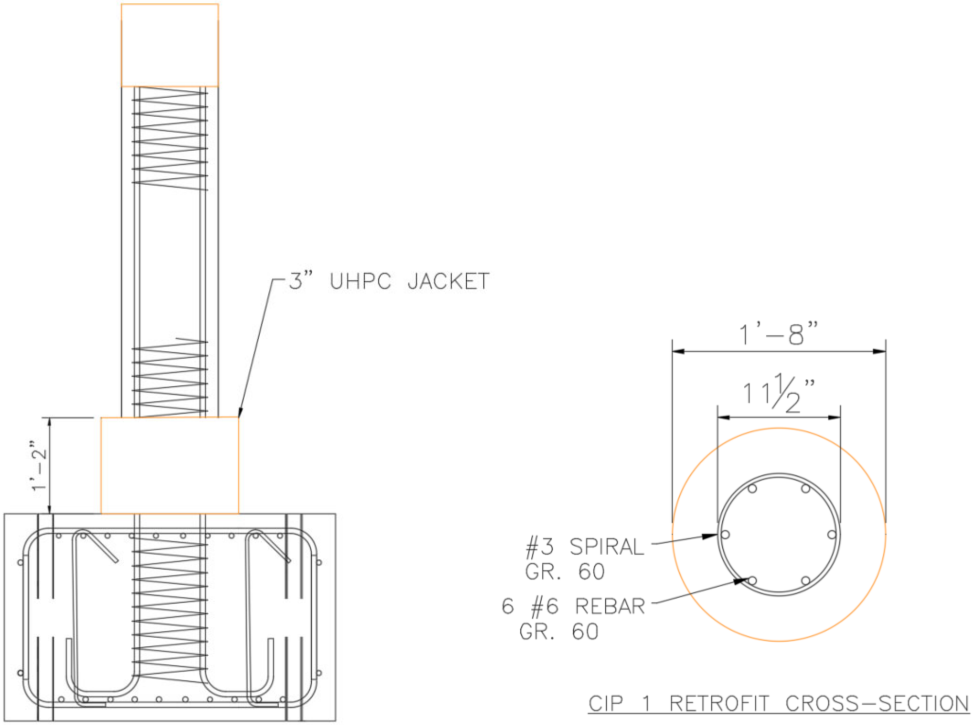

Figure 3.80 CIP 1 Retrofit Details

Construction

The construction process for CIP 1 follows the same steps as Precast 2. The surface of CIP 1 is roughened and the formwork is mounted for the jacket. The form work is Sonotube that has been cut to a 20 in. diameter.

CIP 1 is poured under a 30-kip gravity load to simulate the load of the superstructure. CIP 1 is allowed to cure for 72 hours under the gravity load. After 72 hours the load is removed and the formwork is removed. High-strength grout is used for cosmetic patching between the column and jacket. The jacket is then cured for 28 days. After the jacket is cured, it is painted and marked with a 1 in. grid for monitoring of cracks.

Testing Arrangement

The testing arrangement of CIP 1 is the exact same as Precast 1 and Precast 2. There are no changes made between the two set-ups. CIP 1 is placed under a gravity load of 30 kip, while lateral loading is applied using the hydraulic actuator.

Instrumentation

For ease of test set-up, the instrumentation set up used for CIP 1 is the exact same as the set up used for Precast 1 and Precast 2.

Loading Protocol

Similarly, the loading protocol is kept consistent for testing of CIP 1, as the jacket and columns are the same height.

Testing Results

Starting the test at $0.5\Delta_y$, no cracks appeared. Hairline began to surface on the east and west face of the column during the $2\Delta_y$ cycle. Hairline cracking continued to spread through the $5\Delta_y$ cycle. Negligible gap opening was witnessed at this time. The largest cracks in the column were visible directly above the jacket. During the $6\Delta_y$ the cracks on the east and west faces measured 0.04 in. (Figure 3.81).

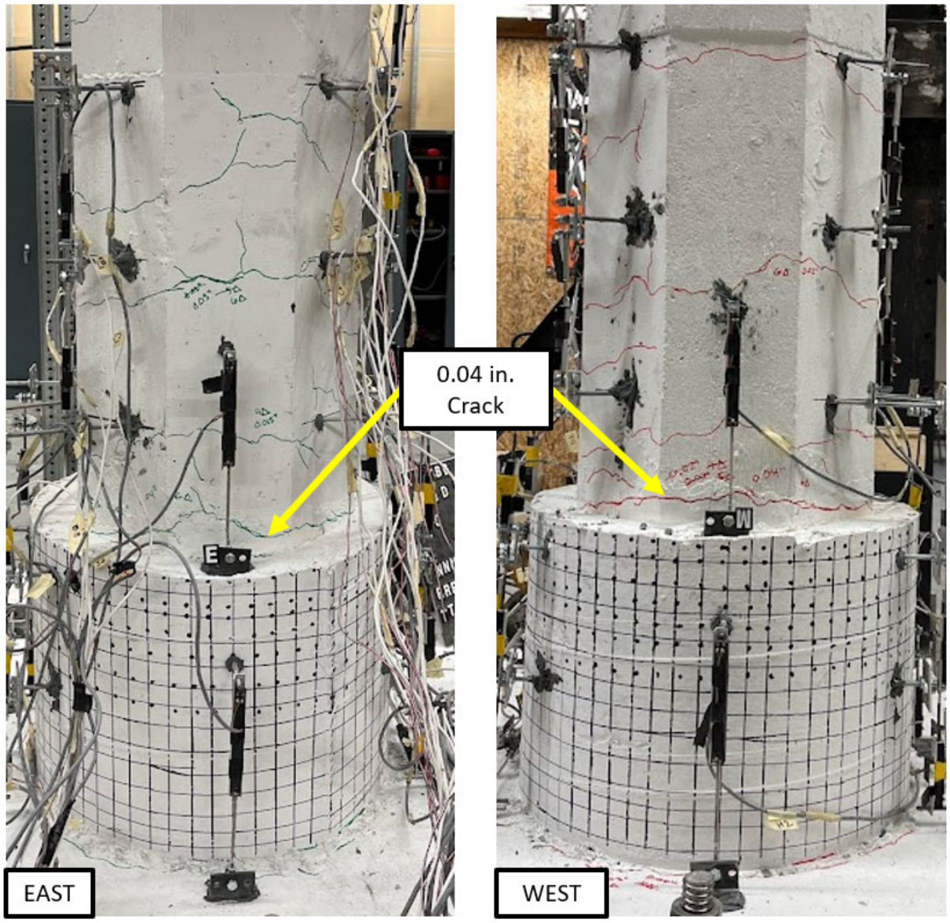

Figure 3.81 CIP 1 after Cycle $6\Delta_y$

As testing continued spalling began to occur above the jacket during the 8Δ_y cycle. Even though gap opening was minimal up until this time, after the 10Δ_y cycle the gap opening at the jacket-to-footing interface was measured to be 0.06 in. As testing continued, spalling of the column continued above the jacket. By the 15Δ_y cycle stirrups were exposed on both the east and west face of the column. Longitudinal bar was exposed on the west face by 16Δ_y and on the east face by 19Δ_y, Figure 3.82 and Figure 3.83 respectively.

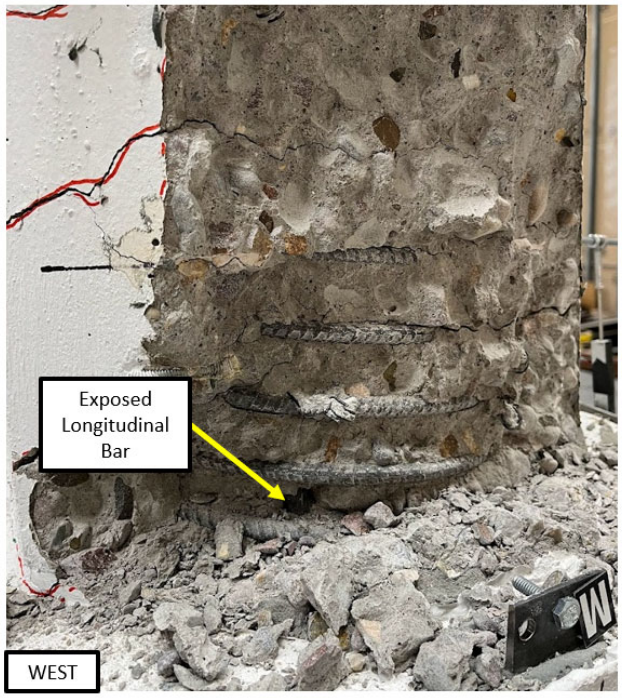

Figure 3.82 CIP 1 after Cycle 16Δ_y

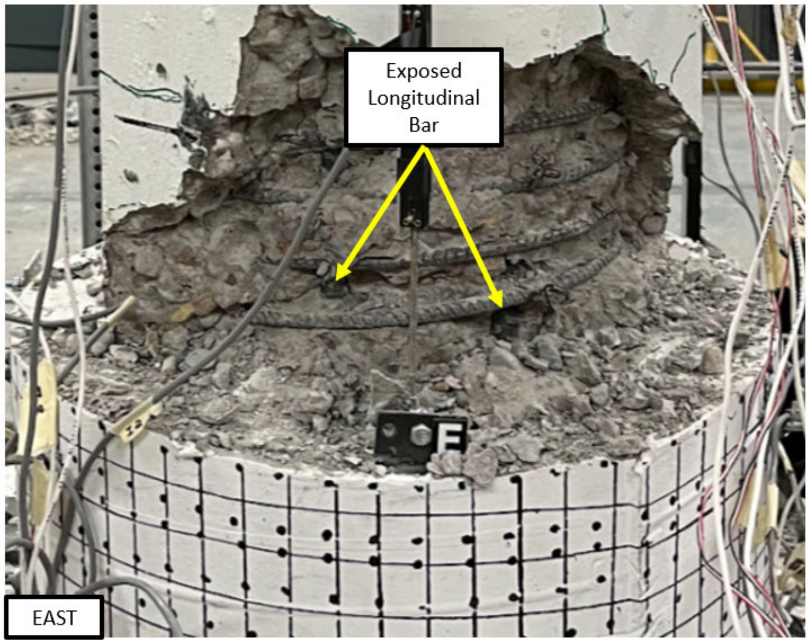

Figure 3.83 CIP 1 after Cycle 19Δ_y

By 21Δ_y the speed of testing was increased to speed up testing. CIP 1 ended up failing at 26Δ_y, which is when the column reached 20% degradation. Longitudinal bar fracture occurred on the east face of the column (Figure 3.84).

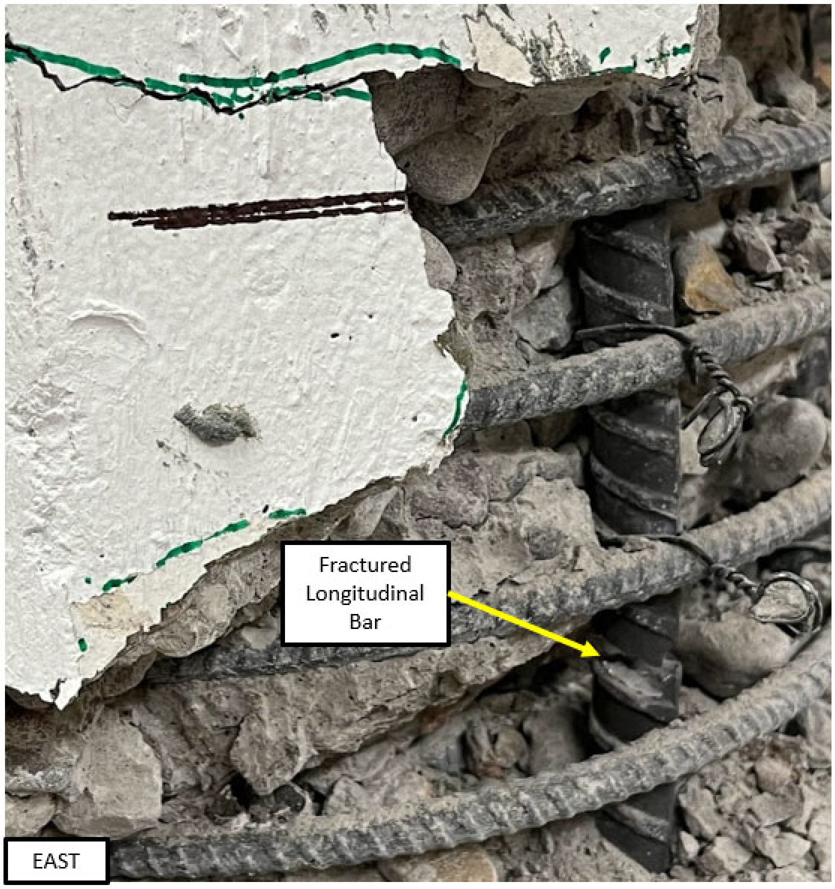

Figure 3.84 CIP 1 Fractured Longitudinal Bar at Cycle 26Δ_y

The CIP 1 retrofit was successful in pushing the plastic hinge of the column above the jacket. An overall image of CIP 1 after failure can been seen in Figure 3.85. Notice that the plastic hinge occurred directly above the jacket, as compared to the Precast columns.

Figure 3.85 CIP 1 Post-Test

The programmed vs actual achieved displacements and drift are summarized in Table 3.25. From here on out, in this section, each cycle will be referred to as its correlating actual drift value.

Table 3.25 CIP 1 Loading Protocol Summary

Cycle	Programmed Displacement (in.)	Programmed Drift (%)	Actual Displacement (in.)	Actual Drift (%)
$0.5\Delta_y$	0.10	0.196	0.09	0.184
Δ_y	0.20	0.392	0.18	0.354
$2\Delta_y$	0.39	0.784	0.30	0.608
$3\Delta_y$	0.59	1.177	0.44	0.885
$4\Delta_y$	0.78	1.569	0.57	1.148
$5\Delta_y$	0.98	1.961	0.73	1.464
$6\Delta_y$	1.18	2.353	0.88	1.765
$7\Delta_y$	1.37	2.746	1.05	2.097
$8\Delta_y$	1.57	3.138	1.23	2.467
$9\Delta_y$	1.77	3.530	1.42	2.837
$10\Delta_y$	1.96	3.922	1.61	3.214
$11\Delta_y$	2.16	4.315	1.81	3.622
$12\Delta_y$	2.35	4.707	2.01	4.012
$13\Delta_y$	2.55	5.099	2.21	4.425
$14\Delta_y$	2.75	5.491	2.42	4.838
$15\Delta_y$	2.94	5.883	2.62	5.242
$16\Delta_y$	3.14	6.276	2.83	5.652
$17\Delta_y$	3.33	6.668	3.02	6.040
$18\Delta_y$	3.53	7.060	3.24	6.481
$19\Delta_y$	3.73	7.452	3.44	6.888
$20\Delta_y$	3.92	7.845	3.64	7.279
$21\Delta_y$	4.12	8.237	3.85	7.694
$22\Delta_y$	4.31	8.629	4.04	8.086
$23\Delta_y$	4.51	9.021	4.25	8.505

Cycle	Programmed Displacement (in.)	Programmed Drift (%)	Actual Displacement (in.)	Actual Drift (%)
$24\Delta_y$	4.71	9.414	4.46	8.922
$25\Delta_y$	4.90	9.806	4.67	9.335
$26\Delta_y$	5.10	10.198	4.91	9.811

*Note drift is calculated from the top of the jacket, i.e. Drift (%) = (Displacement/50 in.)*100

The ultimate displacement achieved during testing was 4.91 in. (9.81% drift), while the ultimate force achieved was 25.08 kip. The ultimate lateral load correlates to a total moment capacity of 133.76 kip-ft, which exceeds the original design column moment capacity of 61.7 kip-ft.

Using Bilinear approximation, the yield force (F_y) and yield displacement (δ_y) are determined for CIP 1. The method used is the same as before. Using the method, the following equations are determined for segment OB and segment BC:

$$\overline{OB}:\ y = 23.531x$$
$$\overline{BC}:\ y = 4.610x + 19.395$$

The experimental data is placed into an EXCEL file and a quartic regression is used to determine the best suitable equation for the experimental data. Note that a quartic function fit the data best for CIP 1. The following equation is determined:

$$Experimental:\ \ y = -6.725x^4 + 2.727x^3 + 7.799x^2 + 19.256x + 0.007$$

Using the method S_1 is calculated to be 0.0133 and S_2 is calculated to be 0.0177. When the constraint is applied, the difference calculated between S_2 and S_1 is 0.0044, which is approximately zero. The values for the approximation are shown in in Table 3.26. Figure 3.86 shows the graph for CIP 1.

Table 3.26 Bilinear Approximation Values Calculated for CIP 1

Parameter	Value
$\delta_{0.6Fy}$	0.615
δ_y	1.025
δ'_y	1.11
δ_u	1.234
$0.6F_y$	14.472
F_y	24.120
F'_y	24.500
F_u	25.083

*Where F'_y is the values corresponding to δ'_y

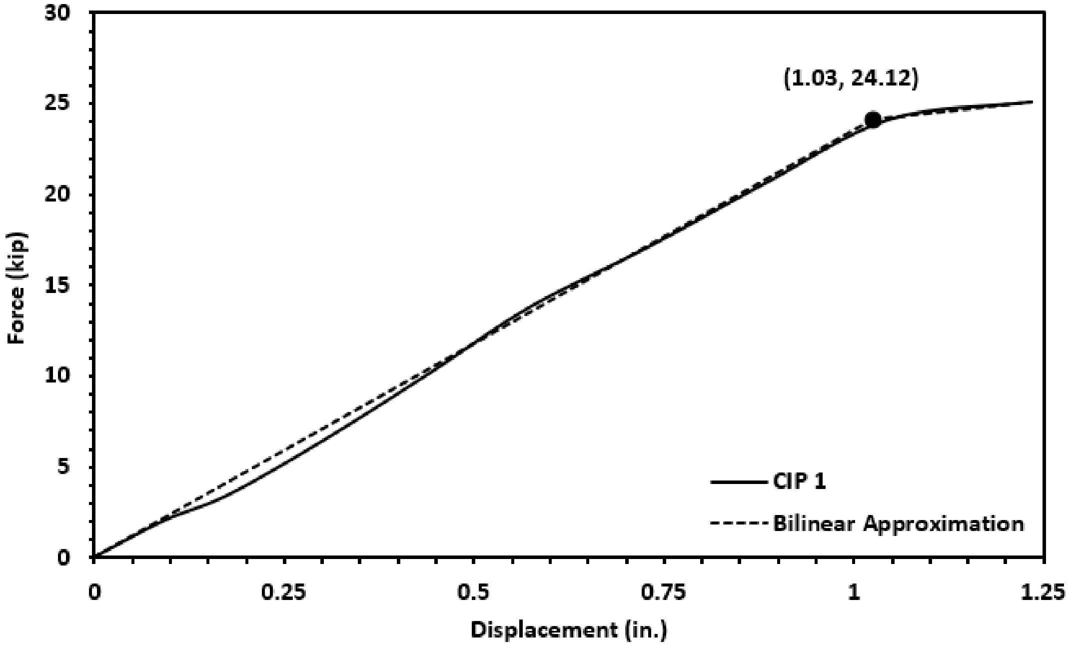

Figure 3.86 Bilinear Approximation of CIP 1

Furthermore, the hysteresis of CIP 1 is mapped in Figure 3.87 (force-displacement) and 3.89 (force-drift). The yield point is marked on both graphs. The yield displacement of 1.03 in. correlates to a drift value of 2.06%. It can also be noted that CIP 1 surpassed the original CIP pier base shear of 11.22 kip, which is also noted on both graphs. Note, quadrant I for both figures signifies the is column in push, while quadrant III signifies the column is in pull. From observation of Figure 3.87 and Figure 3.88, CIP 1 had similar strength and displacement in both push and pull.

Figure 3.89Figure 3.90 provides the force-drift backbone curve for CIP 1. The performance points for CIP 1 are also given in Figure 3.89. The backbone is created using the maximum force, and its corresponding displacement, of each cycle. Note that the maximum force does not always correspond with the maximum displacement; therefore, the maximum drift seen on Figure 3.89 is 9.601%. Using the backbone curve, the initial stiffness of CIP 1 can be calculated from the slope of the curve prior to yield. The initial stiffness of CIP 1 is calculated to be 23.19 kip/in.

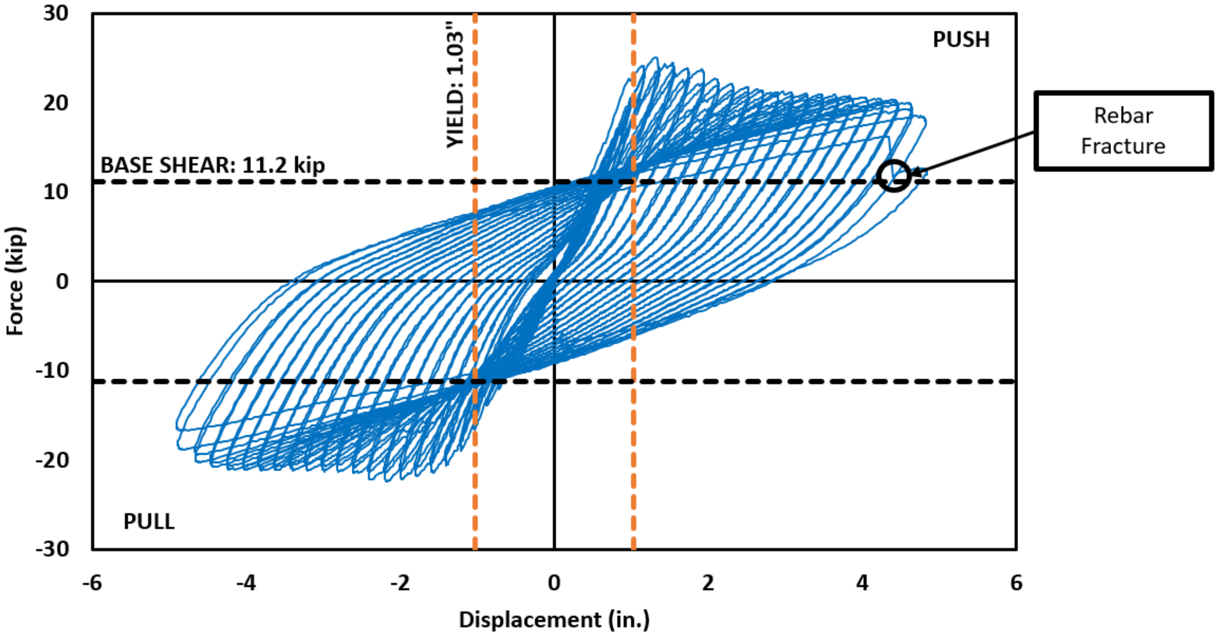

Figure 3.87 CIP 1 Force-Displacement Hysteresis

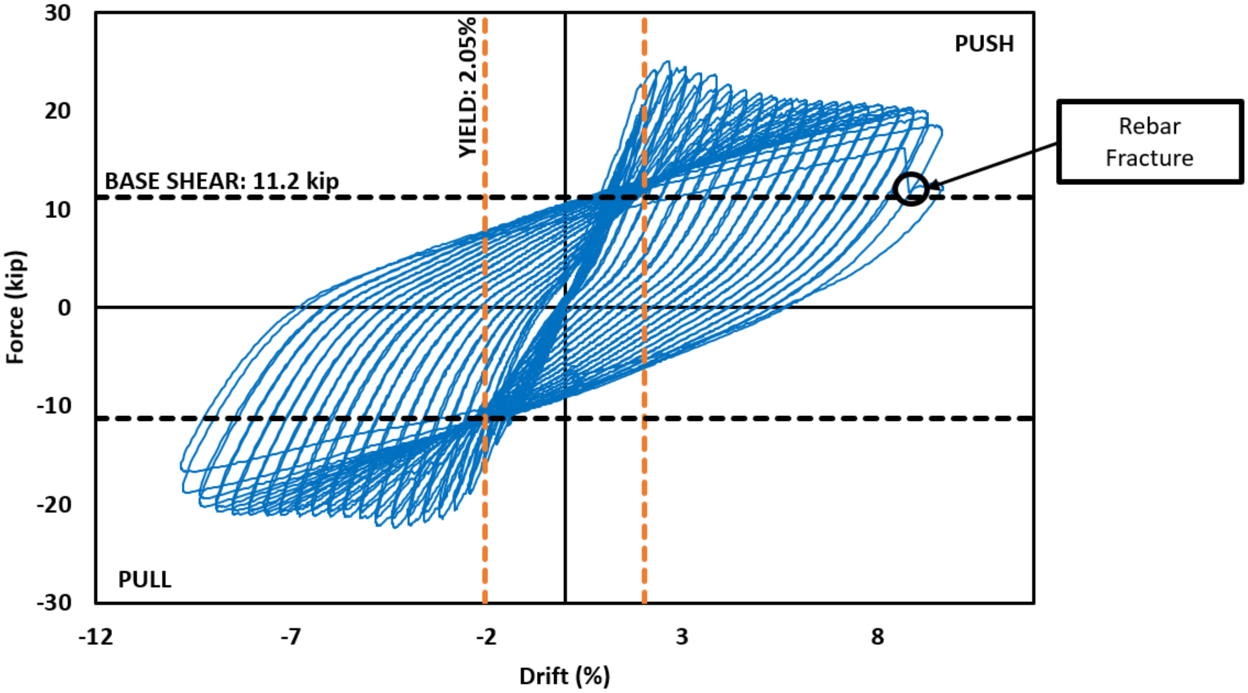

Figure 3.88 CIP 1 Force-Drift Hysteresis

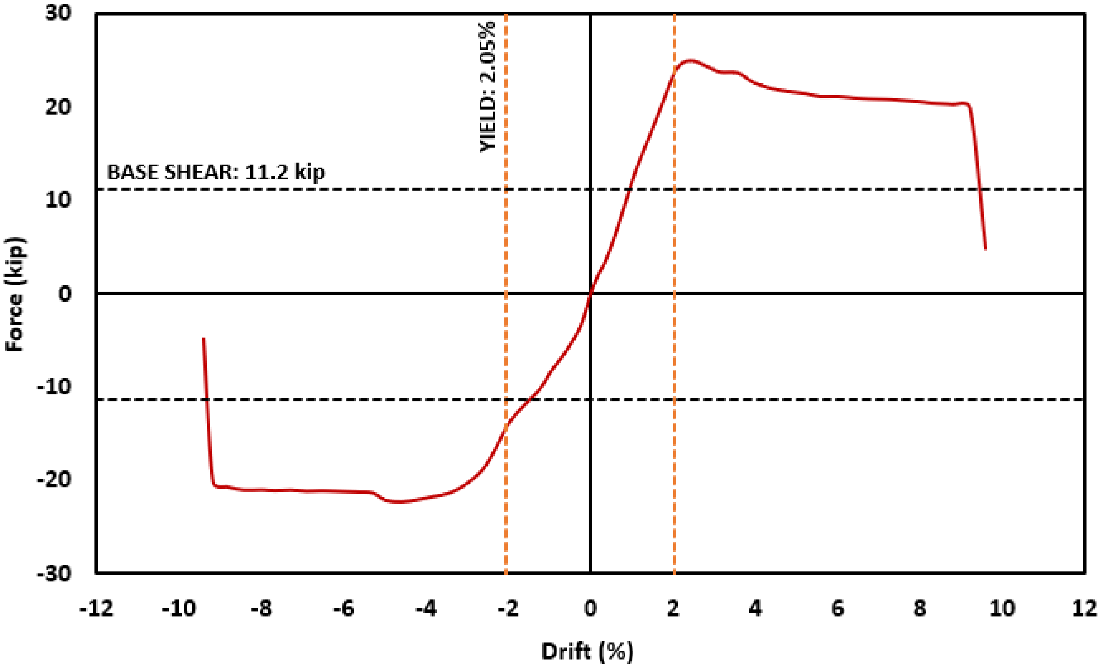

Figure 3.89 CIP 1 Force-Drift Backbone Curve

Instrumentation from testing is used to map the moment-curvature of CIP 1 (Figure 3.90). The potentiometer data is used to find the corresponding curvature from the plastic hinge location to the moment of the column. Note that the CIP plastic hinge occurred 8 inches lower than the Precast columns.

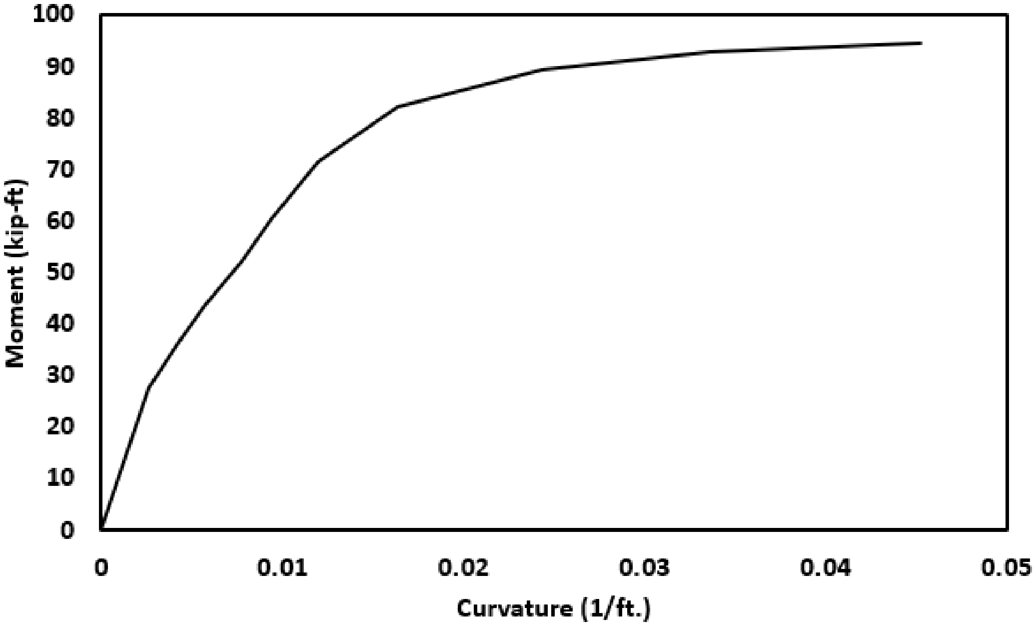

Figure 3.90 CIP 1 Moment-Curvature from the Plastic Hinge

Similarly, the average gap opening of CIP 1 can also be mapped using the potentiometer data (Figure 3.91). The graph gives the average gap opening, along with the corresponding moment achieved during each cycle of testing. Figure 3.91 highlights the development of the plastic hinge in the column. As testing progresses, gap opening increases until the plastic hinge forms. After the plastic hinge begins to deform the column, the gap opening decreases. The maximum gap opening of CIP 1 was 0.0854 in. at a moment of 114.53 kip-ft.

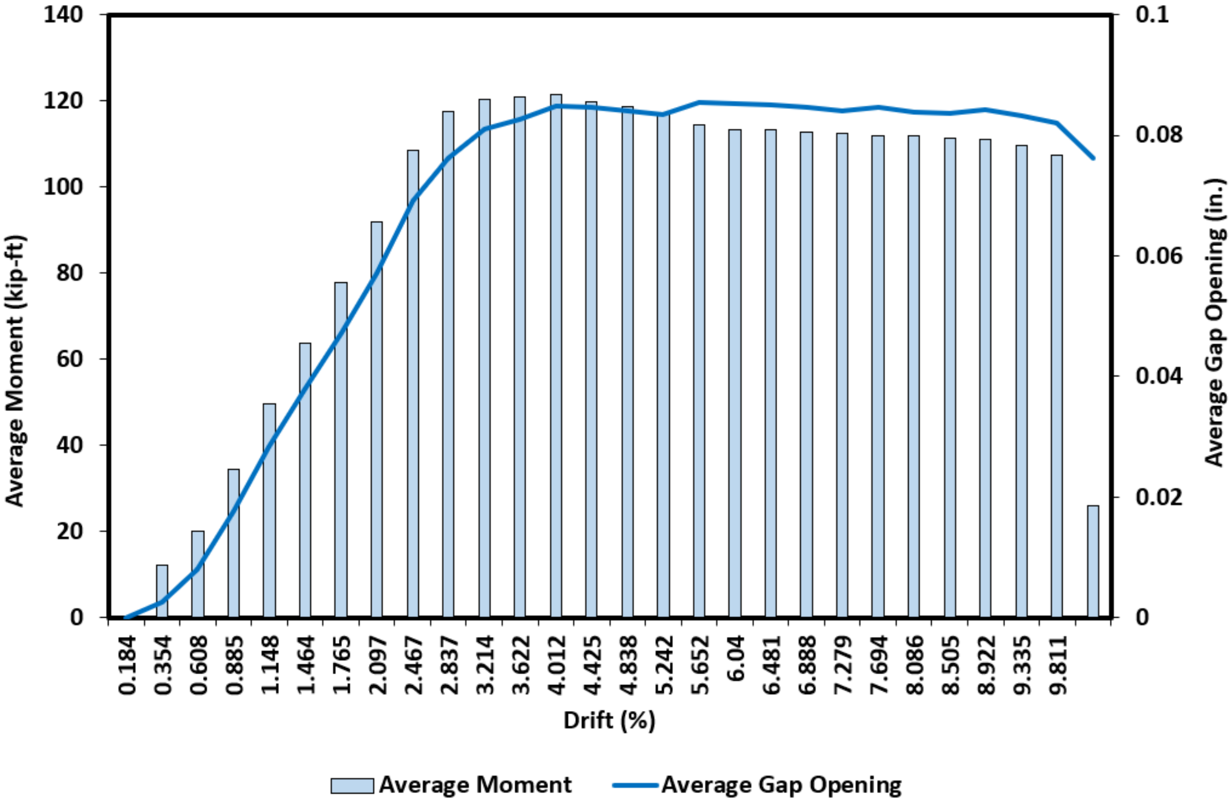

Figure 3.91 CIP 1 Average Moment and Gap Opening vs Drift

The next step in processing results is to calculate the energy dissipation of CIP 1. The energy dissipation is calculated using the same method as the other columns. The results can be seen in Figure 3.92. The graph shows the energy dissipated during the first and second cycle of each drift. Figure 3.92 also shows the cumulative dissipated energy after each drift. CIP 1 was able to dissipate a total of 316.09 kJ.

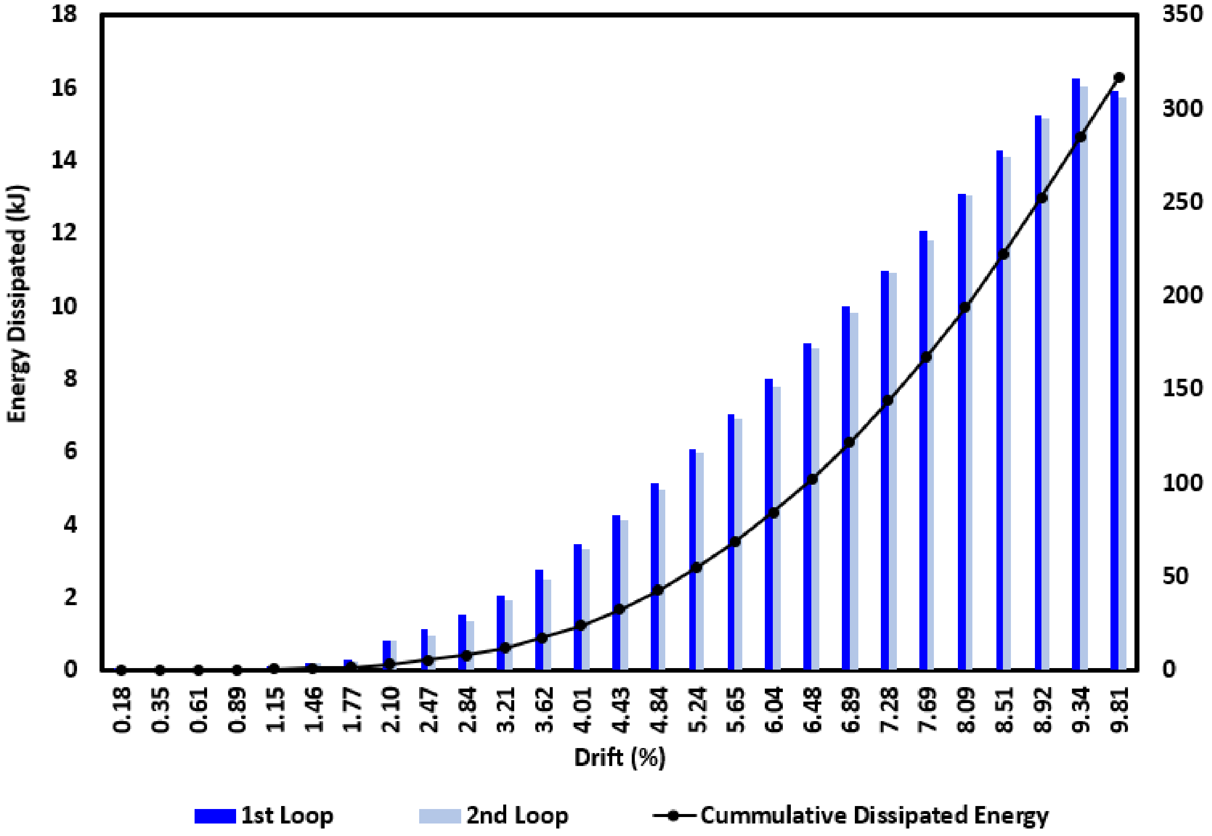

Figure 3.92 CIP 1 Dissipated Energy

Further analysis of the experimental results allows the determination of the overstrength factor (Ω_0), using the equation from the previous section, the overstrength factor is calculated to be 1.73. Similarly, the displacement ductility for ultimate (μ_u) and failure (μ_f) are calculated to be 2.01 and 7.52, respectively.

Summary

CIP 1 is retrofitted to determine the ability of UHPC jacketing as a retrofit method for CIP connections. The retrofit is designed using SAP2000 modeling capabilities to design the thickness of the jacket. CIP 1 is rehabilitated in the SLAB, instrumented, and then tested under quasi-static, cycling loading. The loading protocol is based off of the original protocol used during Phase I (ITD Report 281, 2021). Testing results showed that CIP 1 performed well. CIP 1 was able to achieve, and go beyond the original experimental moment capacity of the connection (81.84 kip-ft), achieving an overall moment capacity of 133.76 kip-ft. The maximum force experienced by CIP 1 is 25.08 kip. The stiffness calculated from testing is 23.19 kip/in. CIP 1 was able to achieve a 1.03 in. yield displacement and a 4.91 in. ultimate displacement. CIP 1 saw negligible gap opening at the jacket-to-footing interface. Furthermore, the UHPC jacket saw negligible damage. CIP 1 is able to dissipate 316.09 kJ of energy, while achieving an overstrength factor of 1.73, an ultimate displacement ductility of 2.01, and a failure displacement ductility of 7.52.

Cast-in-Place 2 Retrofit

Introduction

This section presents the design, construction, and testing of a CIP column retrofit with UHPC with the intention of establishing a comparison with the CIP 1 column. A review of the construction process is presented. The full testing arrangement used for the experimental work is presented, followed by the experimental testing carried out and its resulting performance.

Design

CIP 2 is designed using SAP2000 to determine the expected moment capacity of the retrofit. The goal is to bring the original column from the CIP bent back to its original moment capacity and push the plastic hinge up the face of the column, above the jacket; while also minimizing jacket size. The moment yield capacity (M_y) of the original column is 55.79 kip-ft, the plastic moment (M_p) of the original column is 81.84 kip-ft. CIP 2 is modeled with 7 longitudinal bars as fracture did not occur in this column during testing of the CIP Bent.

The retrofit is designed using moment-curvature analysis of the cross section. The moment-curvature analysis is performed in SAP2000, an axial load is placed on the column of 30 kip, to correspond to the 5% gravity load of the bent specimen during testing. CIP 2 is designed without dowels and caging. The model placed into SAP2000 of the original CIP pier cross section, the CIP 1 retrofit, and the CIP 2 retrofit are shown in Figure 3.93.

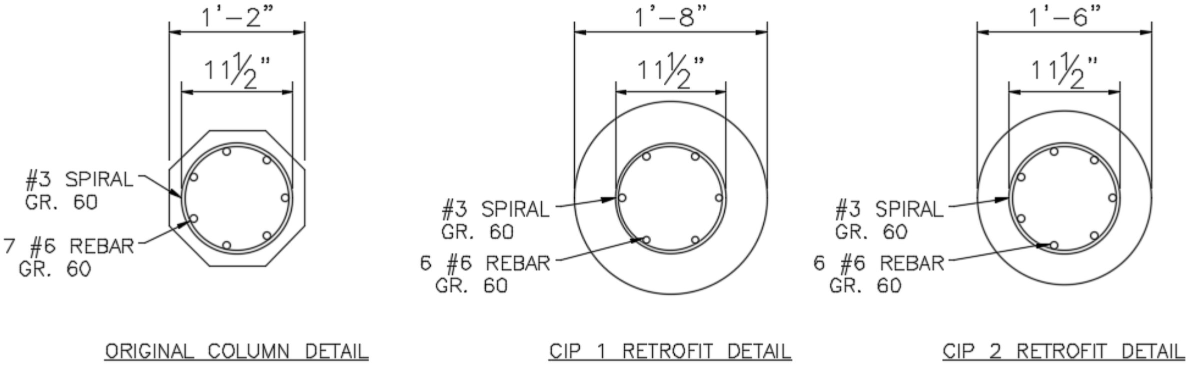

Figure 3.93 Original CIP Pier, CIP 1 Retrofit, and CIP 2 Retrofit SAP2000 Cross-Sections

The model is checked against the original pier cross-section to ensure that the CIP 2 retrofit has a strong enough moment capacity. Furthermore, different jacket sizes are analyzed to see with size will work best for CIP 2. The results from the SAP2000 model are shown in Figure 3.94 and Table 3.27. The results show that a jacket of 2.0 in. thickness would be sufficient. The height of the jacket is to be equivalent to Precast 1 jacket height (14 in.). The overall design for CIP 2 is shown in Figure 3.95.

Table 3.27 Moment-Curvature Analysis of CIP 2 Retrofit

Jacket Thickness (in.)	Moment Yield Capacity, M_y (kip-ft)	Plastic Moment, M_p (kip-ft)
2.5	84.99	110.91
2.0	80.47	108.90
CIP 1	89.83	116.71
Original CIP Pier	55.79	81.84
CIP 2	80.47	108.90

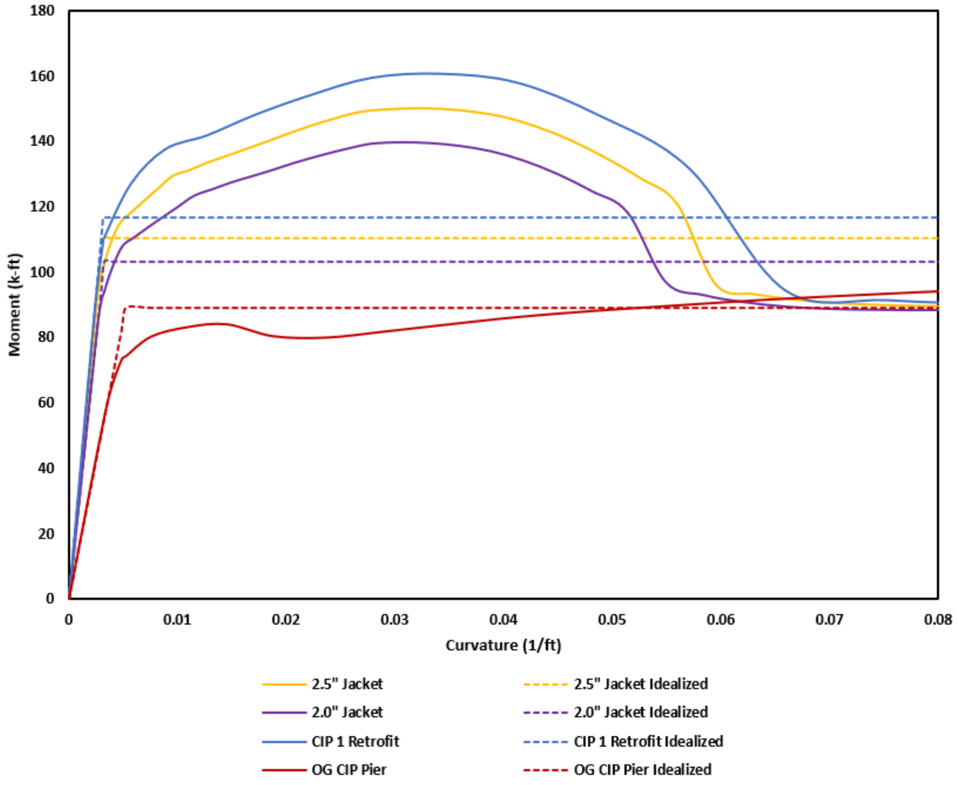

Figure 3.94 Moment-Curvature Analysis of CIP 2 Retrofit

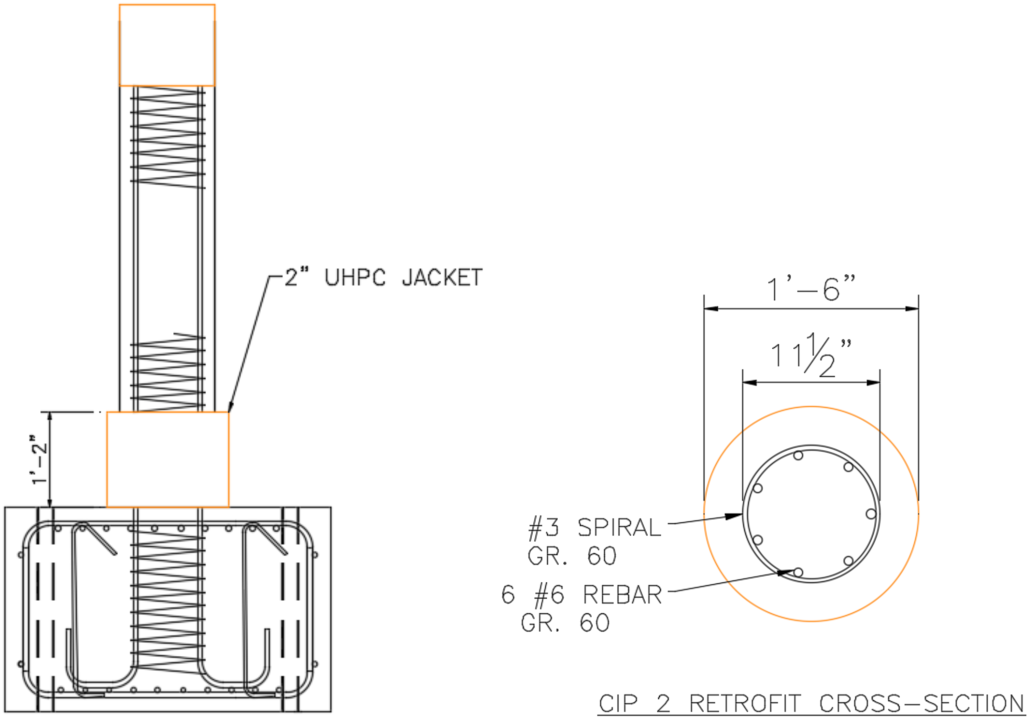

Figure 3.95 CIP 2 Retrofit Detail

Construction

The construction process for CIP 2 follows the same steps as CIP 1. The surface of CIP 2 is roughened and the formwork is mounted for the jacket. The form work is an 18 in. diameter Sonotube.

CIP 2 is poured under a 30-kip gravity load to simulate the load of the superstructure. CIP 2 is allowed to cure for 72 hours under the gravity load. After 72 hours the load is removed and the formwork is removed. High-strength grout is used for cosmetic patching between the column and jacket. The jacket is then cured for 28 days. After the jacket is cured, it is painted and marked with a 1 in. grid for monitoring of cracks.

Testing Arrangement

The testing arrangement of CIP 2 is the exact same as the previous columns. There are no changes made between the two set-ups. CIP 2 is placed under a gravity load of 30 kip, while lateral loading is applied using the hydraulic actuator.

Instrumentation

For ease of test set-up, the instrumentation set up used for CIP 2 is the exact same as the set up used for the previous columns.

Loading Protocol

Similarly, the loading protocol is kept consistent for testing of CIP 2, as the jacket and columns are the same height.

Testing Results

Starting the test at 0.5Δ_y, no cracks appeared. Hairline began to surface on the east and west face of the column during the Δ_y cycle. At this time hairline cracks also appeared at the jacket-to-footing interface. Hairline cracking continued to spread through the 5Δ_y cycle (Figure 3.96). Similarly, hairline cracking at the base of the jacket continued to grow. During the 6Δ_y the cracks at the base of the jacket on the east and west faces measured 0.04 in. (Figure 3.97).

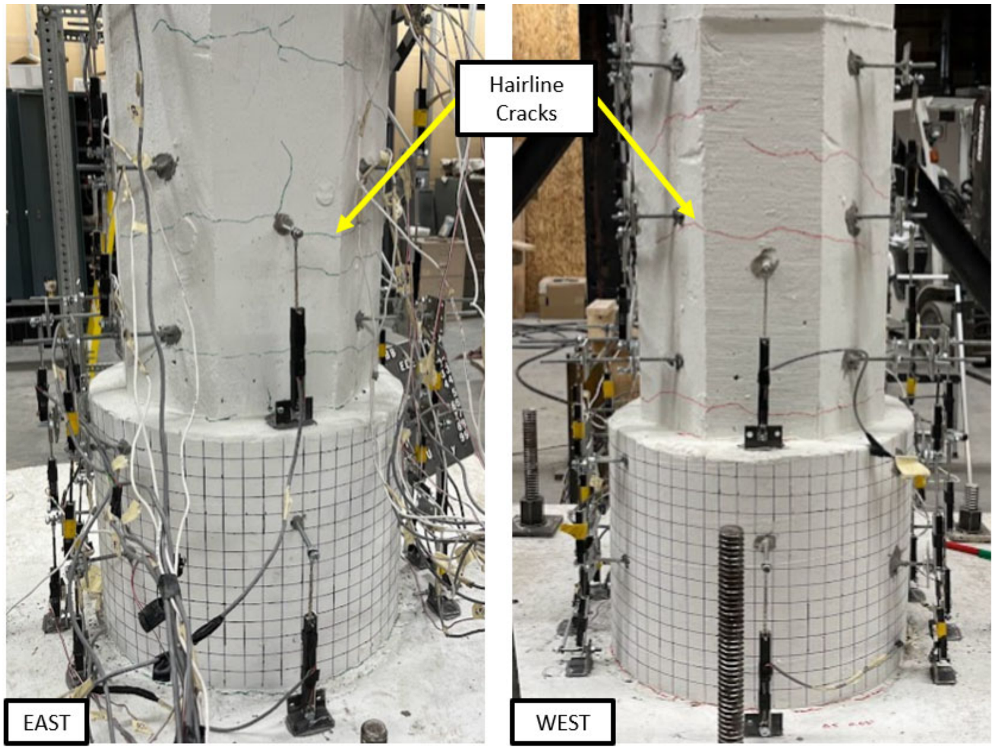

Figure 3.96 CIP 2 after Cycle 5Δ_y

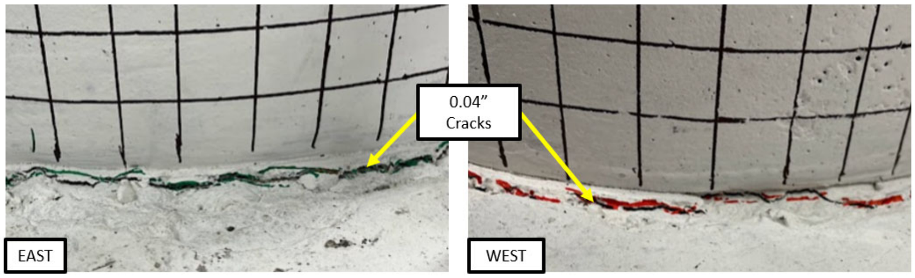

Figure 3.97 Jacket-to-Footing Interface of CIP 2 after 6Δ_y

As testing continued the gap opening at the jacket-to-footing interface became more apparent. After cycle 9Δ_y the gap was 0.06 in. At this time the cracks above the jacket continued to propagate, with the largest cracks being 0.04 in. and 0.03 in. on the east and west faces, respectively (Figure 3.98).

Spalling began to occur above the jacket during the 12Δ_y cycle. The column achieved maximum loading during the 13Δ_y, with a value of 25.2 kip while undergoing pull. As spalling continued, stirrups became visible on the west face during the 15Δ_y cycle. By cycle 18Δ_y longitudinal bar was exposed on the west face (Figure 3.99). The column continued to deteriorate as testing progressed. By the 19Δ_y cycle stirrups became visible on the east face, and after the 21Δ_y cycle longitudinal bar was exposed (Figure 3.100). Note that as deterioration continued above the jacket, the gap opening ceased to grow. Also note that testing speed is increased after 21Δ_y.

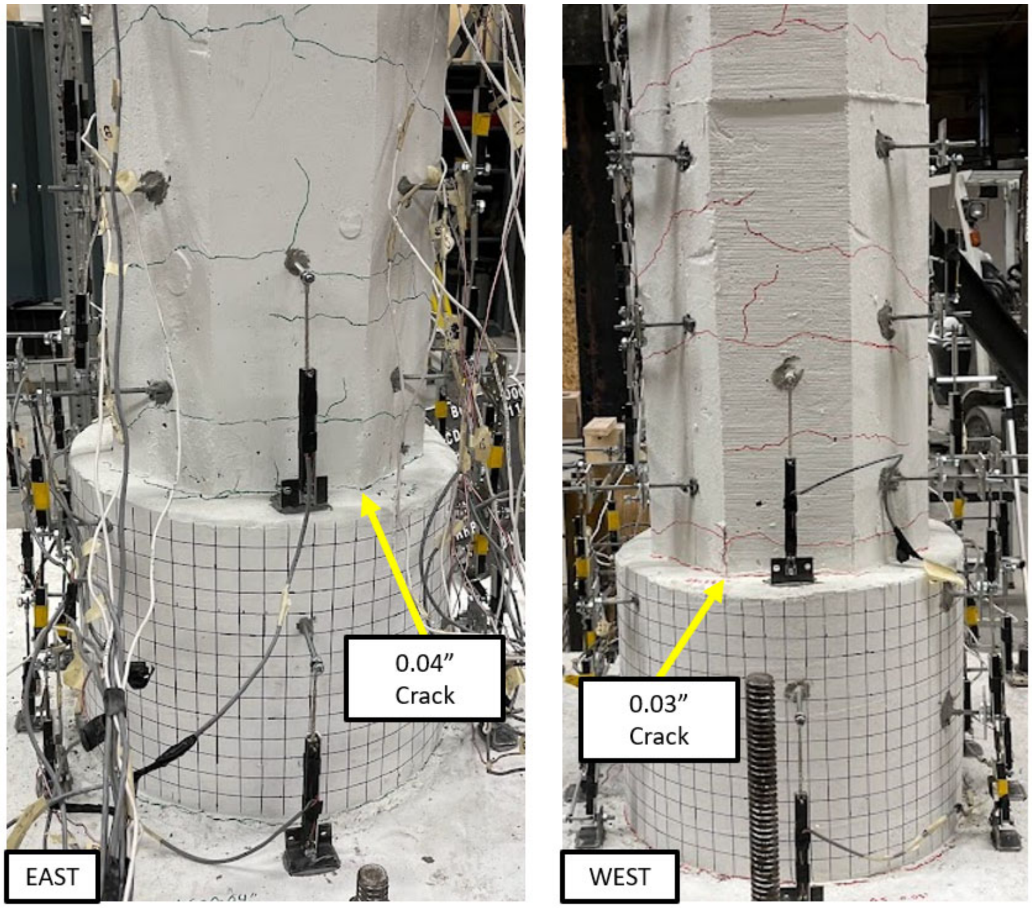

Figure 3.98 CIP 2 after 9Δ_y Cycle

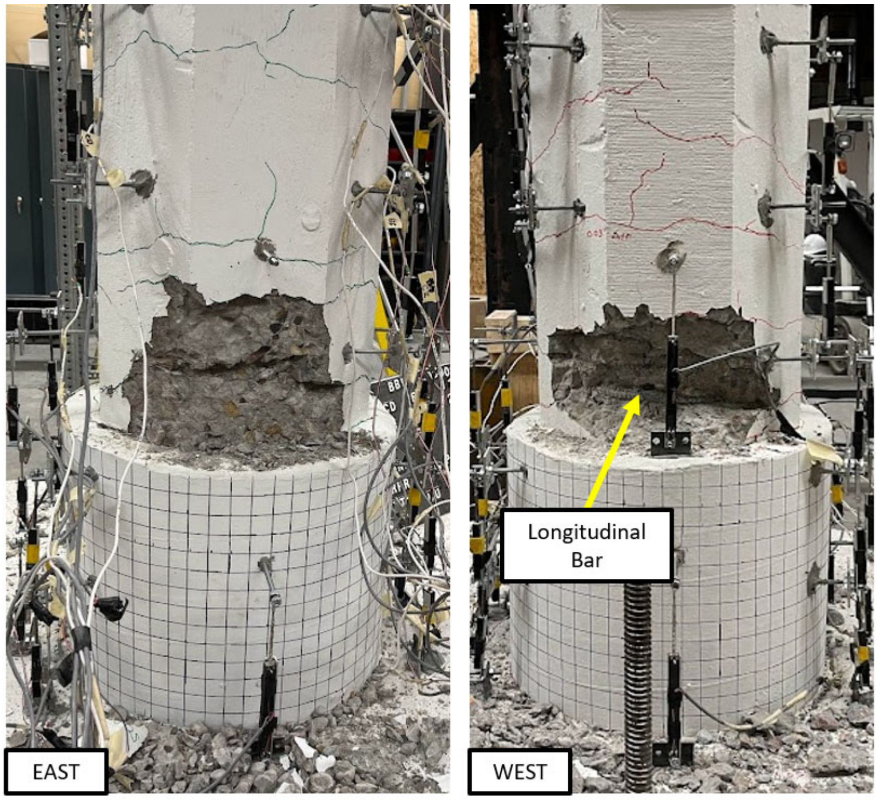

Figure 3.99 CIP 2 after 18Δ_y Cycle

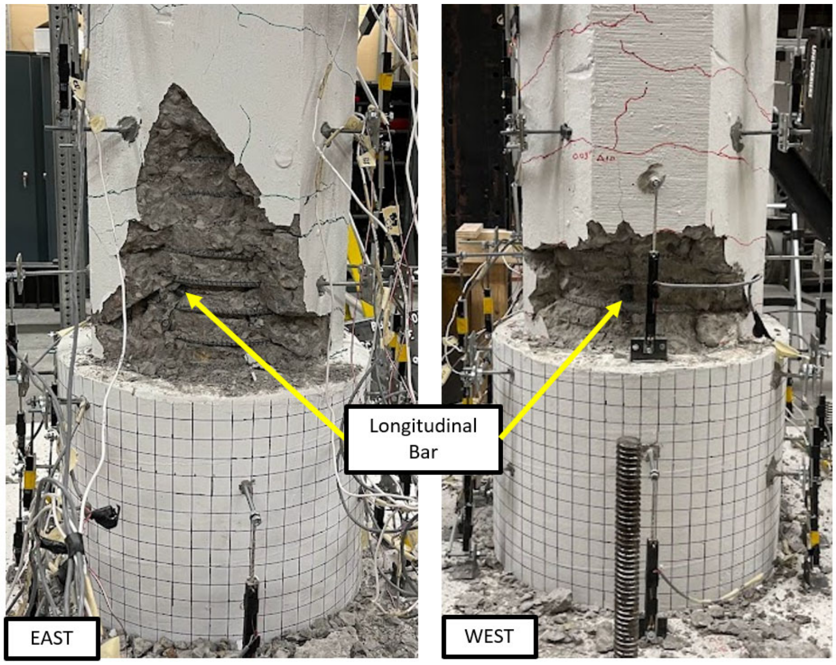

Figure 3.100 CIP 2 after 21Δ_y Cycle

CIP 2 testing progressed up to 28Δ_y. Testing was stopped, even though the column did not achieve 20% degradation. Testing was terminated due to lack of stroke in the actuator. CIP 2 did not fracture any rebar. CIP 2 is shown after testing in Figure 3.101.

Figure 3.101 CIP 2 Post-Test

The programmed vs actual achieved displacements and drift are summarized in Table 3.28. From here on out, in this section, each cycle will be referred to as its correlating actual drift value.

Table 3.28 CIP 2 Loading Protocol Summary

Cycle	Programmed Displacement (in.)	Programmed Drift (%)	Actual Displacement (in.)	Actual Drift (%)
$0.5\Delta_y$	0.10	0.196	0.10	0.201
Δ_y	0.20	0.392	0.18	0.357
$2\Delta_y$	0.39	0.784	0.32	0.645
$3\Delta_y$	0.59	1.177	0.47	0.935
$4\Delta_y$	0.78	1.569	0.59	1.172
$5\Delta_y$	0.98	1.961	0.73	1.450
$6\Delta_y$	1.18	2.353	0.88	1.756
$7\Delta_y$	1.37	2.746	1.03	2.063
$8\Delta_y$	1.57	3.138	1.20	2.391
$9\Delta_y$	1.77	3.530	1.37	2.737
$10\Delta_y$	1.96	3.922	1.53	3.063
$11\Delta_y$	2.16	4.315	1.72	3.443
$12\Delta_y$	2.35	4.707	1.90	3.806
$13\Delta_y$	2.55	5.099	2.09	4.183
$14\Delta_y$	2.75	5.491	2.29	4.584
$15\Delta_y$	2.94	5.883	2.48	4.951
$16\Delta_y$	3.14	6.276	2.67	5.346
$17\Delta_y$	3.33	6.668	2.87	5.734
$18\Delta_y$	3.53	7.060	3.07	6.150
$19\Delta_y$	3.73	7.452	3.28	6.564
$20\Delta_y$	3.92	7.845	3.49	6.971
$21\Delta_y$	4.12	8.237	3.69	7.385
$22\Delta_y$	4.31	8.629	3.89	7.774
$23\Delta_y$	4.51	9.021	4.10	8.198

Cycle	Programmed Displacement (in.)	Programmed Drift (%)	Actual Displacement (in.)	Actual Drift (%)
$24\Delta_y$	4.71	9.414	4.30	8.601
$25\Delta_y$	4.90	9.806	4.50	9.000
$26\Delta_y$	5.10	10.198	4.70	9.396
$27\Delta_y$	5.30	10.600	4.90	9.795
$28\Delta_y$	5.49	10.980	5.09	10.189

*Note drift is calculated from the top of the jacket, i.e. Drift (%) = (Displacement/50 in.)*100

The ultimate displacement achieved during testing was 5.09 in. (10.19% drift), while the ultimate force achieved was 25.20 kip. The ultimate lateral load correlates to a total moment capacity of 134.40 kip-ft, which exceeds the original design column moment capacity of 61.7 kip-ft.

Using Bilinear approximation, the yield force (F_y) and yield displacement (δ_y) are determined for CIP 2. The method used is the same as the one used for the other columns. Using the method, the following equations are determined for segment OB and segment BC:

$$\overline{OB}: \; y = 18.743x$$
$$\overline{BC}: \; y = 5.209x + 13.489$$

The experimental data is placed into an EXCEL file and a quadratic regression is used to determine the best suitable equation for the experimental data. Note that a quadratic function fit the data best for CIP 2. The following equation is determined:

$$Experimental: \quad y = -4.022x^2 + 20.189x + 0.573$$

Using the method S_1 is calculated to be 0.6765 and S_2 is calculated to be 0.6711. When the constraint is applied, the difference calculated between S_2 and S_1 is 0.0054, which is approximately zero. The values for the approximation are shown in in Table 3.29. Figure 3.102 shows the graph for CIP 2. Note that CIP 2 achieved ultimate force during pull, therefore the absolute values of the pull cycle are used to create the bilinear approximation.

Table 3.29 Bilinear Approximation Values Calculated for CIP 1

Parameter	Value
$\delta_{0.6Fy}$	0.598
δ_y	0.997
δ'_y	1.355
δ_u	2.248
$0.6F_y$	11.208
F_y	18.681
F'_y	20.549
F_u	25.200

*Where F'_y is the values corresponding to δ'_y

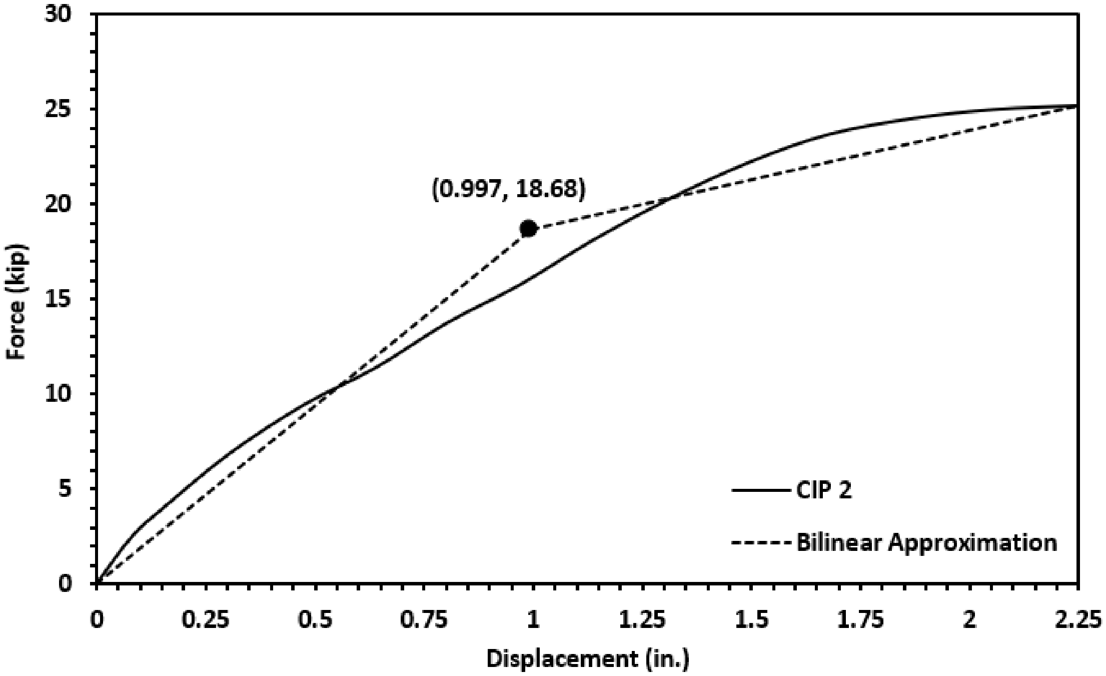

Figure 3.102 Bilinear Approximation of CIP 2

Furthermore, the hysteresis of CIP 2 is mapped in Figure 3.103 (force-displacement) and Figure 3.104 (force-drift). The yield point is marked on both graphs. The yield displacement of 0.997 in. correlates to a drift value of 1.99%. It can also be noted that CIP 2 surpassed the original CIP pier design base shear of 11.22 kip, which is also noted on both graphs. Note, quadrant I for both figures signifies the is column in push, while quadrant III signifies the column is in pull. From observation of Figure 3.103 and Figure 3.104, CIP 2 had similar strength and displacement in both push and pull.

Figure 3.105 provides the force-drift backbone curve for CIP 2. The performance points for CIP 2 are also given in Figure 3.105. The backbone is created using the maximum force, and its corresponding displacement, of each cycle. Note that the maximum force does not always correspond with the maximum displacement; therefore, the maximum drift seen on Figure 3.105 is 9.74%. Using the backbone curve, the initial stiffness of CIP 2 can be calculated from the slope of the curve prior to yield. The initial stiffness of CIP 2 is calculated to be 17.74 kip/in.

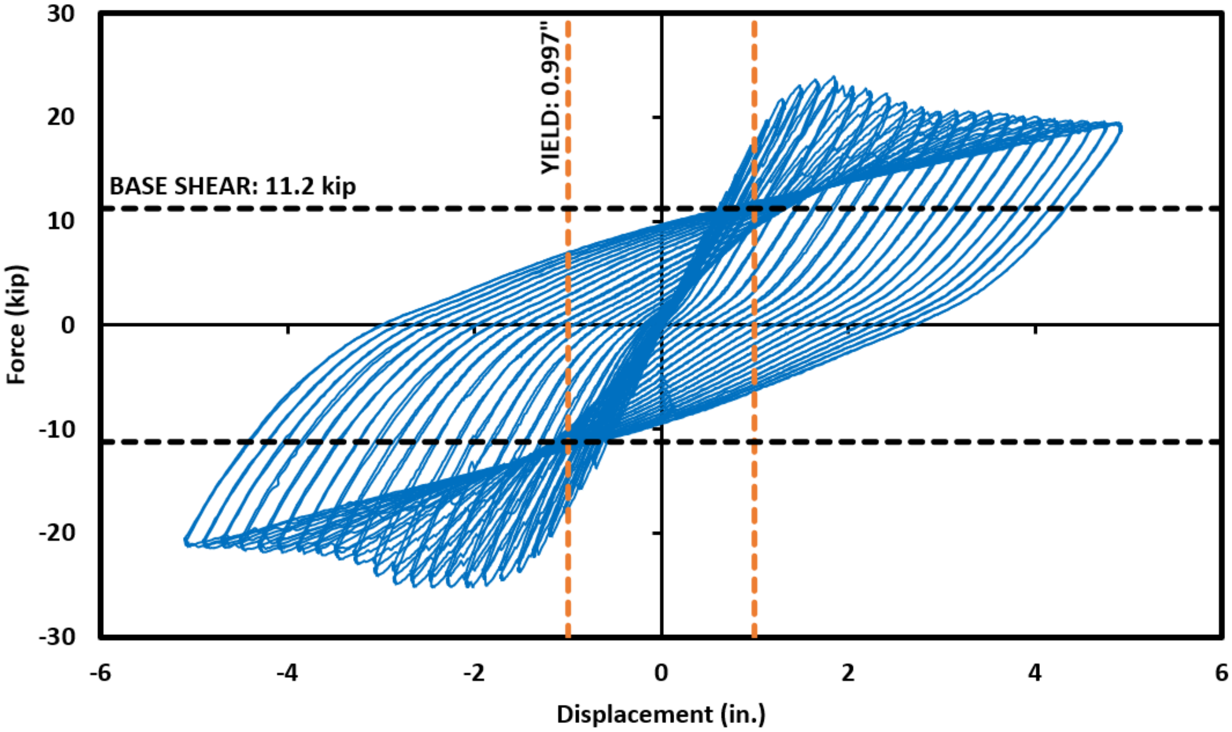

Figure 3.103 CIP 2 Force-Displacement Hysteresis

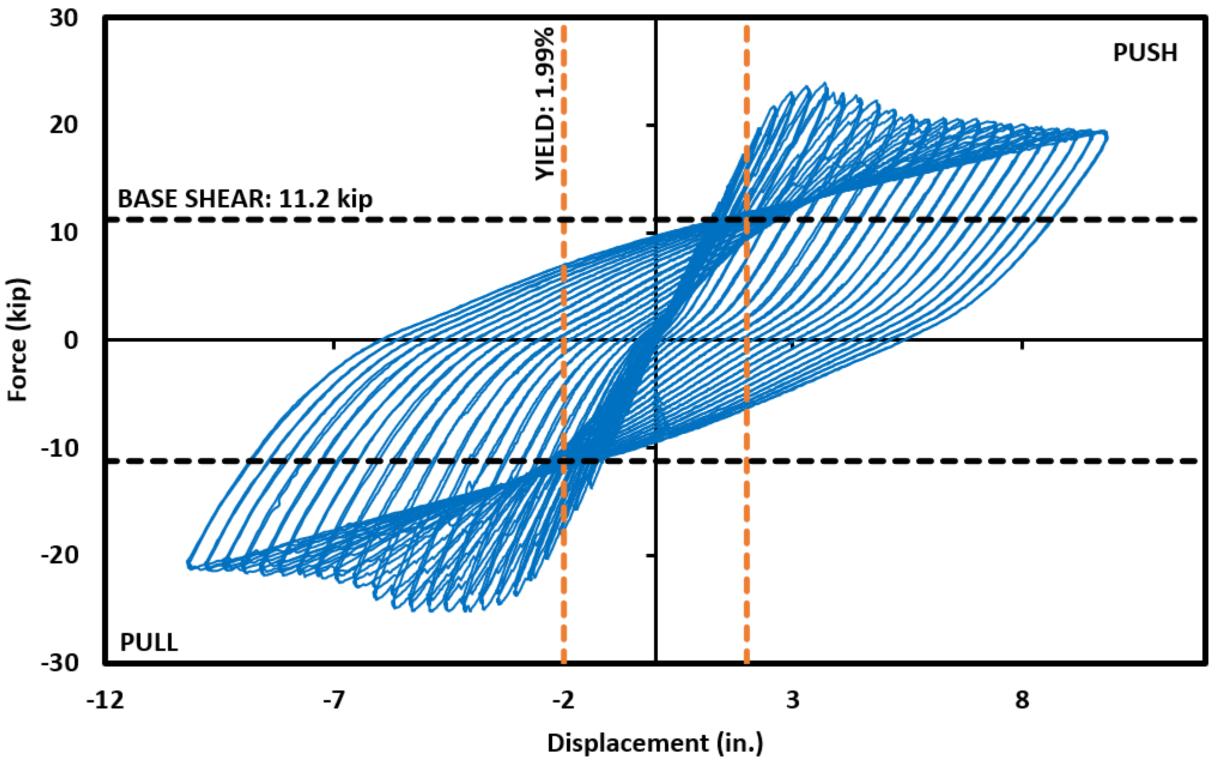

Figure 3.104 CIP 2 Force-Drift Hysteresis

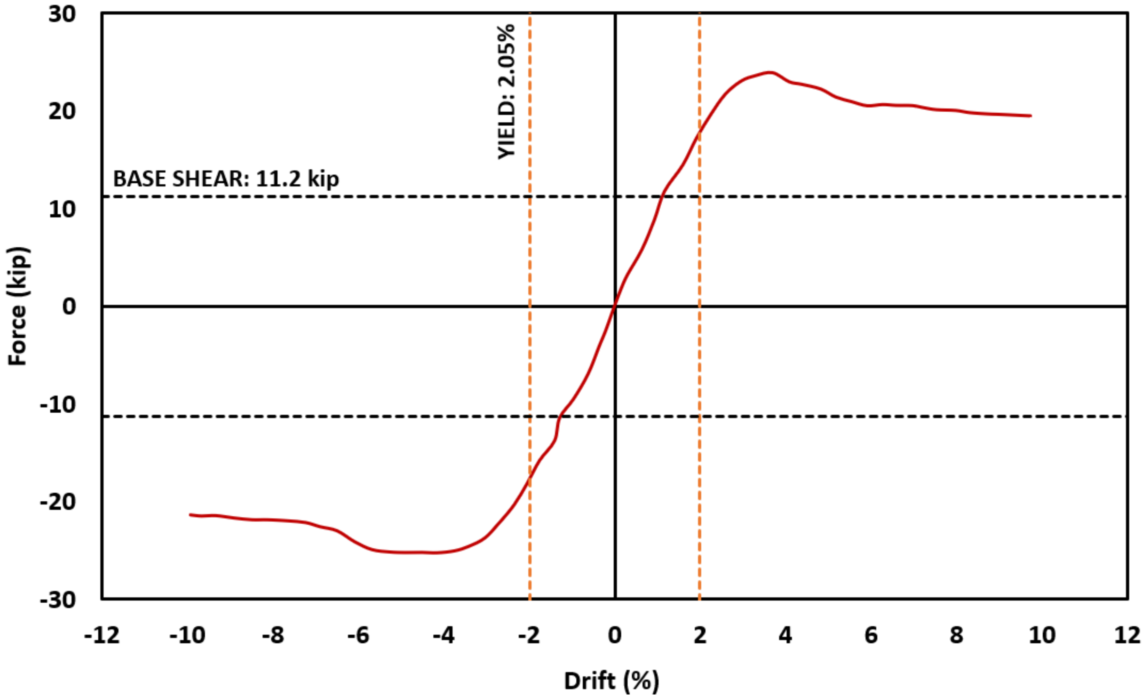

Figure 3.105 CIP 2 Force-Drift Backbone Curve

Instrumentation from testing is used to map the moment-curvature of CIP 2 (Figure 3.106). The potentiometer data is used to find the corresponding curvature from the plastic hinge location to the moment of the column. The plastic hinge of CIP 2 occurred in the same location as CIP 1, directly above the jacket.

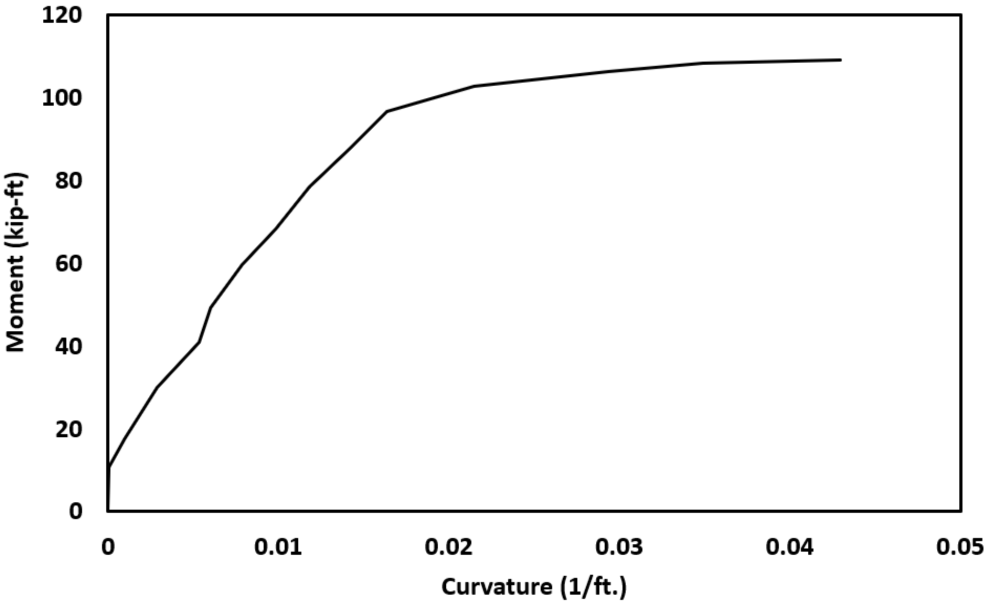

Figure 3.106 CIP 2 Moment-Curvature from the Plastic Hinge

Similarly, the average gap opening of CIP 2 can also be mapped using the potentiometer data (Figure 3.107). The graph gives the average gap opening, along with the corresponding moment achieved during each cycle of testing. Figure 3.107 highlights the development of the plastic hinge in the column. As testing progresses, gap opening increases until the plastic hinge forms. After the plastic hinge begins to deform the column, the gap opening decreases. The maximum gap opening of CIP 2 was 0.132 in. at a moment of 122.81 kip-ft.

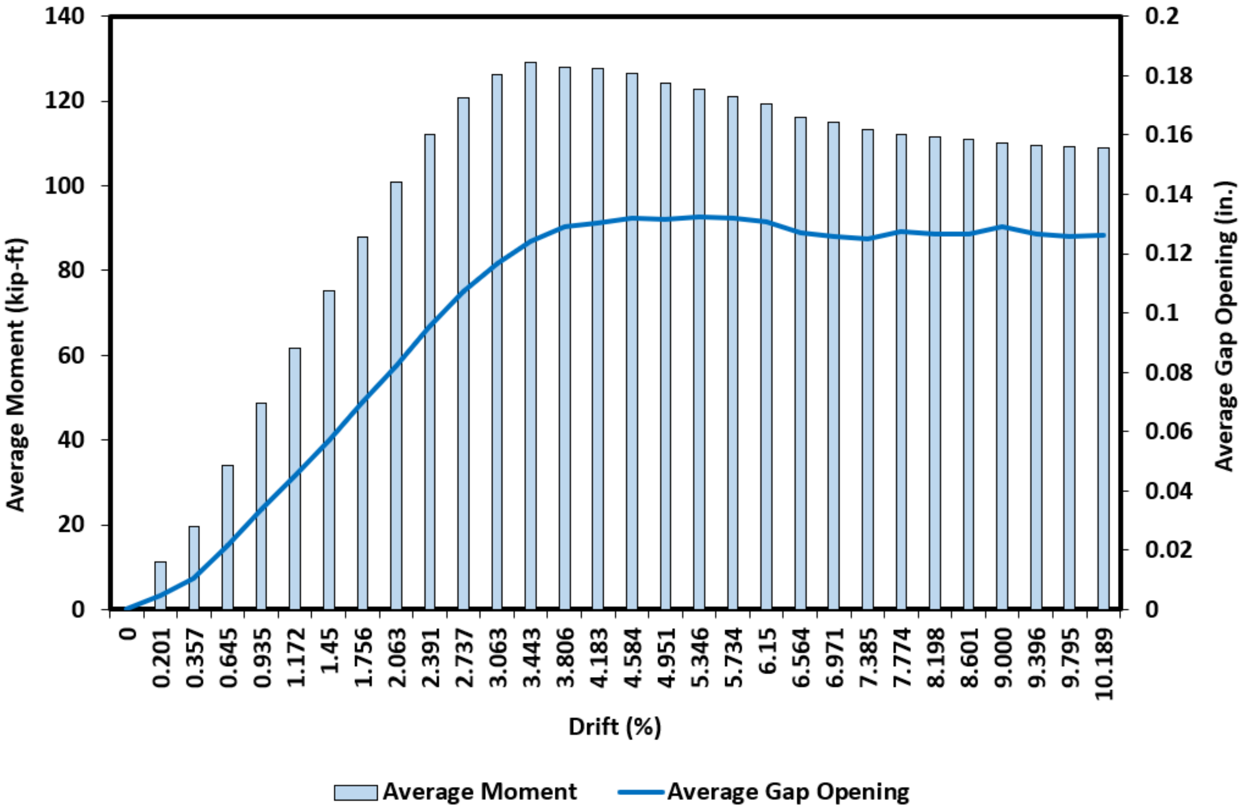

Figure 3.107 CIP 2 Average Moment and Gap Opening vs Drift

The next step in processing results is to calculate the energy dissipation of CIP 2. The energy dissipation is calculated using the same method as the other columns. The results can be seen in Figure 3.108. The graph shows the energy dissipated during the first and second cycle of each drift. Figure 3.108 also shows the cumulative dissipated energy after each drift. CIP 2 was able to dissipate a total of 322.77 kJ.

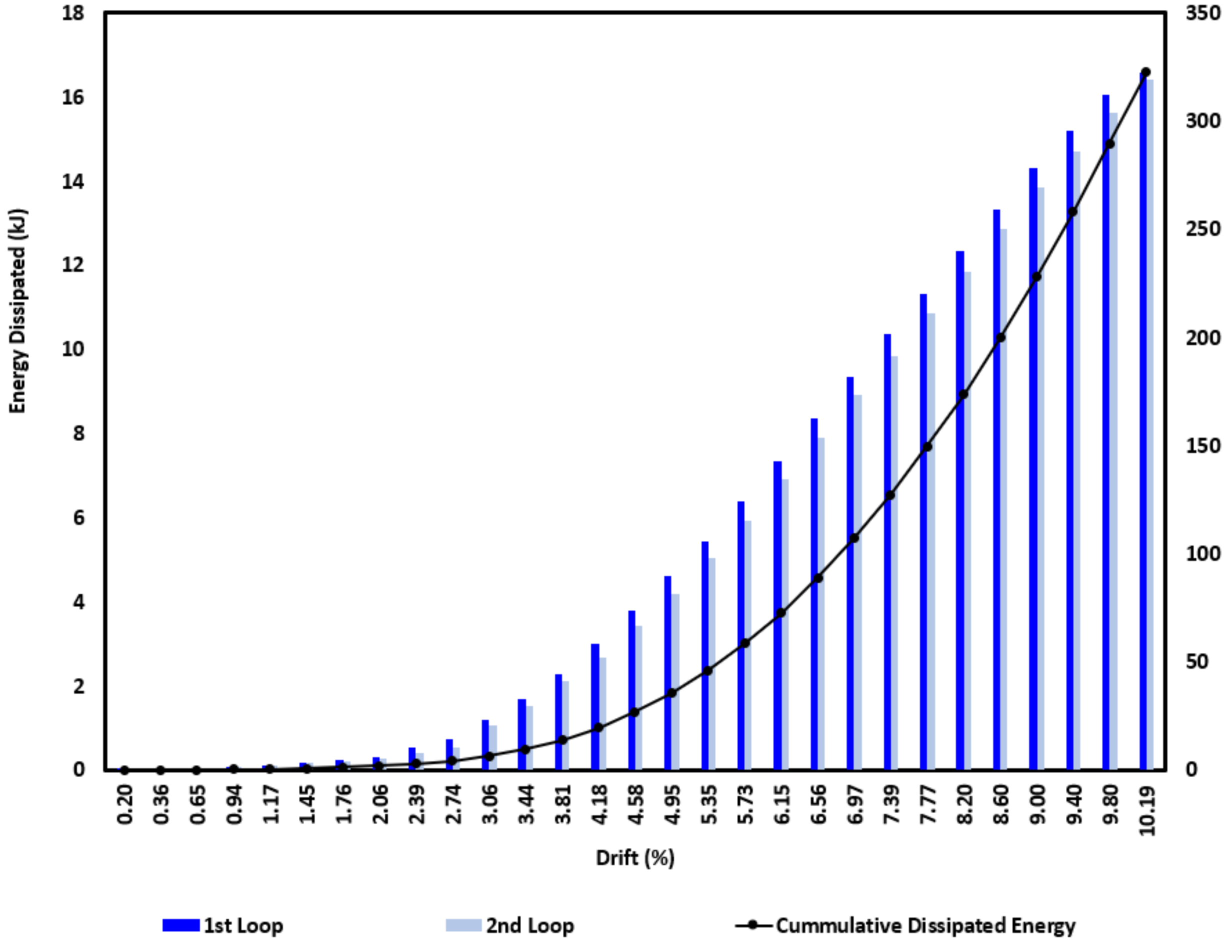

Figure 3.108 CIP 2 Dissipated Energy

Further analysis of the experimental results allows the determination of the overstrength factor (Ω_0), using the equation from the previous section, the overstrength factor is calculated to be 2.25. Similarly, the displacement ductility for ultimate (μ_u) is calculated to be 2.26. The displacement ductility for ultimate cannot be calculated for CIP 2, as the pier was unable to achieve 20% degradation.

Summary

CIP 2 is retrofitted to compare UHPC jacket size affect with CIP 1. The retrofit is designed using SAP2000 modeling capabilities to design the thickness of the jacket. CIP 2 is rehabilitated in the SLAB, instrumented, and then tested under quasi-static, cycling loading. The loading protocol is based off of the original protocol used during Phase I (ITD Report 281, 2021). Testing results showed that CIP 2 performed well. CIP 2 was able to achieve, and go beyond the original experimental moment capacity of the connection (81.84 kip-ft), achieving an overall moment capacity of 134.40 kip-ft. The maximum force experienced by CIP 2 is 25.20 kip. The stiffness calculated from testing is 17.74 kip/in. CIP 2 was able to achieve a 0.997 in. yield displacement and a 5.10 in. ultimate displacement. CIP 2 saw sizable gap opening at the jacket-to-footing interface. Despite this, the UHPC jacket saw negligible damage. CIP 2 is able to dissipate 322.77 kJ of energy, while achieving an overstrength factor of 2.25 and an ultimate displacement ductility of 2.26.

Cast-in-Place Columns: CIP 1 Retrofit vs. CIP 2 Retrofit

Both CIP column retrofits performed as expected and designed. Both retrofits utilized the similar geometry and loading protocol. The difference between CIP 1 and CIP 2 was the jacket size. CIP 1 had a 3.0 in. thick jacket while CIP 2 utilized a 2.0 in. thick jacket. Both jackets had no reinforcing in the retrofitted section. Despite the size of the jacket, both retrofits exhibited similar capacity, and were successful at pushing the plastic hinge of the column above the retrofit.

Despite the success of both retrofits, CIP 2 exhibited more debonding from the footing, which caused gap opening at the jacket-to-footing interface of CIP 2. To place the gap opening into perspective, Figure 3.109 shows the width of the gap over the span of the test for CIP 1 and CIP 2. As shown in Figure 3.109, CIP 1 (blue) exhibited less gap opening than CIP 2, which had a maximum of 0.132 in.

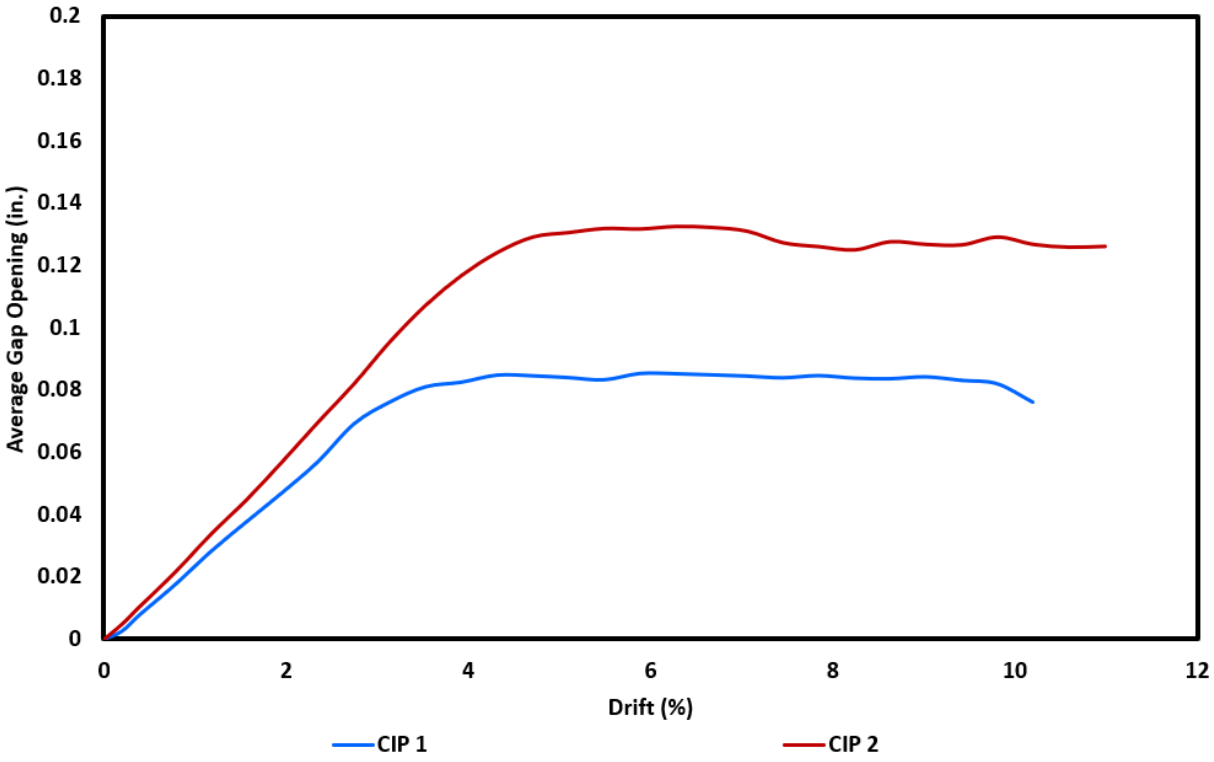

Figure 3.109 Average Gap Opening of Cast-In-Place Columns

Furthermore, the reduction in size allowed for CIP 2 to withstand more cycles, and therefore a higher drift value than CIP 1. CIP 2 had a maximum drift of 10.19%, while CIP 1 attained a maximum drift of 9.81%. CIP 2 had an increased drift ratio, but similar capacity to CIP 1, which reinforces the fact that CIP 2 is less stiff than CIP 1. CIP 1 had a stiffness of 23.19 kip/in, while CIP 2 only produced 17.74 kip/in, in stiffness. The difference in stiffness can be seen in the Backbone curves in Figure 3.110. Furthermore, a summary of the results from CIP 1 and CIP 2 can be seen in Table 3.30. Also note that the significant drop in the CIP 1 backbone (blue) is due to rebar fracture. CIP 2 did not fracture rebar, and did not achieve 20% degradation.

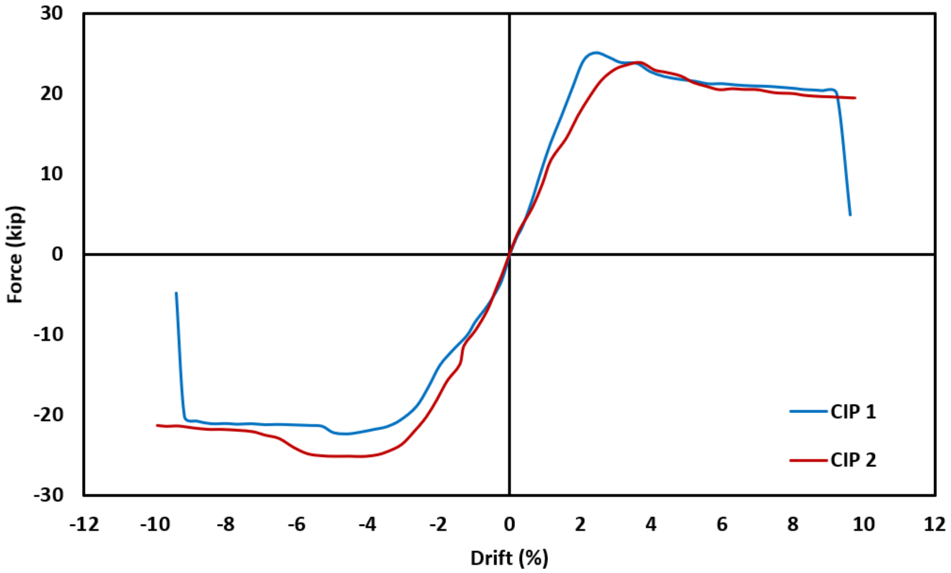

Figure 3.110 CIP Columns Backbone Curves

Table 3.30 Precast Columns Results Summary

	CIP 1 (3.0 in.)	**CIP 2 (2.0 in.)**
Maximum Force	25.08 kip	25.20 kip
Maximum Displacement	4.91 in. (9.81%)	5.10 in. (10.19%)
Moment Capacity	133.76 kip-ft	134.40 kip-ft
Initial Stiffness	23.19 kip/in.	17.74 kip/in.
Initial Yield	0.62 in. (1.24%)	0.60 in. (1.20%)
Global Yield (Bilinear Approximation)	1.03 in. (2.06%)	0.997 in. (1.99%)
Moment at Global Yield	100.50 kip-ft	77.84 kip-ft
Energy Dissipation	316.09 kJ	322.77 kJ (258.09 kJ)*
Overstrength Factor	1.73	2.25
Displacement Ductility (Ultimate Base Shear)	2.01	2.26
Displacement Ductility (Failure Point)	7.52	N/A

*CIP 2 Cumulative Dissipated Energy at Failure of CIP 1

4. Design and Detailing Considerations

Introduction

This chapter discusses design/detailing considerations, construction/assembly technology and limitations for the retrofit method.

Construction Technology and Assembly

It is recommended that the materials used in this report be a minimum for practical applications. When placing dowels, care should be taken to avoid damaging existing rebar in the footing, especially in critical rebar locations. To locate existing rebar, construction plans from the original project should be utilized, as well as a rebar scanner to ensure no critical rebar is damaged. Another viable option for avoiding existing rebar is to remove the concrete cover on the foundation. The size of the jacket can be changed due to construction tolerance. For example, if a 4.0 in. jacket is deemed adequate, but the rebar would conflict during construction, it is recommended to extend the jacket thickness.

It is critical that the surface of the footing is roughened at least 1/4 in. prior to pouring of the UHPC. When the UHPC is poured, care should be taken in order to prevent uplift of the form which would cause excess concrete to seep out of the bottom of the form. In regard to forming the UHPC, when a circular style is used, North Carolina State University introduced using a flexible form instead of slicing Sonotube, which can be difficult. The flexible form can be seen in Figure 4.1. The flexible form is recommended for retrofit work.

It is also critical that the directions for mixing UHPC is followed meticulously. Furthermore, when pouring into the form, the UHPC will shrink. Therefore, it is recommended that the UHPC is poured at minimum 1.0 in. taller than the desired height. This is due to shrinkage of the UHPC which causes voids in the top inch of the jacket. Structurally this top inch provides no aid to the retrofit as it is riddled with voids. It is recommended for a smooth surface, for this to be ground down using a grinder.

Research is recommended on the effects of using different cross-section styles for the jacket. Research is also recommended to investigate the necessity of hoop stirrups in the jacket.

Figure 4.1 Example of Flexible Form (Tasdemir et. al., 2018)

Limitations

The limitations of the retrofit method are minimal. The main limitation is in construction. The difficulty of finding existing rebar is high. The limitation of stirrups is a foreseeable issue. If the stirrups are necessary tying these around an existing column will be a difficult task. However, if the stirrups are proven to be unnecessary in further research this limitation is negatable. Furthermore, the unit price of UHPC is high, but little quantity is required in the retrofit method. The simplicity of calculation and design is evident in the process.

Inspection

Inspection during construction and regular service would be similar to other concrete pier projects. Special attention should be given to the gap opening of the jacket-to-footing interface and the location of termination of the pipe in the precast elements. For CIP connections, inspection would be similar in inspecting gap opening and the section directly above the jacket.

Obviously, the plastic hinge zones are critical locations for inspection post-seismic activity. In post-earthquake inspection, smaller cracks without spalling of the cover concrete indicates that there is little to no yielding of the longitudinal bars inside the connections. However, loss of cover concrete in plastic hinge zones may require further intrusive inspection of the column.

5. Conclusions and Recommendations

In the initial phase of the ITD project, four half-scale bridge bents were meticulously designed using nearly identical materials. Among these bents, two of them consisted of cast-in-place columns, while the remaining two had novel precast pier connection known as the telescoping pipe connection. Rigorous testing was conducted within the controlled environment of the ISU laboratory. Beyond the evident advantages in terms of construction, installation, and safety, the results of these tests illuminated a notable difference in seismic performance between the two configurations. The precast pier connection demonstrated superior seismic resilience, enduring a higher number of cycles and dissipating a substantially greater amount of energy compared to the cast-in-place column. In light of these findings, the project's second phase commenced with a strategic retrofitting approach. This phase involved the application of Ultra-High-Performance Concrete (UHPC) jacketing within the plastic hinge zone of the pier to push the plastic hinge up to the face of the column from the base.

The loading protocol in all the columns is the same as ITD Phase I (ITD Report 281) in every case. Notably, the Ultra-High-Performance Concrete (UHPC) jackets showed no wear on any of the columns, which made it possible for the plastic hinge to move above the jacket.

A 14-inch height and a consistent UHPC thickness of 4 inches were seen for Precast 1 and Precast 2. However, the use of dowels the main differentiator. Precast 2 lacked any caging arrangement, whereas Precast 1 had 12 no. 6 dowels with no. 3 circular hoops. As a result, Precast 2 had a longer sequence of drift cycles, totaling 25 cycles as opposed to Precast 1's 21 cycles. Precast 1 also shown noticeably greater stiffness, which was measured at 38.17 kip/in, a significant 61.73% increase in stiffness over Precast 2. Notably, Precast 1 had a maximum displacement of 4.08 inches, or an 8.16% drift, whereas Precast 2 had a maximum displacement of 4.69 inches, or a 9.38% drift. Precast 1 recorded maximum values of 30.76 kip and 164.05 kip-ft for force and moment capacity, respectively. Whereas, Precast 2 measured 30.65 kip and 163.47 kip-ft. The difference in energy dissipation between Precast 1 and Precast 2 is 216.51 kJ vs. 262.70 kJ, respectively. Precast 1 dissipated less energy, in total. Furthermore, Precast 2 showed a noticeable gap opening of 0.492 inches at the interface between the jacket and the footing, a feature not seen in Precast 1.

From analysis of results of experimental testing of the precast columns, recommendations for retrofit of the ITD ABC connection are to use dowels for piers that have experienced a Maximum Considered Earthquake (MCE). When a retrofit is required for a pier with the ITD ABC Connection that has not undergone an MCE, a jacket without dowels is likely to be sufficient (although further research is recommended in this area). The reason for this recommendation is that if the pier has suffered pipe fracture from MCE, it is no longer considered a fixed connection and allows for rocking to occur (as seen in the study of Precast 2). If rocking is allowed, the plastic hinge may not form and predicting the entire behavior of the bridge would be complicated.

Regarding the CIP columns, CIP 1 had a 3-inch-thick UHPC jacket that was 14 inches in height. CIP 1 had experienced a rebar fracture during the bent testing in Phase 1, therefore during the retrofit of the column, only 6 longitudinal bars were accounted for. In contrast, CIP 2 did not experience rebar fracture during Phase 1, and 7 longitudinal bars were accounted for. CIP 2 utilized a 2-inch-thick UHPC jacket. Significantly, CIP 2 withstood more drift cycles, totaling 28 cycles, as opposed to CIP 1's 26 cycles. Additionally, CIP 1 had much greater stiffness than CIP 2, which was measured at 23.19 kip/in and represented a significant 30.72% increase in stiffness, from CIP 2, which achieved a stiffness value of 17.74 kip/in. Notably, the greatest displacement for CIP 1 was 4.91 inches, or a 9.81% drift, whereas the maximum displacement for CIP 2 was 5.09 inches, or a 10.19% drift. Maximum force and moment capacities for CIP 1 and CIP 2 were 25.08 kip and 133.75 kip-ft, respectively, and 25.20 kip and 134.40 kip-ft, respectively, for CIP 1. But similar to the Precast columns, it's important to note that CIP 1 dissipated less energy—316.09 kJ—than CIP 2, which dissipated 322.77 kJ. It is also important to point out that CIP 2 showed a distinct gap opening of 0.132 inches at the jacket-to-footing interface, a feature that was not present from CIP 1.

Recommendations

From the research conducted the following recommendations are given for incorporating the retrofit method:

- Dowels are recommended for UHPC jacketing for the ITD Precast pier connection, when retrofitting a column that has already withstood an MCE load.
- Precast jacket thickness should be accommodated for dowels.
- The jacket height should be a minimum height equal to the column diameter.
- Roughening and chipping out of the foundation for the concrete joint between NSC and UHPC is recommended for precast and CIP piers.
- Dowels are not required for CIP piers.

Future Research Recommendations

The following topics are recommended for future research:

- Refining the jacket thickness required for Precast and CIP piers.
- Experimental and analytical work to determine the necessity of stirrups in the jacket.
- Refining the jacket height for Precast and CIP piers.
- Analytical work to validate the results of this research, in coordination with ITD Report 281.

- Bi-directional quasi-static cyclic, shake table testing, and consideration of soil-structure interaction for the proposed retrofit method will provide valuable data about its performance for a wider application and various seismic hazard/ground motion types.

Cited Works

ACI committee 318. (2019). *Building Code Requirements for Structural Concrete (ACI 318-19) and Commentary*. American Concrete Institute, Farmington Hills, MI.

ACI Committee 374. (2013). *Guide for testing reinforced concrete structural elements under slowly applied simulated seismic loads (ACI 374.2R-13)*. American Concrete Institute, Farmington Hills, MI.

Ahlborn, T. M., Harris, D. K., Misson, D. L., & Peuse, E. J. (2011). Characterization of Strength and Durability of Ultra-High-Performance Concrete under Variable Curing Conditions. *Transportation Research Record*, (2251), https://doi.org/10.3141/2251-07.

ASTM C1018 (1991). Standard Test Method for Flexural Toughness and First Crack Strength of Fiber-Reinforced Concrete (Using Beam with Third-Point Loading). Annual Book of ASTM Standards.

ASTM C109/C109M (2016). Standard Test Method for Compressive Strength of Hydraulic Cement Mortars (Using 2-in. or [50-mm] Cube Specimens). ASTM International, West Conshohocken, PA.

ASTM C1856/C1856M (2017). Standard Practice for Fabricating and Testing Specimens of Ultra-High Performance Concrete. ASTM International.

ASTM C293/C293M-10 (2010). Standard Test Method for Flexural Strength of Concrete (Using Simple Beam with Center-Point Loading). ASTM International, West Conshohocken.

ASTM C39/C39M (2016) Standard Test Method for Compressive Strength of Cylindrical Concrete Specimens.

ASTM C496/C496M-17, Standard Test Method for Splitting Tensile Strength of Cylindrical Concrete Specimens. ASTM International, West Conshohocken.

Bazaez, R., & Dusicka, P. (2018). Performance assessment of multi-column RC bridge bents seismically retrofitted with buckling-restrained braces. *Bulletin of Earthquake Engineering*, 16, 2135-2160.

Beck, J. L., & Skinner, R. I. (1974). The Seismic Response of a Reinforced Concrete Bridge Pier Designed to Step. *International Journal of Earthquake Engineering and Structural Dynamics*, 2(4), 343-358.

Benjamin A., Graybeal. (2006). Material Property Characterization of Ultra-High Performance Concrete (Report No. FHWA-HRT-06-103). *Federal Highway Administration*.

Beschi, C., Meda, A., & Riva, P. (2011). Column and Joint Retrofitting with High Performance Fiber Reinforced Concrete Jacketing. *Journal of Earthquake Engineering*, 15(7). https://doi.org/10.1080/13632469.2011.552167

Beydokhty, E. Z., & Shariatmadar, H. (2016). Behavior of Damaged Exterior RC Beam-Column Joints Strengthened by CFRP Composites. *Latin American Journal of Solids and Structures*, 13(5). https://doi.org/10.1590/1679-78252258

Billington, S., Barnes, R., & Breen, J. (2001). Alternate Substructure Systems for Standard Highway Bridges. *Journal of Bridge Engineering* - J BRIDGE ENG, 6(4), 87-94. https://doi.org/10.1061/(ASCE)1084-0702(2001)6:2(87)

Brühwiler, E., & Denarié, E. (2008). Rehabilitation of Concrete Structures Using Ultra-High Performance Fibre Reinforced Concrete. In *UHPC-2008*: The Second International Symposium on Ultra High Performance Concrete.

Bumstead, J., Korat, J., & Stephens, M. T. (2019). Repair Strategies for Earthquake-Damaged CFST Bridge Columns. In Structures Congress 2019: Bridges, Nonbuilding and Special Structures, and Nonstructural Components - Selected Papers from the *Structures Congress 2019* (pp. 16-22). https://doi.org/10.1061/9780784482230.016

CALTRANS (2013). Caltrans seismic design criteria, version 1.7. *California Department of Transportation, California*, USA, April, 2013.

Christopoulos, C., and Filiatrault, A. (2006). Principles of Passive Supplemental Damping and Seismic Isolation. IUSS Press, Pavia, Italy.

Doiron, G. (2016). Pier Repair/Retrofit Using UHPC—Examples of Completed Projects in North America. In International Interactive Symposium on Ultra-High Performance Concrete, 1.

El-Shweekh, A. T. M. A., Fahmy, M. F. M., & Abdel-Shafy, A. G. A. (2022). EVALUATION OF SEISMIC RESPONSE OF CFST BRIDGE COLUMNS WITH DIFFERENT CONNECTIONS TO FOUNDATION. *International Journal of Advances in Structural and Geotechnical Engineering*, 6(2). https://doi.org/10.21608/asge.2022.280715

Farzad, M., Rastkar, S., Sadeghnejad, A., & Azizinamini, A. (2019). Simplified Method to Estimate the Moment Capacity of Circular Columns Repaired with UHPC. Infrastructures, 4(3). https://doi.org/10.3390/infrastructures4030045

Farzad, M., Shafieifar, M., & Azizinamini, A. (2019). Retrofitting of Bridge Columns Using UHPC. Journal of Bridge Engineering, 24(12). https://doi.org/10.1061/(ASCE)BE.1943-5592.0001497

Fib Bulletin. (2003). Seismic assessment and retrofit of reinforced concrete buildings (Bulletin 24). *International Federation for Structural Concrete*.

Galal, K., Garcia, R., Mendis, P. & Hajjar, J.F. (2005). Retrofit of RC square short columns. *Engineering Structures*, 27(5), 801–813. https://doi.org/10.1016/j.engstruct.2005.01.003

Graybeal, B. (2020). Ultra-High Performance Concrete: A Bridge of the Future Solution. Presentation slides. https://nesmea.engr.uconn.edu/wp-content/uploads/sites/2933/2020/01/4-Ultra-High-Performance-Concrete-B-Graybeal.pdf

HIT-HY 100 Adhesive Anchor Technical Supplement. (2018).

Infanti, S., Kang, H.T., & Castellano, M.G. (2004). Retrofit of bridges in KOREA using viscous damper technology. In Proceedings of the 13th World Conference on Earthquake Engineering. (pp. 2211-2216). Vancouver BC.

Iqbal, A., Pampanin, S., Palermo, A., & Buchanan, A. (2010). Seismic response of post-tensioned timber walls. In Proceedings of 14th European Conference on Earthquake Engineering. Skopie-Ohrid, Republic of Macedonia.

Islam, N., & Hoque, M. M. (2017). Strengthening of Reinforced Concrete Columns by Steel Jacketing: A State of Review. Retrieved from https://www.researchgate.net/publication/313350544

Joe, C. D., & Moustafa, M. (2016). Cost and Ecological Feasibility of Using UHPC in Bridge Piers. In International Interactive Symposium on Ultra-High Performance Concrete.

Joel E. Parks, J. Ameli, Chris P. Pantelides, & Brown, D. N. (2016). Seismic Repair of Severely Damaged Precast Reinforced Concrete Bridge Columns Connected with Grouted Splice Sleeves. *ACI Structural Journal*, 113(3). https://doi.org/10.14359/51688756

Kalyoncuoğlu, A., Ghaffari, P., Goksu, C., & Ilki, A. (2012). Rehabilitation of Corrosion-Damaged Substandard RC Columns Using FRP Sheets. *Advanced Materials Research*, 639(1), 1096–1103. https://doi.org/10.4028/www.scientific.net/AMR.639-640.1096

Kaveh, A., & Zakian, P. (2012). Performance based optimal seismic design of RC shear walls incorporating soil-structure interaction using CSS algorithm. In *INTERNATIONAL JOURNAL OF OPTIMIZATION IN CIVIL ENGINEERING Int. J. Optim. Civil Eng* (Vol. 2, Issue 3). https://www.researchgate.net/publication/272182495

Keats, G. Palermo, A., & Mashal, M. Energy Dissipation Device. United States Provisional Patent Application: 61/149, 199. Filing Date April 17 2015.

Kelly, J. M., Skinner, R. I., & Heine, A. J. (1972). Mechanism of Energy Absorption in Special Devices for Use in Earthquake Resistant Structures. Bulletin of *N. Z. Society for Earthquake Engineering*, 5(3), 63-88.

Koo, I.Y., & Hong, S.G. (2016). Strengthening RC Columns with Ultra High Performance Concrete. In The *2016 Structures Congress*. Jeju Island, Korea.

Krish, Z. F., Kowalsky, M. J., Nau, J. M., & Rudolf, S. (2018). RAPID REPAIR OF REINFORCED CONCRETE BRIDGE COLUMNS VIA PLASTIC HINGE RELOCATION UTILIZING CONVENTIONAL MATERIALS. In *Eleventh U.S. National Conference on Earthquake Engineering*.

Kulicki, J. M. (2017). AASHTO LRFD bridge design specifications (8th ed.). In Bridge engineering handbook: Fundamentals (2nd ed.).

Lavorato, D., Bergami, A. V., Nuti, C., Briseghella, B., Xue, J., Tarantino, A. M., Marano, G. C., & Santini, S. (2017). Ultra-High-Performance Fibre-Reinforced Concrete Jacket for the Repair and the Seismic Retrofitting of Italian and Chinese RC Bridges. In COMPDYN 2017 - Proceedings of the 6th International Conference on Computational Methods in Structural Dynamics and Earthquake Engineering, 1. https://doi.org/10.7712/120117.5556.18147

Lee, D., and Taylor, D. P. (2001). Viscous Damper Development and Future Trends. *The Structural Design of Tall Buildings*, 10(5):311-320.

Mamlouk, M. S., & Zaniewski, J. P. (2011). Materials for Civil and Construction Engineers. Retrieved from https://books.google.com/books?id=ySorAAAAQBAJ

Maras, M. M., & Kantarcı, F. (2021). Structural Performance of Reinforced Concrete (RC) Moment Frame Connections Strengthened Using FRP Composite Jackets. *Arabian Journal for Science and Engineering*, 46(11), 10519–10532. https://doi.org/10.1007/s13369-021-06120-6

Marsh, M. L., Wernli, M., Garrett, B. E., Stanton, J. F., Eberhard, M. O., & Weinert, M. D. (2011). Application of Accelerated Bridge Construction Connections in Moderate-to-High Seismic Regions (Report No. 698). *Transportation Research Board*.

Mashal, M. (2015). Post-Tensioned Earthquake Damage Resistant Technologies for Accelerated Bridge Construction.

Mashal, M., Ebrahimpour, A., Acharya, M., Cantrell, J., Marshall, C., & Shokrgozar, A. (2021). A Precast Pier System for Accelerated Bridge Construction (ABC) in Idaho (Idaho Transportation Department Report No. 281). Boise, Idaho.

Mashal, M., White, S., & Palermo, A. (2012). Concepts and Developments for Accelerated Bridge Construction and Dissipative Controlled Rocking. In *15th World Conference on Earthquake Engineering.*

Paschalis, S. A., & Lampropoulos, A. P. (2022). DOWELS EFFECTIVENESS INVESTIGATION BETWEEN ULTRA HIGH PERFORMANCE FIBER REINFORCED CONCRETE AND REINFORCED CONCRETE. In Acta Polytechnica CTU Proceedings, 33, 0452-0459. https://doi.org/10.14311/APP.2022.33.0452

Priestley, M.J.N., Calvi, G.M. and Kowalsky, M. (2007). Displacement-based seismic design of structures. *Iuss Press*.

Raza, S., Khan, K., Menegon, S., Tsang, H. H., & Wilson, J. (2019). Strengthening and Repair of Reinforced Concrete Columns by Jacketing: State-of-the-Art Review. Sustainability, 11(14), 3208. https://doi.org/10.3390/su11113208

Ren, L., Fang, B., Wang, K., & Yuan, F. (2022). Numerical Investigation on Plastic Hinge Length of Ultra-High Performance Concrete Column under Cyclic Load. *Journal of Earthquake Engineering*, 26(3), 1281–1299. https://doi.org/10.1080/13632469.2020.1713929

Ritter, R., & Curbach, M. (2015). Material Behavior of Ultra-High-Strength Concrete under Multiaxial Stress States. *ACI Materials Journal*, 112(5). https://doi.org/10.14359/51687663

Shafieifar, M., & Azizinamini, A. (2018). New Connection Details to Connect Precast Cap Beams to Precast Columns Using Ultra High Performance Concrete (UHPC) for Seismic and Non-Seismic Regions (Order No. 10808647) [Doctoral dissertation, Florida International University]. ProQuest Dissertations and Theses.

Shao, Y., Nguyen, W., Bandelt, M. J., Ostertag, C. P., & Billington, S. L. (2022). Seismic Performance of High-Performance Fiber-Reinforced Cement-Based Composite Structural Members: A Review. *Journal of Structural Engineering*, 148(10), 3122004. https://doi.org/10.1061/(ASCE)ST.1943-541X.0003428

Skokandić, D., Vlašić, A., Kušter Marić, M., Srbic, M., & Mandić Ivanković, A. (2022). Seismic Assessment and Retrofitting of Existing Road Bridges: State of the Art Review. *Materials,* 15(13), 2523. https://doi.org/10.3390/ma15072523

Steel construction manual (14th ed.). (2005). American Institute of Steel Construction.

Stephens, M. T., Lehman, D. E., & Roeder, C. W. (2016). Design of CFST Column-to-Foundation/Cap Beam Connections for Moderate and High Seismic Regions. *Engineering Structures*, 122, 199-212. https://doi.org/10.1016/j.engstruct.2016.05.023

Tasdemir, E., Seracino, R., Kowalsky, M. J., Nau, J. M., & others. (2018). Repair of Reinforced Concrete Bridge Columns via Plastic Hinge Relocation: Volume 2: Repair Using CFRP Materials.

U.S. Department of Transportation, Federal Highway Administration. (2021, December). Deployments of UHPC in highway bridge construction.

https://usdot.maps.arcgis.com/apps/webappviewer/index.html?id=41929767ce164eba934d70883d775582

Valikhani, A., Jahromi, A. J., Mantawy, I. M., & Azizinamini, A. (2020). Numerical Modelling of Concrete-to-UHPC Bond Strength. Materials, 13(6). https://doi.org/10.3390/ma13061379

Vandoros, K. G., & Dritsos, S. E. (2008). Concrete Jacket Construction Detail Effectiveness When Strengthening RC Columns. *Construction and Building Materials*, 22(3), 264–276. https://doi.org/https://doi.org/10.1016/j.conbuildmat.2006.08.019

Wang, D., Ju, Y., Zheng, W., & Shen, H. (2018). Seismic Behavior and Shear Bearing Capacity of Ultra-High Performance, Fiber-Reinforced Concrete (UHPFRC) Beam-Column Joints. *Applied Sciences*, 8(5). https://doi.org/10.3390/app8050810

White, S. (2014). Controlled Damage Rocking Systems for Accelerated Bridge Construction (Master's thesis). University of Canterbury, Christchurch, New Zealand.

White, S., & Palermo, A. (2016). Quasi-static testing of posttensioned nonemulative column-footing connections for Bridge Piers. *Journal of Bridge Engineering,* 21(6). https://doi.org/10.1061/(ASCE)BE.1943-5592.0000872

WSDOT (2019). Bridge Design Manual M 23-50.19.

Wu, R., & Pantelides, C. P. (2017). Rapid Seismic Repair of Reinforced Concrete Bridge Columns. *ACI Structural Journal*, 114(5), 1339-1350.

Wu, Y. F., Griffith, M. C., & Oehlers, D. J. (2003). Improving the Strength and Ductility of Rectangular Reinforced Concrete Columns through Composite Partial Interaction: Tests. *Journal of Structural Engineering*, 129(9), 1183–1190.

Yu, R., Spiesz, P., & Brouwers, H. J.H. (2014). Mix Design and Properties Assessment of Ultra-High Performance Fibre Reinforced Concrete (UHPFRC). *Cement and Concrete Research*, 56. https://doi.org/10.1016/j.cemconres.2013.11.002

Zhou, Z., & Qiao, P. (2020). Direct Tension Test for Characterization of Tensile Behavior of Ultra-High Performance Concrete. *Journal of Testing and Evaluation*, 48(4), 2730-2749.